Abstract

ZHOU, JIAN. Fumed oxide-based nanocomposite polymer electrolytes for rechargeable lithium batteries. (Under the direction of Professor Peter S. Fedkiw.)

Rechargeable lithium batteries are promising power sources for portable electronic devices, implantable medical devices, and electric vehicles due to their high-energy density, low self-discharge rate, and environmentally benign materials of construction. However, the high reactivity of lithium metal limits the choice of electrolytes and impedes the commercialization of rechargeable lithium batteries. One way to tackle this problem is to develop electrolytes that are kinetically stable with lithium. Composite polymer electrolytes (CPEs) based on fumed oxides presented in this work are promising candidates for rechargeable lithium batteries.

The effects of fumed oxides (SiO_2, Al_2O_3, TiO_2) and binary mixtures of oxides (SiO_2/Al_2O_3) on ionic conductivity of CPEs based on poly(ethylene oxide) (PEO) oligomers (M_w =250, 200, 1000, and 2000) + lithium bis(trifluromethylsulfonyl)imide [$LiN(CF_3SO_2)_2$] (LiTFSI) (Li:O=1:20) are studied using electrochemical impedance spectroscopy (EIS), differential scanning calorimetry (DSC), and Fourier transform infrared spectroscopy. Fillers show similar effect on conductivity in all systems: no distinguishable effect is found with filler type, and addition of filler decreases conductivity at temperatures above the melting point (T_m) but increases conductivity at temperatures below. The insulating nature of fillers and stiffening of the polymer solvent (as evidenced by FTIR and DSC data) in the presence of fillers cause a decrease in

conductivity at temperatures above T_m, which remains constant upon addition of fillers. The increase in conductivity at temperatures below T_m can be attributed to faster ion transport along the filler surface. Addition of fumed oxides increases electrolyte viscosity (and elasticity) and the extent of enhancement varies with filler type: fumed silica shows the strongest and titania the least. Elastic modulus, yield stress, and normalized viscosity of gel-type composite electrolytes decrease with increasing oligomer M_w when electrolytes are amorphous. The reduction in structure strength may be ascribed to the enhanced interactions between surface hydroxyl groups on fumed oxides and polyether oxygens. Thus, the number of accessible –OH groups is reduced for interactions among fumed oxide particles, which dictates the strength of solid-like structure.

The interfacial stability between electrolyte and lithium is enhanced in the presence of fumed silica. The enhancement in interfacial stability is seen as a decrease in interfacial resistance and cell polarization, and an increase in lithium cycleability and cell capacity. The improved interfacial stability between CPE and lithium is attributed to less lithium corrosion (fillers scavenge water impurities that corrode lithium) and dendrite formation (electrolyte elasiticty inhibits dendrite formation). The extent of the enhancing effect of fumed silica depends on its surface chemistry, with the largest effect seen with hydrophilic fumed silica, which has the largest scavenging capacity and highest elasticity.

The effect on cycle capacity is reported of cathode material (metal oxide, carbon, and current collector) in lithium/metal oxide cells cycled with fumed silica-based composite electrolytes. Cells with composite electrolytes show higher capacity and less cell polarization than those with filler-free electrolyte. Among the three active materials

studied ($LiCoO_2$, V_6O_{13}, and Li_xMnO_2), V_6O_{13} cathodes deliver the highest capacity and Li_xMnO_2 cathodes render the best capacity retention. Discharge capacity of Li/$LiCoO_2$ cells is affected greatly by cathode carbon type and discharge capacity increases with decreasing carbon particle size. Current collector materials also play a significant role in cell cycling performance: Li/V_6O_{13} cells deliver increased capacity using Ni foil and carbon fiber current collectors in comparison to an Al foil.

In summary, fumed oxide-based nanocomposite electrolytes are promising candidates for lithium battery applications with high room-temperature conductivity, good mechanical strength, stable interface between lithium metal and electrolytes, and reasonable capacity and capacity retention with optimized cathode compositions.

FUMED OXIDE-BASED NANOCOMPOSITE POLYMER ELECTROLYTES FOR RECHARGEABLE LITHIUM BATTERIES

by

Jian Zhou

A dissertation submitted to the Graduate Faculty of
North Carolina State University
in partial fulfillment of the
requirements for the Degree of
Doctor of Philosophy

Department of Chemical Engineering

Raleigh, NC

December 2002

Approved By:

Peter S. Fedkiw Chairman of Advisory Committee	Saad A. Khan
Daniel L. Feldheim	John H. van Zanten

This work is dedicated to my parents, Mr. Junru Zhou and Ms. Yifen Gao, my husband, Mr. Dong Niu, and my brother, Mr. Yue Zhou, for their support, encouragement, patience, and love.

Biography

Jian Zhou was born to Mr. Junru Zhou and Ms. Yifen Gao in CiXi city, Zhejiang Province on January 2, 1971. In September 1989, she attended Tsinghua University in Beijing, where she spent eight years studying chemical engineering and earned her bachelor's and master's degrees in June 1994 and 1997. Both her undergraduate and graduate thesis research was done at Fluidization Laboratory of Tsinghua University (FLOTU) directed by Professor Yong Jin, who is a member of Chinese Academy of Engineering. During her study, she met Mr. Dong Niu who became her husband in March 1997. Jian and Dong then joined the Department of Chemical Engineering at North Carolina State to pursue their Ph.D.s together in August 1997. Her dissertation research was done under the direction of Dr. Peter S. Fedkiw.

Acknowledgments

I would like to thank my advisor, Professor Peter Fedkiw, for his guidance, patience, support, and encouragement throughout my educational endeavors. I would also like to acknowledge Professor Saad Khan for his assistance and advice. I am grateful to both Dr. Fedkiw and Dr. Khan for their mentorship and introducing me to the electrochemistry and rheology. In addition, I want to express my appreciations to Dr. Daniel Feldheim and Dr. John van Zanten for serving on my advisory committee. Special thanks also go to Dr. Jan Ganzer and Dr. Benny Freeman for their support.

I also gratefully acknowledge Dr. Michael Riley and Dr. Srinivasa Raghavan for tutoring me on electrochemical and rheological techniques. I also want to express my gratitude to Mr. Jeffrey Yerian, Ms. Ruchi Singhal, Ms. Hua Deng, and Dr. Yangxing Li for their help and cooperation in experimental work and thoughtful discussions. I would also like to thank Dr. Khan's research group in the Chemical Engineering Department, Dr. Franzen's research group (Mr. Simon Lappi and Mr. Scott Brewer) in the Chemistry Department, and Dr. Balik's research group (Ms. Jennifer Ayres and Mr. Marcus Hunt) in the Material Science Department for the training and accessibility to rheology, FTIR-ATR, and DSC measurements.

In addition, I gratefully acknowledge funding from the Department of Energy, Office of Basic Energy Sciences and Office of Transportation Technologies. I would also like to thank 3M for providing LiTFSI salt and Degussa for supplying fumed metal oxides. My appreciation also goes to Dr. Tim Mccarthi from Degussa Corp. for providing the information on –OH density of TiO_2.

Table of Contents

List of Tables

List of Figures

Chapter 1: Introduction

1.1 Motivation

The need to increase the energy density of rechargeable cells has become more urgent as a result of the recent rapid development of new applications, such as portable electronic devices (e.g., laptop, cellular phone, camcorder, etc.), electric vehicles, load leveling, and implantable biomedical devices (e.g., ventricular assist device and artificial heart) [1-3]. Because of the limited energy density of the active electrode components in aqueous cells based on the lead-acid or nickel-cadmium systems, conventional batteries do not meet the requirements of modern consumer electronic devices, nor those of electric traction [4,5]. Due to low density (0.53 g/cm^3) and low electronegativity (Li/Li^+ couple is –3.04 V vs. standard hydrogen electrode, SHE) of lithium metal [6], rechargeable lithium batteries are preferred power sources for the above mentioned applications. In addition, the small size of the lithium cation allows a range of intercalation cathode materials, which gives some design freedom of storage systems to suit different applications [7]. However, the high reactivity of lithium metal greatly limits the choice of usable electrolytes and impedes the commercialization of secondary lithium metal batteries. Alternative materials to a lithium metal anode such as lithium alloys and lithiated carbons are less reactive and more stable but at the cost of decreased voltage and capacity. One way to use lithium and hinder its corrosion is to develop a new type of electrolyte that is kinetically stable to lithium metal.

Fumed oxides including fumed silica, alumina, titania, and binary mixtures of fumed silica and alumina are often used as additives to a liquid and provide a higher viscosity than that of the parent liquid [8,9]. Native fumed oxides are hydrophilic due to surface hydroxyl groups, which determine many of physicochemical properties of these materials [10]. Hydrophobic fumed oxides can be produced by chemically modifying the surface hydroxyl groups with alkylsilanes, polysiloxanes, or organofunctional silanes [8,11-13]. Due to its unique surface chemistry, a three-dimensional network (gel) can be formed in the liquid. Fumed oxides also have properties such as extremely small particle size, high surface area, and high purity. Fumed oxide-based composite electrolytes studied in this work consist of three components: low-molecular weight poly(ethylene oxide) (PEO) (namely, poly(ethylene glycol) dimethyl ether, PEG-dm) + lithium salt (lithium bis(trifluromethylsulfonyl)imide [$LiN(CF_3SO_2)_2$], LiTFSI) + fumed oxide and combine the high conductivity of low-molecular weight PEO and mechanical strength of fumed oxide. Previous studies on fumed silica-based composite electrolytes showed that these composites possess encouraging properties as electrolytes for rechargeable lithium metal batteries: high room-temperature conductivity ($>10^{-3}$ S/cm), feasible mechanical strength ($G' > 10^5$ Pa for the composite with 20 wt.% R805 in PEG-dm (250) and LiTFSI salt), and stabilized electrolyte/lithium electrode interface [14-18].

1.2 Objectives

The primary objective of this research was to investigate the electrochemical and mechanical properties of fumed oxide-based composite electrolytes designed for

rechargeable lithium batteries. Effects of filler type, filler content, surface area (primary particle size), surface chemistry, and PEO oligomer molecular weight on ionic conductivity were examined. Fourier transform infrared spectroscopy and differential scanning calorimetry measurements were employed to understand the role fumed oxide fillers play in Li^+ transport in composite electrolytes. Effects of filler type and oligomer molecular weight on rheological properties (e.g., apparent viscosity, elastic modulus, and yield stress) were studied by steady state and dynamic rheology measurements. Lithium/lithium, Li/Li(Ni), and full-cell cycling in conjunction with electrochemical impedance spectroscopy was employed to study interfacial stability between fumed silica-based composite electrolytes and lithium with various surface chemistry of fumed silicas. Cell performance of fumed silica-based composite electrolytes in lithium full cells was evaluated to simulate practical rechargeable lithium batteries. Effects of cathode components such as active materials (intercalation metal oxides), carbon conductors, and current collectors on cell capacity were investigated. The ultimate objective of this research is to provide guidance and suggestions for design and synthesis of electrolytes that are suitable for rechargeable lithium batteries. The development of a practical rechargeable lithium battery also requires optimization of cathode compositions for particular electrolytes, but is beyond the scope of this research.

1.3 Outline of Thesis

A literature review introducing background of rechargeable lithium batteries is presented in Chapter 2, followed by an experimental section that provides details of

material preparations and characterizations in Chapter 3. Experimental results are presented in the following four chapters: Chapter 4 illustrates the study of Li^+ transport properties by electrochemical impedance spectroscopy, Fourier transform infrared spectroscopy, and differential scanning calorimetry measurements; Chapter 5 shows data of the interfacial stability between composite electrolytes and lithium obtained through half- and full-cell cycling in addition to electrochemical impedance spectroscopy methods; Chapter 6 demonstrates cell performance of composite electrolytes emphasizing the effect of cathode compositions; and Chapter 7 presents rheological properties of composite electrolytes by steady-state and dynamic rheology measurements. Chapter 8 concludes the experimental results and recommends future work.

1.4. References

[1] G.-A. Nazri, *MRS Bull.*, **27**, 628 (2002).

[2] D. R. Sadoway and A. M. Mayes, *MRS Bull.*, **27**, 590 (2002).

[3] E. S. Takeuchi and R. A. Leising, *MRS Bull.*, **27**, 624 (2002).

[4] H. A. Kiehne ed., *Battery Technology Handbook*, Marcel Dekker, Inc.: New York and Basel (1989).

[5] C. F. Holmes and A. R. Landgrebe eds., *Batteries for portable applications and electric vehicles*, The Electrochem. Soc.: Pennington, NJ (1997).

[6] J.-M. Tarascon and M. Armand, *Nature*, **414**, 359 (2001).

[7] R. Arnaud, D. Benrabah, and J.-Y. Sanchez, *J. Phys. Chem.*, **100**, 10882 (1996).

[8] G. Michael and H. Ferch, *Basic Characteristics of AEROSlL®*, Degussa Technical Bulletin Pigment No. 11, Akron, OH (1998).

[9] J. Mathias and G. Wannemacher, *J. Colloid & Interf. Sci.*, **125**, 61 (1988).

[10] V. M. Gun'ko, V. I. Zarko, V. V. Turov, R. Leboda, E. Chibowski, E. M. Pakhlov, E. V. Goncharuk, M. Marciniak, E. F. Voronin, and A. A. Chuiko, *J. Colloid & Interf. Sci.*, **220**, 302 (1999).

[11] M. Ettlinger, T. Ladwig, and A. Weise, *Prog. in Organic Coatings*, **40**, 31 (2000).

[12] V. M. Gun'ko, D. J. Sheeran, S. M. Augustine, and J. P. Blitz, *J. Colloid & Interf. Sci.*, **249**, 123 (2002).

[13] M. Ettlinger, *Highly Dispersed Metallic Oxides Produced by the AEROSIL® Process*, Degussa Technical Bulletin Pigments No. 56, Akron, OH (2002).

[14] J. Fan and P. S. Fedkiw, *J. Electrochem. Soc.*, **144**, 399 (1997).

[15] J. Fan, S. R. Raghavan, X. Y. Yu, S. A. Khan, P. S. Fedkiw, J. Hou, and G. L. Baker, *Solid State Ionics*, **111**, 117 (1998).

[16] J. Fan and P. S. Fedkiw, *J. Power Sources*, **72**, 165 (1998).

[17] S. R. Raghavan, M. W. Riley, P. S. Fedkiw, and S. A. Khan, *Chem. Mater.*, **10**, 244 (1998).

[18] S. R. Raghavan, H. J. Walls, and S. A. Khan, *Langmuir*, **16**, 7920 (2000).

Chapter 2: Literature Review

Due to their highest volumetric and gravimetric energy density (Figure 2.1 [1]), Li batteries (Li-ion and Li-metal batteries) are the most promising systems that can meet the special requirements of portable electronic devices, implantable medical devices, and electric vehicles. The achievements in this area are also encouraging: laboratory research has been rewarded by the commercialization of AA size lithium metal cells and several lithium-ion cells, which take over a great portion of secondary battery markets (Li-ion cells power 63% of portable electronic devices worldwide [1]). Figure 2.2 [1] schematically illustrates rechargeable lithium batteries: lithium-metal (Figure 2.2a) and lithium-ion (Figure 2.2b). Three major components of batteries are anode, electrolyte/separator, and cathode. Lithium ions migrate from anode to cathode during battery discharge but move at the opposite direction during battery charge. The anode and the cathode must be physically and electronically separated to avoid a short circuit. The electrolyte should be ionically conductive but electronically insulating. If the electrolyte is not self-supporting, such as liquid and gel electrolytes, a tough, thin and microporous polymer film such as Celgard® is used to provide an electronically insulating, ionically conductive spacer between electrodes. Moreover, the separator could also act as a fuse to withstand an internal short circuit without fire or explosion. The following literature review provides a brief summary of materials for rechargeable lithium battery technology.

2.1 Electrodes

A variety of materials have been studied for use in lithium batteries. The most common are lithium metal, lithium alloy, and carbon intercalation anode materials and transition metal oxide-based intercalation cathode materials. Primary factors for the selection of electrode materials are electrode potential versus lithium, capacity, stability and cycling behavior under a variety of conditions. Figure 2.3 shows the potential of a number of commonly used electrode materials versus lithium metal [2]. Note that for anode materials, a potential close to that of lithium metal is desirable. Likewise, high potentials of cathode materials are also desirable, though their use will be limited by the electrolyte stability with potential. For all materials, a relatively constant voltage profile versus capacity is desirable to provide constant power delivery.

2.1.1 Anodes

A variety of materials have been under investigation as the anode for rechargeable lithium batteries (Table 2.1) [3]. These include: metallic lithium, lithium alloys, lithiated carbon, redox polymer and its composite materials, transition metal oxide and sulphide, and lithium nitride. Lithium metal anodes, while providing the highest theoretical voltage, are also the most unstable, with problems ranging from highly resistive passivation films to poor morphology and dendrite formation. Alternative materials with a lower Li activity can greatly reduce the risk of passivation of the anode and increase the cell safety but at the cost capacity and voltage (Table 2.1).

2.1.1.1 Lithium Metal

Lithium is the lightest and most reactive metal with a theoretical capacity of 3860 mAh/g. The high energy of lithium metal encourages an attempt to realize a practical lithium metal anode cell. However, lithium metal is chemically very reactive and thermodynamically reacts with any organic electrolyte used in lithium batteries. The reactivity of lithium usually leads to a poor cycling efficiency and a relatively low available energy density of rechargeable lithium metal cells. So far, the commercialization of rechargeable lithium metal batteries is only available in Israel [4,5].

It is generally believed that a passive film, solid electrolyte interphase (SEI) film, is formed on the lithium surface which prevents further reaction and lowers lithium cycling efficiency. Figure 2.4 [6] schematically represents the lithium (Li)/polymer electrolyte (PE) or composite polymer electrolyte (CPE) interface [7]. Solid PEs have a rough surface, so when they are in contact with lithium, some spikes, like "2" in Figure 2.4, penetrate the oxide layer and the lithium metal, and a fresh SEI is formed at the Li/PE interface. In other parts of the interface, softer contacts between the PE and lithium are formed ("1" and "3" in Figure 2.4). Here the fresh SEI forms on the native oxide layer or, as a result of the retreat of lithium during its corrosion, the native oxide layer breaks and the gap is filled by a fresh SEI ("1" in Figure 2.4). As a result, only a portion of electrolyte intimately contacts the lithium [7].

Reasons for less than 100% lithium cycling efficiency are [8]: (i) Lithium is consumed by reaction with electrolyte during deposition and stripping process; (ii) Lithium is isolated in the passive film; and (iii) Deposited lithium exfoliates from the

base anode. This lithium is called “dead lithium”, which is electrochemically inert but chemically active. However, the main reason of poor cycling efficiency is believed to be the formation of “dead lithium” which is intimately affected by the morphology of the lithium surface.

There are three kinds of morphology of lithium: dendritic, granular, and mossy. Mossy lithium is formed when the deposition current is small and the salt concentration is high. This mossy lithium provides a high-cycling efficiency. A possible mechanism for lithium deposition onto the lithium surface with a passive film is proposed by Yoshimatsu et al. and follows the following sequence [9,10] (Figure 2.5):

(1) Lithium is deposited on a lithium anode under the passive film without serious damage to the film.

(2) Further lithium deposition often occurs at spots with higher lithium-ion conductivity, such as pits caused by discharge, crystalline defects, and the grain boundaries of lithium. Therefore, the lithium deposits non-uniformly.

(3) Mechanical stress is created by the non-uniform deposition under the protective film. As a result, the film is broken in certain places on the lithium surface. If the deposition current is small enough, the stress may not be strong enough to break the film and the deposited lithium may be particle-like or amorphous.

(4) Fiber-like lithium grows, like an extrusion of lithium, through these broken holes in the film. If the deposition continues for a long time, the lithium electrode becomes covered with long, fiber-like lithium. In this situation,

lithium-ion transport is hindered by the fiber-like lithium, thus lithium can not be deposited directly on the lithium electrode.

(5) Particle-like or amorphous lithium begins to be deposited on the crystalline defects (tip and bending points) of the fiber-like lithium. If the deposition continues, the fiber-like lithium will be covered by particle-like lithium at its top and bending points and the morphology of the lithium as a whole becomes mushroom-like (Figure 2.6) [9].

The dissolution process of plated lithium may be the reverse of the plating process. First the particle-like lithium on the kinks of the fiber-like film is dissolved. Then, the fiber-like lithium is dissolved. During this process, the fiber-like lithium is sometimes cut from the lithium substrate and becomes dead lithium. There is a large amount of dead lithium when the diameter of the fiber-like lithium is small under conditions of high-rate and/or low-temperature deposition, because the whiskers are easily cut.

Methods employed to study the morphology of lithium include Scanning Electron Microscopy (SEM) [10-25], Transmission Electron Microscopy (TEM) [22], Atomic Force Microscopy (AFM) [26-29], Electrochemical Quartz Crystal Microbalance (EQCM) [12,30-33], and optical microscopy [34]. Since the morphology of lithium is determined, in a large extent, by the nature of SEI film, studies of lithium metal anode mainly focus on the surface film. The methods used so far are Electrochemical Impedance Spectroscopy (EIS) [12,13,19,22,32,35-42], Infrared Spectroscopy (IR) or Fourier-transform Infrared Spectroscopy (FTIR) [11,13-18,27,43-64], X-ray

Photoelectron Spectroscopy (XPS or ESCA) [12,13,22,27,48-53,56,60,61,63,65-72], Energy Dispersive X-ray Analysis (EDAX) [18,73], X-ray Diffraction (XRD) [16,22,48,74,75], Energy Dispersive Spectroscopy (EDS) [51,70], Auger Electron Spectroscopy (AES) [11,27,75], UV-vis optical spectroscopy [33], Ellipsometry (E) [76,77], Raman spectroscopy [78], NMR [64], Scanning Vibrating Electrode Technique (SVET) [79], Temperature-Programmed Decomposition Mass Spectroscopy (TPD-MS) [11], Ion Chromatography (IC) [11], Gas Chromatography (GC) [64,73], Atomic Adsorption Spectroscopy (AAS) [11], and viscometry [80]. Due to the limitation of each method, usually more than one is needed to get a complete picture of the surface film. The surface film is affected by many factors including the cell materials (anode, electrolyte and cathode), impurities (H_2O, O_2, etc.), additives (CO_2, etc.) and operating conditions (open circuit or loaded, charge/discharge rate, voltage, etc.). The compositions of surface films on lithium metal and carbon anodes and the possible reactions of lithium salts and solvents are presented in the appendix 2.A.

2.1.1.2 Alternative Anode Materials to Lithium Metal

Alternative anodes must possess several key properties: (1) a low-equivalent weight; (2) a small free-energy change for the insertion reaction with Li; (3) a high diffusivity for Li^+ in the solid-state structure of the anode; (4) high reversibility for the insertion reaction; (5) good electronic conductivity; (6) thermal stability and chemical compatibility with the electrolyte; and (7) ease of fabrication into suitable electrode structures [81]. Lithium alloys and lithiated carbon materials are two major classes of

alternatives to metallic lithium anodes. The following sections will focus on the reviews of lithiated carbon materials that are commonly used in lithium-ion batteries.

Carbon was proposed as an insertion anode material as early as 1973 by Armand [82]. However, recent interest in this material has been aroused by the Sony rechargeable $C/LiCoO_2$ cell [83] apparently capable of greater than 1000 full depth of discharge cycles. Most carbonaceous materials that are capable of reversible lithium intercalation can be classified roughly as graphitic (layered structure) and non-graphitic (disordered).

The electron insertion reaction of mobile lithium ions into a solid carbon host proceeds according to the general reaction scheme [84]:

$$Li_xC_6 \underset{charge}{\overset{discharge}{\rightleftharpoons}} xLi^+ + xe^- + C_6 \qquad (2.1)$$

where $0 < x < 1$ for graphite. But some non-graphitic carbons can have much higher capacity with the values of x in Li_xC_6 as high as 5 [8]. The stage formation of lithiated graphite and the distribution of Li in LiC_6 are shown in Figure 2.7 and 2.8 [85]. The distribution of Li in high capacity non-graphitic carbons is shown in Figure 2.9 [8] according to various mechanism.

There is a significant loss of capacity during the first Li intercalation/de-intercalation cycle for both graphitic and non-graphitic carbons. Figure 2.10 shows first constant-current cycle for graphite (Figure 2.10a) and coke (Figure 2.10b), respectively. The potential profile of coke differs from that of graphite, in the sense that there is no distinguishable plateau of the curve slopes. This behavior is a consequence of the disordered structure providing electronically and geometrically nonequivalent sites, whereas for a particular intercalation stage in highly crystalline graphite the sites are

basically equivalent [86]. The irreversible charge loss during the first cycle is mainly caused by the formation of a solid-electrolyte-interphase (SEI) film due to electrolyte decomposition. Other factors are also believed to be responsible for (additional) irreversible charge losses: (i) irreversible reduction of impurities such as H_2O or O_2 on the carbon surface, (ii) reduction of "surface complexes" such as "surface oxide complexes" at the exterior surfaces of carbon, and (iii) irreversible lithium incorporation into the carbon matrix ("formation of residue compounds", e.g., by irreversible reduction of intercalation compounds such as graphite oxides).

For graphite anodes, co-intercalation of polar solvent molecules between the graphene layers also induces the additional irreversible specific charge [8]. This so-called "solvated intercalation reaction" (Figure 2.11) depends on (i) the crystallinity of the parent carbonaceous material, and (ii) the composition of the electrolyte. The mechanical destruction and the higher irreversible specific charge loss due to solvent co-intercalation seriously complicate the operation of graphitic anode materials. The first [87], and for a long time only, effective solvent to suppress solvent co-intercalation was ethylene carbonate (EC), which can form effectively protecting SEI films on the external graphite surfaces to filter out solvent molecules allowing only Li^+ migration into the graphite [16,88]. Usually mixtures of EC with low-viscosity and high-melting point solvents such as dimethyl carbonate (DMC) and diethyl carbonate (DEC) are used instead of high-viscosity, low-melting point, pure EC [13,85,89-92]. However, non-graphitic carbon anodes can operate in EC-free electrolytes. Consequently, the first practically applicable lithiated carbon anodes [93,94] were based on non-graphitic carbons. But

because of the flat potential profile and low cost of graphite, many battery companies such as Sanyo, Nikkiso, Matsushita/Panasonic, Moli Energy Ltd., Varta, and A&T use graphite in their prototype or already-commercialized lithium cells [8].

In order to promote the performance of graphite, numerous research activities have focused on the improvement of the protective films and the suppression of solvent co-intercalation. Besides ethylene carbonate, significant improvements have been achieved with other film-forming electrolyte components such as CO_2 [95-97], N_2O [98], SO_2 [88,99,100], S_x^{2-} [98,101], methyl propyl carbonate [59], ethyl methyl carbonate [58,102], and other asymmetric alkyl methyl carbonates [103], vinylpropylene carbonate [104], ethylene sulfite [8], S,S-dialkyl dithiocarbonates [105], vinylene carbonate [106], and species which evolve CO_2 during reduction including dimethyl pyrocarbonate [107], and chloroethylene carbonate [108-110].

2.1.2 Cathodes

The vast majority of cathode materials are intercalation compounds, capable of including and excluding lithium ions without a change in morphology. The desired properties are similar to anode materials: high capacity, high cycle life, stable to electrolyte, low impedance, high electronic conductivity, high lithium diffusivity, and mechanical stability. In addition, a high, constant potential relative to lithium is also desirable. So far, the most stable and widely studied materials are layered metal oxides $LiCoO_2$ [111-120], $LiNiO_2$ [117,121], and spinel $LiMn_2O_4$ [117,122-124].

$LiCoO_2$ and $LiNiO_2$ have a general formula of $LiMO_2$ with layered structures in which the Li^+ and the M^{3+} ions occupy octahedral sites in alternative layers between cubic close-packed oxygen layers (Figure 2.12) [8]. The reversible reaction during Li intercalation and de-intercalation is:

$$LiMO_2 \underset{charge}{\overset{discharge}{\rightleftharpoons}} Li_{1-x}MO_2 + xLi \qquad (2.2)$$

where M=Co or Ni, 0.1<x<0.9 for cobalt oxide and 0<x<0.5 for nickel oxide [84].

Presently, Li-based cobalt oxide is widely used in commercial Li-ion batteries [125]. The reason for the popularity of $LiCoO_2$ is that it has a stable structure that is easy to prepare with the ideal layered configuration. Although as high as 1070 Wh/kg of theoretical energy density can be achieved in $Li/Li_{1-x}CoO_2$ cells with x=1, the practical cycleability of process is generally limited to 0<x<0.5 (~ 200 Wh/kg of practical energy density) [84]. This drawback of the cobalt oxide system is due to the instability of extensively delithiated (charged) $Li_{1-x}CoO_2$ electrodes when $x \geq 0.5$, which are prone to oxygen loss in the presence of an organic electrolyte solvent, particularly when cells reach an operating temperature of 50°C or more [8]. Another disadvantage of cobalt oxide system is the high cost. Although $LiNiO_2$ is cheaper and is capable of providing high capacity (>130 mAh/g [8]), $LiNiO_2$ has been abandoned because of safety problems. Co-doped $LiNiO_2$ phase can make the system safer. Moreover, it can prevent the occurrence of extra lithium in the intersheet gap of pure $LiNiO_2$ [86,126,127]. Recent data have shown that a rechargeable capacity of approximately 180 mAh/g can be achieved from electrodes of composition of $LiNi_{1-x}Co_xO_2$ (0.1<x<0.3) [127].

Among all the systems, the spinel $LiMn_2O_4$ system remains the most attractive in terms of cost, material abundance, and nontoxicity although it has a lower capacity. The spinel framework of λ-MnO_2, the structure observed after full de-intercalation of lithium ions from $LiMn_2O_4$, is more open than the layered structure (Figure 2.13 [8]). One major problem of $Li_xMn_2O_4$ is its poor cycling stability. Several factors are believed to cause the capacity fade: (i) dissolution of spinel framework at the end of discharge by a disproportionation reaction: $2Mn^{3+}_{(solid)} \rightarrow Mn^{4+}_{(solid)} + Mn^{2+}_{(solution)}$ [128,129]; (ii) The onset of a crystallographic distortion in the spinel structure in the range of $1<x<2$ in $Li_xMn_2O_4$, which causes the fracture of the spinel particles at the surface [129]. For the range $1<x<2$ in $Li_xMn_2O_4$, the electrode consists of two phases: lithiated $Li_2Mn_2O_4$ spinel particles with tetragonal symmetry on the surface and unlithiated $LiMn_2O_4$ spinel particles with cubic symmetry in the bulk. The phase transition from cubic to tetragonal symmetry can cause a structural distortion (Jahn-Teller (tetragonal) distortion); and (iii) an instability of highly delithiated spinel particles in the organic electrolyte [89]. Adding cation dopants such as Li, Co, Ni, Cr, and Al [130-132] and fabricating thin-film $LiMn_2O_4$ [122,133] are the main strategies to improve the cycling stability of spinel $LiMn_2O_4$ systems.

2.2 Electrolytes/Separators

The electrolyte and separator should be ionically conductive while electronically insulating, which allows fast ionic transport and physically separate anode and electrode. The ideal electrolyte for practical lithium batteries would possess the following properties: (1) high conductivity (at least 1×10^{-3} S/cm) at ambient temperature, (2)

chemically and electrochemically stable to electrodes over a wide range of temperature and voltage (1.5-3.5 V for lithium metal batteries and more than 4.5 V for lithium-ion cells), (3) mechanically stable to keep electrodes apart, (4) easy processibility, (5) low toxicity, and (6) low price.

Lithium battery electrolytes can be divided into three categories: liquid, solid, and composite (solid and liquid hybrids). Each of these types has advantages and disadvantages. Liquid electrolytes generally show better leveling capabilities for temperature and concentration discontinuities, maintenance of a permanent interfacial contact at electrodes, allowance for small volume changes, offer larger electrochemical windows, and higher conductivity. Typical advantages of solid electrolytes are exclusive cationic or anionic conductivity, no need for separators, no gassing and leakage problems, resistance to mechanical stresses, and ease of cell assembly. The composites attempt to combine the advantages of both liquid and solid electrolytes.

2.2.1 Electrolyte Properties

Ionic conductivity (σ) of a liquid or a crystalline solid can be described by classical Arrhenius theory [134]:

$$s = \frac{A}{T}\exp(\frac{-E}{T}) \qquad (2.3)$$

where A is a pre-exponential factor related to ion mobility and ion association and E is the activation energy. For polymer electrolytes, the Arrhenius theory only holds true well above the glass transition temperature, T_g. Conductivity in polymer electrolytes is

generally fitted in terms of a Vogel-Tamman-Fulcher (VTF) equation [134]:

$$s = \frac{A}{T^m}\exp\left[\frac{-E_0}{(T-T_0)}\right] \qquad (2.4)$$

where $m \in \{-1/2, 0, 1/2, 1\}$, E_0 is an apparent activation energy different from E, and T_0 is an apparent glass-transition temperature related to T_g; T_0 has been reported to be approximately 30 to 50°C lower than T_g. It does not appear that m is related to any physical properties of the electrolyte.

Although conductivity is a useful measurement in determining an electrolyte's value, it does not give a complete picture. Conductivity is a measure of the current carried not only by lithium ions, but also by the anions present in the system as well. The useful conductivity is that carried by lithium ions. In systems where ion association occurs, it is impossible to distinguish between lithium ions and other charged species containing lithium ions. In these cases, the conductivity of interest is that carried by the lithium ion constituent, which is characterized by lithium transference number. The transference number of a cation or anion constituent is the net number of (electrochemical) gram-equivalents of that ion constituent that crosses an imaginary plane in the solution, in the direction of the cathode or anode respectively, when one faraday of electricity passes across that plane [135]. Because the total number of gram-equivalents of all the ion constituents transferred in both directions is equal to the number of faradays passed through the solution, the sum of all transference numbers for a given system must be unity.

The electrochemical stability is also an important parameter for electrolytes. Potential window, the potential range under which the electrolyte is neither oxidized nor reduced, is often used to characterize the electrochemical stability. This value must cover potentials from the anodic limit E_{ox} and cathodic limit E_{Red}. The potential window is generally measured by cyclic voltammetry (CV) or linear-sweep voltammetry. Therefore this value depends on the experimental conditions such as scan rate and current density. The electrolyte must be also chemically stable with the anode and cathode. Many factors affect the electrode/electrolyte stability such as the history of electrode (cycling, storage, etc.), electrolyte composition (salt and solvent type and salt concentration), impurities, and additives.

2.2.2 Electrolyte types

Liquid electrolytes for lithium batteries mostly include the solutions of lithium salts (LiX) in aprotic solvents (most commonly ethers and carbonates) and organic molten salts. The aprotic solvents used in lithium batteries include polyethers (poly(propylene oxide) (PEO)), cyclic esters (ethylene carbonate (EC), propylene carbonate (PC)), open-chain esters (dimethyl carbonate (DMC), methyl ethyl carbonate (MEC), diethyl carbonate (DEC), methyl propyl carbonate (MPC)), and ethers (1,3-dioxolane (DIOX), dimethoxyetane (DME), tetrahydrofuran (THF), 2-methyltetrahydrofuran (2Me-THF)), as well as inorganic sulfur compounds (SO_2, $SOCl_2$). Acetonitrile (AN) and γ-butyrolactone (GBL) are also used as solvents. Lithium salts include $LiClO_4$, $LiBF_4$, $LiAsF_6$, $LiPF_6$, $LiCF_3SO_3$ (LiTrif), $Li[N(SO_2CF_3)_2]$ (LiIm or

LITFSI), $LiN(C_2F_5SO_2)_2$ (LiBETI), $Li[N(SO_2)(CF_2)_4(SO_2)]$, $Li[N(SO_2)(CF_2)_n(SO)_2]$ (n=1-3), $Li[C(SO_2CF_3)_3]$ (LiMe), $Li[C(SO_2CF_3)_2(SO_2C_4F_9)]$, $Li_2[C_2(SO_2CF_3)_4(S_2O_4C_3F_6)]$. Liquid electrolytes often offer high conductivity (10^{-2} S/cm at room temperature), but they need mechanical support in the form of an inert microporous separator. Other disadvantages of liquid electrolytes are the possible leakage problem and gassing problem related to volatile organic solvents.

Solvent-free solid polymer electrolytes (SPEs) can bypass many problems of liquid electrolytes and have the following advantages [136]: (i) suppression of dendritic growth, (ii) enhanced endurance to varying electrode volume, (iii) reduced reactivity with liquid electrolytes, (iv) improved safety, and (v) better shape flexibility and manufacturing integrity. An SPE is composed of a lithium salt dissolved in a high-molecular weight polyether host (e.g., poly(ethylene oxide) (PEO) and poly(propylene oxide) (PPO)), which acts as a solid solvent. Copolymers made of polyether-grafted polyether, polysiloxane, and polyphosphazene backbones are also used as hosts for lithium salt [136]. However, the ionic conductivities of SPEs at room temperature are less than 10^{-4} S/cm, which is not sufficient for power production [8]. The ionic conduction mechanism of an SPE is intimately associated with the local segmental motions of the polymer's amorphous phase. It is assumed that ions are transported by the semi-random motion of short polymer segments, providing free-volume into which the ion can diffuse under the influence of an electric field. Figure 2.14 shows this type of motion schematically [8].

Composite polymer electrolyte (CPE) or hybrid polymer electrolytes encompass a wide variety of electrolytes that attempt to combine benefits of both liquid and solid electrolytes. Some examples include:

1. Plasticized or gelled SPEs (liquid plasticizer and/or solvent(s) incorporated to polymer matrix such as PEO [137-139], poly(methyl methacrylate) (PMMA) [37], polyacrylonitrile (PAN) [140,141], and poly(vinylidene fluoride) (PVdF) [142,143]).
2. Rubbery salts (polymer electrolytes added to molten salts) [144-146].
3. Physically gelled liquid electrolytes (solid particle added to liquid electrolyte) [147-151].

These electrolytes provide higher conductivity ($>10^{-3}$ S/cm at room temperature) than a pure SPE. Also they showed improved mechanical property and interfacial stability compared to liquid electrolytes.

Of primary relevance to this proposed work are those composites that contain inorganic solid particles. Research on this type of electrolyte has been reviewed by Kumar and Scanlon [152]. Addition of ion-conducting and even some inert ceramic fillers enhances the conductivity of a high-MW PEO electrolyte. This increase is attributed to an increase in volume fraction of amorphous phase [41,153-155]. But the addition of fillers also increases the glass transition temperature that suppresses polymer chain motion and thus the transport of lithium ion [152]. Therefore, a decrease of the conductivity with the addition of fillers was observed [139,141,147,149-151,156]. Numerous experimental evidence consistently shows that the lithium-composite

electrolyte interfaces are more stable and efficient in cycling lithium than metal-parent polymer electrolyte interfaces [141,147,152,157]. The mechanism for the improved stability is not well understood. However, some attribute this improvement to the capability of the fillers to scavenge impurities such as water and oxygen, which can react with lithium and thus accelerate the passivation of lithium [141,157]. For example, Figure 2.15 shows an improvement in the time dependence of the electrolyte with lithium metal by the addition of zeolite particles to a composite gel polymer electrolyte comprised of EC:PC:PAN:$LiAsF_6$ [141]. Previous studies on fumed silica-based composite polymer electrolytes shows that the significant improvement of mechanical strength with a minor loss of conductivity by adding fumed silica to aprotic organic liquid electrolytes (primary PEO oligomers) (Figure 2.16) [151]. And an improvement in the lithium interfacial stability at open circuit was also observed (Figure 2.17) [147].

2.3 References

[1] J.-M. Tarascon and M. Armand, *Nature*, **414**, 359 (2001).

[2] D. Linden ed., *Handbook of Batteries, 2nd edition*., McGRAW-HILL, INC.: New York (1994).

[3] D. Fauteux and R. Koksbang, *J. Appl. Electrochem.*, **23**, 1 (1993).

[4] P. Dan, E. Mengeritski, Y. Geronov, D. Aurbach, and I. Weisman, *J. Power Sources*, **54**, 143 (1995).

[5] P. Dan, E. Mengeritsky, D. Aurbach, I. Weissman, and E. Zinigrad, *J. Power Sources*, **68**, 443 (1997).

[6] G. Ardel, D. Golodnitsky, and E. Peled, *J. Electrochem. Soc.*, **144**, L208 (1997).

[7] E. Peled, D. Golodnitsky, G. Ardel, and V. Eshkenazy, *Electrochim. Acta*, **40**, 2197 (1995).

[8] J. O. Besenhard ed., *Handbook of Battery Materials*, WILEY-VCH: Weinheim (1999).

[9] M. Arakawa, S. Tobishima, Y. Nemoto, M. Ichimura, and J. Yamaki, *J. Power Sources*, **43-44**, 27 (1993).

[10] I. Yoshimatsu, T. Hirai, and J.-i. Yamaki, *J. Electrochem. Soc.*, **135**, 2422 (1988).

[11] A. Kominato, E. Yasukawa, N. Sato, T. Ijuuin, H. Asahina, and S. Mori, *J. Power Sources*, **68**, 471 (1997).

[12] K. Naoi, M. Mori, Y. Naruoka, and W. M. Lamanna, *J. Electrochem. Soc.*, **146**, 462 (1999).

[13] D. Aurbach, B. Markovsky, A. Shechter, Y. Ein-Eli, and H. Cohen, *J. Electrochem. Soc.*, **143**, 3809 (1996).

[14] D. Aurbach, A. Zaban, Y. Ein-Eli, I. Weissman, O. Chusid, B. Markovsky, M. Levi, E. Levi, A. Schechter, and E. Granot, *J. Power Sources*, **68**, 91 (1997).

[15] D. Aurbach, O. Chusid, I. Weissman, and P. Dan, *Electrochim. Acta*, **41**, 747 (1996).

[16] D. Aurbach, Y. Ein-Eli, O. C. (Youngman), Y. Carmeli, M. Babai, and H. Yamin, *J. Electrochem. Soc.*, **141**, 603 (1994).

[17] Y. Ein-Eli and D. Aurbach, *J. Power Sources*, **54**, 281 (1995).

[18] D. Aurbach, I. Weissman, H. Yamin, and E. Elster, *J. Electrochem. Soc.*, **145**, 1421 (1998).

[19] F. Orsini, A. D. Pasquier, B. Beaudoin, J. M. Tarascon, M. Trentin, N. Langenhuizen, E. D. Beer, and P. Notten, *J. Power Sources*, **76**, 19 (1998).

[20] J. Yamaki, S. Tobishima, K. Hayashi, K. Saito, Y. Nemoto, and M. Arakawa, *J. Power Sources*, **74**, 219 (1998).

[21] T. Osaka, T. Momma, Y. Matsumoto, and Y. Uchida, *J. Electrochem. Soc.*, **144**, 1709 (1997).

[22] I. Epelboin, M. Froment, M. Garreau, J. Thevenin, and D. Warin, *J. Electrochem. Soc.*, **127**, 2100 (1980).

[23] Y. Geronov, F. Schwager, and R. H. Muller, *J. Electrochem. Soc.*, **129**, 1422 (1982).

[24] C. Brissot, M. Rosso, J.-N. Chazalviel, P. Baudry, and S. Lascaud, *Electrochim. Acta*, **43**, 1569 (1998).

[25] M. Odziemkowski and D. E. Irish, *J. Electrochem. Chem.*, **140**, 1546 (1993).

[26] D. Aurbach and Y. Cohen, *J. Electrochem. Soc.*, **144**, 3355 (1997).

[27] K.-I. Morigaki and A. Ohta, *J. Power Sources*, **76**, 159 (1998).

[28] A. C. Chu, J. Y. Josefowica, and G. C. Farrington, *J. Electrochem. Soc.*, **144**, 4161 (1997).

[29] K. A. Hirasawa, T. Sato, H. Asahina, S. Yamaguchi, and S. Mori, *J. Electrochem. Soc.*, **144**, L81 (1997).

[30] D. Aurbach and M. Moshkovich, *J. Electrochem. Soc.*, **145**, 2629 (1998).

[31] K. Naoi, M. Mori, and Y. Shinagawa, *J. Electrochem. Soc.*, **143**, 2517 (1996).

[32] A. Lisowska-Oleksiak, *Solid State Ionics*, **119**, 205 (1999).

[33] Y. Mo, Y. Gofer, E. Hwang, Z. Wang, and D. A. Scherson, *J. Electroanal. Chem.*, **409**, 87 (1996).

[34] T. Osaka, T. homma, T. Momma, and H. Yarimizu, *J. Electroanal. Chem.*, **421**, 153 (1997).

[35] A. Zaban and D. Aurbach, *J. Power Sources*, **54**, 289 (1995).

[36] G. B. Appetecchi, F. Croce, G. Dautznberg, M. Mastragostino, F. Ronci, B. Scrosati, F. Soavi, A. Zanelli, F. Alessandrini, and P. P. Prosini, *J. Electrochem. Soc.*, **145**, 4126 (1998).

[37] G. B. Appetecchi, F. Croce, and B. Scrosati, *Electrochim. Acta*, **40**, 991 (1995).

[38] V. E. Kazarinov and V. S. Bagotzky, *J. Power Sources*, **20**, 259 (1987).

[39] D. Fauteux, *Solid State Ionics*, **17**, 133 (1985).

[40] D. Fauteux, *J. Electrochem. Soc.*, **135**, 2231 (1988).

[41] F. Croce and B. Scrosati, *J. Power Sources*, **43-44**, 9 (1993).

[42] N. Takami and T. Ohsaki, *J. Electrochem. Soc.*, **139**, 1849 (1992).

[43] S. Barusseau, B. Beden, M. Broussely, and F. Perton, *J. Power Sources*, **54**, 296 (1995).

[44] D. Aurbach, M. L. Daroux, P. W. Faguy, and E. Yeager, *J. Electrochem. Soc.*, **135**, 1863 (1988).

[45] D. Aurbach and O. C. (Youngman), *J. Electrochem. Soc.*, **140**, L155 (1993).

[46] D. Aurbach, *J. Electrochem. Soc.*, **140**, L1 (1993).

[47] D. Aurbach and O. Chusid, *J. Power Sources*, **68**, 463 (1997).

[48] D. Aurbach and A. Zaban, *J. Electrochem. Soc.*, **141**, L1 (1994).

[49] D. Aurbach, M. L. Daroux, P. W. Faguy, and E. Yeager, *J. Electrochem. Soc.*, **134**, 1611 (1987).

[50] D. Aurbach and Y. Gofer, *J. Electrochem. Soc.*, **138**, 3529 (1991).

[51] D. H. Shen, S. Subbaro, B. J. Nakamuro, S. P. S. Yen, C. P. Bankston, and G. Halpert, in: B. Bro (Ed.), *Primary and Secondary Ambient Temperature Lithium Batteries*, The Electrochemical Society, p. 409 (1988).

[52] S. P. S. Yen, D. H. Shen, R. P. Vasquez, B. J. Carter, and R. B. Somoano, in: A. N. Dey (Ed.), *Lithium Batteries*, The Electrochemical Society, Pennington, NJ, p. 403 (1984).

[53] K. Kanamura, H. Takezawa, S. Shiraishi, and Z.-I. Takehara, *J. Electrochem. Soc.*, **144**, 1900 (1997).

[54] D. Aurbach, O. Youngman, and P. Dan, *Electrochim. Acta*, **35**, 639 (1990).

[55] E. Goren, O. C. (Youngman), and D. Aurbach, *J. Electrochem. Soc.*, **138**, L6 (1991).

[56] D. Aurbach, Y. Gofer, and E. Goren, in: M. Salomon (Ed.), *Primary and Secondary Lithium Batteries*, The Electrochemical Society, Pennington, NJ, p. 247 (1991).

[57] D. Aurbach, *J. Electrochem. Soc.*, **136**, 906 (1989).

[58] Y. Ein-Eli, S. R. Thomas, V. Koch, D. Aurbach, B. Markovsky, and A. Schechter, *J. Electrochem. Soc.*, **143**, L273 (1996).

[59] Y. Ein-Eli, S. F. McDevitt, D. Aurbach, B. Markovsky, and A. Schechter, *J. Electrochem. Soc.*, **144**, L180 (1997).

[60] K. M. Abraham and L. Pitts, *J. Electrochem. Soc.*, **130**, 1618 (1983).

[61] K. M. Abraham and S. M. Chaudri, *J. Electrochem. Soc.*, **133**, 1307 (1986).

[62] Y. Ein-Eli, S. R. Thomas, and V. R. koch, *J. Electrochem. Soc.*, **143**, L195 (1996).

[63] D. Aurbach, I. Weissman, A. Zaban, and O. C. (Youngman), *Electrochim. Acta*, **39**, 51 (1994).

[64] M. Jean, A. Chausse, and R. Messina, *Electrochim. Acta*, **43**, 1795 (1998).

[65] J. P. Contour, A. Salesse, M. Froment, M. Garreau, J. Thevenin, and D. Warin, *J. Microsc. Spectrosc. Electron.*, **4**, 483 (1979).

[66] R. Somoano, B. J. Carter, S. S. Rao, and D. Shen. in *Proc. 20th Intersoc. Energy Convers. Eng. Conf.* (1985).

[67] K. Kanamura, H. Tamura, and Z.-I. Takehara, *J. Electroanal. Chem. Interfacial Electrochem.*, **333**, 127 (1992).

[68] K.-I. Morigaki, N. Kabuto, K. Yoshino, and A. Ohta, *J. Power Sources*, **15**, 267 (1995).

[69] C. R. Anderson, S. D. James, W. P. Kilroy, and R. N. Lee, *Appl. Surf. Sci.*, **9**, 388 (1981).

[70] D. Bar-Tow, E. Peled, and L. Burstein, *J. Electrochem. Soc.*, **146**, 824 (1999).

[71] D. Aurbach, O. Youngman, Y. Gofer, and A. Meitav, *Electrochim. Acta*, **35**, 625 (1990).

[72] V. R. Koch, *J. Electrochem. Soc.*, **126**, 181 (1979).

[73] D. Aurbach, A. Zaban, Y. Gofer, O. Abramson, and M. Ben-Zion, *J. Electrochem. Soc.*, **142**, 687 (1995).

[74] M. Froment, M. Garreau, J. Thevenin, and D. Warin, *J. Microsc. Spectrosc. Electron.*, **4**, 111 (1979).

[75] G. Nazri and R. H. Muller, *J. Electrochem. Soc.*, **132**, 1385 (1985).

[76] F. Kong, J. Kim, X. Song, M. Inaba, K. Kinoshita, and F. McLarnon, *Electrochem. and Solid State Lett.*, **1**, 39 (1998).

[77] R. V. Moshtev, *J. Power Sources*, **11**, 93 (1984).

[78] M. Odziemkowski and D. E. Irish, *J. Electrochem. Soc.*, **139**, 3063 (1992).

[79] M. Ishikawa, S. Yoshitake, M. Morita, and Y. Matsuda, *J. Electrochem. Soc.*, **141**, L159 (1994).

[80] A. N. Dey and E. J. Rudd, *J. Electrochem. Soc.*, **121**, 1294 (1974).

[81] K. M. Abraham, *Electrochim. Acta*, **38**, 1233 (1993).

[82] M. B. Armand, in: W. V. Gool (Ed.), *Fast Ion Transport in Solids*, North Holland, Amsterdam, p. 665 (1973).

[83] T. Nagaura. *A lithium ion battery*. in *4th International Rechargeable Battery Seminar*, Deerfield Beach, Florida (1990).

[84] J. Lipkowski and P. N. Ross eds., *The Electrochemistry of Novel Materials*, VCH Publishers, Inc.: New York (1994).

[85] M. Wakihara and O. Yamamoto eds., *Lithium Ion Batteries Fundamentals and Performances*, Wiley-VCH: Weinheim (1998).

[86] G. Pistoia ed., *Lithium Bateries New Materials, Developments and Perspectives*. Industrial Chemistry Library, Volume 5, Elsevier Science B. V.: Amsterdam (1994).

[87] R. Fong, U. v. Sacken, and J. R. Dahn, *J. Electrochem. Soc.*, **137**, 2009 (1990).

[88] J. O. Besenhard, M. Winter, J. Yang, and W. Biberacher, *J. Power Sources*, **54**, 228 (1995).

[89] D. Guyomard and J. M. Tarascon, *Solid State Ionics*, **69**, 222 (1994).

[90] D. Guyomard and J. M. Tarascon, *J. Power Sources*, **54**, 92 (1995).

[91] D. Aurbach, A. Zaban, A. Schechter, Y. Ein-Eli, E. Zinigrad, and B. Markovsky, *J. Electrochem. Soc.*, **142**, 2873 (1995).

[92] A. Ohta, H. Koshina, H. Okuno, and H. Murai, *J. Power Sources*, **54**, 6 (1995).

[93] M. Mohri, N. Yanagisawa, Y. Tajima, H. Tanaka, T. Mitate, S. Nakajima, M. Yoshida, Y. Yoshimoto, T. Suzuki, and H. Wada, *J. Power Sources*, **26**, 545 (1989).

[94] R. Kanno, Y. Takeda, T. Ichikawa, K. Nakanishi, and O. Yamamoto, *J. Power Sources*, **26**, 535 (1989).

[95] O. Y. Chusid, Y. E. Ely, and D. Aurbach, *J. Power Sources*, **43-44**, 47 (1993).

[96] D. Aurbach and A. Zaban, *J. Electrochem. Soc.*, **141**, 1808 (1994).

[97] D. Aurbach, M. D. Levi, and A. Schechter, *J. Phys. Chem. B*, **101**, 2195 (1997).

[98] J. O. Besenhard, M. W. Wagner, M. Winter, A. D. Jannakoudakis, P. D. Jannakoudakis, and E. Theodoridou, *J. Power Sources*, **44**, 413 (1993).

[99] Y. Ein-Eli, S. R. Thomas, and V. R. Koch, *J. Electrochem. Soc.*, **144**, 1159 (1997).

[100] Y. Ein-Eli, S. R. Thomas, and V. R. Koch, *J. Electrochem. Soc.*, **144**, L195 (1997).

[101] M. W. Wagner, C. Liebenow, and J. O. Besenhard, *J. Power Sources*, **68**, 328 (1997).

[102] H. Nakamura, H. Komatsu, and M. Yoshio, *J. Power Sources*, **62**, 219 (1996).

[103] Y. Ein-Eli, S. F. McDevitt, and R. Laura, *J. Electrochem. Soc.*, **145**, L1 (1998).

[104] C. F. Holmes and A. R. Landgrebe eds., *Batteries for portable applications and electric vehicles*, The Electrochemical Society: Pennington, NJ (1997).

[105] Y. Ein-Eli and S. F. McDevitt, *J. Solid State Electrochem.*, **1**, 227 (1997).

[106] Y. Naruse, S. Fujita, and A. Omaru, *Non-aqueous liquid electrolyte secondary cell* (1998).

[107] F. Coowar, A. M. Christie, P. G. Bruce, and C. A. Vincent, *J. Power Sources*, **75**, 144 (1998).

[108] M. Winter and P. Novak, *J. Electrochem. Soc.*, **145**, L27 (1998).

[109] Z. X. Shu, R. S. McMillan, and J. J. Murray, *J. Electrochem. Soc.*, **142**, L161 (1995).

[110] Z. X. Shu, R. S. McMillan, J. J. Murray, and I. J. Davisdson, *J. Electrochem. Soc.*, **143**, 2230 (1996).

[111] H. Wang, Y.-I. Jang, B. Huang, D. R. Sadoway, and Y.-M. Chiang, *J. Electrochem. Soc.*, **146**, 473 (1999).

[112] M. D. Levi, G. Salitra, B. Markovsky, H. Teller, D. Aurbach, U. Heider, and L. Heider, *J. Electrochem. Soc.*, **146**, 1279 (1999).

[113] E.-D. Jeong, M.-S. Won, and Y.-B. Shim, *J. Power Sources*, **70**, 70 (1998).

[114] T. J. Boyle, D. Ingersol, T. M. Alam, C. J. Tafoya, M. A. Rodriguez, K. Vanheusden, and D. H. Doughty, *Chem. Mater.*, **10**, 2270 (1998).

[115] K. Ozawa, *Solid State Ionics*, **69**, 212 (1994).

[116] J. B. Goodenough, K. Mizushima, and T. Takeda, *Japanese J. Appl. Phy.*, **19**, 305 (1980).

[117] M. Winter, J. O. Besenhard, M. E. Spahr, and P. Novak, *Adv. Mater.*, **10**, 725 (1998).

[118] J. N. Reimers and J. R. Dahn, *J. Electrochem. Soc.*, **140**, 2752 (1993).

[119] H. Wang, Y. Jang, B. Huang, D. R. Sadoway, and Y.-M. Chiang, *J. Electrochem. Soc.*, **146**, 473 (1999).

[120] J. Cho, Y. J. Kim, and B. Park, *J. Electrochem. Soc.*, **148**, A1110 (2001).

[121] J. R. Dahn, U. v. Sacken, M. R. Juzkow, and H. Al-Janaby, *J. Electrochem. Soc.*, **138**, 2207 (1991).

[122] P. Liu, J.-G. Zhang, J. A. Turner, C. E. Tracy, and D. K. Benson, *J. Electrochem. Soc.*, **146**, 2001 (1999).

[123] H. Huang, C. A. Vincent, and P. G. Bruce, *J. ELectrochem. Soc.*, **146**, 481 (1999).

[124] A. D. Pasquier, A. Blyr, P. Courjal, D. Larcher, G. Amatucci, B. Gerand, and J.-M. Tarascon, *J. Electrochem. Soc.*, **146**, 428 (1999).

[125] T. Nagaura and K. Tazawa, *Prog. Batt. Sol. Cells*, **9**, 20 (1990).

[126] C. Delmas, I. Saadoune, and A. Rougier, *J. Power Sources*, **44**, 595 (1993).

[127] W. Li and J. C. Currie, *J. Electrochem. Soc.*, **144**, 2773 (1997).

[128] D. H. Jang, Y. J. Shin, and S. M. Oh, *J. Electrochem. Soc.*, **143**, 2204 (1996).

[129] M. M. Thackeray, *J. Electrochem. Soc.*, **142**, 2558 (1995).

[130] G. Li, H. Ikuta, T. Uchida, and M. Wakihara, *J. Electrochem. Soc.*, **143**, 178 (1996).

[131] P. Arora, B. N. Popov, and R. E. White, *J. Electrochem. Soc.*, **145**, 807 (1998).

[132] J. M. Tarascon, E. Wang, F. K. Shokoohi, W. R. Mckinnon, and S. Carlson, *J. Electrochem. Soc.*, **138**, 2859 (1991).

[133] A. Rougier, K. A. Striebel, S. J. Wen, and E. J. Cairns, *J. Electrochem. Soc.*, **145**, 2975 (1998).

[134] I. Olsen and R. Koksbang, *J. Electrochem. Soc.*, **143**, 570 (1996).

[135] M. Spiro, *J. Chem. Edu.*, **33**, 464 (1956).

[136] J. Y. Song, Y. Y. Wang, and C. C. Wan, *J. Power Sources*, **77**, 183 (1999).

[137] G. B. Appetecchi, G. Dautzenberg, and B. Scrosati, *J. Electrochem. Soc.*, **143**, 6 (1996).

[138] G. B. Appetecchi, F. Croce, and B. Scrosati, *J. Power Sources*, **66**, 77 (1997).

[139] M. C. Borghini, M. Mastragostino, S. Passerini, and B. Scrosati, *J. Electrochem. Soc.*, **142**, 2118 (1995).

[140] F. Croce, F. Gerace, G. Dautzemberg, S. Passerini, G. B. Appetecchi, and B. Scrosati, *Electrochim. Acta*, **39**, 2187 (1994).

[141] S. Slane and M. Salomon, *J. Power Sources*, **55**, 7 (1995).

[142] J. M. Tarascon, A. S. Gozdz, C. N. Schmutz, F. Shokoohi, and P. C. Waren, *Solid State Ionics*, **86**, 49 (1996).

[143] H. S. Choe, J. Giaccai, M. Alamgir, and K. M. Abraham, *Electrochim. Acta*, **40**, 2289 (1995).

[144] S. Lascaud, M. perrier, A. Vallee, S. Besner, J. Prud'homme, and M. Armand, *Macromolecules*, **27**, 7469 (1994).

[145] A. Angell, C. Liu, and E. Sanchez, *Nature*, **362**, 137 (1993).

[146] M. Watanabe, S.-I. Yamoda, and N. Ogata, *Electrochim. Acta*, **40**, 2285 (1995).

[147] J. Fan and P. S. Fedkiw, *J. Electrochem. Soc.*, **144**, 399 (1997).

[148] J. Fan and P. S. Fedkiw, *J. Power Sources*, **72**, 165 (1998).

[149] S. A. Khan, G. L. Baker, and S. Colson, *Chem. Mater.*, **6**, 2359 (1994).

[150] J. Hou and G. L. Baker, *Chem. Mater.*, **10**, 3311 (1998).

[151] S. R. Raghavan, M. W. Riley, P. S. Fedkiw, and S. A. Khan, *Chem. Mater.*, **10**, 244 (1998).

[152] B. Kumar and L. G. Scanlon, *J. Power Sources*, **52**, 261 (1994).

[153] J. Plocharski and W. Wieczorek, *Solid State Ionics*, **28-30**, 979 (1988).

[154] J. Plocharski, W. Wieczorek, J. Przyluski, and K. Such, *Appl. Phys. A*, **49**, 55 (1989).

[155] H. P. Fritz and K. Stein, *J. Power Sources*, **37**, 315 (1992).

[156] J. E. Weston and B. C. H. Steele, *Solid State Ionics*, **7**, 75 (1982).

[157] F. Capuano, F. Croce, and B. Scrosati, *J. Electrochem. Soc.*, **138**, 1918 (1991).

[158] J. Fan and P. S. Fedkiw, *J. Electrochem. Soc.*, **144**, 399 (1997).

[159] M. Odziemkowski, M. Krell, and D. E. Irish, *J. Electrochem. Soc.*, **139**, 3052 (1992).

[160] D. Aurbach, Y. Ein-Ely, B. Markovsky, A. Zaban, S. Luski, Y. Carmeli, and H. Yamin, *J. Electrochem. Soc.*, **142**, 2882 (1995).

[161] D. Aurbach, Y. Gofer, M. Ben-Zion, and P. Aped, *J. Electroanl. Chem.*, **339**, 451 (1992).

[162] M. Jean, A. Tranchant, and R. Messina, *J. Electrochem. Soc.*, **143**, 391 (1996).

Table 2. 1. Comparison of different anode materials [3]

No.	Material	Ah kg^{-1}	Ah dm^{-3}	Average voltage, V (relative to Li)	Ah kg^{-1} (relative to Li)	Ah dm^{-3} (relative to Li)
1	Li	3860	2061	0	1	1
Alloys						
2	LiAl	790	1280	0.36	0.20	0.62
3	$Li_{4.4}Si$	2010	1749	0.2	0.54	0.85
4	$Li_{4.4}Pb$	500	1270	0.45	0.13	0.62
5	$Li_{4.4}Sn$	790	1003	0.5	0.20	0.49
6	Li_ySn (0.7<y<2.53)	350	444	0.53	0.09	0.22
7	Li_4Sb	715	~	0.95	0.19	~
8	Li_4Bi	453	~	0.83	0.12	~
9	LiZn	371	~	0.2	0.10	~
10	Li_3Cd	604	~	0.08	0.16	~
Dimensionally stable electrodes						
11	Li-B:Li_7B_6 17Li	1920	~	0.02	0.50	~
12	β-LiAl/Cu 80/20 w/o	632	~	0.36	0.16	~
13	$Li_3Cd/Li_{4.4}Sn$ Cd/Sn=1	285	~	0.80	0.14	~
Wood's alloy type						
14	Bi/Cd 60/40 w/o	~	1761	0.3	~	0.85
15	Pb/Cd 60/40 w/o	~	1489	0.3	~	0.72
16	Cd/Sn 70/30 w/o	~	1479	0.3	~	0.72
17	Bi/Cd/Pb 50/30/20 w/o	~	1963	0.3	~	0.95
18	Pb/Cd/Sn 60/30/10 w/o	~	1720	0.3	~	0.84
Insertion compounds						
19	$Li_6Fe_2O_3$	800	~	0.75	0.21	~
20	$LiWO_2$	120	~	0.75	0.03	~
21	WO_2	125	~	0.75	0.03	~
22	MoO_2	210	~	1.5	0.05	~
Carbon based anodes						
23	Graphite	340	~	0.5	0.09	~
24	Pyr. carbon*	350	~	0.5	0.08	~
25	PPCA[&], 1st cyc.	600	~	<1	0.16	~
	PPCA, 5th cyc.	140	~	<1	0.04	~
26	PVdF, 1st cyc.	580	~	<1	0.15	~
	PVdF[$], 5th cyc.	14	~	<1	0.004	~

Table 2.1. Comparison of different anode materials [3] (Cont'd)

No.	Material	Ah kg^{-1}	Ah dm^{-3}	Average voltage, V (relative to Li)	Ah kg^{-1} (relative to Li)	Ah dm^{-3} (relative to Li)
27	Carbon fibers, 1st cyc.	180	~	<1	0.05	~
	Carbon fibers, 5th cyc.	80	~	<1	0.02	~
Redox polymers[#]						
28	PPq	94	140	1.5	0.02	0.07
29	PPP	190	240	0.7	0.05	0.12
30	PAc	340	410	1.0	0.09	0.20
Alloy/polymer electrolyte composites						
31	LiAl/PEO/$LiClO_4$ 50/33/17 w/o	386	~	0.36	0.10	~
32	LiSi/PEO/$LiClO_4$ 57/29/14 w/o	1117	~	~	0.29	~
33	LiSi/PEO/$LiClO_4$/C 45/13/30/13 w/o	860	~	~	0.22	~
Alloy/redox polymer composites						
34	$(Li_{4.3}Pb)_{0.8}(PPP)_{0.18}$	230	450	0.4	0.06	0.22
35	$(Li_{4.3}Pb)_{0.24}(PAc)_{0.69}$	280	370	0.3	0.07	0.18
36	$(LiAl)_{0.11}(PAc)_{0.89}$	220	130	0.3	0.06	0.06
Linode						
37	$Li_5(Li_3N)$	3400	~	0	0.88	~

* Prepared by thermal decomposition of benzene

[&] PPCA = poly-2-chloro-1-phenylacetylene

[$] PVdF = poly-vinylidenefluoride

[#] PPq = poly(phenylquinoline), PPP = poly(paraphenylene), PAc = polyacetylene

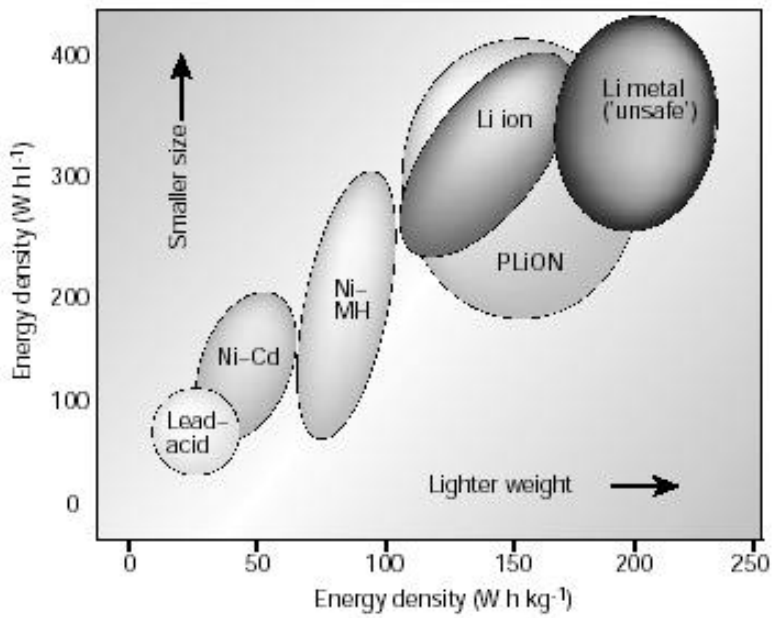

Figure 2. 1. Comparison of different battery technologies in terms of volumetric and gravimetric energy density [1].

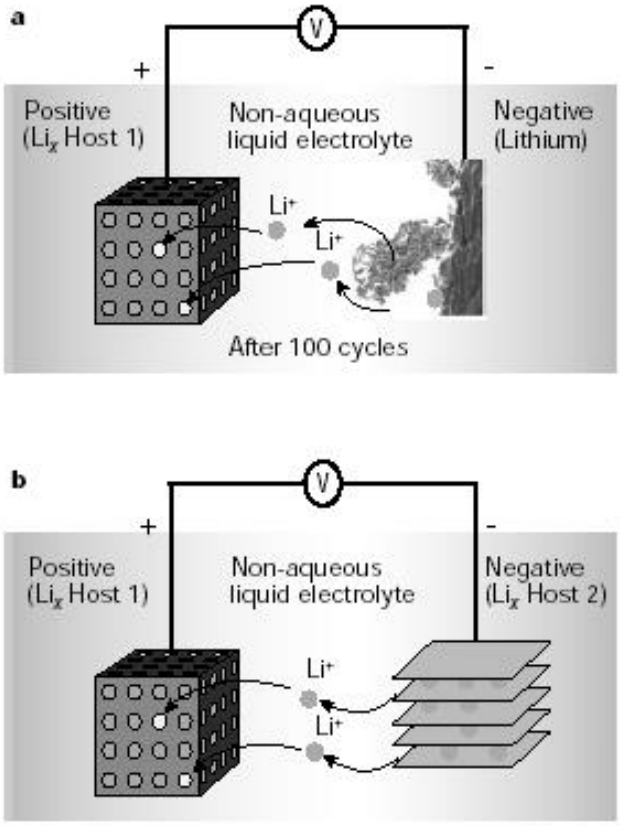

Figure 2. 2. Schematic representation and operating principles of Li batteries [1]. a. Rechargeable Li-metal battery (the picture of the dendrite growth at the Li surface was obtained directly from *in situ* scanning electron microscopy measurements). b. Rechargeable Li-ion battery.

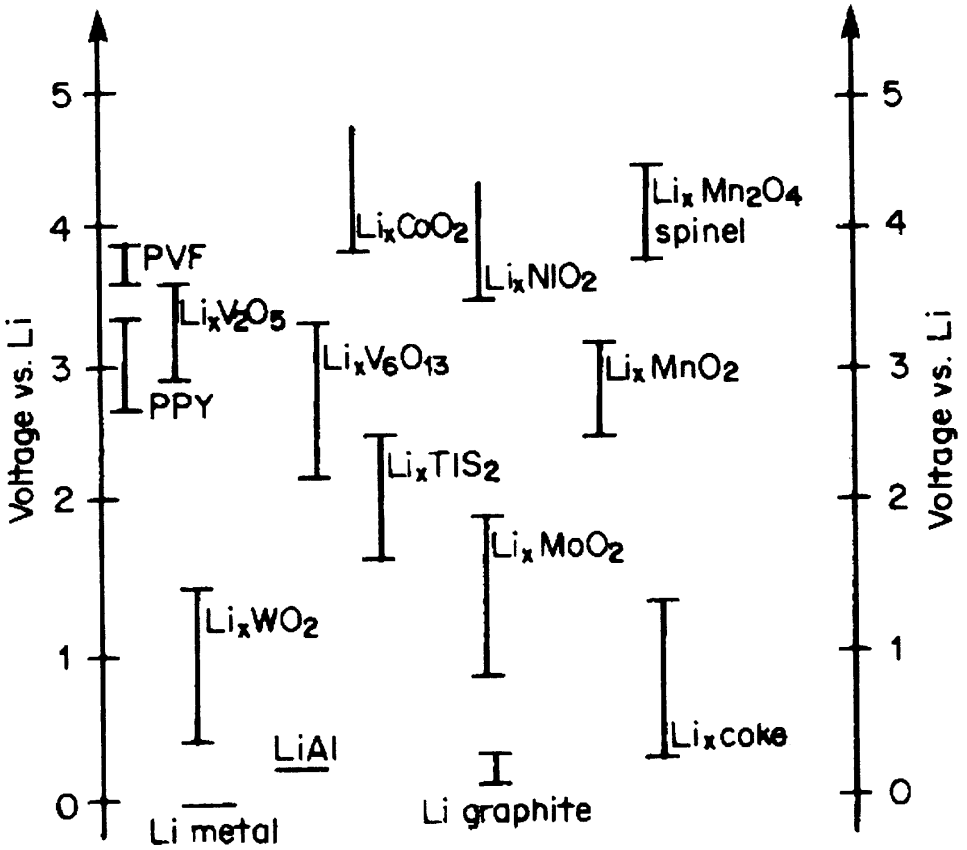

Figure 2. 3. Electrochemical potential of some Li-intercalation compounds vs. Li metal [2]. PPY=polypyrrole.

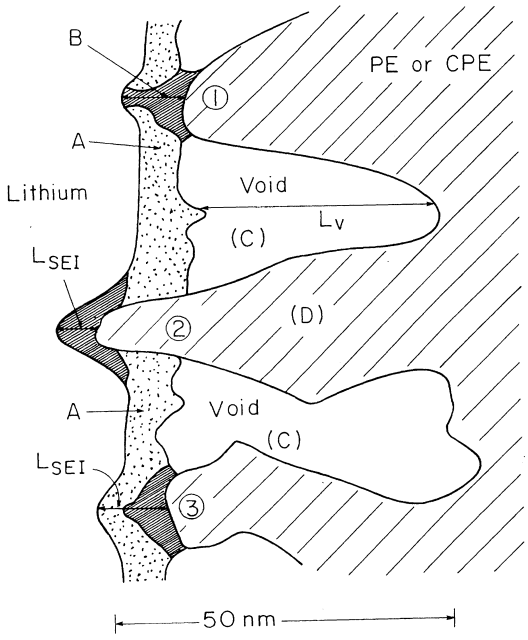

Figure 2. 4. Schematic representation of Li/polymer electrolyte (PE) or composite polymer electrolyte (CPE) interphase; A, native oxide film; B, freshly formed SEI; C, void; D, PE (solid) [6].

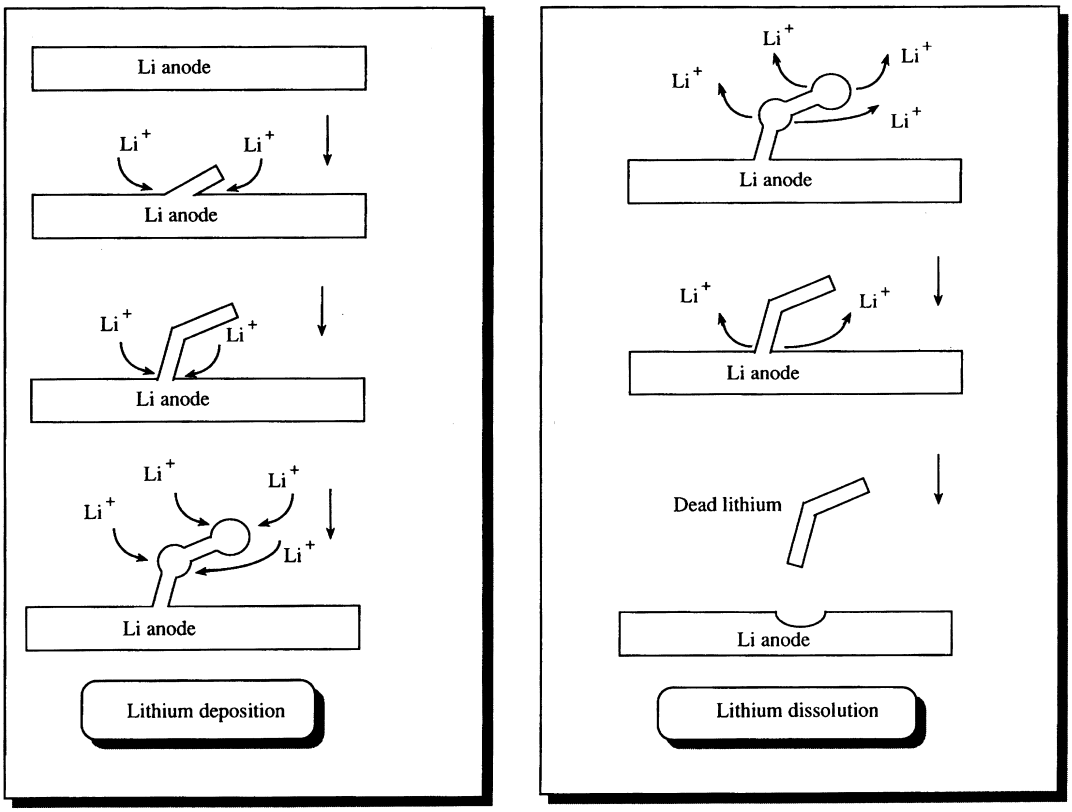

Figure 2. 5. A possible mechanism for lithium deposition (left) and lithium dissolution (right) [8].

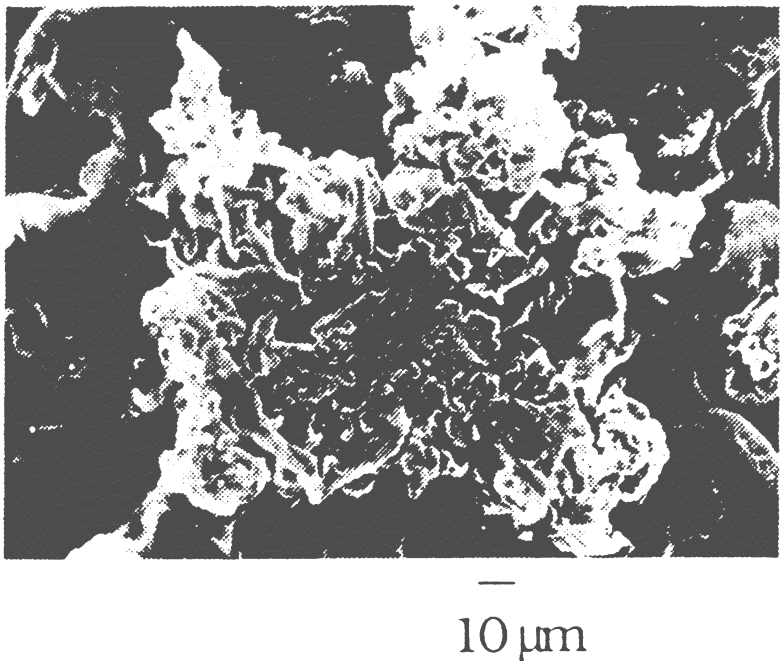

Figure 2. 6. Mushroom-like morphology of lithium at low current density [9].

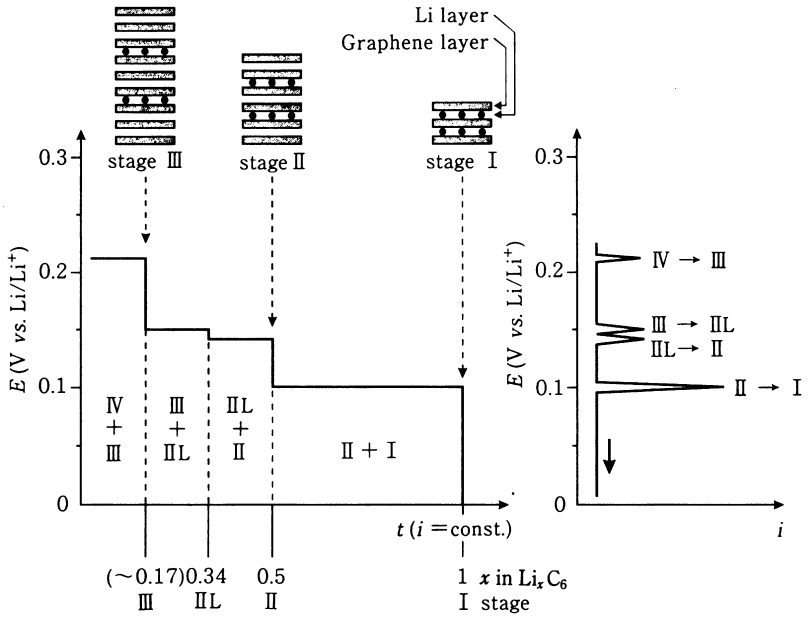

Figure 2. 7. Electrochemical lithium intercalation with stage formation [85]. Left: Schematic constant current E/*x* in Li_xC_6 curve. Right: Voltammetric i/E curve ($\Delta E/\Delta t$=constant).

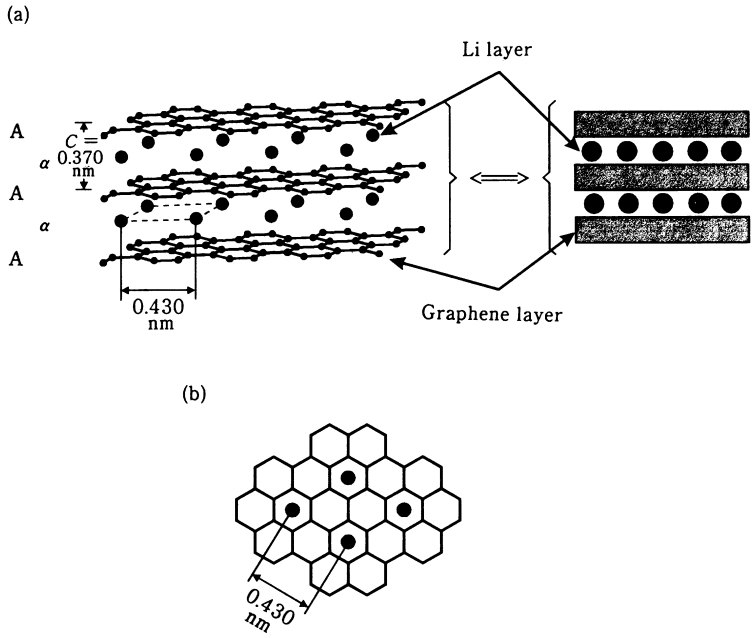

Figure 2. 8. Structure of LiC_6. (a) Left: Schematic showing lithium intercalation into graphene layer. Right: Showing simplified schematic representation. (b) In-layer ordering of LiC_6 [85].

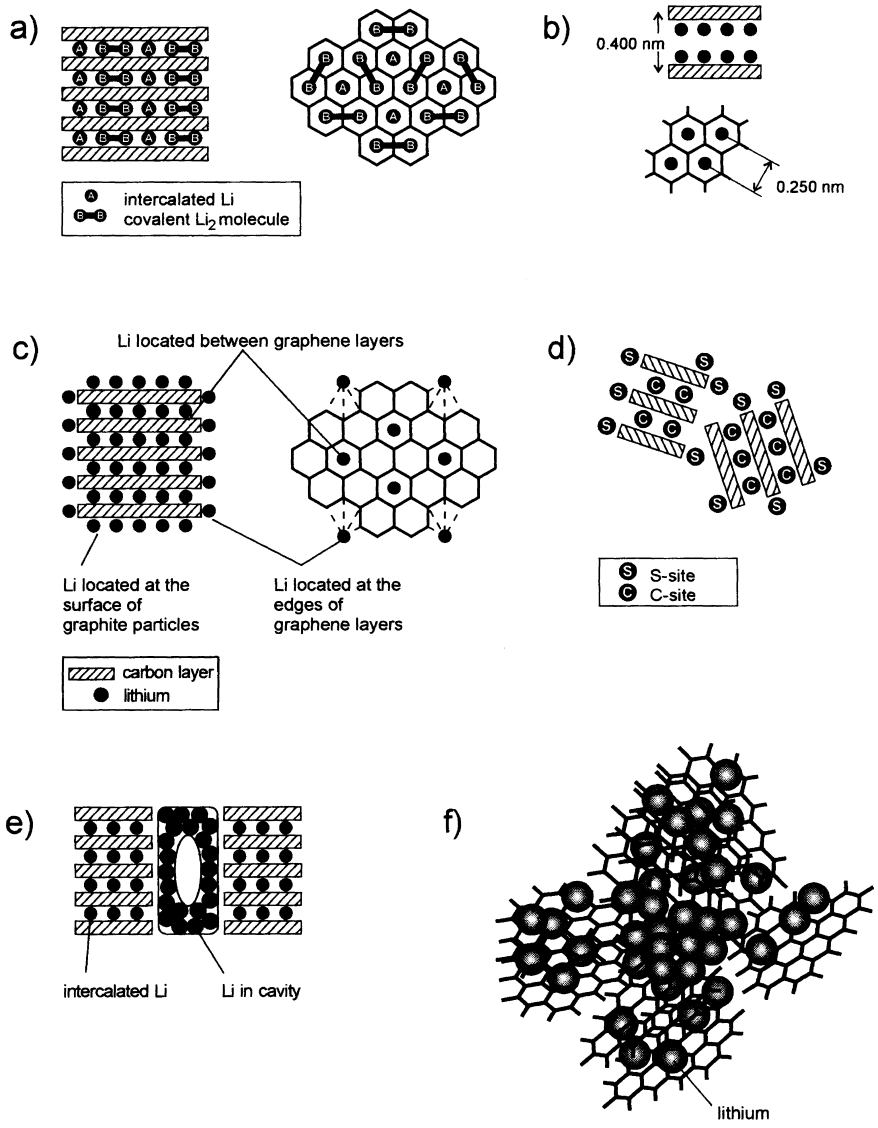

Figure 2. 9. Some mechanisms of reversible lithium storage in "high-specific-charge" lithiated carbon [8].

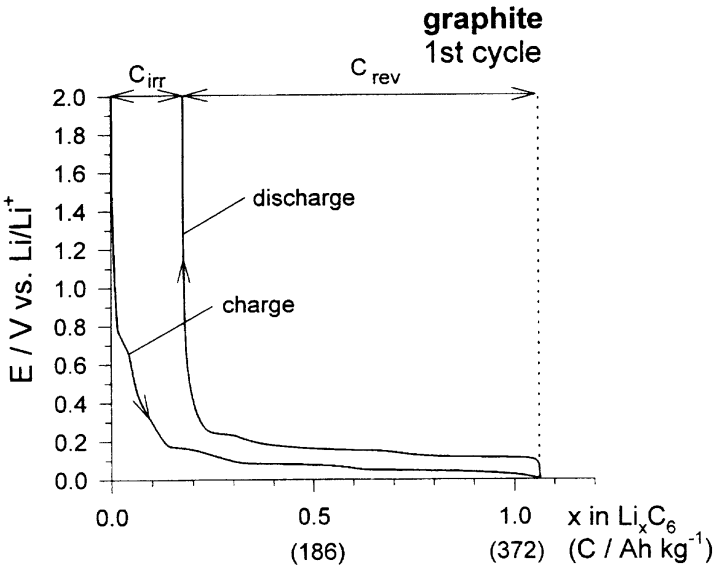

(a)

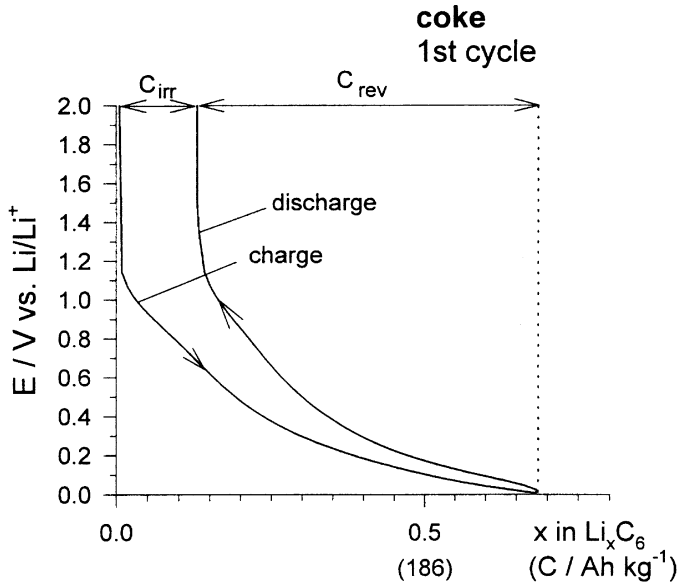

(b)

Figure 2. 10. First constant-current charge/discharge curves of (a) graphite Timex® KS44 and (b) coke (Conoco) in $LiN(SO_2CF_3)_2$/ethylene carbonate/dimethyl carbonate as the electrolyte (C_{irr}=irreversible specific charge; C_{rev}=reversible specific charge) [8].

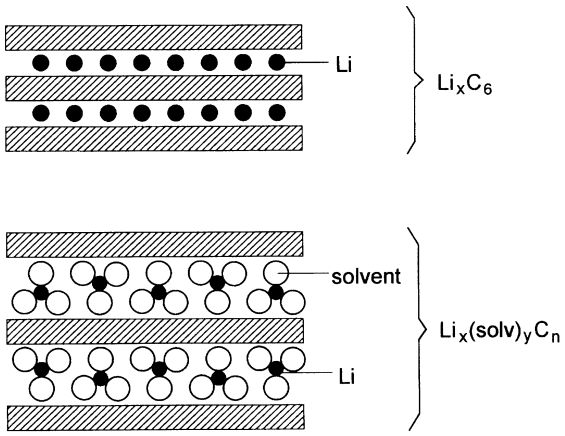

Figure 2. 11. Schematic drawing of binary (Li_xC_n) and ternary [$Li_x(solv)_yC_n$] lithiated graphite [8].

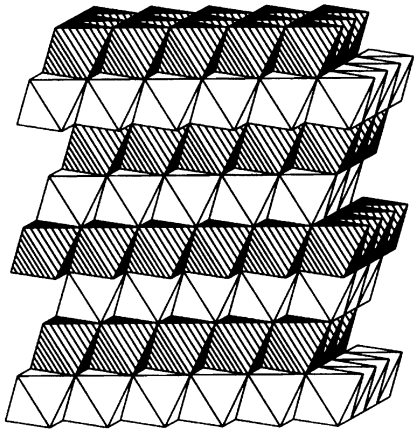

Figure 2. 12. Layered $LiMO_2$ structure (M=Ni or Co). The layers of shaded and unshaded octahedra are occupied by M and Li ions, respectively [8].

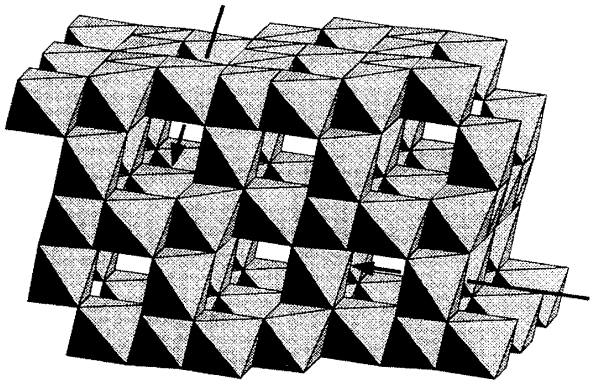

Figure 2. 13. The framework of λ-MnO_2 of $LiMn_2O_4$ spinel [8].

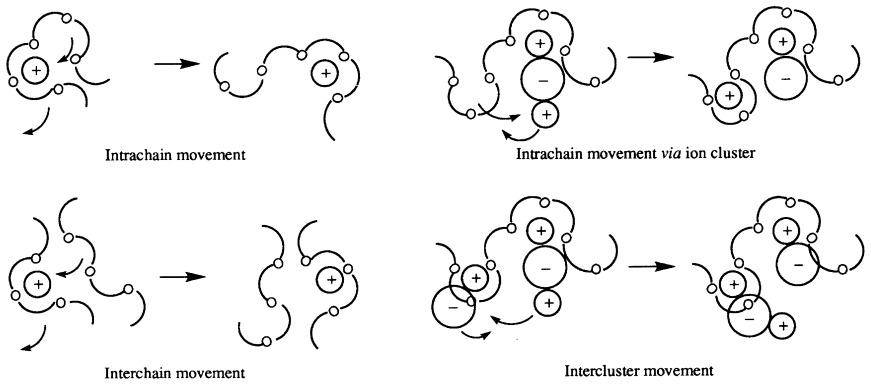

Figure 2. 14. Two representations (on the left) of cation motion in a polymer electrolyte assisted by polymer chain motion only, and two (on the right) showing cation motion taking account of ionic cluster contributions [8].

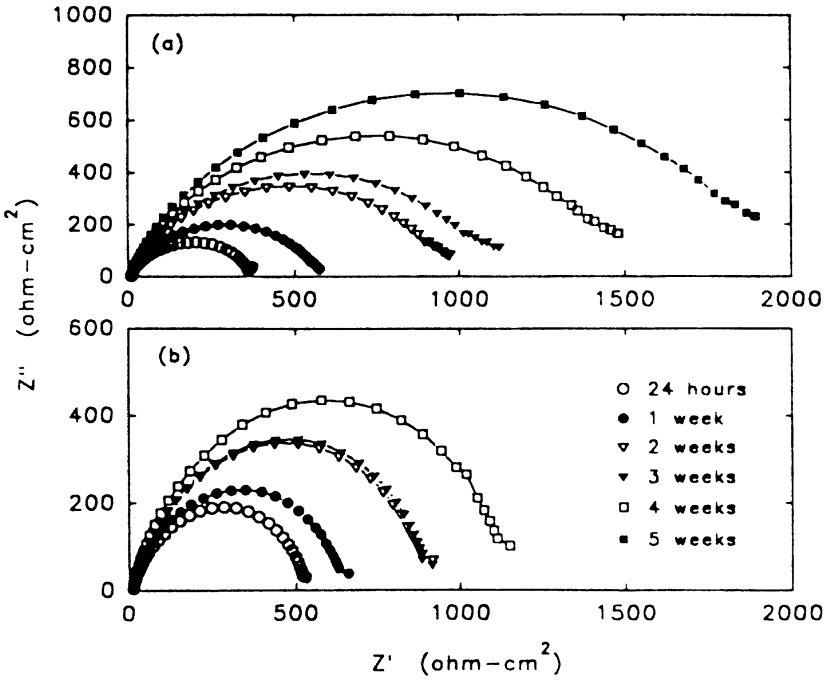

Figure 2. 15. Time evolution of impedance response of Li/PAN-EC-PC-$LiAsF_6$/Li cells: (a) no fillers, (b) composite with 5 wt.% zeolite powder, 10 Å, 40 μm [141].

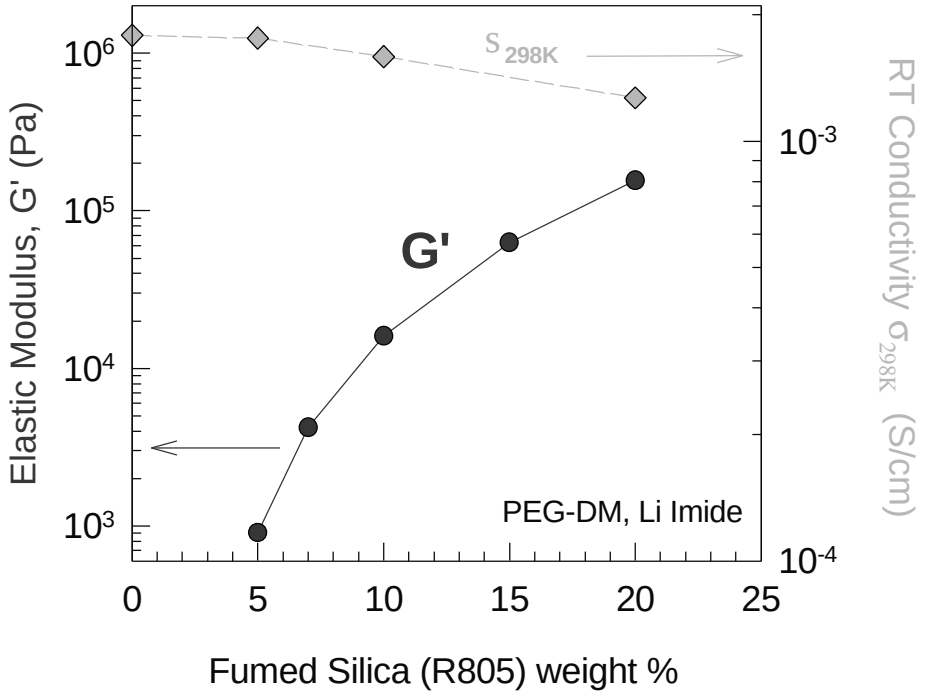

Figure 2. 16. Variation of elastic modulus (G') and room-temperature conductivity (σ_{298K}) with silica (R805) weight fraction for the composite polymer electrolytes [151].

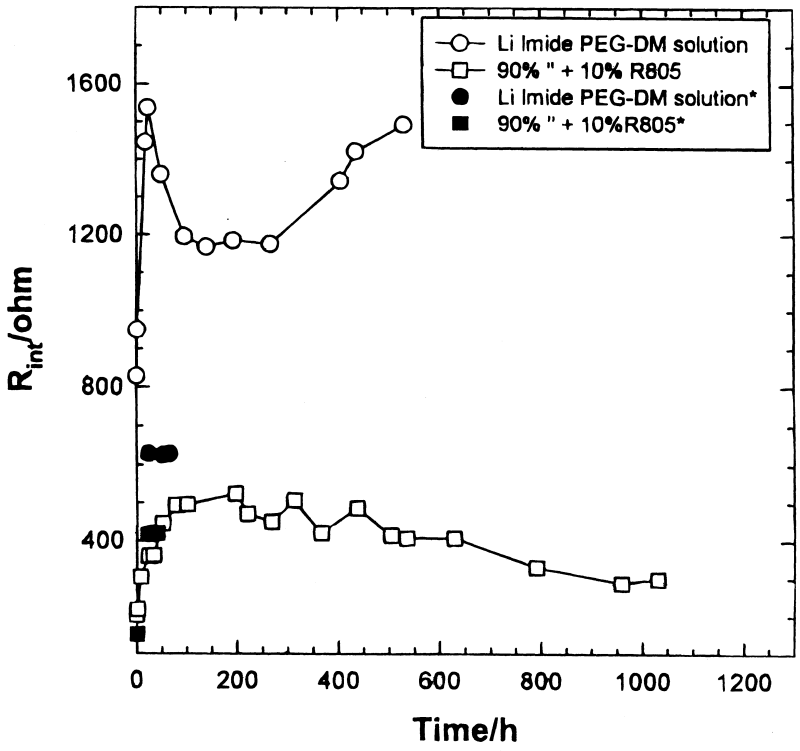

Figure 2. 17. Time dependence of interfacial resistance R_{int} between the electrolyte and lithium electrode for Li imide/PEG-dm solution [Li:O=1:20] and its corresponding 10% R805-based composite. These cells were exposed to several cyclic voltammetry runs before the impedance measurement [158].

Appendix 2.A

Table 2.A.1. Composition of surface films at lithium and lithiated carbons

Solid Phase(s) /electrode (s)	Liquid phase/ Electrolyte	Method	Species	Year	Ref.
Pt	THF/$LiClO_4$	Viscometry	Living polymers, M≈2×10^5 g mol^{-1}	1974	[80]
Li	PC/$LiClO_4$	XPS	Li_2CO_3,LiCl,$LiClO_4$,Li_2O,LiOH	1979	[65]
Li	THF/$LiAsF_6$	IR,EA,ESCA	As_2O_3, LiF	1979	[72]
Li	PC/$LiClO_4$	XRD	Li_2CO_3,LiCl,$LiClO_4$ in polymer	1979, 1980	[22,74]
Li, discharged	SO_2+AN/$LiAsF_6$	XPS	Li_2SO_3,As_2O_3, F(40%),C(32%),O(16%),S(3%)	1981	[69]
Li	SO_2	EA,IR,XPS	$Li_2S_2O_4$, Li_2S,Li_2SO_3,$Li_2S_2O_5$,Li_2SnO_6	1983, 1986	[60,61]
Li/TiS_2	3-Me-SL/$LiAsF_6$	XPS, FTIR	LiF,Li_2O,RSO_2Li,$R'Sli$,RS,$R'S$, RSO,$(-As-S-)_n$ R=$-(CH_2)_2CH(CH_3)CH_2^-$, $R'=(CH_2=C(CH_3)(CH_2)_2^-)$	1984	[52]
Li	PC/$LiClO_4$	in-situ ellipsometry	Li_2CO_3 with minor LiCl	1984	[77]
Li/TiS_2	2Me-THF/$LiAsF_6$	XPS	$LiAs(OR)_xF_{6-x}$, $(-As-O-)_n$, As_0	1985	[66]
Li	PC/$LiClO_4$	XRD,AES,EL	Li_2O dense,bottom; Li_2CO_3 in polymer,top.	1985	[75]
Li	PC/$LiAsF_6$	FTIR,XPS,IR	alkyl carbonates, Li_2CO_3 (from water), LiF	1987	[49]
Li	PC/ LiTri	FTIR,XPS,IR	alkyl carbonates, Li_2CO_3 (from water), LiF	1987	[49]
Li	PC/$LiClO_4$	FTIR,XPS,IR	alkyl carbonates, Li_2CO_3 (from water), LiCl	1987	[49]
Li/TiS_2	2Me-THF/$LiAsF_6$	EDS, ESCA, FTIR	As, F, C, O, S (elements);-OH-,-CH-, -CF-,-AsF (groups);ROLi, AsF_3, As_2O_3, LiF, As^0, $(-As-O-)_n$	1988	[51]
Ag, Au, Pt	GBL(H_2O)/$LiClO_4$	FTIR	LiOH,$HO(CH_2)_3CO_2Li$	1989	[57]
Ag, Au, Pt	GBL(O_2)/$LiClO_4$	FTIR	$LiO(CH_2)_3CO_2Li$,Li_2O,$LiO(CH_2)_3(C=O)O_2Li$	1989	[57]
Ag, Au	GBL/$LiClO_4$	FTIR	$LiO_2C(CH_2)_2CH_3$, β-ketoestedianion	1989	[57]
Li	DIOX/$LiClO_4$	FTIR,ESCA	LiOR,LiCl,$LiOCH_2OCH_2CH_3$, polymer	1990	[71]
Li	DIOX(H_2O)/$LiClO_4$	FTIR	LiOR, LiOH	1990	[54]
Pt	DIOX,LiOH(H_2O) / $LiClO_4$	FTIR	LiOR, LiCl, no LiOH	1990	[54]
Li	2Me-THF+EC/$LiAsF_6$ THF+EC/ $LiAsF_6$ EC/ $LiAsF_6$	FTIR	$ROCO_2Li$	1991	[50]
Li	2Me-THF+EC or THF+EC or EC	FTIR	$ROCO_2Li$, Li_2CO_3 (aging)	1991	[50]

Table 2.A.1. Composition of surface films at lithium and lithiated carbons (Cont'd)

Solid Phase(s) /electrode (s)	Liquid phase/ electrolyte	Method	Species	Year	Ref.
Pt (0.3Vvs Li)	DME/$LiAsF_6$	FTIR (in situ)	ROLi	1991	[55]
Li	DME+PC/$LiClO_4$	FTIR (in situ)	$ROCO_2Li$ (PC), ROLi (DME)	1991	[56]
Pt (0.3Vvs Li)	GBL/$LiClO_4$	FTIR (in situ)	RCO_2Li	1991	[55]
Pt (0.3Vvs Li)	PC/$LiAsF_6$	FTIR (in situ)	$ROCO_2Li$	1991	[55]
Pt (0.3Vvs Li)	PC/$LiClO_4$	FTIR (in situ)	$ROCO_2Li$	1991	[55]
Li	PC/$LiAsF_6$	FTIR	$ROCO_2Li$	1991	[50]
Li	PC (H_2O)/$LiClO_4$	FTIR (in situ)	$ROCO_2Li$, Li_2CO_3 (from water)	1991	[55]
Li	PC+THF/$LiAsF_6$	FTIR,ESCA	R'OLi(THF), $ROCO_2Li$(PC), LiF, As	1991, 1991	[50,56]
Li	PC/$LiAsF_6$	XPS	LiOH, Li_2CO_3, Li_2O, (a little LiF) (native film); no N compounds	1992	[67]
Li	PC/$LiClO_4$	XPS	LiOH,Li_2CO_3,Li_2O, (a little LiCl) (native film); no N compounds	1992	[67]
Li	PC/$LiPF_6$	XPS	mainly LiF	1992	[67]
Li	PC/$LiBF_4$	XPS	mainly LiF	1992	[67]
Li	THF/$LiAsF_6$ or THF (H_2O)/$LiAsF_6$	In-situ Raman spectroscopy	mainly PTHF; $LiAsF_6$ (trace), H_2O suppressed polymerization of THF	1992	[159]
Li	2Me-THF/$LiAsF_6$	Ex-situ Raman spectroscopy	F-As-O-As-F | | F F	1992	[159]
Graphite, Lonza, KS	EC/DMC, $LiAsF_6$, LiIm, $LiPF_6$, $LiBF_4$	FTIR, XPS, XRD, SEM	Main product $(CH_2OCO_2Li)_2$	1994	[48]
Li	PC/LiBr	FTIR, ESCA	$ROCO_2Li$, Li_2CO_3 (traces, from water?)	1994	[63]
Li	PC/LiTri, LiIm	FTIR,ESCA	mainly salt reaction products, Li_2O, (Li_3N from LiIm only), -(C-F),-(CF_3),-(C-S)-,-(C-O)-,sulfone (SO_2), (sulfone amide SO_2-N, LiIm only), and a little $ROCO_2Li$, Li_2CO_3 (S>F, PC only; less than LiIm)	1994	[63]
Li	PC/LiTri, LiIm, CO_2	FTIR,ESCA	Li_2CO_3 (main compound)	1994	[63]
Li	THF/LiTri,LiIm	FTIR,ESCA	Sulfone amide SO_-N (LiIm only), (CF_3), Li_2O, (O, C > F, S)	1994	[63]
Graphite, KS44, Lonza	EC+DEC/$LiAsF_6$, or $LiClO_4$	FTIR	$(LiO_2COCH_2)_2$ (from EC), Li_2CO_3 (traces)	1995	[160]
Graphite, KS44, Lonza	EC+DEC/ $LiBF_4$	FTIR	Small carbonate content, B-F	1995	[160]
Graphite, KS44, Lonza	EC+DEC/ $LiPF_6$	FTIR	Few $(LiO_2COCH_2)_2$ (from EC), Li_2CO_3 in contrast to Li electrodes	1995	[160]
Graphite, KS44, Lonza	EC+DEC, p(CO_2)= 6atm/$LiAsF_6$	FTIR	Few $(LiO_2COCH_2)_2$ (from EC), Li_2CO_3	1995	[160]
Li	PC/$LiClO_4$	XPS	LiCl, Li_2CO_3, Li_2O, LiOH	1995	[68]
Li	PC+EC+DME/$LiAsF_6$	SNIFTIR, EMIRS	$ROCO_2Li$, Li_2CO_3, peroxides, ketals	1995	[43]

Table 2.A.1. Composition of surface films at lithium and lithiated carbons (Cont'd)

Solid Phase(s) /electrode (s)	Liquid phase/ electrolyte	Method	Species	Year	Ref.
Li	THF/$LiAsF_6$	FTIR,EDAX	ROLi, traces of Li_2CO_3 and $ROCO_2Li$ (from CO_2 and H_2O contamination), LiF, Li_xAsF_y, As^0, but no –(As-O)-	1995	[73]
Li	DIOX/LiMe, LiIm, $LiAsF_6$	FTIR (ex situ)	Li_2CO_3, $ROCO_2Li$, ROLi, LiO_2CH (LiMe and $LiAsF_6$ only), reaction products from LiIm; NS, S=O, CF bonds Li_xAsF_y from $LiAsF_6$	1996	[15]
Li	DIOX, $LiAsF_6$	FTIR (in situ)	ROLi, , LiO_2CH, Li_xAsF_y from $LiAsF_6$	1996	[15]
Li	DIOX/ LiIm	FTIR (in situ)	ROLi, , LiO_2CH,;S_2O-N,S_2O,S-O, CF_3, C-S, C-F (from anion)	1996	[15]
Li	DIOX/ LiMe	FTIR (in situ)	ROLi, , LiO_2CH,;S-O, C-S, C-F (from anion)	1996	[15]
Graphite, SAFT	SO_2+ PC/$LiAsF_6$	FTIR	$ROCO_2Li$, $LiO_2COCH_2O(OCO_2Li)CHCH_3$, Li_2CO_3, $Li_2S_2O_4$, Li_xAsF_y, Li_2SO_3,$Li_2S_2O_5$, Li_2S	1996	[62]
Grphite,KS-6, Lonza	EMC/$LiAsF_6$, $LiPF_6$ DMC/$LiAsF_6$, $LiPF_6$	FTIR	$ROCO_2Li$, Li_2CO_3, ROLi, Li_xPF_y ($LiPF_6$ only)	1996	[58]
Li	DEC/$LiClO_4$	FTIR, XPS	$ROCO_2Li$, ROLi, Li_2CO_3	1997	[53]
Li	DEC/$LiPF_6$	FTIR, XPS	LiF, Li_2O	1997	[53]
Li	MPC/$LiAsF_6$	FTIR	$ROCO_2Li$, CH_3OLi,C_3H_7OLi,Li_2CO_3 on storage	1997	[59]
Graphite,KS-6	MPC/$LiAsF_6$	FTIR	$ROCO_2Li$, Li_2CO_3	1997	[59]
Li	EC+DMC/$LiPF_6$, $LiClO_4$, LiIm	AES	C, O, Li-O, metallic Li, Li-F ($LiPF_6$ only)	1997	[11]
Li	EC+DMC/$LiPF_6$, $LiClO_4$, LiIm	FTIR	$ROCO_2Li$, Li_2CO_3, LiOH	1997	[11]
Li	EC+DMC/$LiPF_6$, $LiClO_4$, LiIm	TPD-MS	H_2O, $(CH_2OCO_2Li)_2$, CH_3OCO_2Li	1997	[11]
Li	EC+DMC/$LiPF_6$, $LiClO_4$, LiIm	IC, AAS	LiF/total Li mole or ratio=1/3 ($LiPF_6$) No F anion detected (LiIm)	1997	[11]
Li	PC/$LiClO_4$	DMFTIR, XPS, AES	$ROCO_2Li$, Li_2CO_3, Li_2O	1998	[27]
Petroleum coke, XP-3,CONOCO	PC+EC+DMC/LiTri	FTIR, NMR, GC	RCO_3Li, Li_2CO_3, ROLi	1998	[64]
Li	PC/LiBETI, $LiPF_6$ $LiOSO_2CF_3$, LiIm	XPS	LiF (LiBETI and $LiPF_6$), Li_2CO_3, LiOH, LiF (LiIm and $LiOSO_2CF_3$)	1999	[12]
Graphite,ZYH, Advanced Ceramics Corp.	EC+DEC(1:2)/ $LiAsF_6$	XPS, EDS	LiF, Li_2O, As^0, Li-O-C	1999	[70]

R refers to different alkyl groups.

The following reactions are examples of the reductive decomposition reactions of anions with lithium [12-15,161]:

$[N(C_2F_5SO_2)_2]^- + 4e^- + 4Li^+ \rightarrow 4LiF + [N(CF_2{=}CFSO_2)_2]^-$

$[N(C_2F_5SO_2)_2]^- + 2e^- + 2Li^+ \rightarrow 2LiF + [(:CF_2CF_2SO_2)_2\,N]^-$

$[(:CF_2CF_2SO_2)_2\,N]^- + 2e^- + 2Li^+ \rightarrow 2LiF + [N(CF_2{=}CFSO_2)_2]^-$

$[(:CF_2CF_2SO_2)_2\,N]^- \rightarrow -(CF_2\text{-}CF_2\text{-}CF_2\text{-}CF_2\text{-}S_2NO_4)_n^-$

$LiN(CF_3SO_2)_2 + ne^- + nLi^+ \rightarrow Li_3N + Li_2S_2O_4 + LiF + Li_yC_2F_x$

$LiN(CF_3SO_2)_2 + 2e^- + 2Li^+ \rightarrow Li_2NSO_2CF_3 + LiSO_2CF_3$

$Li_2S_2O_4 + 6e^- + 6Li^+ \rightarrow 2\,Li_2S + 4Li_2O$

$Li[C(SO_2CF_3)_3] + ne^- + nLi^+ \rightarrow \frac{1}{2}\,Li_2S_2O_4 + mLiF + \frac{1}{2}\,Li_yC_2F_x + Li_2C(SO_2CF_3)_2$

$Li[C(SO_2CF_3)_3] + 2e^- + 2Li^+ \rightarrow LiC(SO_2CF_3)_2 + LiSO_2CF_3$, etc.

$Li_2S_2O_4 + 4e^- + 4Li^+ \rightarrow Li_2SO_3 + Li_2S + Li_2O$

$LiAsF_6 + 2e^- + 2Li^+ \rightarrow 3LiF\,(s) + AsF_3\,(sol)$

$AsF_3 + 2xLi^+ + 2xe^- \rightarrow Li_xAsF_{3-x}\,(s) + xLiF\,(s)$

$PF_6^- + 2e^- + 3Li^+ \rightarrow 3LiF\,(s) + PF_3$

$LiPF_6 \rightarrow LiF + PF_5$

$PF_5 + H_2O \rightarrow PF_3O + 2HF$

$PF_5 + 2xLi^+ + 2xe^- \rightarrow Li_xPF_{5-x}\,(s) + xLiF\,(s)$

$PF_3O + 2xLi^+ + 2xe^- \rightarrow Li_xPF_{3-x}O(s) + xLiF\,(s)$

$BF_4^- + xe^- + xLi \rightarrow yLiF + Li_{x-y}BF_{4-y}$

The decomposition reactions of some organic carbonate solvents are [14,58,162]:

$PC + 2e^- + 2Li^+ \rightarrow Li_2CO_3\,(s) + CH_3CH{=}CH_2\,(g)$

$2PC + 2e^- \rightarrow CH_3CH(OCO_2^-)CH_2OCO_2^- + CH_3CH{=}CH_2\,(g)$

$2PC + 2e^- + 2Li^+ \rightarrow CH_3CH(OCO_2Li)CH_2OCO_2Li\,(s) + CH_3CH{=}CH_2\,(g)$

$2EC + 2e^- + 2Li^+ \rightarrow (CH_2OCO_2Li)_2\,(s) + CH_2{=}CH_2\,(g)$

$2DMC + 2e^- + 2Li^+ \rightarrow CH_3OCO_2Li\,(s) + CH_3CH_3\,(g)$

$2DMC + 2e^- + 2Li^+ \rightarrow CH_3OLi\,(s) + CH_3OCOOCOCH_3$

$2ROCO_2Li + H_2O \rightarrow Li_2CO_3\,(s) + 2ROH + CO_2$

$EMC + e^- + Li^+ \rightarrow CH_3OCO{\cdot}CH_3CH_2OLi$

$EMC + e^- + Li^+ \rightarrow CH3CH2OCO{\cdot}CH_3OLi$

$EMC + e^- + Li^+ \rightarrow CH_3OCO_2Li + CH_3CH_2{\cdot}$

MPC reacts in a similar way as EMC [59].

Alkyl (R·) and acyl (ROCO·) radicals react according to:

$R{\cdot} + e^- + Li^+ \rightarrow RLi$

$ROCO{\cdot} + e^- + Li^+ \rightarrow ROLi + CO$

Where ROLi may react with EMC yielding ethers or other alkoxides and carboxylate anions. Li_2CO_3 is formed in two ways:

$ROCO_2Li + e^- + Li^+ \rightarrow R{\cdot} + Li_2CO_3\,(s)$

$2ROCO_2Li + H_2O \rightarrow CO_2\,(g) + 2ROH + Li_2CO_3\,(s)$

Chapter 3: Experimental

This section summarizes methods for material preparations and characterizations of composite electrolytes based on low- to intermediate-molecular weight (M_w) methyl-terminated poly(ethylene oxide) (PEO) oligomers using fumed oxides as fillers. Material preparations include composite electrolyte preparation, cathode fabrication, and coin cell assembly. Material characterizations include electrochemical (conductivity, electrochemical impedance spectroscopy, and cell cycling), rheological (dynamic and steady), differential scanning calorimetry (DSC), and Fourier transform infrared spectroscopy (FTIR) measurements.

3.1 Material Preparations

3.1.1 Composite Electrolyte Preparation

The composite electrolytes consist of three materials: lithium bis(trifluromethylsulfonyl)imide [$LiN(CF_3SO_2)_2$] (LiTFSI, 3M), fumed oxide (Degussa, or surface-modified fumed silica synthesized at MSU [1,2]), and poly(ethylene glycol)dimetheyl ether (PEG-dm, M_w=250, 500, 1000, and 2000, Aldrich). Lithium salt was dried at 110°C under vacuum for 24 hours before use. Two different pretreatment and drying procedures are employed for liquid oligomers (M_w=250 and 500) and solids (M_w=1000 and 2000). For low-M_w oligomers, the inhibitor [butylated hydroxytoluene (BHT), 100 ppm] was first removed using an inhibitor-removing column (Aldrich). The

PEG-dm was then dried over 4Å molecular sieves for at least two weeks prior to use. Medium-M_w (1000 and 2000) oligomers were melted and dried over 4Å molecular sieves in a sealed container at 80°C for at least a month before being transferred to an Argon-filled glove box. Water content of both materials was controlled under 20 ppm, as determined by Karl-Fisher titration. Fumed oxides were dried at 120°C under vacuum for 3-4 days to achieve a water content of 150-200 ppm before being transferred to the glove box.

Composite electrolytes were prepared in an argon-filled glove box. First, a baseline electrolyte was made by dissolving LiTFSI in a PEG-dm oligomer liquid (room-temperature) or melt (~ 80°C for M_w =1000 and 2000) with a fixed ratio of Li:O (1:20) to maintain high conductivity [1]. A certain weight of fumed oxide was then added to the baseline electrolyte and dispersed by use of a high-shear mixer (Tissue Tearor^{TM}, Model 398, BioSpec Products, Inc.) [3]. After preparation, the electrolytes based on PEG-dm (M_w=1000 and 2000) with and without fillers, are solids at room temperature. The baseline electrolytes based on low-M_w PEG-dm (M_w=250 and 500) are liquids, while the corresponding composite electrolytes are solid-like gels except for TiO_2 composites, which are suspensions. Water content of the baseline electrolyte and the composites was under 20 and 50 ppm, respectively.

3.1.2 Cathode Preparation

All components of metal-oxide cathodes, $LiCoO_2$ (OM Group, Inc., OMG), $LiMn_2O_4$ (Merck), V_6O_{13} (Kerr-McGee), or Li_xMnO_2 (synthesized by Doeff's group at

Lawrence Berkeley National Laboratory [4]), poly(vinylidene fluoride) (PVDF, Kynar® Flex 2800-00, Elf Atochem North America), carbon additives, and 1-methyl-2-pyrrolidinone (NMP, Aldrich) were used as received. Conducting carbons used in this study include three types of graphite from Timcal, Ltd. (Timrex® SFG 15, SFG 44, and KS 6), and two types of carbon blacks (Vulcan XC72R from Cabot Corp. and Ketjenblack (KJB) EC-600JD from Akzo Nobel Inc.). The KS graphite consists of round particles, whereas the SFG type is in the form of flat flakes [5]. The number in the graphite designation indicates the particle size; that is, SFG 15, SFG 44, and KS6, ~ 90% of the particles are smaller than 15, 44, and 6 μm, respectively. For rather round particles, as in the KS-type graphite, more prismatic surfaces are expected than for flat flakes (SFG type). Carbon properties and cathode compositions are listed in Table 3.1. In $LiCoO_2$ electrodes, 6 wt% graphite (SFG 15 or SFG 44) or 3 wt% carbon black (KJB EC-600JD or Vulcan XC72R) was used as the electronic conductor. In all $LiCoO_2$ cathodes except those containing KJB, 3% PVDF was used as the binder; in the latter case, 5% PVDF was used due to the high surface area of KJB particles. The typical composition for a $LiMn_2O_4$ cathode is approximately 91 wt% metal oxide, 6 wt% graphite, and 3 wt% PVDF binder [6]. Aluminum foil (0.024-mm thick, Fisher Scientific) was used as the current collector for $LiCoO_2$ and $LiMn_2O_4$ cathodes. The effect of current collector materials is studied using V_6O_{13} cathodes, which consist of 75 wt% V_6O_{13}, 20 wt% SFG15 graphite, and 5 wt% PVDF. The current collectors are: Al foil, Ni foil (0.125-mm thick, Aldrich), and 0.127-mm thick sheet of carbon fiber (Techimat® 6100-035, Lydall Technical Papers). Lithium manganese dioxide (Li_xMnO_2)

cathodes are composed of 84 wt% Li_xMnO_2, 8 wt% binary carbon mixture (graphite KS6:KJB = 1:1), and 8 wt% PVDF. Aluminum foil was used as the current collector. Usually, a fixed amount of metal oxide and carbon additive(s) are thoroughly grinded and mixed using mortar and pestle. Then, the mixture of metal oxide and carbon(s) was dispersed into a solution of PVDF using NMP as solvent. The resulting slurry was coated onto the current collector by a doctor blade, and the final thickness of wet cathode films was approximately 0.20 mm for cathodes using Al current collector and 0.30 mm for those with thicker Ni or carbon fiber current collector. The film was dried at 80°C overnight and cut into 12.7-mm diameter disks that were hot-compacted by a hydraulic press at 150°C and 770 MPa. After compaction, cathode disks were dried at 150°C under vacuum for 24 h.

3.1.3 Preparation of Coin Cells

Coin cells in which an electrolyte/separator is sandwiched between a thin sheet of lithium metal and another electrode (lithium foil, nickel foil, or metal-oxide composite cathode) were used in the cycling measurements (Figure 3.1). In these cells, a Celgard® 2400 separator (25-μm thick) is either wetted by the baseline electrolyte or sandwiched between two layers of composite electrolyte. A stainless steel spacer and spring are used to maintain good contact of electrolyte, electrode, and current collector.

3.2 Electrochemical Measurements

3.2.1 Electrolyte Conductivity

Electrolyte conductivities were measured using two-electrode (0.64 mm platinum wire, Fisher Scientific) cells, shown in Figure 3.2. The measurements were carried out by ac impedance technique with an EG&G Princeton Applied Research 273 potentiostat and an EG&G 5210 lock-in amplifier controlled by the EG&G PowerSuite impedance software. The measurements were performed over the temperature range from 0 to 100°C (M_w = 250 and 500) and from 25 to 100°C (M_w = 1000 and 2000). Temperature was controlled by an Isotope 1016P (Fisher Scientific) circulating water bath with the accuracy of ±0.5°C. All conductivity data were averaged over three samples and the typical deviation from the average was 5%.

3.2.2 Half-Cell Cycling

An Arbin battery cycler (Model BT2042) controlled by Arbin ABTS software is employed to carry out constant-current cell cycling. In Li/electrolyte/Li cells, current densities of 0.2 and 1.0 mA/cm^2 with fixed charge density of 120 mC/cm^2 were applied. Cell cycling was terminated upon reaching the fixed maximum cycle number of 584 or by reaching the voltage safety limit of ±10 V. In cycling the Li(Ni)/electrolyte/Li cells, a known charge was first passed through the cell at 0.2 mA/cm^2 to prepare the lithium electrode (Q_D=2.4 C/cm^2, nominal Li thickness of 3.0 μm). Then, a fraction of this charge (cycling charge, Q_c= 0.24 C/cm^2, Depth of Discharge (DOD)=10%)) was alternately cycled across the cell for 20 lithium deposition-dissolution cycles, and the

lithium stripping overvoltage was monitored upon cycling. Finally, the remaining Li on Ni surface was anodically removed during the last dissolution half-cycle and the amount of charge passed, Q_f, was monitored. The cut-off voltage for the dissolution half-cycle was set at 1.5 V vs. Li metal. The mean value of the lithium electrode cycling efficiency, η, was calculated by [7]:

$$h = \frac{Q_c - \left(hQ_D - Q_f\right)/n}{Q_c} \times 100\% \qquad (3.1)$$

where $n = 20$ or $n =$ actual number of cycles in which 0.24 C/cm^2 Li is stripped from Ni .

3.2.3 Full-Cell Cycling

Lithium/lithium cobalt dioxide cells were cycled between 2.5 to 4.2 V at a constant current density of 0.11 mA/cm^2 (C/40) for graphite-containing cathodes, 0.08 mA/cm^2 (C/40) for Vulcan XC72R-containing cathodes, and 0.08 mA/cm^2 (C/17), 0.39 mA/cm^2, and 0.80 mA/cm^2 (C/1.7) for KJB-containing cathodes. Lithium/lithium manganese oxide ($LiMn_2O_4$) were cycled between 3.0 to 4.2 V at a constant current density of 0.08 mA/cm^2 (C/40). Lithium/vanadium oxide (V_6O_{13}) cells were cycled at 0.08 mA/cm^2 (C/55) between 1.8 to 3.0 V, while Li/Li_xMnO_2 cells were cycled between 2.5 to 3.6 V at 0.05 mA/cm^2 (C/10).

3.2.4 Electrochemical Impedance Spectroscopy

The lithium surface before and after Li/electrolyte/Li cycling was also studied via electrochemical impedance spectroscopy (EIS) using a Zahner impedance analyzer IM6e.

Open-circuit impedance data were collected in a range of 100 kHz to 100 mHz with an ac amplitude of 10 mV. The interfacial resistance (R_{int}) between the lithium metal and the electrolyte was determined according to the method of Fauteux [8].

3.3 Rheological Measurements

Rheological measurements were conducted using a Rheometrics Dynamic Stress Rheometer (DSR II) (Rheometric Scientific). Cone and plate or serrated parallel plate geometries of 25 mm diameter were used for the measurements. Cone and plate thickness was set at 0.05 mm, while that for the serrated plates was 1 mm. All measurements were performed at either 60°C (above the melting point of electrolytes) or room temperature (approximately 25°C).

3.3.1 Dynamic Measurements

Dynamic measurements were primarily used to probe the gel microstructures with minimal disturbance of samples [9]. In this technique, a sinusoidally varying strain (γ) is applied to a sample at a fixed frequency (ω) and a maximum stress-amplitude (γ_0):

$$g = g_0 \sin wt \qquad (3.2)$$

Within the region of linear viscoelasticity, the resulting stress is sinusoidal and can be deconvoluted into an in-phase and an out-of phase component [10]:

$$t = G'g_0 \sin wt + G''g_0 \cos wt \qquad (3.3)$$

The elastic or storage modulus, G', related to the stress in the phase with the

strain, qualitatively provides information about the elastic nature of the material [10]. The viscous or loss modulus, G″ is related to the stress out of phase with the displacement and linked to the viscous dissipation of energy in the system. Both elastic and viscous moduli are functions only of the oscillation frequency for low deformation in the linear viscoelastic (LVE) regime, where the stress is linearly proportional to the imposed strain.

Dynamic stress sweep was used to determine the linear viscoelastic regime of each sample (with a frequency of 1 rad/s), as well as the dynamic yield stress (τ_y). Dynamic frequency sweeps were used to examine G′ and G″ in the LVE regime. The relative magnitude and shapes of G′ and G″ curves indicate the type and extent of microstructure of samples [10].

3.3.1 Steady Shear Measurements

During steady shear measurements, a sample is subjected to a constant shear rate $\dot{\gamma}$ by applying a continuous rotation at a fixed rate on a rotational instrument. The response of the sample is measured as a shear stress τ. In steady shear, the apparent viscosity, η is measured as a function of the steady shear rate, $\dot{\gamma}$:

$$\eta(\dot{\gamma}) = \tau/\dot{\gamma} \qquad (3.4)$$

The baseline electrolytes without fumed oxide fillers showed Newtonian behavior (constant viscosity independent of shear rate) while composite electrolytes show shear-thinning behavior (viscosity decreases with increasing shear rate).

3.4 Electrolyte Thermal Properties by DSC Measurements

Thermal analysis was conducted to measure glass transition (T_g) and melting temperature (T_m) by using a Dupont Instruments 910 differential scanning calorimeter (DSC) equipped with a TA Instruments DSC cell controlled by TA Instruments 2200 Thermal Analyzer. The temperature scale was calibrated from the melting point of indium. Empty aluminum pans, matched in weight to within 0.02 mg, were used for the sample and reference. Samples (~15-20 mg) in aluminum pans were stabilized at –110°C by slowly cooling from room temperature using liquid nitrogen and then heated at 10°C/min to 150°C. Glass transition temperatures (T_g) and melting temperatures (T_m) were determined in the conventional manner. The estimated uncertainty in the determination of T_g and T_m is ±2°C.

3.5 Interactions among Polymer Chain, Lithium Salt, and Filler Surface Groups by FTIR-ATR Measurements

The samples prepared in the glove box were sealed in argon-filled vials and stored in a desiccator before infrared spectra were taken. Infrared spectra in the attenuated total reflection mode (FTIR-ATR) were obtained using an IR microscope (model number UMA-500) attached to a Digilab FTS 6000 FTIR spectrometer (Bio-Rad) euipped with a Cassegranian objective containing a germanium crystal for single-pass ATR with a spot size of approximately 30 microns. The entire microscope was encased in a dry nitrogen-filled glove bag, which reduced atmospheric water or CO_2 contamination of the spectra

and samples. The spectrometer was equipped with a liquid nitrogen cooled mercury-cadmium-telluride (MCT)/A detector, and the spectra were recorded at a resolution of 2 cm^{-1} with a spectral range of 4000-650 cm^{-1} at 25 ± 2°C. Each absorption spectrum was the average of ten accumulations of 64 scans and corrected against the background spectrum of air.

3.6 References

[1] J. Fan, S. R. Raghavan, X. Y. Yu, S. A. Khan, P. S. Fedkiw, J. Hou, and G. L. Baker, *Solid State Ionics*, **111**, 117 (1998).

[2] J. Hou, *Composite Polymer Electrolytes Using Functionalized Fumed Silica and Low Molecular Weight PEO: Synthesis and Characterization,* Ph.D. Thesis, Ann Arbor (1997).

[3] H. J. Walls, J. Zhou, J. A. Yerian, P. S. Fedkiw, S. A. Khan, M. K. Stowe, and G. L. Baker, *J. Power Sources*, **89**, 156 (2000).

[4] M. M. Doeff, A. Anapolsky, L. Edman, T. J. Richardson, and L. C. D. Jonghe, *J. Electrochem. Soc.*, **148**, A230 (2001).

[5] M. Winter, P. Novak, and A. Monnier, *J. Electrochem. Soc.*, **145**, 428 (1998).

[6] J. Fan and P. S. Fedkiw, *J. Power Sources*, **72**, 165 (1998).

[7] D. Aurbach, Y. Gofer, and J. Langzam, *J. Electrochem. Soc.*, **136**, 3198 (1989).

[8] D. Fauteux, *Solid State Ionics*, **17**, 133 (1985).

[9] S. R. Raghavan, M. W. Riley, P. S. Fedkiw, and S. A. Khan, *Chem. Mater.*, **10**, 244 (1998).

[10] C. W. Macosko, *Rheology: Principles, Measurements, and Applications,* VCH publishers, Inc., New York (1994).

Table 3. 1. Cathode Compositions and Carbon Properties

Carbon Name	Carbon Type	Manufacturer	Particle Size (μm)	BET Surface Area (m^2/g)	Cathode Composition
Timrex® SFG 15	Graphite	Timcal, Ltd.	15	8.5	**4V**: 91% $LiCoO_2$ or $LiMn_2O_4$ 6% SFG 15 3% PVDF **3V**: 75% V_6O_{13} 20% SFG 15 5% PVDF
Timrex® SFG 44	Graphite	Timcal, Ltd.	44	4.3	**4V**: 91% $LiCoO_2$ 6% SFG 44 3% PVDF
Ketjenblack EC-600JD	Carbon Black	Akzo Nobel, Inc.	0.03-0.1	1250	**4V**: 92% $LiCoO_2$ 3% KJB 5% PVDF
Vulcan XC72R	Carbon Black	Cabot Corp.	0.03	254	**4V**: 94% $LiCoO_2$ 3% Vulcan 3% PVDF
Timrex® KS6	Graphite	Timcal, Ltd.	6	19.4	**3V**: 84% Li_xMnO_2 4% KS6 + 4% KJB 8% PVDF

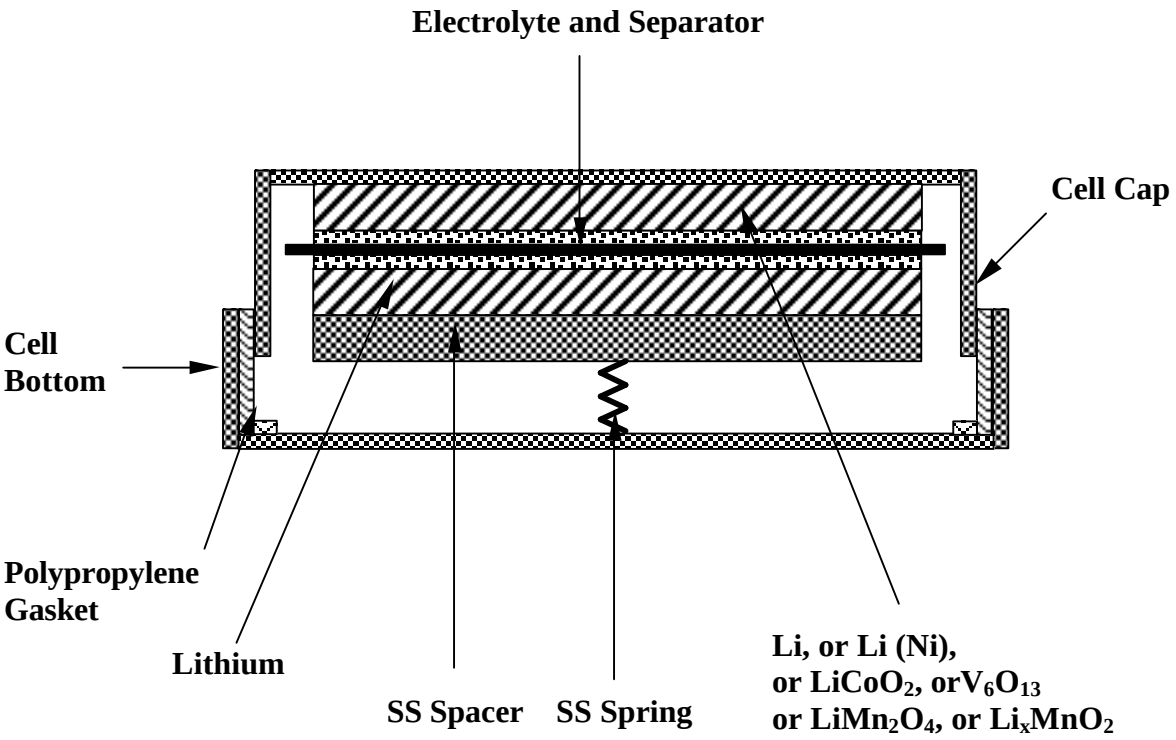

Figure 3. 1. Coin cell for cycling studies (Not to scale).

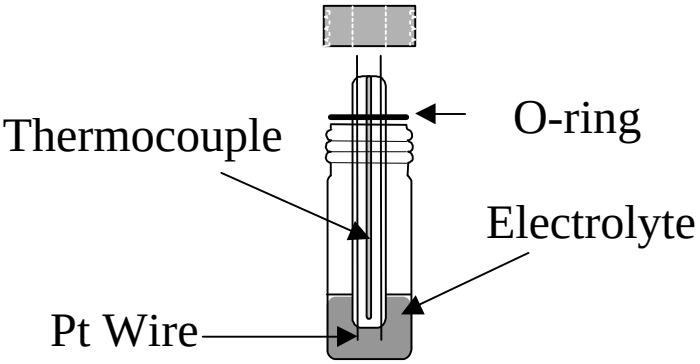

Figure 3. 2. Schematic illustration of two-electrode cell for conductivity measurement.

Chapter 4: Ionic Conductivity of Composite Electrolytes Based on Oligo(Ethylene Oxide) and Fumed Oxides

Jian Zhou and Peter S. Fedkiw

Department of Chemical Engineering

North Carolina State University

Raleigh, NC 27695-7905

In preparation for submission to

Solid State Ionics

December 18, 2002

Abstract

The effects of fumed oxide fillers (SiO_2, Al_2O_3, TiO_2) and binary mixtures of oxide fillers (SiO_2/Al_2O_3) on ionic conductivity of composite electrolytes based on poly(ethylene oxide) oligomers (M_w =250, 200, 1000, and 2000) + lithium bis(trifluromethylsulfonyl)imide [$LiN(CF_3SO_2)_2$] (LiTFSI) (Li:O=1:20) are studied using electrochemical impedance spectroscopy (EIS), differential scanning calorimetry (DSC), and Fourier transform infrared spectroscopy in the attenuated total reflectance mode (FTIR-ATR). Fillers show similar effect on conductivity in all systems: no distinguishable effect is found with filler type, and addition of filler decreases conductivity at temperatures above the melting point but increases conductivity at temperatures below. The addition of fillers stiffens polymer segments, as evidenced by enhancement in Li^+-polymer interactions seen in the IR spectra and an increase in T_g found from the DSC analysis. No reduction in ion-pairing upon addition of filler is observed from the IR spectra. The increase in conductivity at temperatures below the melting point is believed to be due to faster ion transport along the filler surface rather than through enhanced mobility of polymer segments. The insulating nature of fillers and stiffening of the polymer solvent in the presence of fillers cause a decrease in conductivity at temperatures above the melting point and is correlated solely with volume fraction of the filler.

Keywords: Fumed oxides; Ionic conductivity; Composite electrolytes; Oligo(ethylene oxide); Rechargeable lithium batteries

4.1. Introduction

Rechargeable lithium batteries with high-specific energies are promising power sources for modern portable electronic products and electrical cars since Li is the lightest metal (equivalent weight = 6.94 g/mol, and specific gravity = 0.53 g/cm^3) and has the most negative redox potential (Li/Li^+ couple is –3.04 V vs. standard hydrogen electrode, SHE) [1]. In addition, the small size of the lithium cation allows a range of intercalation cathode materials, which gives some design freedom for storage systems to suit different applications [2]. However, the reactivity of lithium metal greatly limits the choice of usable electrolytes and impedes the commercialization of secondary lithium batteries. Since liquid electrolytes significantly decrease lithium battery lifetime and safety, solid and solid-like electrolytes appear more suitable for high-capacity lithium batteries [2]. Among all solid and solid-like electrolytes, composite electrolytes with promising electrochemical properties (e.g., conductivity, interfacial stability, and ionic transport properties) and mechanical properties (e.g., viscous and elastic moduli, yield stress) are viable in secondary lithium battery applications [3-8]. Most composite electrolytes reported in the literature are formed by dispersing ceramic fillers (e.g., Al_2O_3, SiO_2, TiO_2) into high-molecular weight (M_w) poly(ethylene oxide) (PEO) polymers doped with lithium salts LiX [3,6-18]. Addition of ion-conducting fillers (e.g., γ-$LiAlO_2$ [3,6,8], Li_3N [3,11]) and even inert ceramic fillers (e.g., SiO_2 [5], TiO_2 [18], MgO [19]) enhances conductivity of a high-M_w PEO electrolyte, with the effect from the inert fillers attributed to an increase in volume fraction of the conductive amorphous phase. Experimental

evidence from various groups consistently shows that the interface between lithium and a composite electrolyte is more stable and efficient in cycling in comparison to the filler-free electrolyte [3,6,8,9]. The enhanced interfacial stability is suggested to be affected by filler particles scavenging impurities such as water and oxygen [7], which react with lithium and accelerate its corrosion. Newman [20] concludes from his modeling work that electrolyte elasticity inhibits lithium dendrite formation, the origin of electrochemically inactive ("dead") lithium. However, the ionic conductivity of composite electrolytes based on high-M_w PEO at ambient temperature is 10^{-4} to 10^{-5} S/cm, which is too low for some applications [8,18]. In recent years, our group has been developing a composite electrolyte by dispersing fumed silica (FS) into low- to moderate-M_w PEO [4,5,21-23]. Unlike high-M_w based PEO composites, the solid-like structure is formed by the filler (fumed silica) instead of PEO chains. Prior research has demonstrated that composites consisting of fumed silica + poly(ethylene glycol) dimethyl ether oligomer (PEG-dm, M_w=250) + lithium salts are promising materials for rechargeable lithium batteries in terms of their high conductivity (>10^{-3} S/cm at room temperature) and good mechanical strength (elastic modulus G'>10^5 Pa) [4,5,22,23]. A significant improvement of lithium interfacial stability with the electrolyte upon incorporation of fumed silica is also observed at open circuit and during cell cycling [5,24].

In this present work, ionic conductivity is reported of composite electrolytes based on methyl-terminated oligo(ethylene oxide) with a M_w range from 250 to 2000 and a variety of fumed oxide fillers (e.g., SiO_2, Al_2O_3, TiO_2, and SiO_2/Al_2O_3). The oligomers

are liquids at 250 and 500 M_w and wax-like solids at 1000 and 2000 M_w. The purpose of expanding the oligomer M_w from totally amorphous (250 and 500) to semicrystalline (1000 to 2000) at ambient temperature is to use these systems as models to provide insight into high-M_w solid PEO system. In addition, the effects of filler type, specific surface area, filler concentration, and surface chemistry are studied. Fourier transform infrared (FTIR) spectroscopy with an Attenuated Total Reflectance (ATR) accessory and Differential Scanning Calorimeter (DSC) measurements are also employed to analyze ion-ion and ion-polymer interactions and thermal properties of the composites.

4.2. Fumed Oxides

Fumed oxides including fumed silica, alumina, and titania are synthesized by high-temperature hydrolysis of the corresponding gaseous metal chlorides ($SiCl_4$, $AlCl_3$, and $TiCl_4$) in an O_2/H_2 flame [25,26]. Due to the pyrogenic synthesis method, all fumed oxides possess unique properties: high-chemical purity (e.g., fumed silica >99.8%, fumed alumina >99.6%, and fumed titania > 99.5% for Degussa products) [25,26]; nanoscale spherical primary particles (5-50 nm) [27]; large specific surface area (up to 600 m^2/g) [27]; and, nonporous structure [25,26]. The predominant particle structures are branch-like aggregates (100-500 nm, apparent packing density is about 30% of SiO_2, Al_2O_3, or TiO_2), which cannot be disrupted by shear and consist of partially fused primary particles (~10 nm) [27-30]. Agglomerates (>1 μm) with a significant fractality (mass fractal dimension of ≈2.1) can be formed as a result of dipole-dipole forces, hydrogen-bonding (H-bonding), and other non-specific forces between aggregates but can be disturbed by

simple mixing [27,29,30]. Another important property of native fumed oxides is that they are hydrophilic due to surface hydroxyl (silanol) groups, which determine many of the physicochemical properties of these materials [27]. Hydrophobic fumed oxides can be produced by chemically modifying the surface hydroxyl groups with alkylsilanes, polysiloxanes, or organofunctional silanes [25,26,31,32]. In addition to individual fumed oxides, binary and ternary fumed oxides with various compositions synthesized by high-temperature hydrolysis of the corresponding metal chloride mixtures are also widely used as pigments, fillers, additives, adsorbents, catalysts, and catalyst supports [26,27,33]. The Brønsted (B) acid sites of $-\overset{|}{\underset{|}{M_{(1)}}}-O(H)-\overset{|}{\underset{|}{M_{(2)}}}$ ($M_{(1)}$, $M_{(2)}$=Al, Si, Ti, etc.) in mixed fumed oxides play an important role in particle-medium and particle-particle interactions, which significantly differ from those in single-metal fumed oxide systems. The physicochemical properties of mixed fumed oxides can also be manipulated by varying the compositions of metal chloride mixtures during synthesis [27,34].

Five types of fumed oxides commercially available from Degussa Corp. are employed in this study (Degussa product designations are used): (I) fumed silica: hydrophilic Aerosil® OX 50, 200, and 380 and hydrophobic R805 (octyl-modified) and R816 (hexadecyl-modified); (II) fumed alumina: Aerosil® Aluminum Oxide C; (III) fumed titania: hydrophilic P25 and hydrophobic T805 (octyl-modified); (IV) fumed silica and alumina mixture Aerosil® COK 84 with 84% A200 and 16% Al_2O_3 C; and (V) mixed fumed oxide Aerosil® MOX 170 consisting of 99% SiO_2 doped with 1% Al_2O_3. The physical properties (e.g., primary particle size, specific surface area, dominant surface

group, and hydroxyl density) of fumed oxides are shown in Figure 4.1, with hydroxyl density values determined either by titration with lithium aluminum hydride ($LiAlH_4$) (OX 50, A200, A380, R805, and TiO_2 T805) [25,26,31,35] or H-D exchange (TiO_2 P25) [36]. Aerosil® OX 50, 200, and 380 are native fumed silica with specific surface areas of 50 m^2/g, 200 m^2/g, and 380 m^2/g. Hydrophobic fumed silica R805 is obtained by reacting A200 with octyltrimethoxysilane (OTMS) [26], while R816 is generated by reacting A200 with hexadecyltrimethoxysilane (HDTMS) [31]. Although all fumed silicas are amorphous, fumed alumina and titania are crystalline. Aluminum Oxide C crystallographically belongs to the δ-group based on X-ray diffraction (XRD) data. Degussa's P25 TiO_2 is a mixture of 70 wt% anatase and 30 wt% rutile. The crystalline mixture results from high temperature and short residence time in the hot zone during synthesis [37]. There are equimolar amounts of acidic and basic hydroxyl groups on the surface of TiO_2; one half of these hydroxyl groups reacts acidically and accumulates ammonia or is esterified with diazomethane, while the other half has a basic character and can be interchanged with certain anions [38,39]. The coexistence of equimolar amounts of acidic and basic hydroxyl groups is also evident from the zeta potential, which is zero at an almost neutral pH of 6.5 [25]. Hydrophobic fumed titania T805 is produced by reaction between native fumed titiania P25 and octyltrimethoxysilane (OTMS). There are two types of dual fumed oxide systems: (1) a simple mixture of two types of single-component fumed oxides and (2) mixed fumed oxides generated by flame hydrolysis of the corresponding metal chloride mixture. Aerosil® COK 84 belongs to the first category and MOX 170 belongs to the second.

4.3. Literature Review: Effect of Fillers on Li^+ Transport in Composite Electrolytes

Considerable effort has been devoted to understand the effect of fillers on Li^+ transport properties in composite electrolytes [18,40-55]. Although it is well accepted that fillers play an important role in Li^+ transport, different trends in conductivity due to addition of fillers are observed, i.e., an increase, decrease, or no change in conductivity have all been reported. This apparent discrepancy can be partly ascribed to the difference in electrolyte materials (polymer, lithium salt, and filler type), their concentration, preparation conditions, and thermal history of the polymer electrolytes. Based on relevancy to this study, the effect of fillers on Li^+ conductivity of EO-type composite electrolytes is summarized in Table 4.1. In the following section we review mechanisms proposed for the role of fillers in affecting Li^+ transport within composite electrolytes.

4.3.1 Lewis Acid-Base Interaction Mechanism

A mechanism based on Lewis acid-base surface interactions was first developed by Wieczorek and coworkers [40,42] to explain the effect of α-Al_2O_3 filler on conductivity of polymer electrolytes based on monomethyl capped poly(ethylene glycol) (PEGM, M_w= 350) + $LiClO_4$ (10^{-6} to 5 mol/kg). Lewis acid surface groups (-OH) of α-Al_2O_3 compete with Li^+ and interact with Lewis base centers of polyether or ClO_4^- oxygen. At high $LiClO_4$ concentration (> 0.5 mol/kg), filler surface groups predominantly interact with ClO_4^-, thus lowering the fraction of neutral ion-pairs and

leading to an increase in conductivity. In addition to increased number of free Li^+, α-Al_2O_3-based composite electrolytes at $LiClO_4$ concentrations above 0.5 mol/kg have lower viscosity and higher polymer chain flexibility than filler-free electrolyte. At low $LiClO_4$ concentration (< 0.5 mol/kg), however, Lewis acid surface groups of α-Al_2O_3 predominantly interact with polyether oxygens, thus increasing the viscosity and resulting in reduced polyether flexibility and lower conductivity. In order to verify the proposed Lewis acid-base interaction mechanism, Wieczorek and coworkers tested Al_2O_3 fillers with neutral, basic, and acidic surface groups [41] and a strong Lewis acid filler ($AlBr_3$) [43] in PEGM (350) + $LiClO_4$. Similar to α-Al_2O_3-based composites, addition of all three types of Al_2O_3 fillers leads to an enhancement in conductivity at salt concentrations above 0.5 mol/kg but a decrease in conductivity at $LiClO_4$ concentrations below. For neutral and acidic Al_2O_3 fillers, Lewis acid-base interactions among polymer chain, lithium salt, and filler surface groups are similar to those in α-Al_2O_3 systems. For basic Al_2O_3, basic surface groups compete with polyether oxygen to interact with Li^+ or positively charged triplets leading to less polymer-Li^+ complexation that results in a decrease in electrolyte viscosity and increase in flexibility of polyether chain. In addition, interaction of filler basic surface groups with Li^+ decreases the fraction of neutral ion-pairs, thus leading to an enhancement in conductivity at high-salt concentration. The decrease in conductivity at low-salt concentration with addition of basic Al_2O_3 is attributed to the immobilization of Li^+ with basic surface groups. Although $AlBr_3$ is a stronger Lewis acid than Al_2O_3, composite electrolytes containing 10 wt% $AlBr_3$ have lower conductivities than those containing 10 wt% acidic Al_2O_3 at both

0.1 and 1 mol/kg $LiClO_4$, with the conductivities varying, respectively, as 10% acidic Al_2O_3 ≅filler-free > 10% $AlBr_3$ and 10% acidic Al_2O_3 > filler-free > 10% $AlBr_3$. The acidic sites on a filler surface can increase conductivity by reducing ion-pairs via interactions with ClO_4^- or decrease conductivity by stiffening the polymer chain via complexation with polyether oxygen. Both interactions become stronger in $AlBr_3$-based composites than in acidic Al_2O_3-based composites, and the relative degree of these two competing effects depends on filler type, salt concentration, and filler loading.

Wieczorek and coworkers [45] also studied the effect of fillers with Lewis acidic surface chemistry including $AlBr_3$ [46], $AlCl_3$ [45,46], and α-Al_2O_3 [45,46] on conductivity of electrolytes based on high-M_w $P(EO)_{10}LiClO_4$. The authors believed that aluminum halides ($AlBr_3$ and $AlCl_3$) interact with ClO_4^- anions leading to the formation of complex anions ($O_3ClOAlX_3^-$ with X=Br and Cl) that act as plasticizing agents for PEO matrixes, thus increasing the ionic conductivity. The plasticizing effect of aluminum halides was supported by the fact that all composite electrolytes containing aluminum halides are amorphous. However, Lewis acids also interact with PEO leading to the formation of PEO-filler complexes, thus stiffening polymeric electrolytes and reducing the conductivity. The first factor dominates at low aluminum halide concentration (< 25 wt%) while the latter dominates at high-filler concentration (> 25 wt%). The increase in conductivity upon addition of α-Al_2O_3 into high-M_w PEO electrolytes, however, was ascribed to different acid-base interactions in comparison to aluminum halides. The authors postulate [45,46] that α-Al_2O_3 particles can act as

nucleation centers for the crystalline PEO. There are a large number of such nucleation centers, and as a consequence polycrystalline microphases are formed, resulting in greater disorder in composite electrolytes than filler-free electrolyte. The increase in disorder was evidenced by a decrease in the fraction of crystalline phase upon addition of α-Al_2O_3.

Scrosati and coworkers [47] further explored the Lewis acid-base interaction mechanism in high-M_w $P(EO)_{20}LiCF_3SO_3$ (Lithium triflate, LiTf) with 10 wt% acidic, basic, or neutral Al_2O_3 fillers. At temperatures above 60°C (the melting point of PEO), all fillers enhance conductivity in the order of neutral > acidic > basic > filler-free. However, at temperatures below 60°C the conductivity is in the order acidic > neutral > filler-free > basic. Two orders of magnitude increase in room-temperature conductivity is observed with addition of acidic Al_2O_3 fillers. They also report an increase in Li^+ transference number upon addition of fillers in the order of acidic > neutral > basic > filler-free. The acidic surface groups of Al_2O_3 are –OH which can H-bond with ether oxygen and oxygen of $CF_3SO_3^-$. The surface groups of basic Al_2O_3 are $\begin{matrix} O \\ / \quad \backslash \\ Al\text{-}Al \end{matrix}$ and form transient crosslinking centers with Li^+-polymer by Lewis acid-base interactions. Both acidic and basic surface groups coexist on neutral alumina, which interacts with $CF_3SO_3^-$ anions through acidic sites by hydrogen bonding and with Li^+ through basic sites by Lewis acid-base interactions. Since hydrogen bonding is stronger than ion-dipole interactions, neutral alumina promotes salt dissociation most efficiently, followed by acidic and asic fillers. In addition to promoting salt dissociation, the polar surface

groups of the inorganic filler also act as cross-linking centers for PEO segments and for X^- anions. Such interaction lowers the PEO crystallization tendency (i.e., the fillers act as "solid plasticizers") and thus promote a structure modification of polymer chains. Such a structure modification provides conducting pathways for Li^+ at the filler surface, which accounts for the improvement in Li^+ transport.

Although Jayathilaka et al. [50] agree that Lewis acid-base interactions among polymer chain, lithium salt, and filler surface groups play a significant role in enhancing Li^+ transport properties of both low- and high-M_w EO-based composite electrolytes, the authors claim that such interactions enhance ionic mobility rather than increase charge carrier concentration from the dissociation of ion-pairs as claimed by both Wiezcorek and Scrosati's groups [45-47]. Jayathilaka et al. studied conductivity and thermal properties of high-M_w $P(EO)_9LiN(CF_3SO_2)_2$ (LiTFSI) + 10 wt% Al_2O_3 (acidic, basic, neutral, weakly acidic) electrolytes using impedance spectroscopy, broadband dielectric spectroscopy, and DSC measurements. The addition of fillers increases conductivity at temperatures range from 0 to 110°C and the maximum enhancement is found with acidic alumina, followed by basic, neutral, and weakly acidic alumina. No change in T_g upon addition of Al_2O_3 was found, which implies that segmental flexibility of PEO chains is essentially unaffected by addition of fillers. Dielectric relaxation spectra showed that ion mobility is increased due to addition of fillers in high-M_w $(PEO)_9$LiTFSI and the increase follows the same trend as conductivity. The authors [50] believed that the interaction of acidic surface groups and $TFSI^-$ create more effective conduction pathways for $TFSI^-$ thus increasing $TFSI^-$ mobility without affecting the mobility of Li^+ and polymer chains.

Likewise, basic surface groups enhance Li^+ mobility without affecting mobility of $TFSI^-$ and polymer chains. In the filler-free electrolyte, anion migration is only weakly influenced by the polymer whereas cation migration is assisted by making/breaking of links with ether oxygens. Therefore, the enhancement in anion migration by acidic alumina is more significant than that in cation migration by basic aluminua. Neutral alumina has equal number of acidic and basic sites, with acidic sites promoting anion migration and basic sites promoting cation migration. However, anions that are transiently 'bonded' to acidic sites on a neutral Al_2O_3 surface can form ion-pairs with cations that are bonded to basic sites on the filler surface. Such ion-pairing decreases the mobility of both cation and anion species, thus leading to a less enhanced ionic mobility by addition of neutral Al_2O_3 than acidic or basic fillers. The authors attributed the lowest conductivity of weakly acidic alumina to: (1) less enhanced cation and anion mobility than pure acidic and basic alumina due to cation-anion interactions induced by coexistence of acidic and basic surface groups, as with neutral alumina, and (2) less enhanced Li^+ mobility due to fewer basic surface groups than neutral alumina and more cation-anion interactions than neutral alumina. However, arguments for lower conductivity for weakly acidic than neutral alumina due to less enhanced Li^+ mobility seem contradictory to their statement of greater conductivity enhancement upon addition of acidic than basic filler. Although weakly acidic alumina enhances Li^+ mobility less than neutral alumina due to fewer basic surface groups, it should enhance $TFSI^-$ mobility because of more acidic surface groups. Since acidic surface groups enhance conductivity more than basic surface groups, we would expect the weakly acidic filler-based

composite electrolyte to have higher conductivity than neutral filler-based electrolyte if the degree of cation-anion interactions and the total number of surface groups are same for both fillers. Table 4.2 compares results on composite electrolytes based on Al_2O_3 fillers with different acidity from three groups: Wieczorek et al. [41], Scrosati et al. [47], and Jayathilaka et al. [50] However, no consistent trend was observed regarding the extent of conductivity enhancement by different surface groups. It seems that the major difference may arise from the different lithium salt and polymer used.

4.3.2 "Solid Plasticizer" Mechanism

It is widely accepted [18,48,49,51] that reduction of crystallinity of high-M_w PEO composite electrolytes upon addition of ceramic fillers (i.e., fillers act as "solid plasticizer") affects an increase in conductivity at temperatures below the melting point. Scrosati and coworkers [18,48,49] have studied thermally treated composite electrolytes and filler-free counterparts to verify the "plasticizing" effect of fillers. Composite electrolytes examined were: $P(EO)_8LiClO_4$ + 10 wt% TiO_2 [18,48,49], Al_2O_3 [48,49], or SiO_2 [49], and $P(EO)_{30}LiClO_4$ + 10 wt% SiO_2 [18]. The conductivity of as-prepared composite electrolytes is consistently higher than filler-free electrolytes. In addition, a dramatic increase is observed in ambient conductivity of composite electrolytes after annealing at temperatures above the PEO crystalline-to-amorphous transition point (60°C) [18,48,49]. The conductivity increase is sustained for a long period of time (e.g., 20 to 60 days). However, no steady-state change in ambient-temperature conductivity was observed with filler-free electrolyte. Energy dispersive X-ray diffraction data

indicated that the structure of composite electrolytes was changed after annealing [49]. The ^{7}Li nuclear magnetic resonance (NMR) data [49] showed that the increase in ionic conductivity of composite electrolytes after annealing is not attributable to an enhancement in polymer segmental motion, but more likely a weakening of the polyether-cation association induced by nanoparticles. Based on their results, the authors [48] conclude that the increase in conductivity of composite electrolytes at ambient temperature after annealing is due to the preservation of a high degree of disorder since fillers act as a "solid plasticizer" to prevent PEO chain reorganization.

Kumar and Scanlon [51] deduce through conductivity measurements that high-M_w PEO-based composite electrolytes (PEO + $LiBF_4$ + TiO_2 or ZrO_2) can be maintained in an amorphous state below PEO melting point after annealing, thus increasing conductivity. Higher annealing temperature, longer heat-treatment time, and faster cooling rate from the annealing temperature favor a reduction in crystallinity of PEO in composite electrolytes. Dai et al. [52] also observed that Al_2O_3 fillers suppress the formation of crystalline phases of $P(EO)_3LiI$ and LiI in $P(EO)_{\leq 3}LiI$ + Al_2O_3 composite electrolytes. The nuclear magnetic resonance (NMR) results [52] implied that the presence of inorganic additive (Al_2O_3) improves Li^+ transport through grain boundaries parallel to the current flow in the electrolytes.

4.3.3 Summary

Filler surface groups can form transient crosslinks with polymer segments or lithium salt by Lewis acid-base interactions. Such interactions play significant roles in

affecting Li^+ transport properties of polymer electrolytes. Different mechanisms influence the filler effect on Li^+ transport properties above and below the polymer melting (crystallization) point. Usually, a less significant impact of fillers on conductivity is observed when polymers are completely amorphous (i.e., above the melting point). In addition, the change in conductivity upon addition of fillers depends on electrolyte materials (polymer, salt, and filler), salt and filler concentrations, filler surface acidity, and thermal history of electrolytes. The effects of fillers on Li^+ transport properties of electrolytes can be categorized as follows: (1) Fillers act as "plasticizers" and lower the crystallinity of the polymer matrix to increase the fraction of amorphous phase [55], thus increasing conductivity. This enhancement mechanism only affects composite electrolytes at temperatures below the polymer melting point; (2) Fillers act as crosslinking centers for polymer segments and X^- anions to create highly conductive pathways along filler surface inducing an increase in conductivity; (3) Fillers break ion aggregation to free either Li^+ or X^- ions by forming complexes between acidic surface groups and anions or between basic surface groups and cations. The increase in number of charge carriers due to enhanced salt dissociation induces an increase in conductivity; (4) Fillers increase ion mobility by providing additional sites for Li^+ or X^- migration due to Lewis acid-base interactions between surface groups and lithium salt, thus leading to increase in conductivity; (5) Fillers can transiently crosslink the polymer chain by Lewis acid-base interactions and stiffen the polymer matrix thus hindering Li^+ transport leading to lower conductivity of composite electrolytes than their filler-free counterparts; and (6) Inert fillers decrease conductivity due to a simple dilution effect [4].

4.4. FTIR Spectroscopy Measurements of Interactions among Polymer, Lithium Salt, and Filler

Wieczorek and coworkers [40,42,44] employed FTIR spectroscopy to study ion-polymer and ion-ion interactions with $LiClO_4$ in PEG (350) and PEG-dm (500) systems. The authors associate changes in the intensity, shape, and peak position (wavenumber) of the C-O-C stretching mode with polyether-$LiClO_4$ interactions, whereas the ν_4 stretch of ClO_4^- is associated with ion-ion interactions. A downshift in wavenumber of the C-O-C stretching mode corresponds to a weaker ion-polymer interaction that provides more free Li^+ for improved ionic transport. The ν_4 stretch of ClO_4^- can be resolved into two contributions with maxima at ~ 623 and 635 cm^{-1}, which are assigned as free ClO_4^- and bound or contact ClO_4^- to Li^+, respectively. The decrease of the ratio of the area under the 635 cm^{-1} mode to the total area under the ν_4 ClO_4^- envelope corresponds to a decrease in ion association accompanied by an increase in conductivity. In the present communication, the FTIR-ATR technique is employed to explore polymer-salt-filler interactions in low-M_w PEG-dm + LiTFSI electrolytes. To our knowledge, IR data of composite electrolytes using LiTFSI salt has not been published.

Different approaches are reported to identify ion aggregation in systems containing LiTFSI. Wen et al. [56] used band shifts in the 1100-1400 cm^{-1} region as indicators of ion association (e.g., the peak around 1350 cm^{-1} for antisymmetric SO_2 stretch mode [$\nu(SO_2)_a$] and the peak around 1200 cm^{-1} for symmetric CF_3 stretch

mode[$\nu(CF_3)_s$]); whereas Rey et al. [57] tentatively attributed an asymmetrical broadening of the symmetric CF_3 bending mode (δ_sCF_3, 740 cm^{-1}) to ion-pair formation. Rey et al. [58] later suggested that assigning a symmetric deformation of the CF_3-group (δ_sCF_3) to a "free" anion is oversimplified; the 740 cm^{-1} mode involves a complex mixing of a number of internal coordinates which makes the entire $TFSI^-$ molecule expand and contact. Abbrent et al. [59] monitored ion-pairing by IR spectroscopy from shifts of three $TFSI^-$ bands in the 730-800 cm^{-1} region (740 cm^{-1} for S-N stretching band, 760 cm^{-1} for the combined C-S and C-F stretching, and 785 cm^{-1} for the combined C-S and S-N stretching) and Li^+-polymer interaction from the intensity change of a CH_2 rocking band at 995 cm^{-1}. In view of the literature, we decided to examine cation-polymer interactions by monitoring the shift of the C-O-C stretching mode following the approach of Wieczorek and coworkers [40,42,44]. Ion-ion interactions of $TFSI^-$ were studied by inspecting the band shifts in two regions: 1100-1400 cm^{-1} ($\nu(SO_2)_a$ and $\nu(CF_3)_s$) and 730-800 cm^{-1} (S-N stretching, the combination of C-S and C-F stretching, and the combination of C-S and S-N stretching). Since our technique is reflectance instead of transmission mode, the peak position is not at the exact wavenumber reported in the literature but rather in its vicinity.

4.5. Experimental

4.5.1 Materials

Different pretreatment and drying procedures are employed for liquid oligomers (M_w=250 and 500) and solids (M_w=1000 and 2000). For low-M_w oligomers, the inhibitor

[butylated hydroxytoluene (BHT), 100 ppm] was first removed using an inhibitor-removing column (Aldrich). The PEG-dm was then dried over 4Å molecular sieves for at least two weeks prior to use. Medium-M_w (1000 and 2000) oligomers were melted and dried over 4Å molecular sieves in a sealed container at 80°C for at least a month before being transferred to the argon-filled glove box. At this point, molecular sieves were replaced with dry sieves, which settled to the bottom of the container, and the oligomer was allowed to cool to a solid at room temperature. Lithium bis(trifluromethylsulfonyl)imide [$LiN(CF_3SO_2)_2$] (LiTFSI, 3M) was dried at 110°C under vacuum for 24 hours before use. Water content of oligomers and LiTFSI was controlled under 20 ppm, as determined by Karl-Fisher titration. Fumed oxides were dried at 120°C under vacuum for at least 3-4 days to achieve a water content of 150-200 ppm before being transferred to the glove box.

4.5.2 Composite Electrolyte Preparation

Composite electrolytes were prepared in an argon-filled glove box. First, a baseline electrolyte was made by dissolving LiTFSI in a PEG-dm oligomer liquid (room-temperature) or melt (~ 80°C for M_w =1000 and 2000) with a fixed ratio of Li:O (1:20) to maintain high conductivity [60]. A certain weight of fumed oxide was then added to the baseline electrolyte and dispersed by use of a high-shear mixer (Tissue Tearor^{TM}, Model 398, BioSpec Products, Inc.) [61]. After preparation, the electrolytes based on PEG-dm (M_w=1000 and 2000), with and without fillers, are solids at room temperature. The baseline electrolytes based on low-M_w PEG-dm (M_w=250 and 500) are liquids, while the

corresponding composite electrolytes are solid-like gels except for TiO_2 composites, which are suspensions. Water content of the baseline electrolyte and composite electrolytes was under 20 and 50 ppm, respectively.

4.5.3 Conductivity Measurements

Conductivities were measured using two-electrode cells (described elsewhere [62]) by ac impedance technique with an EG&G Princeton Applied Research 273 potentiostat and an EG&G 5210 lock-in amplifier controlled by the EG&G PowerSuite impedance software. The measurements were performed over the temperature range from 0 to 100°C (M_w = 250 and 500) and from 25 to 100°C (M_w = 1000 and 2000). Temperature was controlled by an Isotope 1016P (Fisher Scientific) circulating water bath with an accuracy of ±0.5°C. All conductivity data were averaged over three samples and the typical deviation from the average was ±5%.

4.5.4 DSC Measurements

Thermal analysis was conducted to measure glass transition (T_g) and melting temperature (T_m) by using a Dupont Instruments 910 differential scanning calorimeter (DSC) equipped with a TA Instruments DSC cell controlled by TA Instruments 2200 Thermal Analyzer. The temperature scale was calibrated from the melting point of indium. Empty aluminum pans, matched in weight to within 0.02 mg, were used for the sample and reference. Samples (~15-20 mg) in aluminum pans were stabilized at –110°C by slowly cooling from room temperature using liquid nitrogen and then heated at

10°C/min to 150°C. Glass transition temperature (T_g) and melting temperature (T_m) were determined in the conventional manner. The estimated uncertainty of T_g and T_m is ±2°C.

4.5.5 FTIR-ATR Measurements

The samples prepared in the glove box were sealed in argon-filled vials and stored in a desiccator before infrared spectra were taken. Infrared spectra in the attenuated total reflection mode (FTIR-ATR) were obtained using an IR microscope (model number UMA-500) attached to a Digilab FTS 6000 FTIR spectrometer (Bio-Rad). The latter was equipped with a Cassegranian objective containing a germanium crystal to produce a single-pass ATR with a spot size of approximately 30 microns. The entire microscope was encased in a dry nitrogen-filled glove bag, which reduced atmospheric water or CO_2 contamination of the spectra and samples. The spectrometer was equipped with a liquid nitrogen cooled mercury-cadmium-telluride (MCT)/A detector, and the spectra were recorded at 25 ± 2°C with a resolution of 2 cm^{-1} in a spectral range of 4000-650 cm^{-1}. Each absorption spectrum was the average of ten accumulations of 64 scans and corrected against the background spectrum of air.

4.6. Results

4.6.1 Conductivity of Composite Electrolytes

4.6.1.1 Effect of Filler Type on Ionic Conductivity

Figure 4.2 is an Arrhenius plot of ionic conductivity from 0 to 100°C of the baseline liquid electrolyte [PEG-dm (250) + LiTFSI (Li:O=1:20)] and the corresponding

composite-electrolytes containing 10 wt% filler of five different types: A200, Al_2O_3 C, TiO_2 P25, COK 84, and MOX 170. The conductivity of filler-free electrolyte is slightly higher than that of composite electrolytes at all temperatures and the filler type does not have a significant effect on conductivity at the experimental conditions employed.

4.6.1.2 Effect of Specific Surface Aarea on Ionic Conductivity

Figure 4.3 shows conductivity of filler-free electrolyte and composite electrolytes containing 10 wt% fillers with different specific surface area: 50 m^2/g (OX 50), 200 m^2/g (A200), and 380 m^2/g (A380). The conductivity of 10% OX 50 composite is about same as that of 10% A200 composite and both are much higher than that of 10% A380 composite. Apparently, the increase of specific surface area reduces conductivity of electrolytes in a non-linear trend. The room-temperature conductivity remains above 10^{-3} S cm^{-1} even with the 10% A380 composite electrolyte.

4.6.1.3 Effect of Surface Chemistry on Ionic Conductivity

Figure 4.4 shows conductivity of filler-free electrolyte and composite electrolytes containing 10 wt% fumed silicas with different surface groups: -OH (A200), octyl (R805), and hexadecyl (R816). There is no substantial difference in conductivity of composite electrolytes based on fumed silicas with native surface hydroxyl groups and octyl groups. However, upon addition of fumed silica with hexadecyl surface groups, the conductivity of composite electrolytes is slightly lower, especially at temperatures below

50 °C. Conductivities of composite electrolytes based on fumed titania with native surface hydroxyl and octyl- groups are practically identitcal, as shown in Figure 4.5.

4.6.1.4 Effect of Filler Content on Ionic Conductivity

Figure 4.6 shows conductivity of filler-free electrolyte and composite electrolytes with 5, 10, 15, and 20 wt% Al_2O_3 C from 0 to 100°C. In general, addition of Al_2O_3 C filler decreases conductivity at all temperatures studied. Figure 4.7 shows the normalized conductivity (s/s_0, σ_0=1.97×10^{-3} S/cm) of composite electrolytes at 25°C versus volume fraction of solvent (1-ϕ_s). The room-temperature conductivity of all electrolytes is greater than 1×10^{-3} S cm^{-1} ($s/s_0 > 0.5$) in all instances. The normalized conductivity of the composite electrolytes increases as (1-ϕ_s)$^{2.76}$, as indicated by the solid straight line on the figure, for all fumed oxide fillers except A380. In comparison to other fillers, addition of A380 in PEG-dm (250) + LiTFSI electrolyte causes a dramatic drop in conductivity at the same liquid volume fraction.

4.6.1.5 Effect of Oligomer Molecular Weight (M_w) on Ionic Conductivity

Figure 4.8 is the Arrhenius plot of ionic conductivity for PEG-dm (500) + LiTFSI (Li:O=1:20) of filler-free and composite electrolytes containing 10 wt% fumed silica, alumina, titania, the mixture of silica and alumina, and alumina-doped silica. The conductivity of composite electrolytes at 0°C is essentially the same and much higher than that of filler-free electrolyte. At $T \geq 15°C$, however, addition of all inert fillers other than TiO_2 into the baseline liquid electrolyte slightly decreases conductivity almost

the same extent, as seen with PEG-dm (250)-based electrolytes. There is essentially no difference in conductivity of composite electrolyte containing 10 wt% fumed titania and filler-free electrolyte at $T \geq 15°C$. Figure 4.9 presents ionic conductivity of PEG-dm (1000)-based electrolytes without filler and with 10 wt% hydrophilic fillers: A200, Al_2O_3 C, TiO_2 P25, COK 84, and MOX 170. Similar to PEG-dm (500)-based electrolytes, addition of fillers enhances conductivity at low temperature (25°C) and decreases conductivity at high temperatures (≥40°C). However, no substantial difference in conductivity is observed due to fumed oxide type at all temperatures. Figure 4.10 shows ionic conductivity of PEG-dm (2000)-based electrolytes without filler and with 10 wt% of various hydrophilic fillers: A200, Al_2O_3 C, TiO_2 P25, COK 84, and MOX 170. Again, incorporation of fillers into the polymer electrolyte enhances conductivity at low temperatures (< 40°C) and decreases conductivity at high temperatures (≥55°C). At all temperatures, MOX 170-based composite electrolyte has the lowest conductivity while COK 84 enhances conductivity the most at low temperatures among all composites. The conductivity of composite electrolytes containing A200, Al_2O_3 C, and TiO_2 P25 is practically same at all temperatures. From Figs. 2, 8, 9, and 10, we see that conductivity decreases with increasing M_w for both filler-free and composite electrolytes, especially at low temperatures. Two regions where fumed-oxide fillers have a distinct effect on conductivity are observed in the Arrhenius plots. The transition temperature where fillers change from impairing to enhancing effect in conductivity increases with increasing M_w.

4.6.2 Thermal Properties of Composite Electrolytes

Table 4.3 lists glass transition temperatures (T_g) and melting points (T_m) of filler-free electrolytes and corresponding composite electrolytes containing 10 wt% A200 and Al_2O_3 using various M_w PEG-dm. The composite electrolyte containing 10 wt% A380 in PEG-dm (250) + LiTFSI is also included in the table. For PEG-dm (250)-based electrolytes, T_g increases and T_m decreases slightly (3°C at most) with addition of fillers. Composite electrolytes with 10% Al_2O_3 and 10% A200 have the same T_g and T_m. Composite electrolyte containing 10 wt% A380 shows the highest T_g but the same T_m as those containing Al_2O_3 and A200. For PEG-dm (500)-based electrolytes, T_g increases upon addition of fillers in the order of filler-free < 10% Al_2O_3 < 10% A200. However, T_m remains constant upon addition of fillers. For PEG-dm (1000)-based electrolytes, addition of fillers increases T_g in the order of filler-free < 10% A200 < 10% Al_2O_3. The melting point is essentially same for all three electrolytes. For PEG-dm (2000)-based electrolytes, an increase in T_g upon addition of 10% A200 was observed but no significant change in T_g with addition of 10% Al_2O_3 was found. The melting point decreases upon incorporation of fillers into the baseline solid electrolyte in the order of filler-free > 10% Al_2O_3 > 10% A200.

4.6.3 Interactions among Polymer Chain, Lithium Salt, and Filler: FTIR Spectroscopy of Composite Electrolytes

Figure 4.11 reports FTIR-ATR spectra of filler-free electrolyte and electrolytes containing 10 wt% A200 or Al_2O_3 + PEG-dm + LiTFSI (Li:O=1:20) with M_w of 250 and

Figure 4.12 reports the same but with M_w of 2000. The IR spectrum of electrolyte containing 10 wt% A380 in PEG-dm (250) + LiTFSI is also shown in Figure 4.11 to illustrate the effect of particle size of fumed silica on interactions among polymer, lithium salt, and filler. Molecular weights of 250 and 2000 are chosen to illustrate the difference in IR spectra of electrolytes based on liquid (M_w=250) and solid (M_w=2000) oligomers. Table 4.4 summarizes the characteristic peak position for polymer-Li^+ interaction (C-O-C stretching, CH_2 rocking, and CH_2 wagging mode) for filler-free electrolyte and electrolytes containing 10 wt% A200 and Al_2O_3 based on PEG-dm with M_w of 250, 500, 1000, and 2000. Composite electrolyte containing 10 wt% A380 in PEG-dm (250) + LiTFSI is also listed. Table 4.5 lists peak positions of characteristic peaks representing ion-ion interactions of $TFSI^-$ for these electrolytes. As described in the literature review, the band-shift of C-O-C stretch mode at around 1100 cm^{-1} was employed as an indicator of the Li^+-polymer interaction. The C-O-C stretch mode is assigned at 1096 cm^{-1} for the PEG-dm (250) + LiTFSI electrolyte. No significant change in C-O-C peak position is observed in presence of 10 wt% A200 (1098 cm^{-1}), Al_2O_3 (1099 cm^{-1}), or A380 (1098 cm^{-1}). Three characteristic peaks between 700 to 800 cm^{-1} are identified in PEG-dm (250) + LiTFSI electrolyte as follows [59]: 738 cm^{-1} for S-N stretching, 761 cm^{-1} for the combination of C-S and C-F stretching, and 787 cm^{-1} for the combination of C-S and S-N stretching. No shifts or broadening are seen in these three peaks for the composite electrolytes containing 10% A200 (739 cm^{-1}, 761 cm^{-1}, and 787 cm^{-1}), Al_2O_3 (739 cm^{-1}, 760 cm^{-1}, and 786 cm^{-1}), and A380 (740 cm^{-1}, 761 cm^{-1}, and 787 cm^{-1}). Symmetric CF_3

stretching mode ($\nu(CF_3)_s$) is assigned to 1190 cm^{-1} and $\nu(SO_2)_a$ is assigned to 1353 cm^{-1} with a shoulder peak at 1336 cm^{-1} in PEG-dm (250) + LiTFSI electrolyte.

The C-O-C stretching is at 1098 cm^{-1} for PEG-dm (500) + LiTFSI and decreases to 1094 cm^{-1} and 1096 cm^{-1} for composites with 10 wt% A200 and Al_2O_3, respectively. In terms of ion-ion interactions in PEG-dm (500), we found no band shift in three CF_3 peaks (739 cm^{-1}, 760 cm^{-1}, and 787 cm^{-1}), $\nu(CF_3)_s$ (1189 cm^{-1}), or $\nu(SO_2)_a$ (1352 cm^{-1} with a shoulder at 1335 cm^{-1}) upon addition of fillers.

The C-O-C stretching peak is at 1108 cm^{-1} for PEG-dm (1000) + LiTFSI. The addition of 10 wt% A200 causes a downshift of the peak to 1088 cm^{-1} while addition of Al_2O_3 induces no shift (1107 cm^{-1}). Compared to IR spectra of PEG-dm (250) or PEG-dm (500)-based electrolytes, new peaks between 900 to 1000 cm^{-1} are observed for PEG-dm (1000)-based electrolytes. The new peak at 963 cm^{-1} is identified as the CH_2 rocking band and remains unchanged upon addition of 10 wt% A200 but disappears upon addition of 10 wt% Al_2O_3. Similar to PEG-dm (250) and PEG-dm (500) systems, no significant shift, peak broadening, and splitting are observed in five major characteristic peaks for ion-ion interactions upon addition of fillers in PEG-dm (1000)-based electrolytes (739 cm^{-1}, 761 cm^{-1}, and 787 cm^{-1}, 1190 cm^{-1}, and 1352 cm^{-1} with a shoulder at 1336 cm^{-1}).

The C-O-C stretching peak is at 1104 cm^{-1} for PEG-dm (2000) + LiTFSI and decreases to 1092 and 1093 cm^{-1} upon addition of 10 wt% A200 and Al_2O_3, respectively. However, no significant change is observed in five characteristic peaks for ion-ion interactions as in PEG-dm (1000) system (740 cm^{-1}, 761 cm^{-1}, and 788 cm^{-1}, 1189 cm^{-1},

and 1353 cm^{-1} with a shoulder at 1333 cm^{-1}). The CH_2 rocking band is at 962 cm^{-1} for filler-free and composite electrolyte containing 10 wt% A200 in PEG-dm (1000) + LiTFSI. However, it disappears in the spectra of composite electrolyte containing 10 wt% Al_2O_3. The CH_2 wagging mode ($\omega(CH_2)_a$) peak shows up in PEG-dm (2000) + LiTFSI electrolyte around 1343 cm^{-1} and peak intensity decreases in composite containing 10 wt% A200. The peak disappears in composite electrolyte containing 10 wt% Al_2O_3.

4.7. Discussion

4.7.1 Conductivity

From the analysis of conductivity data (Figures 4.2 to 4.10) and thermal properties (T_m, Table 4.3), a common trend is observed for all composite electrolytes independent of oligomer M_w: conductivity is decreased in the presence of fillers at temperatures above the electrolyte melting point and is increased at temperatures below. It is recognized [18,48,49,53,54] that different mechanisms determine the effect of filler on Li^+ transport above and below the melting point; and it is also acknowledged [18,48,49,53,54] that the effect filler is less pronounced at temperatures above the melting point than below. Thus, it is not surprising to see an abrupt change in the Arrhenius plot around the melting point (Figs. 8 to 10), as Scrosati and coworkers observed for electrolytes without annealing [18,48,49]. Wieczorek and coworkers [44] reported that the presence of fumed silica (5 to 20 wt%) enhances conductivity by about 10 to 59% at $LiClO_4$ concentration of 1 mol/kg in PEG-dm (500) at 25°C. In contrast, we

observe a decrease (~ 20% to 28%) in conductivity upon addition of 10 wt% fumed silica in PEG-dm (500) + LiTFSI (1 mol/kg). The different effect of filler in LiTFSI-containing and $LiClO_4$-containing electrolytes is not surprising. The LiTFSI salt has a low-lattice energy and a bulky anion [50] and is, consequentially, more dissociated in polyether electrolytes than $LiClO_4$ [53]; therefore, LiTFSI-based electrolytes have higher conductivity at equal salt content. For example, conductivity of filler-free electrolyte and composite electrolyte containing 10 wt% fumed silica at $LiClO_4$ concentration of 1 mol/kg in PEG-dm (500) is approximately 2.2×10^{-4} and 3.6×10^{-4} S/cm, respectively at 25°C [44], but the analogous systems containing LiTFSI salt have conductivities of 6.1×10^{-4} and 4.8×10^{-4} S/cm, respectively. Although the conductivity of composite electrolyte containing 10 wt% fumed silica is lower than that of filler-free electrolyte in PEG-dm (500)+ LiTFSI electrolyte, it is still higher than that of fumed silica-based composite electrolyte in PEG-dm (500) + $LiClO_4$ at the same salt and filler concentration. Addition of filler is expected to have a more significant effect in enhancing conductivity by freeing Li^+ from neutral ion-pairs in $LiClO_4$-containing than LiTFSI-containing electrolyte. On the other hand, the dilution effect by inert fillers causes a reduction in conductivity. At $LiClO_4$ concentration of 1 mol/kg in PEG-dm (500) + $LiClO_4$ electrolytes [44], the enhancement in ion dissociation dominates leading to an increase in conductivity upon addition of filler. At LiTFSI concentration of 1 mol/kg in PEG-dm (500) + LiTFSI, however, the dilution effect dominates resulting in a reduction in conductivity upon addition of fillers. Best et al. [53,54] also observed less enhancement in conductivity with LiTFSI-containing than $LiClO_4$-containing electrolytes at the same

salt concentration in P(EO:PO=3:1) polymer. The authors observed that fumed TiO_2 and Al_2O_3 fillers do not significantly affect conductivity at lithium salt ($LiClO_4$ and $LiCF_3SO_3$) concentration of 1 mol/kg in P(EO:PO=3:1) polymer but increases conductivity substantially (factor of 2-3) at higher salt concentration. However, the authors report no significant change in conductivity using LiTFSI salt at the two concentrations studied (1.5 and 2.0 mol/kg). Best et al. [53] observed that conductivity of a composite electrolyte containing 10 wt% TiO_2 with $LiClO_4$ salt is comparable to that of filler-free electrolyte with LiTFSI salt at the same salt concentration. Another possible reason for the difference in the effect of fumed silica on conductivity in the PEG-dm (500) system is that fumed silicas are from different sources [Aldrich (no information of manufacturer) [44] and Degussa in this study], possibly different manufacturers. In order to fundamentally understand the mechanism that controls filler effect on ionic transport properties of composite electrolytes, it is important to investigate the interactions among polymer segment, lithium salt, and filler.

4.7.2 Thermal Properties of Composites

A slight increase in T_g is observed (Table 4.3) upon addition of fillers in all PEG-dm systems studied. We interpret this increase as a reduction in flexibility of polymer segments. There are at least two factors that would cause the reduction. Lewis-acid centers (-OH groups) on the filler surface interact with Lewis-base centers of the polymer (polyether oxygens), thus forming polymer-filler complexes or even transiently crosslink polymer segments at the surface of filler particles and restricting polymer segment

movement. The polymer segment motion is reduced most with composite electrolyte containing 10 wt% A380 (380 m^2/g-surface area) among all electrolytes based on PEG-dm (250) + LiTFSI, as evidenced by the highest T_g (Table 4.3) and the lowest normalized conductivity (Figure 4.7). Apparently, addition of filler in PEG-dm (M_w = 250 to 2000) + LiTFSI does not slow the recrystallization of polymer chains or increase the amorphous phase within polymer matrix since a decrease in T_g is not observed. The conductivity enhancement observed below the melting point must originate from other factors, some of which are discussed below.

4.7.3 Polymer-Li^+ Complexes

As discussed in the literature review, prior research suggests that interactions between filler surface groups and polyether oxygens can break polymer-Li^+ complexes to increase the concentration of free Li^+ [40,44-46,63]. In addition, interaction between filler surface groups and X^- anions can reduce ion-pairing and thus increase the concentration of free X^-. Both effects increase the number of charge carriers, and thereby conductivity. Although the increase in T_g upon addition of 10 wt% A380 implies a reduction in polymer segment mobility, no significant difference in C-O-C stretching mode is observed for electrolytes based on PEG-dm (250) + LiTFSI with and without fillers. Apparently, IR is not sensitive enough to detect such change in polymer chain flexibility. The FTIR data shows a downshift of the C-O-C stretching mode upon addition of fillers in PEG-dm + LiTFSI electrolytes with $M_w \geq 500$ (Table 4.4), which indicates that polyether oxygen experiences an increased bond energy, thus leading to an

increase in stiffness of the polymer. Based on this data, a decrease in polymer-Li^+ complexation is not detected. Both the peak position of C-O-C stretching (~1100 cm^{-1}) and the intensity of the CH_2 rocking band (~950 cm^{-1}) indicate the strength of Li^+-polymer coordination. In both PEG-dm (1000) + LiTFSI and PEG-dm (2000) + LiTFSI systems, we observe a decrease in the intensity of CH_2 rocking mode. According to Abbrent et al. [59], an intensity decrease of the CH_2 rocking band indicates a stronger Li^+-polymer coordination. In addition, we observed an intensity decrease in CH_2 wagging mode (1350-1150 cm^{-1}) in PEG-dm (2000) + LiTFSI system. We believe that this intensity reduction also indicates an enhanced polymer-Li^+ complexation since both wagging and rocking modes are CH_2 bending motions. It seems that fumed oxide fillers do not generate additional free Li^+ to participate in Li^+ transport in the PEG-dm systems under study. This is in good agreement with the electrophoretic NMR (ENMR) data reported by Walls et al. [64]. The authors observed little change in lithium transference number (T_{Li}) and spin-lattice relaxation (T_1) of ^7Li with fumed silica content. The increase in stiffness of polymer chain causes a decrease in conductivity, which is a contributing factor to the decrease in conductivity upon incorporation of fillers into polymer electrolytes we observed at temperatures above the melting point.

4.7.4 Ion-Pairing

The FTIR data shows no wavenumber shift, broadening, or split in the five characteristic peaks of $TFSI^-$ in all PEG-dm systems under study (Figures 4.11 and 4.12, Table 4.5), which indicates no reduction in ion-pairing effected by the fillers. Less ion-

pairing is expected in electrolytes based on LiTFSI than in $LiClO_4$ salt due to the better solvation in polyether electrolytes of the former [53]. Since the degree of ion-pairing is low in LiTFSI-containing electrolytes, it is not surprising to observe no noticeable reduction in ion aggregation upon addition of fumed oxide fillers in our study compared to a more pronounced effect in $LiClO_4$ system [40]. Best et al. [54] did not observe any reduction in ion aggregation in composite electrolytes with LiTFSI salt studied using Raman spectroscopy, which is in good agreement with our observations from FTIR measurements.

4.7.5 Conductivity Enhancement at Temperatures below T_m

Apparently, conductivity enhancement below the melting point of the composite electrolytes under study is not due to an increase in the fraction of amorphous phase or enhanced salt dissociation. One remaining factor that might affect the observed enhancement is the formation of conductive pathways on polymer-filler grain boundaries. Addition sites for $TFSI^-$ migration are created via the interactions between surface Lewis acid groups and $TFSI^-$ anions without affecting ion-pairing, as suggested by Jayathilaka et al. [50] Fumed titiania fillers have both acidic and basic surface –OH groups that can form complexes with both Li^+ and $TFSI^-$ ions and enhance mobility of cations and anions to increase conductivity. The Lewis acid-base interactions among polymer chain, lithium salt, and filler surface groups have competing factors in affecting ionic transport properties: (1) reduction in flexibility of polymer chains upon addition of fillers causes a decrease in conductivity, and (2) additional sites for ion migration induce an increase in

conductivity. In addition, the insulating (ion-blocking) nature of fillers also affects a decrease in conductivity. At temperatures above T_m, enhanced stiffness of polymer chain and filler-dilution effect dominate, while at temperatures below T_m the improved ion mobility dominates

Table 4.6 shows the effective concentration of Lewis acid surface groups in composites containing 10 wt% fillers in PEG-dm + LiTFSI (Li:O=1:20). Lithium salt concentration is around 1 mol/kg and Lewis-acid surface groups are about one to two orders of magnitude lower, at 10^{-2} to 10^{-1} mol/kg. Since Li:O=1:20, the ratio of polyether oxygen to surface hydroxyl groups is about 200 to 2000 (two to three orders of magnitude ratio in available sites for Lewis acid-base interactions). No significant reduction in ion-pairing is expected since interactions between the Lewis-acid surface groups and polyether oxygens dominate. Although different filler type, surface chemistry, or surface area causes different concentration of Lewis acidic –OH groups, we expect a similar degree of complexation between polymer chains and –OH groups for all fillers because of the excess polyether oxygens. Therefore, the lack of any significant effect of filler type, surface chemistry, and surface area in conductivity is reasonable. However, mechanical properties (viscosity, elastic and viscous moduli [23,65,66]) of electrolytes vary with physical properties of fillers since the strength of interaction forces among surface functional groups vary with filler type.

One exception in conductivity data is that the surface area of fillers shows a relatively significant impact on conductivity at the high value (380 m^2/g). The reason for this most pronounced impact may be due to the particle agglomerate formation because

of the small primary particle size [26]. This aggregation or agglomeration increases the stiffness of electrolytes, which is evidenced by the highest T_g (-94°C) among the electrolytes in PEG-dm (250) systems studied, thus decreasing conductivity more significantly.

4.8. Summary

The effects of individual fumed oxide fillers and binary mixtures of oxide fillers on ionic conductivity of composite electrolytes based on PEG-dm + LiTFSI (Li:O=1:20) were studied using EIS, DSC, and FTIR-ATR techniques. The addition of fillers affects an enhancement in Li^+-polymer coordination and thus an increase in T_g. This enhancement effect increases with increasing M_w of the PEO oligomers. However, the fillers do not break ion aggregations according to the IR spectroscopy data. The increase in conductivity at temperatures below T_m upon addition of fillers apparently is not due to an increase in polymer chain flexibility or number of charge carriers. It is believed that there are two pathways for Li^+ to transport in composite electrolytes: (1) Li^+ ions hop from one polymer segment to another dependent on the flexibility of polymer segments, and (2) Li^+ ions are transferred along the filler surface. The ion transport by movement of polymer segments is comparable with or greater than that occurring on the filler surface when electrolytes are amorphous (above T_m); whereas Li^+ transport on the filler surface is faster and preferable when electrolytes are semicrystalline (below T_m). Lewis acid-base interactions between salt ions and filler surface groups generate additional sites for ion-migration, thus improving ion mobility and increasing conductivity at

temperatures below T_m. In contrast, the insulating nature of fillers and the stiffening of polymer electrolytes upon addition of fillers cause a decrease in conductivity at temperatures above T_m. No significant effect of filler type, surface chemistry, and surface area on conductivity is expected due to the similar degree of interactions between polymer chains and filler surface groups. The abnormally pronounced effect of filler on conductivity at high surface area (about 380 m^2/g) is mainly caused by the most reduction in polymer chain motion, as evidenced by the highest T_g.

4.9 Acknowledgements

The authors gratefully acknowledge funding from the Department of Energy, Office of Basic Energy Sciences and Office of Transportation Technologies. We also thank 3M for providing LiTFSI salt and Degussa for supplying fumed metal oxides. Our appreciation also goes to Dr. Tim Mccarthi from Degussa Corp. for providing us the information on –OH density of TiO_2. The authors also want to express our gratitude to Prof. Franzen's research group (Mr. Simon Lappi and Mr. Scott Brewer) in the NCSU Chemistry Department and Prof. Balik's research group (Ms. Jennifer Ayres and Mr. Marcus Hunt) in the NCSU Materials Science Department for the training and accessibility to FTIR-ATR and DSC measurements. Finally, we thank Mr. Jeff Yerian in the Chemical Engineering Department at NCSU for the automation of conductivity data acquisition.

4.10 References

[1] J.-M. Tarascon and M. Armand, *Nature*, **414**, 359 (2001).

[2] R. Arnaud, D. Benrabah, and J.-Y. Sanchez, *J. Phys. Chem.*, **100**, 10882 (1996).

[3] B. Kumar and L. G. Scanlon, *J. Power Sources*, **52**, 261 (1994).

[4] J. Fan, S. R. Raghavan, X. Y. Yu, S. A. Khan, P. S. Fedkiw, J. Hou, and G. L. Baker, *Solid State Ion.*, **111**, 117 (1998).

[5] J. Fan and P. S. Fedkiw, *J. Electrochem. Soc.*, **144**, 399 (1997).

[6] G. B. Appetecchi, S. Scaccia, and S. Passerini, *J. Electrochem. Soc.*, **147**, 4448 (2000).

[7] G. B. Appetecchi, F. Croce, L. Persi, F. Ronci, and B. Scrosati, *Electrochim. Acta*, **45**, 1481 (2000).

[8] F. Capuano, F. Croce, and B. Scrosati, *J. Electrochem. Soc.*, **138**, 1918 (1991).

[9] M. C. Borghini, M. Mastragostino, S. Passerini, and B. Scrosati, *J. Electrochem. Soc.*, **142**, 2118 (1995).

[10] J. E. Weston and B. C. H. Steele, *Solid State Ion.*, **7**, 75 (1982).

[11] S. Skaarup, K. West, and B. Zachauchristiansen, *Solid State Ion.*, **28**, 975 (1988).

[12] J. Plocharski and W. Wieczorek, *Solid State Ion.*, **28-30**, 979 (1988).

[13] J. Plocharski, W. Wieczorek, J. Przyluski, and K. Such, *Appl. Phy. A-Mater. Sci. & Proc.*, **49**, 55 (1989).

[14] B. K. Choi, Y. W. Kim, and K. H. Shin, *J. Power Sources*, **68**, 357 (1997).

[15] Y. Dai, Y. Wang, S. G. Greenbaum, S. A. Bajue, D. Golodnitsky, G. Ardel, E. Strauss, and E. Peled, *Electrochim. Acta*, **43**, 1557 (1998).

[16] F. Croce, R. Curini, A. Martinelli, L. Persi, F. Ronci, B. Scrosati, and R. Caminiti, *J. Phys. Chem. B*, **103**, 10632 (1999).

[17] W. Wieczorek, K. Such, H. Wycislik, and J. Plocharski, *Solid State Ion.*, **36**, 255 (1989).

[18] B. Scrosati, F. Croce, and L. Persi, *J. Electrochem. Soc.*, **147**, 1718 (2000).

[19] B. Kumar, S. J. Rodrigues, and L. G. Scanlon, *J. Electrochem. Soc.*, **148**, A1191 (2001).

[20] J. Newman, *Improved electrochemical models.* 2002: BATT review meeting.

[21] S. A. Khan, G. L. Baker, and S. Colson, *Chem. Mater.*, **6**, 2359 (1994).

[22] H. J. Walls, J. Zhou, J. A. Yerian, P. S. Fedkiw, S. A. Khan, M. K. Stowe, and G. L. Baker, *J. Power Sources*, **89**, 156 (2000).

[23] S. R. Raghavan, M. W. Riley, P. S. Fedkiw, and S. A. Khan, *Chem. Mater.*, **10**, 244 (1998).

[24] J. Zhou, P. S. Fedkiw, and S. A. Khan, *J. Electrochem. Soc.*, **149**, A1121 (2002).

[25] M. Ettlinger, *Highly Dispersed Metallic Oxides Produced by the AEROSIL® Process,* Degussa Technical Bulletin Pigments No. 56, Akron, OH (2002).

[26] G. Michael and H. Ferch, *Basic Characteristics of AEROSlL®*, Degussa Technical Bulletin Pigment No. 11, Akron, OH (1998).

[27] V. M. Gun'ko, V. I. Zarko, V. V. Turov, R. Leboda, E. Chibowski, E. M. Pakhlov, E. V. Goncharuk, M. Marciniak, E. F. Voronin, and A. A. Chuiko, *J. Colloid & Interf. Sci.*, **220**, 302 (1999).

[28] V. Khavryutchenko, A. Khavryutchenko, and H. Barthel, *Macromol. Symp.*, **169**, 1 (2001).

[29] V. Khavryutchenko, H. Barthel, and E. Nikitina, *Macromol. Symp.*, **169**, 7 (2001).

[30] H. Barthel, L. Rosch, and J. Weis, in: N. Auner, J. Weis (Ed.), *Organosilicon Chemistry II. from molecules to materials*, VCH, Weinheim, p. 761, 1996.

[31] M. Ettlinger, T. Ladwig, and A. Weise, *Prog. Org. Coat.*, **40**, 31 (2000).

[32] V. M. Gun'ko, D. J. Sheeran, S. M. Augustine, and J. P. Blitz, *J. Colloid Interf. Sci.*, **249**, 123 (2002).

[33] V. M. Gun'ko, V. I. Zarko, R. Leboda, M. Marciniak, W. Janusz, and S. Chibowski, *J. Colloid & Interf. Sci.*, **230**, 396 (2000).

[34] V. M. Gun'ko, V. I. Zarko, R. Leboda, and E. Chibowski, *Adv. Colloid & Interf. Sci.*, **91**, 1 (2001).

[35] T. Mccarthi, Degussa Corp. (private communication, 2002).

[36] H. P. Boehm, *Kolloid Z. & Z. Polym.*, **227**, 17 (1968).

[37] M. Bankmann, R. Brand, B. H. Engler, and J. Ohmer, *Catal. Today*, **14**, 225 (1992).

[38] H. P. Boehm, *Discuss. Faraday Soc.*, **52**, 264 (1971).

[39] H. P. Boehm, *Angewandte chemie international edition*, **5**, 533 (1966).

[40] W. Wieczorek, P. Lipka, G. Zukowska, and H. Wycislik, *J. Phys. Chem.*, **102**, 6968 (1998).

[41] M. Marcinek, A. Bac, P. Lipka, A. Zalewska, G. Zukowska, R. Borkowska, and W. Wieczorek, *J. Phys. Chem. B*, **104**, 11088 (2000).

[42] M. Marcinek, A. Zalewska, G. Zukowska, and W. Wieczorek, *Solid State Ion.*, **136-137**, 1175 (2000).

[43] R. Borkowska, A. Reda, A. Zalewska, and W. Wieczorek, *Electrochim. Acta*, **46**, 1737 (2001).

[44] D. Swierczynski, A. Zalewska, and W. Wieczorek, *Chem. Mater.*, **13**, 1560 (2001).

[45] W. Wieczorek, J. R. Stevens, and Z. Florjanczyk, *Solid State Ion.*, **85**, 67 (1996).

[46] W. Wieczorek, A. Zalewska, D. Raducha, Z. Flojanczyk, and J. R. Stevens, *J. Phys. Chem.*, **102**, 352 (1998).

[47] F. Croce, L. Persi, B. Scrosati, F. Serraino-Fiory, E. Plichta, and M. A. Hendrickson, *Electrochim. Acta*, **46**, 2457 (2001).

[48] F. Croce, G. B. Appetecchi, L. Persi, and B. Scrosati, *Nature*, **394**, 456 (1998).

[49] S. H. Chung, Y. Wang, L. Persi, F. Croce, S. G. Greenbaum, B. Scrosati, and E. Plichta, *J. Power Sources*, **97-98**, 644 (2001).

[50] P. A. R. D. Jayathilaka, M. A. K. L. Dissanayake, I. Albinsson, and B.-E. Mellander, *Electrochim. Acta*, **47**, 3257 (2002).

[51] B. Kumar and L. G. Scanlon, *Solid State Ion.*, **124**, 239 (1999).

[52] Y. Dai, S. Greenbaum, D. Golodnitsky, G. Ardel, E. strauss, E. Peled, and Y. Rosenberg, *Solid State Ion.*, **106**, 25 (1998).

[53] A. S. Best, A. Ferry, D. R. MacFarlane, and M. Forsyth, *Solid State Ion.*, **126**, 269 (1999).

[54] A. S. Best, J. Adebahr, P. Jacobsson, D. R. MacFarlane, and M. Forsyth, *Macromol. Symp.*, **34**, 4549 (2001).

[55] J. Przyluski, M. Siekierski, and W. Wieczorek, *Electrochim. Acta*, **40**, 2101 (1995).

[56] S. J. Wen, T. J. Richardson, D. I. Ghantous, K. A. Striebel, P. N. Ross, and E. J. Gairns, *J. Electroanal. Chem.*, **408**, 113 (1996).

[57] I. Rey, J. C. Lassegues, J. Gorondin, and L. Servant, *Electrochim. Acta*, **43**, 1505 (1998).

[58] I. Rey, P. Johansson, J. Lindgren, J. C. Lassegues, J. Grondin, and L. Servant, *J. Phys. Chem. A*, **102**, 3249 (1998).

[59] S. Abbrent, J. Lindgren, J. Tegenfeldt, and A. Wendsjo, *Electrochim. Acta*, **43**, 1185 (1998).

[60] J. Fan, S. R. Raghavan, X. Y. Yu, S. A. Khan, P. S. Fedkiw, J. Hou, and G. L. Baker, *Solid State Ionics*, **111**, 117 (1998).

[61] H. J. Walls, J. Zhou, J. A. Yerian, P. S. Fedkiw, S. A. Khan, M. K. Stowe, and G. L. Baker, *Journal of Power Sources*, **89**, 156 (2000).

[62] M. W. Riley, P. S. Fedkiw, and S. A. Khan, *J. Electrochem. Soc.*, **149**, A667 (2002).

[63] W. Wieczorek, Z. Florjanczyk, and J. R. Stevens, *Electrochim. Acta*, **40**, 2251 (1995).

[64] H. J. Walls, P. S. Fedkiw, S. A. Khan, and T. Zawodzinski, A., Jr., *J. Electrochem. Soc.*, (submitted, 2002).

[65] S. R. Raghavan, J. Hou, G. L. Baker, and S. A. Khan, *Langmuir*, **16**, 1066 (2000).

[66] S. R. Raghavan, H. J. Walls, and S. A. Khan, *Langmuir*, **16**, 7920 (2000).

[67] S. Skaarup, K. West, P. M. Julian, and D. M. Thomas, *Solid State Ion.*, **40/41**, 1021 (1990).

[68] A. Selvaggi, F. Croce, and B. Scrosati, *J. Power Sources*, **32**, 389 (1990).

[69] B. Kumar, J. D. Schaffer, M. Nookala, and L. G. Scanlon, *J. Power Sources*, **47**, 63 (1994).

[70] J. Cho, G. Kim, H. Lom, and M. Liu, *J. Electrochem. Soc.*, **145**, 1949 (1998).

[71] J. Hou and G. L. Baker, *Chem. Mater.*, **10**, 3311 (1998).

[72] D. R. MacFarlane, P. J. Newman, K. M. Nairn, and M. Forsyth, *Electrochim. Acta*, **43**, 1333 (1998).

Table 4. 1. Effects of fillers on Li^+ conductivity (σ) of ethylene oxide (EO)-based composite electrolytes

Date (year)	Authors	Polymer (M_w, g/mol)	Salt	Filler type, conc., and properties	Temperature (°C)	Salt conc. (mol/kg polymer)	Effect of fillers on s
1982	Weston and Steele [10]	Poly(ethylene oxide) (PEO, 4×10^6)	$LiClO_4$	α-Al_2O_3 (Analar grade, -300 mesh) 10 vol%	25-135	2.8 (Li:O=1:8)	no effect
				20 and 50 vol%			decrease
1988	Skaarup, West, and Zachau-Christiansen [11]	PEO (4×10^6)	$LiCF_3SO_3$ (LiTf)	Li_3N (50 μm) 5 and 8 vol% of PEO	25-120	1.9 (Li:O=1:12)	increase
				16 vol% of PEO	25-100		increase
					100-120		decrease
				32 vol% of PEO	25-50		increase
					50-120		decrease
				64 vol% of PEO	25-120		decrease
1990	Skaarup, West, and Julian[67]	PEO (4×10^6)	LiTf	$1.2Li_2S{\cdot}1.6LiI{\cdot}B_2S_3$ (25-75 μm) 82.5, 91.2, and 95.1 vol%	25-70	2.3 (Li:O=1:10)	N/A $\sigma_{91.2\%}$ is the highest
					25-45 (≠45)		$\sigma_{95.1\%} > \sigma_{82.5\%}$
					45		$\sigma_{95.1\%} = \sigma_{82.5\%}$
					45-70 (≠45)		$\sigma_{95.1\%} < \sigma_{82.5\%}$
1990	Croce et al. [68]	PEO (4×10^6)	$LiClO_4$	β''-Al_2O_3 (< 5 μm, 10 wt%)	60-110	2.8 (Li:O=1:8)	no effect
1991	Capuano, Croce, and Scrosati [8]	PEO (4×10^6)	$LiClO_4$	$LiAlO_2$ (95% γ + 5% α, 4.0 μm) 10 and 20 wt%	25-110	2.8 (Li:O=1:8)	$\sigma_{10\%} > \sigma_{20\%} > \sigma_{30\%}$ increase
				30 wt%	25-60		increase
					60-110		decrease

Table 4.1. Effects of fillers on Li^+ conductivity (σ) of ethylene oxide (EO)-based composite electrolytes (Cont'd)

Date (year)	Authors	Polymer (M_w, g/mol)	Salt	Filler type, conc., and properties	Temperature (°C)	Salt conc. (mol/kg polymer)	Effect of fillers on s
1994	Khan, Baker, and Colson [21]	poly(ethylene glycol) (PEG, 300, 400) monomethyl capped poly(ethylene glycol) (PEGM, 350) Poly(ethylene glycol) dimethyl ether (PEGDM, 400)	$LiClO_4$	Fumed SiO_2 (octyl- surface groups) (10 wt%)	25	1	N/A $\sigma_{PEG\text{-}dm} > \sigma_{PEGM} > \sigma_{PEG(400)} > \sigma_{PEG(300)}$
1994	Kumar et al. [69]	PEO (3×10^5)	$LiBF_4$	$0.4B_2O_3{\cdot}0.4Li_2O{\cdot}$ $0.2\ Li_2SO_4$ (1.5 μm) 7.33 wt%	-2-30	2.8 (Li:O=1:8)	decrease
					30-60		no effect
				13.65 wt%	-2-30		decrease
					30-60		increase
				19.17 wt%	-2-60		increase
1994	Kumar and Scanlon [3]	PEO	$LiBF_4$	Zeolite (0-30%)	27	2.8 (Li:O=1:8)	increase σ_{max} at ~23%
				Li_3N (5, 25, and 40 wt%)	0-100		N/A $\sigma_{40\%} > \sigma_{25\%} > \sigma_{5\%}$
1995	Borghini et al. [9]	PEO (4×10^6)	$LiN(CF_3SO_2)_2$ (LiTFSI)	γ-$LiAlO_2$ (< 1 μm, 10 wt%)	25-50	2.8 (Li:O=1:8)	decrease
				heating cycle	50-90		increase
				cooling cycle	25-90		increase
1996	Wieczorek, Stevens, and Florjanczyk [45]	PEO (5×10^6)	$LiClO_4$	$AlCl_3$ (1.7-24.4 vol%) α-Al_2O_3 (2.6-33.9 vol%, < 5 μm)	25	2.3 (Li:O=1:10)	increase ($AlCl_3$ > α-Al_2O_3 at same loading)

Table 4.1. Effects of fillers on Li^+ conductivity (σ) of ethylene oxide (EO)-based composite electrolytes (Cont'd)

Date (year)	Authors	Polymer (M_w, g/mol)	Salt	Filler type, conc., and properties	Temperature (°C)	Salt conc. (mol/kg polymer)	Effect of fillers on s
1997	Choi, Kim, and Shin [14]	PEO (2×10^6)	$LiClO_4$	10 wt% fillers AlN (10 μm) Al_2O_3 (0.037, 0.05 μm) $BaTiO_3$ (2 μm) BN (1 μm), B_4C (5 μm) $CaSiO_3$ (25 μm) Fe_2O_3 (0.023, 1 μm) MoS_2 (2 μm) $PbTiO_3$ (5 μm) SiC (1 and 13 μm) Si_3N_4 (1 μm) fumed SiO_2 (0.007 and 0.014 μm) TiB_2 (10 μm) TiO_2 (anatase,0.032μm) TiO_2 (rutile, 5 μm) WC (1 μm) ZrO_2 (3 μm)	30, 100	1.4 (Li:O=1:16)	N/A no effect of filler type
1997	Fan and Fedkiw [5]	PEGDM (250)	LiTFSI	fumed SiO_2 (octyl- surface groups) 2.5 and 5 wt%	20-120	1.1 (Li:O=1:20)	no effect
				10 and 20 wt%			decrease
			LiTf	2.5 wt%			no effect
				5, 10, 20 wt%			decrease
			LiTFSI	2.5, 5, 10 wt%			no effect
				20 wt%			decrease
		PEG (300)	LiTf	2.5 and 5 wt%			no effect
				10 and 20 wt%			decrease
		PEGM (350)	LiTf	2.5, 5, 10 wt%			no effect
				20 wt%			decrease

Table 4.1. Effects of fillers on Li^+ conductivity (σ) of ethylene oxide (EO)-based composite electrolytes (Cont'd)

Date (year)	Authors	Polymer (M_w, g/mol)	Salt	Filler type, conc., and properties	Temperature (°C)	Salt conc. (mol/kg polymer)	Effect of fillers on s
1997	Fan and Fedkiw [5]	PEGDM (250)	LiTf	fumed SiO_2 (-OH surface groups) 5 wt%	20-120	1.1 (Li:O=1:20)	no effect
				10 wt%			decrease
1998	Cho et al. [70]	PEO	LiTFSI	$0.4GeS_2{\cdot}0.3Li_2S{\cdot}0.3LiI$ (75, 87, and 93 vol%)	25-80	2.8 (Li:O=1:8)	increase, $\sigma_{87\%} > \sigma_{93\%} > \sigma_{75\%}$
1998	Croce, Appetecchi, and Scrosati [48]	PEO	$LiClO_4$	TiO_2 (13nm, 10 wt%) Al_2O_3 (5.8 nm, 10 wt%)	20-100	2.8 (Li:O=1:8)	increase (annealing electrolytes at $T>T_m$ further increases σ)
1998	Dai et al. [15]	PEO + poly(methylmethacrylate) (PMMA) + ethlylene carbonate (EC) (2.5:0.25:1)	LiI	Al_2O_3 (150 Å, 6%)	50-120	Li:O=1:2.5	N/A $\sigma_{MgO\text{-}CPE} > \sigma_{PEO+EC+Al2O3} > \sigma_{PEO+PMMA+EC+Al2O3}$
		PEO + EC (3:1)		Al_2O_3 (150 Å, 12%)	50-120	Li:O=1:3	
		PEO + PMMA + EC (3:0.25:1)		MgO (150 Å, 6%)	25-120	Li:O=1:3	
1998	Fan et al. [4]	PEGDM (250)	LiTFSI	fumed SiO_2 (EO-, octyl-, -OH, methyl- surface groups) 10, 20 wt%	20-120	1.1 (Li:O=1:20)	decrease (no difference among various surface groups)
1998	Hou and Baker [71]	PEGDM (500)	$LiClO_4$	Cosslinkable fumed SiO_2 (methacrylate modified)	25-100	2.8 (Li:O=1:8) 1.3 (Li:O=1:18) 0.8 (Li:O=1:29) 0.6 (Li:O=1:39) 0.4 (Li:O=1:60)	N/A no change in σ before and after crosslink σ increase with salt content

Table 4.1. Effects of fillers on Li^+ conductivity (σ) of ethylene oxide (EO)-based composite electrolytes (Cont'd)

Date (year)	Authors	Polymer (M_w, g/mol)	Salt	Filler type, conc., and properties	Temperature (°C)	Salt conc. (mol/kg polymer)	Effect of fillers on s
1998	MacFarlane et al. [72]	P(EO:PO=3:1)	LiTf	$Li_{1.3}Al_{0.3}Ti_{0.7}(PO_4)_3$ 2-70 vol%, medium-particle size	25	1	N/A maximum at 46%
				2-40 vol%, fine-particle size			minmum at 6%
1998	Wieczorek et al. [46]	PEO (5×10^6)	$LiClO_4$	$AlBr_3$ (5-50 wt%)	0, 25	2.3 (Li:O=1:10)	increase
				$AlCl_3$ (5-50 wt%)	0, 25		increase
					100		decrease
				α-Al_2O_3 (5-50 wt%, < 5 μm)	0, 25		increase
					100		decrease
		oxymethylene-linked PEO (OMPEO) (4.1×10^4)	$LiClO_4$	$AlBr_3$ 5-50 wt% (< 50%)	0, 25	1.1 (Li:O=1:10)	increase
				50 wt%			decrease
				$AlCl_3$ 5-25 wt%	0, 25		increase
				25-50 wt%			decrease
				5, 10, 15, 25 wt%	100		decrease
				30, 40 wt%	100		increase
				20, 50 wt%	100		no effect
				α-Al_2O_3 (< 5 μm) 5-50 wt%	0		decrease
				20, 50 wt%	25		decrease
				5-50 wt% (≠20, 50%)	25		no effect
				5-50 wt%	100		decrease
1998	Wieczorek et al. [40]	PEGM (350)	$LiClO_4$	α-Al_2O_3 (10 wt%, acidic surface groups)	20-90	0.01-0.1	no effect
						0.1-0.5	decrease
						0.001, 0.5-3	increase
1999	Best et al. [53]	P(EO:PO=3:1) (5000) uncured, cured	$LiClO_4$	fumed TiO_2 (10 wt%)	20-120	1.0, 1.25	No effect
		uncured				1.5	decrease
		cured				1.5	increase
		uncured, cured	LiTFSI	fumed TiO_2 (10 wt%)	20-120	1.5, 2	no effect

Table 4.1. Effects of fillers on Li^+ conductivity (σ) of ethylene oxide (EO)-based composite electrolytes (Cont'd)

Date (year)	Authors	Polymer (M_w, g/mol)	Salt	Filler type, conc., and properties	Temperature (°C)	Salt conc. (mol/kg polymer)	Effect of fillers on s
2000	Marcinek et al. [42]	PEGM (350)	$LiClO_4$	α-Al_2O_3 (10 wt%, < 5 μm, neutral surface groups)	20-90	0.001	increase
						0.01-0.25	decrease
						0.25-5	increase
2000	Marcinek et al. [41]	PEGM (350)	$LiClO_4$	Al_2O_3 (10 wt%, < 5 μm, neutral, basic, and acidic surface groups)	25	10^{-5}, 0.5-5	increase
						10^{-4}-0.5	decrease or no effect
2000	Scrosati, Croce, and Persi [18]	PEO (4×10^6)	$LiClO_4$	TiO_2 (13 nm, 10 wt%) and SiO_2 (7 nm, 10 wt%)	20-100	2.8 (Li : O =1:8)	increase
		PEO (6×10^5)	$LiClO_4$			0.8 (Li : O =1:30)	increase
2001	Best et al. [54]	P(EO:PO=3:1) (5000)	$LiClO_4$	fumed TiO_2 (21 nm, 10 wt%)	20-120	1	No effect
						1.25, 1.5	increase
				fumed Al_2O_3 (13 nm, 10 wt%)	20-120	1	no effect
						1.25	increase
						1.5	decrease
		P(EO:PO=3:1) (5000)	LiTf	fumed TiO_2 (21 nm, 10 wt%)	20-120	1	no effect
						1.5, 1.75	increase
				fumed Al_2O_3 (13 nm, 10 wt%)	20-120	1	no effect
						1.5, 1.75	increase
		PEO (6×10^5)	$LiClO_4$	fumed TiO_2 (21 nm, 10 wt%)	20-120	2.8 (Li: O =1:8)	increase
2001	Borkowska et al. [43]	PEGM (350)	$LiClO_4$	$AlBr_3$ 1, 5, and 10 wt%	20-90	0.1	decrease
				1, 5 wt%		1	increase
				10 wt%		1	decrease
2001	Chung et al. [49]	PEO	$LiClO_4$	TiO_2 (11 nm, 10 wt%) Al_2O_3 (5.8 nm, 10 wt%)	20-100	2.8 (Li : O =1:8)	increase
2001	Croce et al. [47]	PEO	LiTf	Al_2O_3 (10 wt%, 5.8 nm) acidic surface groups	20-100	1.1 (Li:O=1:20)	increase
				basic surface groups	20-60		no effect
					60-100		decrease
				neutral surface groups	20-100		increase

Table 4.1. Effects of fillers on Li^+ conductivity (σ) of ethylene oxide (EO)-based composite electrolytes (Cont'd)

Date (year)	**Authors**	**Polymer (M_w, g/mol)**	**Salt**	**Filler type, conc., and properties**	**Temperature (°C)**	**Salt conc. (mol/kg polymer)**	**Effect of fillers on** s
2001	Swierczynski, Zalewska, and Wieczorek [44]	PEGDM (500)	$LiClO_4$	Fumed SiO_2 (7 nm, 10 wt%)	25	10^{-5}-10^{-4}	decrease
						10^{-3}-10^{-2}, 1	increase
						10^{-2}-5 (≠1)	no effect
2002	Jayathilaka et al. [50]	PEO (5×10^6)	LiTFSI	Al_2O_3 (basic, neutral, weakly acidic, acidic, 5.8 nm, 155 m^2/g, 10 wt%)	0-110	Li : O =1:9	increase

Table 4. 2. Comparison of results from three research groups regarding the degree of conductivity enhancement due to different surface groups of nanoscale Al_2O_3 fillers

Material	**Marcinek et al.[41] (2000)**	**Croce et al. [47] (2001)**	**Jayathilaka et al. [50] (2002)**
Polymer	PEGM* (M_w = 350)	PEO (M_w not reported)	PEO ($M_w = 5\times10^6$)
Salt	$LiClO_4$	$LiCF_3SO_3$	$LiN(CF_3SO_2)_2$
Li : O =1:20 (~ 1 mol/kg for PEGM + $LiClO_4$)	Basic > neutral > acidic >> filler-free	Neutral > acidic > basic > filler-free (> 60°C) Acidic > neutral > basic > filler-free (< 60°C)	N/A
Li : O =1:9 (~ 2 mol/kg for PEGM + $LiClO_4$)	Neutral > acidic >> filler-free (no basic data available)	N/A	Acidic > basic > neutral > weakly acidic > filler-free

* PEGM: Monomethyl capped poly(ethylene glycol)

Table 4. 3. Glass transition temperature (T_g) and melting point (T_m) determined by DSC measurements

M_w	Filler	T_g (°C)	T_m (°C)
250	None	-98	-42
	10 wt%A200	-96	-45
	10 wt% Al_2O_3	-96	-45
	10 wt% A380	-94	-45
500	None	-84	2
	10 wt% A200	-74	2
	10 wt% Al_2O_3	-78	3
1000	None	-74	26
	10 wt% A200	-71	27
	10 wt% Al_2O_3	-68	26
2000	None	-58	46
	10 wt% A200	-54	41
	10 wt% Al_2O_3	-57	44

Note: PEG-dm: poly(ethylene glycol) dimethyl ether
LiTFSI: lithium bis(trifluromethylsulfonyl)imide, $LiN(CF_3SO_2)_2$
A200: fumed silica with native surface hydroxyl groups with specific surface area of 200 m^2/g
A380: fumed silica with native surface hydroxyl groups with specific surface area of 380 m^2/g

Table 4. 4. Wavenumber of polymer-Li^+ interaction characteristic peaks (C-O-C stretching, CH_2 rocking, and CH_2 wagging mode) from FTIR-ATR measurements

M_w	**Filler**	**n(COC) (cm^{-1})**	**r(CH_2) (cm^{-1})**	**w(CH_2) (cm^{-1})**
250	None	1097	N/A	N/A
	10 wt%A200	1098	N/A	N/A
	10 wt% Al_2O_3	1099	N/A	N/A
	10 wt% A380	1098	N/A	N/A
500	None	1097	N/A	N/A
	10 wt% A200	1094	N/A	N/A
	10 wt% Al_2O_3	1096	N/A	N/A
1000	None	1108	963	N/A
	10 wt% A200	1088	963	N/A
	10 wt% Al_2O_3	1107	N/A	N/A
2000	None	1104	962	1343
	10 wt% A200	1092	962	1343
	10 wt% Al_2O_3	1093	N/A	N/A

Note: PEG-dm: poly(ethylene glycol) dimethyl ether
LiTFSI: lithium bis(trifluromethylsulfonyl)imide, $LiN(CF_3SO_2)_2$
A200: fumed silica with native surface hydroxyl groups with specific surface area of 200 m^2/g
A380: fumed silica with native surface hydroxyl groups with specific surface area of 380 m^2/g
ν: stretching mode, ρ: rocking mode, ω: wagging mode

Table 4. 5. Wavenumber of characteristic peaks for ion-ion interactions of $TFSI^-$ from FTIR-ATR measurement

M_w	**Filler**	**n(C-S) + n(S-N) (cm^{-1})**	**n(C-S) + n(C-F) (cm^{-1})**	**n(S-N) (cm^{-1})**	**$n(SO_2)_a$ (cm^{-1})**	**$n(CF_3)_s$ (cm^{-1})**	**$n(SNS)_a$ (cm^{-1})**
250	None	787	761	739	1353	1190	1059
	10 wt%A200	787	761	739	1353	1189	1058
	10 wt% Al_2O_3	786	760	739	1353	1189	1059
	10 wt% A380	787	761	740	1353	1189	1058
500	None	787	760	739	1352	1189	1058
	10 wt% A200	787	760	739	1353	1189	1058
	10 wt% Al_2O_3	787	760	739	1352	1189	1058
1000	None	787	760	739	1352	1190	1059
	10 wt% A200	787	761	739	1352	1185	1056
	10 wt% Al_2O_3	786	760	739	1353	1189	1059
2000	None	788	761	740	1353	1189	1058
	10 wt% A200	787	761	739	1352	1187	1058
	10 wt% Al_2O_3	787	761	739	1352	1186	1056

Note: PEG-dm: poly(ethylene glycol) dimethyl ether
LiTFSI: lithium bis(trifluromethylsulfonyl)imide, $LiN(CF_3SO_2)_2$
A200: fumed silica with native surface hydroxyl groups with specific surface area of 200 m^2/g
A380: fumed silica with native surface hydroxyl groups with specific surface area of 380 m^2/g
ν: stretching mode, a: antisymmetric, s: symmetric

Table 4. 6. Effective Lewis acid group (-OH) concentration of composite electrolytes containing 10 wt% fillers in PEG-dm + LiTFSI (Li:O=1:20) systems

Filler	Concentration (mol/kg PEG-dm)
OX 50	2.4×10^{-2}
A200	1.1×10^{-1}
A380	2.1×10^{-1}
R805	5.5×10^{-2}
P25	2.8×10^{-2} (50% of –OH groups)
T805	1.1×10^{-2} (50% of –OH groups)

Note: OX 50: fumed silica with surface hydroxyl groups with surface area of 50 m^2/g
A200: fumed silica with surface hydroxyl groups with surface area of 200 m^2/g
A380: fumed silica with surface hydroxyl groups with surface area of 380 m^2/g
R805: fumed silica with octyl- surface groups
P25: fumed titania with surface hydroxyl groups
T805: fumed titania with octyl- surface groups

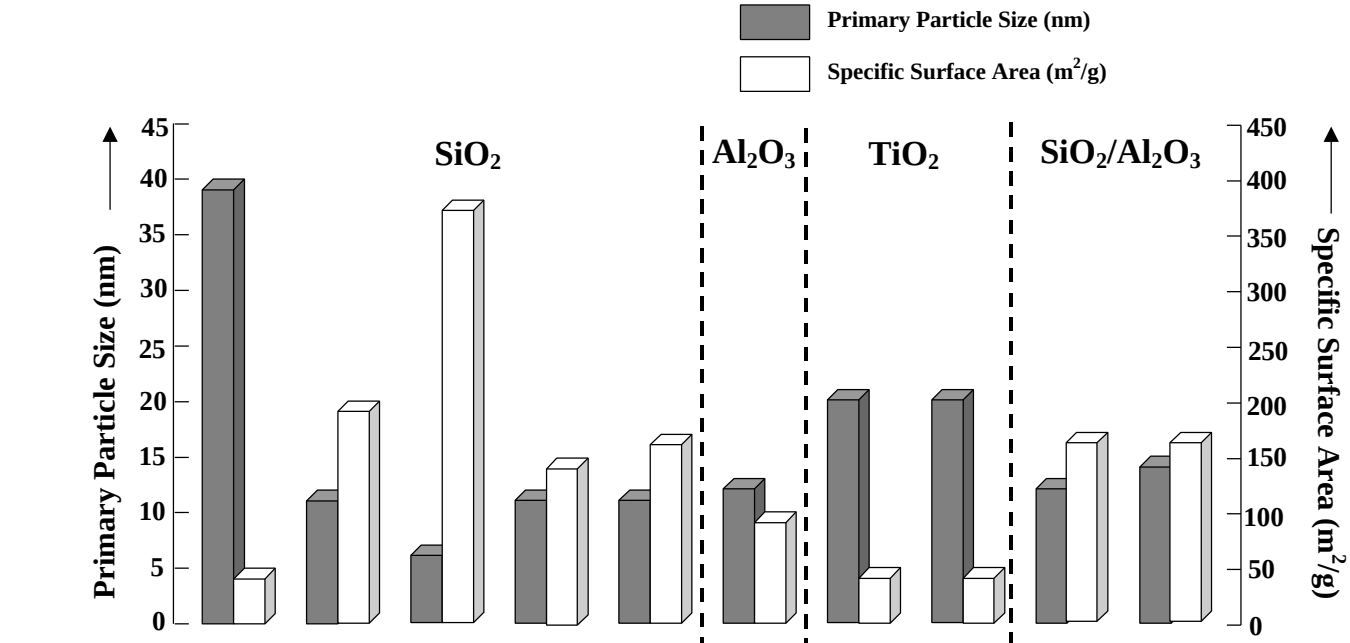

Filler	OX 50	A200	A380	R805	R816	Al_2O_3 C	P25	T805	COK84*	MOX170**
Dominant Surface Group	-OH	-OH	-OH	$-C_8H_{17}$	$-C_{16}H_{33}$	-OH	-OH	$-C_8H_{17}$	-OH	-OH
-OH density per nm^2	2.2+	2.5+	2.5+	1.66+	N/A	N/A	5.0#	2.0#	N/A	N/A

*COK 84: 84% SiO_2 + 16% Al_2O_3 **MOX 170: 1% Al_2O_3 doped SiO_2

+Degussa Technical Bulletin Pigment No. 11 (1998)

#Dr. Tim Macarthi from Degussa Corp. (private communication)

Figure 4. 1. Physical properties of fumed metal oxide fillers. All materials are designated with the manufacturer's (Degussa) nomenclature.

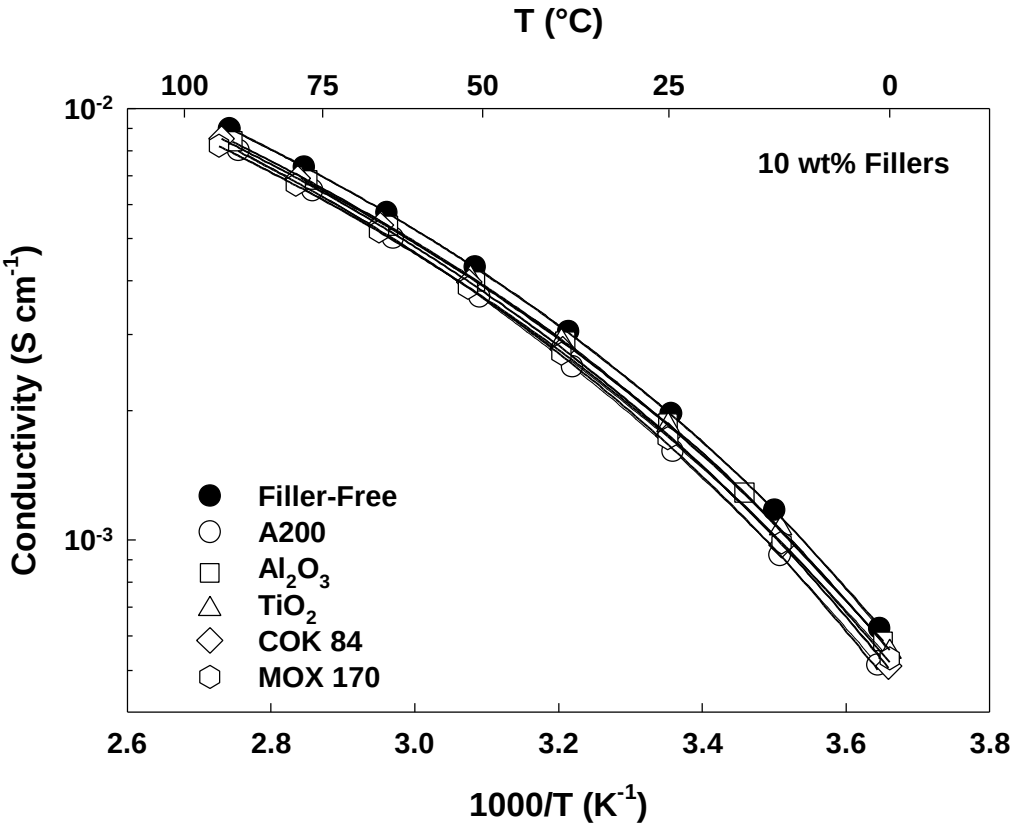

Figure 4. 2. Ionic conductivity of filler-free electrolyte [PEGdm (250) + LiTFSI (Li:O=1:20)] and composite electrolytes with 10 wt% fillers, all with hydroxyl surface groups: A200 (SiO_2), Al_2O_3, TiO_2, COK 84 (84% SiO_2 and 16% Al_2O_3 mixture), and MOX 170 (SiO_2 doped with 1% Al_2O_3).

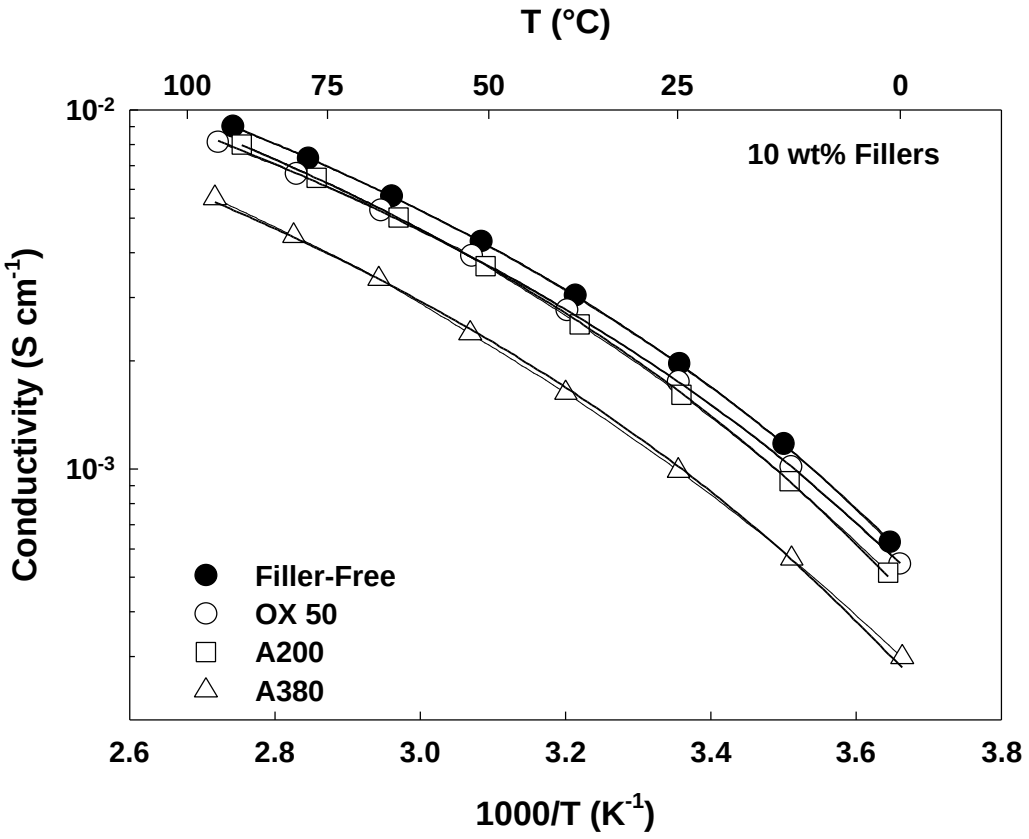

Figure 4. 3. Ionic conductivity of filler-free electrolyte [PEGdm(250) + LiTFSI (Li:O=1:20)] and electrolytes containing 10 wt% fumed silica with hydroxyl surface groups but at varying surface areas: 50 m^2/g (OX 50), 200 m^2/g (A200), and 380 m^2/g (A380).

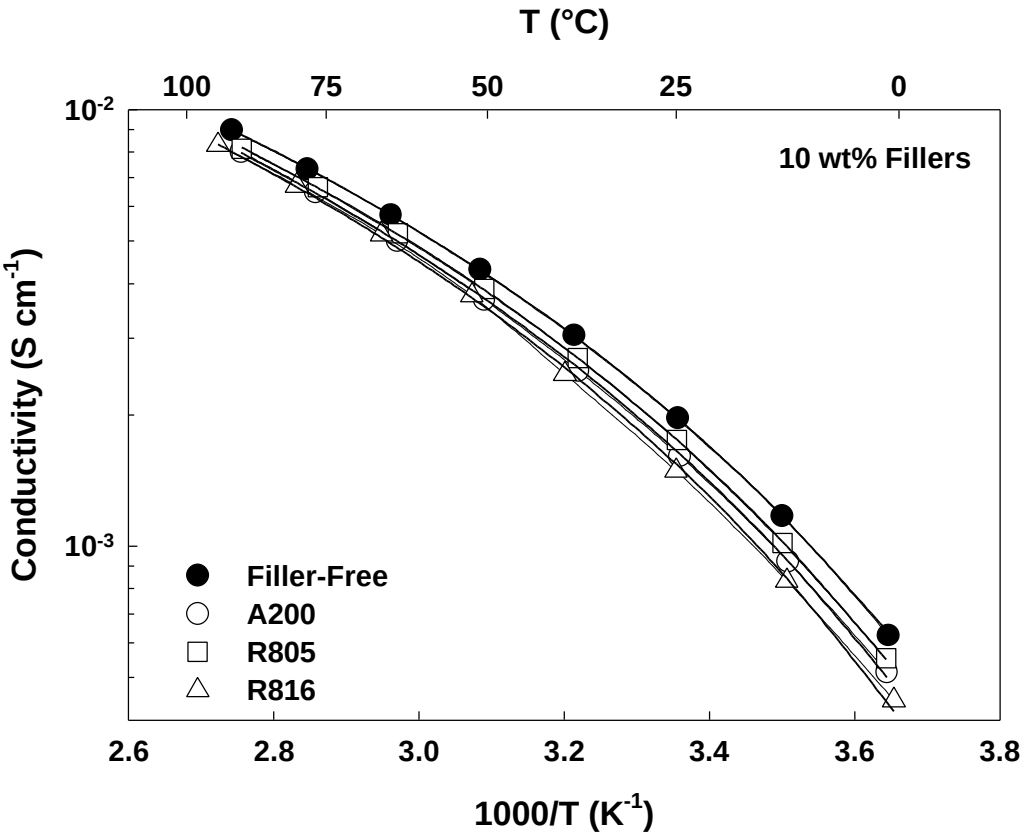

Figure 4. 4. Ionic conductivity of filler-free electrolyte [PEGdm(250) + LiTFSI (Li:O=1:20)] and electrolytes containing 10 wt% fumed silica with different surface groups: –OH (A200), $–C_8H_{17}$ (R805), and $–C_{16}H_{33}$ (R816).

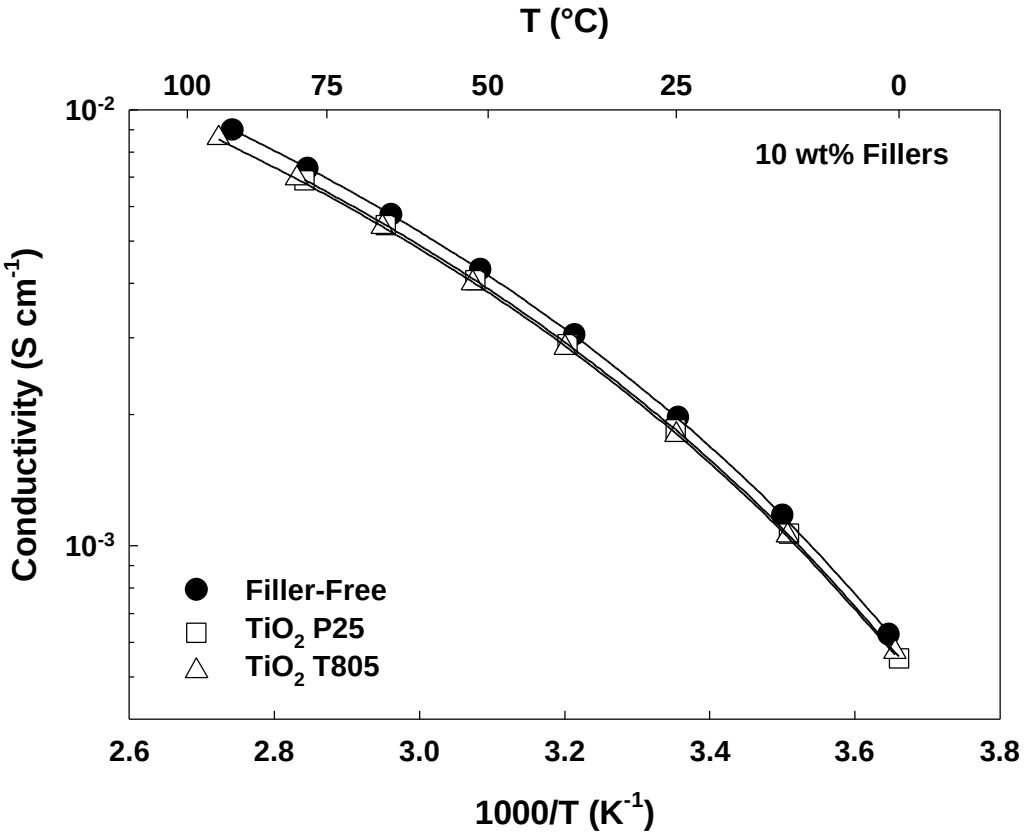

Figure 4. 5. Ionic conductivity of filler-free electrolyte [PEGdm(250) + LiTFSI (Li:O=1:20)] and electrolytes containing 10 wt% fumed titania with different surface groups: –OH (P25) and $–C_8H_{17}$ (T805).

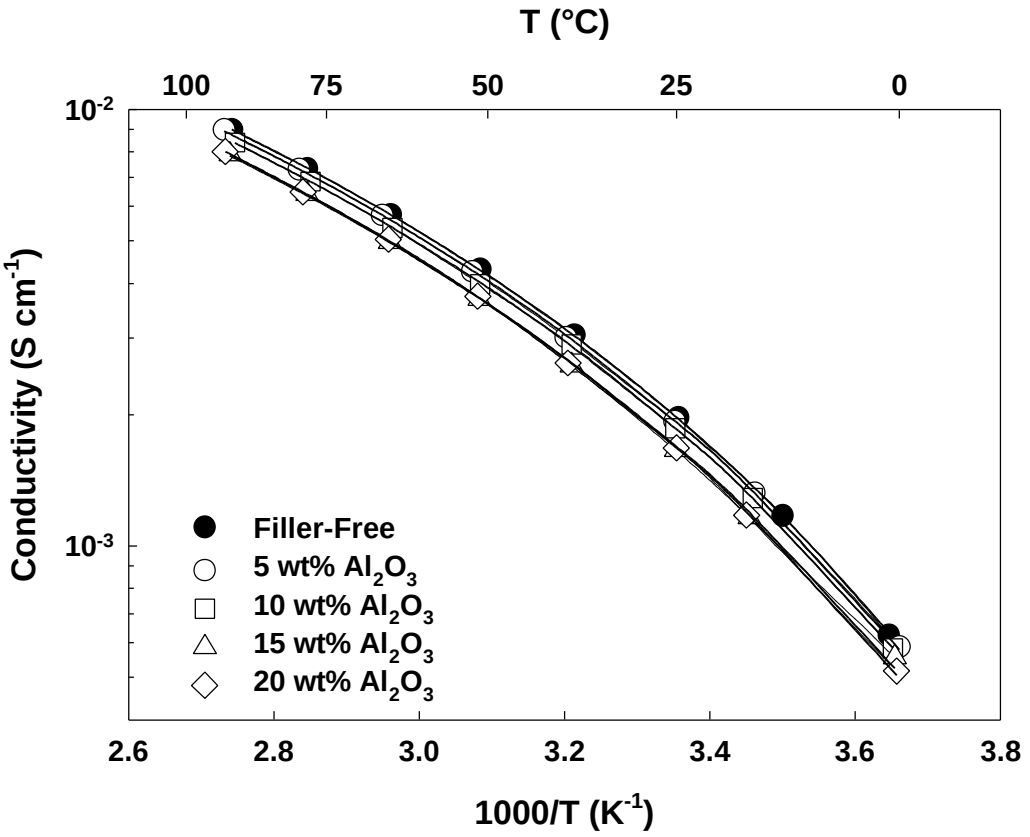

Figure 4. 6. Ionic conductivity of filler-free electrolyte [PEGdm(250) + LiTFSI (Li:O=1:20)] and composite electrolytes containing Al_2O_3 C at different weight fraction.

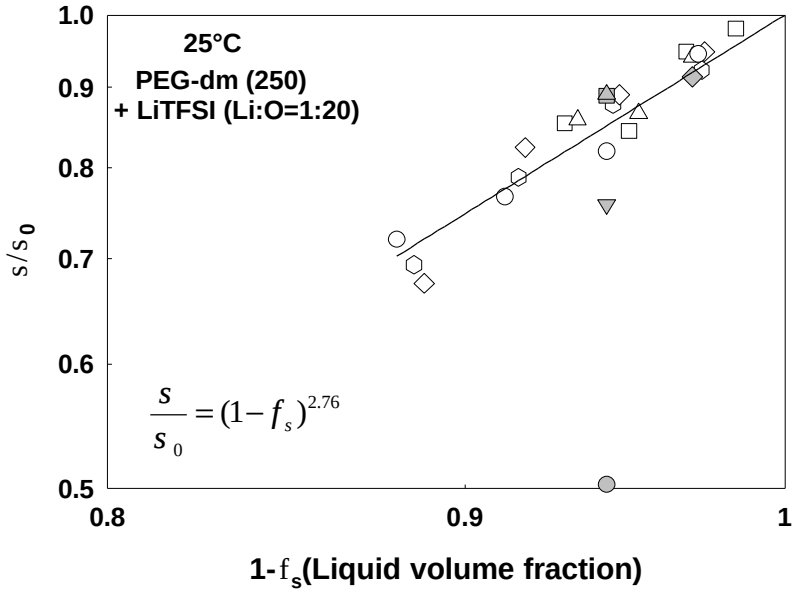

Filler	Type	Surface group	Surface Area (m^2/g)
OX 50	SiO_2	-OH	50
A200			200
A380			380
R805		$-C_8H_{17}$	
R816		$-C_{16}H_{33}$	
Al_2O_3 C	Al_2O_3	-OH	
P25	TiO_2	-OH	
T805		$-C_8H_{17}$	
COK 84	SiO_2/Al_2O_3	-OH	
MOX 170	SiO_2/Al_2O_3	-OH	

Figure 4. 7. Normalized ambient-temperature (25°C) conductivity of composite electrolytes as a function of liquid volume fraction with various fillers in PEG-dm (250) system.

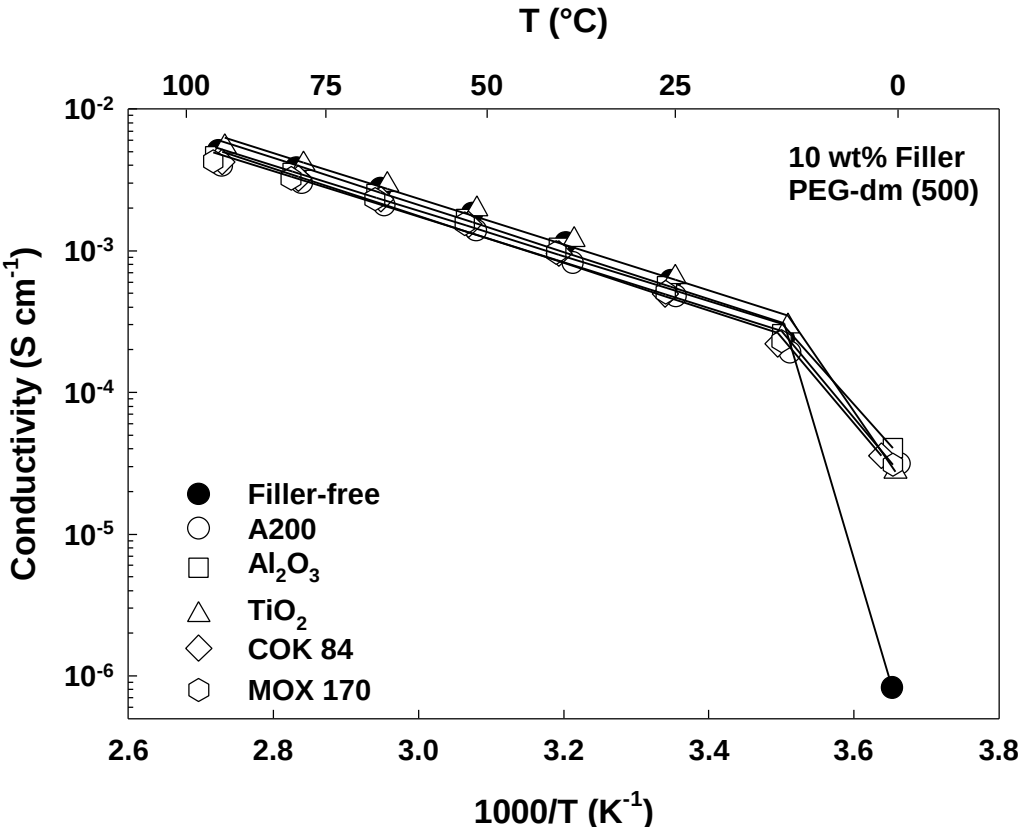

Figure 4. 8. Ionic conductivity of filler-free electrolyte [PEG-dm (500) + LiTFSI (Li:O=1:20)] and electrolyte with 10 wt% fillers, all with hydroxyl surface groups: A200 (SiO_2), Al_2O_3, TiO_2, COK 84 (84% SiO_2 and 16% Al_2O_3 mixture), and MOX 170 (SiO_2 doped with 1% Al_2O_3).

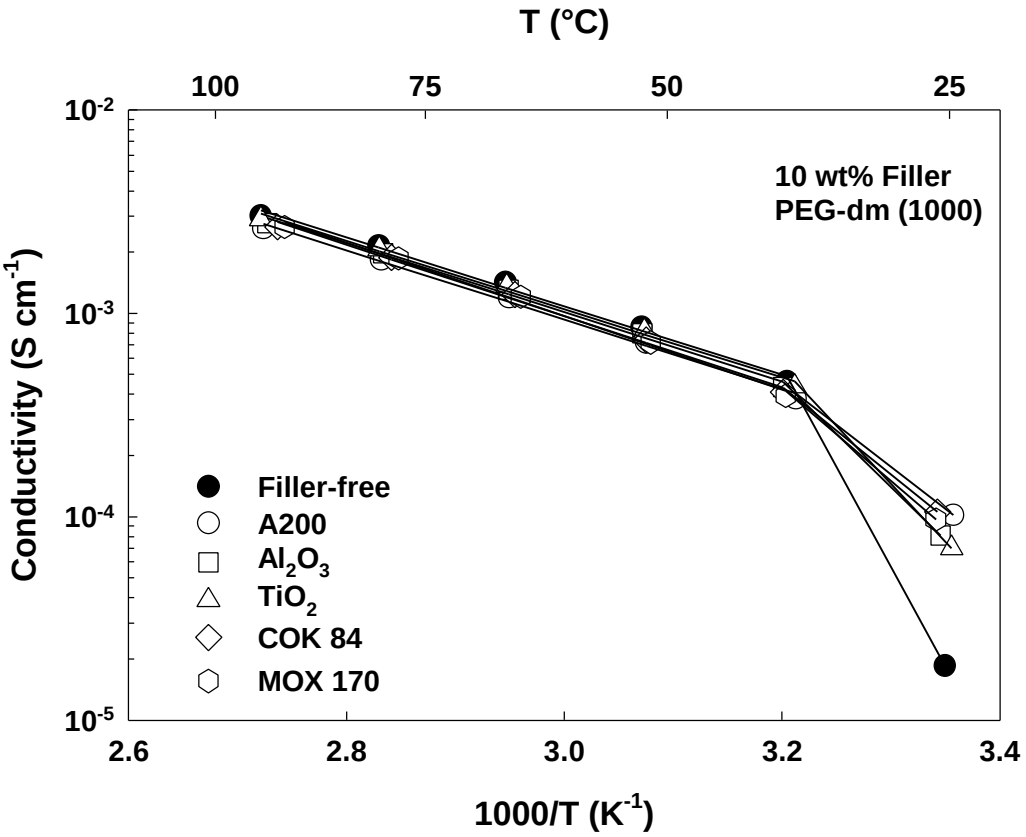

Figure 4. 9. Ionic conductivity of filler-free electrolyte [PEG-dm (1000) + LiTFSI (Li:O=1:20)] and electrolyte with 10 wt% fillers, all with hydroxyl surface groups: A200 (SiO_2), Al_2O_3, TiO_2, COK 84 (84% SiO_2 and 16% Al_2O_3 mixture), and MOX 170 (SiO_2 doped with 1% Al_2O_3).

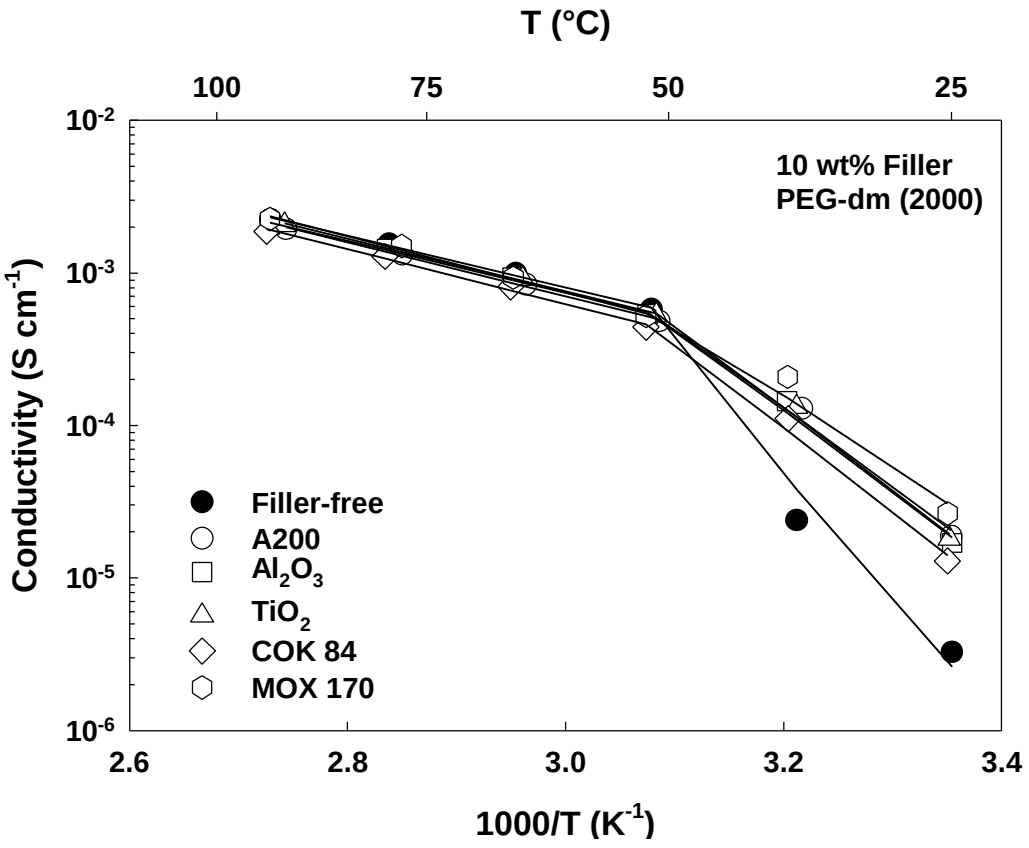

Figure 4. 10. Ionic conductivity of filler-free electrolyte [PEG-dm (2000) + LiTFSI (Li:O=1:20)] and electrolyte with 10 wt% fillers, all with hydroxyl surface groups: A200 (SiO_2), Al_2O_3, TiO_2, COK 84 (84% SiO_2 and 16% Al_2O_3 mixture), and MOX 170 (SiO_2 doped with 1% Al_2O_3).

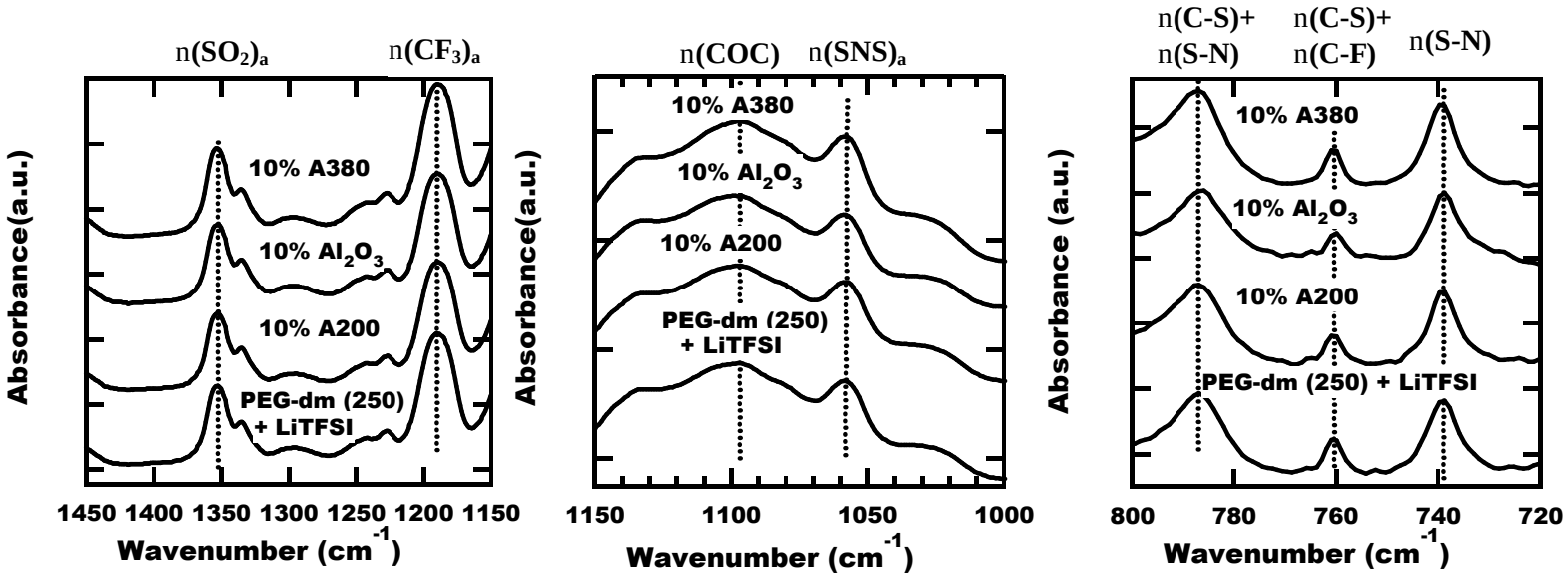

Figure 4. 11. FTIR-ATR spectra for filler-free liquid electrolyte and electrolyte containing 10 wt% A200, A380, and Al_2O_3 fillers based on PEG-dm (250) + LiTFSI (Li:O=1:20).

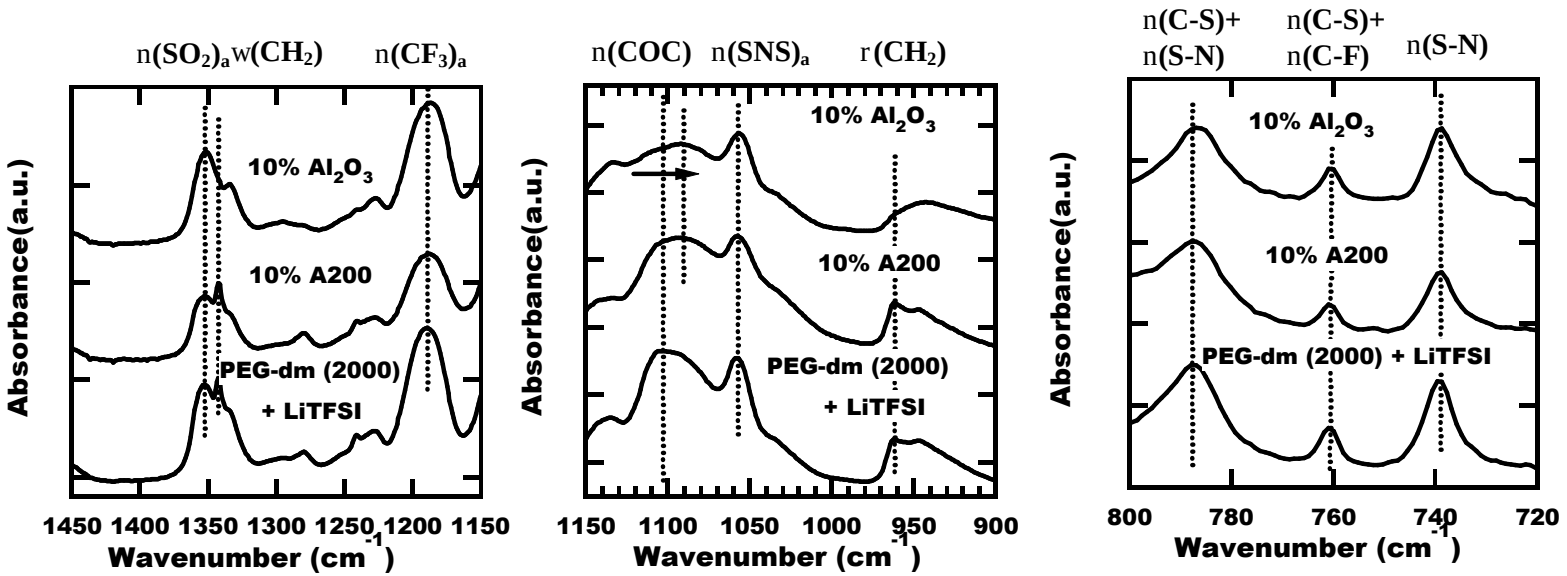

Figure 4. 12. FTIR-ATR spectra for filler-free solid electrolyte and electrolyte containing 10 wt% A200 and Al_2O_3 fillers based on PEG-dm (2000) + LiTFSI (Li:O=1:20).

Chapter 5: Interfacial Stability Between Lithium and Fumed Silica-Based Composite Electrolytes

Jian Zhou, Peter S. Fedkiw, and Saad A. Khan

Department of Chemical Engineering

North Carolina State University

Raleigh, NC 27695-7905

Published in

Journal of the Electrochemical Society

***149**, No. 9, p A1121-A1126 (2002)*

Abstract

Composite electrolytes consisting of methyl-capped poly(ethylene glycol) oligomer ($M_w \approx 250$), lithium bis(trifluoromethylsulfonyl)imide (Li:O=1:20), and fumed silica were investigated. In particular, the effects of fumed silica-surface chemistry and weight percentage in the composite on cycling behavior of Li/electrolyte/Li, Li(Ni)/electrolyte/Li, and Li/electrolyte/metal oxide cells were studied. Four types of fumed silicas with various surface groups were employed: A200 (native hydroxyl groups), R805 (octyl-modified), R974 (methyl-modified), and FS-EG3 (ethylene oxide-modified). The presence of fumed silica enhances lithium cycleability by reducing the interfacial resistance and cell-capacity fading, regardless of surface chemistry. However, the extent of the enhancing effect of fumed silica strongly depends on its surface chemistry, with the largest effect seen with A200 and the least effect seen with FS-EG3. Increasing fumed silica weight fraction intensifies the stabilizing effect.

5.1 Introduction

Although lithium metal is an attractive anode material for rechargeable batteries because of its high-specific energy, the commercialization of rechargeable lithium batteries is impeded by its high reactivity with electrolyte components. One way to overcome this limitation without sacrificing energy density is to develop suitable electrolytes that are kinetically stable to lithium. In addition to good interfacial stability, high conductivity (> 10^{-3} S/cm at room temperature) and mechanical strength are also required. Among currently examined electrolytes, composite electrolytes show promising electrochemical (e.g., conductivity, interfacial stability, and ionic transport properties) and mechanical properties (e.g., viscous and elastic moduli, yield stress) for lithium battery applications [1-6].

Most composite electrolytes reported in the literature are formed by dispersing ceramic fillers (e.g., Al_2O_3, SiO_2, TiO_2) into high-molecular weight (M_w) poly(ethylene oxide) (PEO) polymers doped with lithium salts LiX [1-4,7-16]. Addition of ion-conducting (e.g., γ-$LiAlO_2$ [1,3,4], Li_3N [4,9]) and even inert ceramic fillers (e.g., SiO_2 [5], TiO_2 [16], MgO [17]) enhances the conductivity of a high M_w PEO electrolyte, with the latter attributed to an increase in volume fraction of the conductive amorphous phase due to the presence of a homogeneous dispersion of fine particles. Experimental evidence from various groups consistently shows that the interface between lithium and a composite electrolyte is more stable and efficient in cycling than the filler-free electrolyte [1,3,4,7]. The enhanced interfacial stability is suggested to be affected by the filler particles scavenging impurities such as water and oxygen [2], which can react with

lithium and thus accelerate its corrosion. However, the ionic conductivity of this type of composite electrolyte at ambient temperature is 10^{-4} to 10^{-5} S/cm, which is below the acceptable range for some applications [3,16].

In recent years, our group has developed a new type of composite electrolyte by dispersing fumed silica (FS) into low- to moderate M_w PEO [5,6,18-20]. Unlike high M_w based PEO composites, the solid-like structure is formed by the filler (fumed silica) instead of PEO chains. Earlier research has demonstrated that composites consisting of fumed silica + low M_w PEO + lithium salts are promising materials for rechargeable lithium batteries in terms of their high conductivity (>10^{-3} S/cm at room-temperature) and mechanical strength (elastic modulus G'>10^5 Pa) [5,6,19,20]. A significant improvement of lithium interfacial stability with incorporation of the fumed silica is also observed at open circuit [5].

Fumed silica is an amorphous, nonporous form of silicon dioxide (SiO_2) prepared by flame hydrolysis of silicon tetrachloride [21]. The predominant particle structures of fumed silica are aggregates (ca. 0.1-μm long), which consist of partially fused primary particles (ca. 12-nm diameter) and cannot be disrupted by shear [22]. This aggregated structure is responsible for the unique properties of fumed silica. The surface chemistry of fumed silica also plays a significant role and determines many macroscopic properties in applications.

In the present communication, we report our investigation of the interfacial stability between lithium and fumed silica-based composites by cycling of Li/electrolyte/Li, Li(Ni)/electrolyte/Li, and Li/electrolyte/metal oxide cells. The effects

of current density, surface chemistry, and weight percentage of fumed silica are demonstrated.

Four types of fumed silicas with various surface groups are used in this study: A200 (native hydroxyl groups), R805 (octyl-modified), R974 (methyl-modified), and FS-EG3 (ethylene oxide-modified), with the first three being commercial products from Degussa and designated with the manufacturer's nomenclature and the latter synthesized at Michigan State University (MSU). Details of surface chemistries of these fumed silicas are provided in Table 5.1, with silanol density values determined by titration with lithium aluminum hydride ($LiAlH_4$) [21,23]. The surface of unmodified fumed silica (A200) contains silanols (Si-OH) to the extent of about 2.5 [SiOH] groups/nm^2, or equivalently about 0.84 mmol/g [21,22]. These silanols render the native fumed silica surface hydrophilic. The silanols can be replaced by reaction with various chlorosilanes, alkoxysilanes, or silazanes [24] to generate hydrophobic fumed silicas. Each of the remaining fumed silicas was synthesized using A200 as the starting material. The octyl-modified R805 is obtained by reacting A200 with octyltrimethoxysilane (OTMS), while R974 is generated by reacting A200 with dimethyldichlorosilane (DMDCS). The ethylene oxide-modified FS-EG3 is prepared by reacting A200 with chlorodimethyl(4,7,10,13-tetraoxatetradecyl)silane. The synthetic procedure to prepare FS-EG3 is given by Hou [23]. One significant difference between commercial (A200, R805, and R974) and in-house synthesized fumed silica (FS-EG3) is that the latter has considerably larger agglomerates, as determined by visual observation.

5.2 Experimental

5.2.1 Preparation of Composites

The composite electrolytes consist of three materials: lithium bis(trifluromethylsulfonyl)imide [$LiN(CF_3SO_2)_2$] (LiTFSI, 3M), fumed silica (Degussa, or surface-modified form synthesized at MSU [6,23]), and poly(ethylene glycol)dimetheyl ether (PEG-dm, M_w 250, Aldrich). LiTFSI was dried at 110°C under vacuum for 24 hours before use. PEG-dm was dried over 4Å molecular sieves for at least one week. Water content of both materials was controlled under 20 ppm, as determined by Karl-Fisher titration. Fumed silicas were dried at 120°C under vacuum for 3-4 days to achieve a water content of 150-200 ppm before being transferred to an Argon-filled glove box.

Composite electrolytes were prepared in an argon-filled glove box. First, a baseline electrolyte was made by dissolving LiTFSI in PEG-dm oligomer in a fixed ratio of Li:O (1:20) (1M LiTFSI solution) to maintain the highest conductivity [6]. A certain weight of fumed silica was then added to the baseline electrolyte and dispersed into the electrolyte by use of a high-shear mixer (Tissue Tearor^{TM}, Model 398, BioSpec Products, Inc.) to get the desired concentration [19]. Water content of the baseline electrolyte and the composites was under 20 and 50 ppm, respectively. The baseline electrolyte is a liquid while composite electrolytes are solid-like gels with viscosities and transport properties reported elsewhere [25].

5.2.2 Preparation of Cathodes

All components of the metal-oxide cathodes, $LiCoO_2$ (OM Group, Inc., OMG), $LiMn_2O_4$ (Merck), or V_6O_{13} (Kerr-McGee), poly(vinylidene fluoride) (PVDF, Kynar® Flex 2800-00, Elf Atochem North America), graphite Timrex SFG15 (Timcal), and 1-methyl-2-pyrrolidinone (NMP, Aldrich) were used as received. The typical composition for a 4-V cathode ($LiCoO_2$ or $LiMn_2O_4$) is approximately 91 wt% metal oxide, 6 wt% graphite, and 3 wt% PVDF binder [26]. A 3-V cathode (V_6O_{13}) normally consists of 75 wt% metal oxide, 20 wt% graphite, and 5 wt% PVDF binder. Aluminum foil (0.024-mm thick, Fisher Scientific) and 0.127-mm thick sheet of carbon fiber (Techimat® 6100-035, Lydall Technical Papers) were used as the current collector for 4-V cathodes and a 3-V cathode, respectively. Usually, the mixture of metal oxide and SFG15 graphite was dispersed into a solution of PVDF using NMP as solvent. The resulting slurry was coated onto the current collector by a doctor blade, and the final thickness of wet cathode films was approximately 0.20 mm for $LiCoO_2$ or $LiMn_2O_4$ and 0.30 mm for V_6O_{13}. The film was dried at 80°C overnight and was cut into 12.7-mm diameter disks which were hot-compacted by a hydraulic press at 150°C and 770 MPa. After compaction, cathode disks were dried at 150°C under vacuum for 24 h.

5.2.3 Preparation of Coin Cells

Coin cells in which an electrolyte/separator is sandwiched between a thin sheet of lithium metal and another electrode (lithium foil, nickel foil, or metal-oxide composite cathode) are used in our cycling measurements (Figure 5.1). In these cells, the Celgard®

2400 separator (25-μm thick) is either wetted by the baseline electrolyte or sandwiched between two layers of composite electrolyte. A stainless steel spacer and spring are used to maintain good contact of electrolyte, electrode, and current collector.

5.2.4 Methods and Measurements

An Arbin battery cycler (Model BT2042) controlled by Arbin ABTS software is employed to carry out constant-current cell cycling. In Li/electrolyte/Li cells, current densities of 0.2 and 1.0 mA/cm^2 with fixed charge density of 120 mC/cm^2 were applied. Cell cycling was terminated upon reaching the fixed maximum cycle number of 584 or by reaching the voltage safety limit of ±10 V. In full-cell cycling, cells were cycled at a constant current density of 0.08 mA/cm^2 between 2.5 V to 4.2 V for $LiCoO_2$ cathode, 3.0 V to 4.2 V for $LiMn_2O_4$ cathode, and 1.8 V to 3.0 V for V_6O_{13} cathode. The current density corresponds approximately to a C/40 rate for $LiCoO_2$ and $LiMn_2O_4$ cells and C/75 rate for V_6O_{13} cells. In cycling the Li(Ni)/electrolyte/Li cells, a known charge was first passed through the cell at 0.2 mA/cm^2 to prepare the lithium electrode (Q_D=2.4 C/cm^2, nominal Li thickness of 3.0 μm). Then, a fraction of this charge (cycling charge, Q_c= 0.24 C/cm^2, Depth of Discharge (DOD)=10%)) was alternately cycled across the cell for 20 lithium deposition-dissolution cycles, and the lithium stripping overvoltage was monitored upon cycling. Finally, the remaining Li on Ni surface was anodically removed during the last dissolution half-cycle and the amount of charge passed, Q_f, was monitored. The cut-off voltage for the dissolution half-cycle was set at 1.5 V vs. Li

metal. The mean value of the lithium electrode cycling efficiency, η, was calculated by [27]:

$$h = \frac{Q_c - \left(hQ_D - Q_f\right)/n}{Q_c} \times 100\% \qquad (5.1)$$

where $n = 20$ or $n =$ actual number of cycles in which 0.24 C/cm^2 Li is stripped from Ni . The lithium surface before and after Li/electrolyte/Li cycling was also studied via electrochemical impedance spectroscopy (EIS) using a Zahner impedance analyzer IM6e. Open-circuit impedance data were collected in a range of 100 kHz to 100 mHz with an ac amplitude of 10 mV. The interfacial resistance (R_{int}) between the lithium metal and the electrolyte was determined according to the method of Fauteux [28].

5.3 Results and Discussion

5.3.1 Li/Electrolyte/Li cycling

Figure 5.2 shows voltage waveforms in the absence of fumed silica (left) and with a composite electrolyte containing 10% R805 (right). The voltage of the cell with the composite electrolyte is relatively stable from cycle-to-cycle and over each half-cycle. However, the voltage of the cell without fumed silica increases dramatically after 150 cycles and also changes considerably during the half-cycle. The cells with composite electrolytes consisting of other fumed silicas (R974, A200, and FS-EG3) show similar qualitative behavior. Figure 5.3 compares the cycle-number dependence of the average voltage over a half-cycle of the baseline electrolyte to that of composite electrolytes with various surface groups on the fumed silica: hydroxyl (A200), methyl (R974), octyl

(R805), and ethylene oxide (EO) (FS-EG3). The average voltage without fumed silica increases dramatically around 100 cycles while the average voltage of cells with composite electrolytes stays fairly constant for at least 300 cycles. The average voltage of the cell with the baseline electrolyte varies approximately 2 to 50 times that of cells with the composites and differs with fumed-silica type.

As reported earlier [6], the conductivity of these composite electrolytes is essentially independent of surface chemistry at a given weight fraction of fumed silica; hence, the differing effect of fumed-silica type on the average voltage of Li/electrolyte/Li cells is not due to the bulk conductivity of electrolytes, but may be attributed to the differing effect on the electrolyte/lithium interface. The addition of fumed silica clearly stabilizes the electrolyte and lithium metal interface and this effect is enhanced with increased weight fraction of fumed silica. The surface chemistry of fumed silica influences the extent of improvement. With the same weight fraction, the order of improvement effect is A200 (hydroxyl group) > R974 (methyl group) > R805 (octyl group) > FS-EG3 (EO group).

The improvement effect of fumed silica was also seen in impedance measurements. The impedance of the cells was measured before and after cell cycling. Figure 5.4 shows typical Nyquist plots of cells with the baseline electrolyte (top) and composite electrolyte (bottom). The interfacial resistance increases for both types of cells with cycle number. The interfacial resistance of the baseline electrolyte becomes almost ten times its original value after 336 cycles; the cycling had to be stopped at this point due to the safety limit of the equipment. However, the interfacial resistance of the

composite electrolyte with 10% R805 is only one-fourth that of the baseline electrolyte even after 584 cycles.

Figure 5.5 summarizes the interfacial resistances of Li/electrolyte/Li cells without fumed silica and with various types (R805, R974, A200, and FS-EG3) before and after cycling. The interfacial resistances of the cells show the same trend as that of the average voltage. Some Li/electrolyte/Li cycling was also carried out at a higher charge density of 1 C/cm^2 (not shown). These data also demonstrated that fumed silica improved the electrolyte/Li interface and A200 showed a better effect than R805.

The A200 hydrophilic fumed silica of all those studied produces the most improved Li-electrolyte interface, which suggests that the hydroxyl group on the fumed silica surface does not react appreciably with lithium. Otherwise, we would anticipate that A200 has the least beneficial effect since it has the highest content of surface hydroxyl groups (100%). It has been suggested that the improvement of the electrolyte and lithium metal interface affected by ceramic fillers is due to the fillers' scavenging of impurities in electrolyte materials such as H_2O and O_2 and shielding lithium from corrosion by forming compact thin passivation layers on its surface [2,29,30]. The A200 hydrophilic fumed silica has greater adsorption of H_2O than hydrophobic fumed silicas such as R805 and R974; therefore, based on these effects A200 is expected to have a better improvement effect than R805 and R974.

Although R805 and R974 have nearly the same coverage of surface hydroxyl (48% and 50%, respectively), the hydroxyl on R974 is less shielded by the shorter methyl groups than longer octyl chains on R805 [31]. Therefore, R974 has a better improvement

effect than R805 because of a greater accessibility of surface OH groups, which is supported by a lower degree of hydrophobicity of R974 than R805 [32].

EO-modified fumed silica FS-EG3 also stabilizes the electrolyte and lithium metal interface, indicating that the ethylene oxide chain attached to the fumed silica apparently does not react appreciably with lithium metal. However, we see less improvement with FS-EG3 than the other fumed silicas, which might be explained by several reasons. Although FS-EG3 has the highest molar fraction of silanol groups at the surface among the hydrophobic fumed silicas tested, accessible silanol groups per unit weight are believed to be less than those of R974 and R805. Earlier research of fumed silica fillers in different organic solvents showed that the interaction between surface chains is the cause of gel formation in these systems, and the surface interaction deteriorates when their solvency in the continuous medium is enhanced [31,33]. PEG-dm (250) acts as a good solvent for FS-EG3 due to the compatibility between surface groups of FS-EG3 and PEG-dm (250) solvent. We postulate that the solvent-fumed-silica-surface interaction prevails over fumed-silica/fumed-silica surface interaction in the FS-EG3 system. Because of the strong solvent-surface interaction, PEG-dm molecules form a solvation layer on each silica unit and shield surface silanol groups from mutual interaction or interaction with other molecules. In addition, FS-EG3 has a larger agglomerate size than other fumed silicas. It is recognized [4,14,29,34,35] that particle size of ceramic fillers plays a significant role in electrochemical properties of composite electrolytes such as conductivity, interfacial stability, and ionic transport, which are improved when particle size drops. Hence, the larger agglomerate size further lowers the improvement effect of

FS-EG3 on electrolyte/lithium interfacial stability. The precise mechanism that dictates different effects of various fumed silica on interfacial stability is unresolved and is a focus of ongoing efforts.

The above discussion compared the cell-cycling behavior at 1.0 mA/cm^2, which is a fairly high rate for rechargeable lithium batteries. As a means to determine to what extent current density influences the improvement effect of fumed silica, we cycled cells at 0.2 mA/cm^2 with 0%, 5%, and 10% R805 present in the electrolytes. The results showed that current density greatly influences the effect of fumed silica on interfacial stability. Figure 5.6 shows average voltage versus cycle number at 0.2 mA/cm^2 (left) and at 1.0 mA/cm^2 (right). Again, cells with composite electrolyte show a more stable interface at 0.2 mA/cm^2. Also a higher weight fraction of fumed silica gives lower average voltage and interfacial resistance. However, we see less improvement of the interface at a lower current density; that is, the difference in cells with and without fumed silica is not as pronounced as at 1.0 mA/cm^2. According to the study of Arakawa et al. on the effect of charging current density on lithium morphology [36], a lithium surface is smoother at lower rate, and the available lithium surface for the solvent, lithium salt, and impurities to react within a unit time is less. Thus, the corrosion of the lithium metal is not as severe as that at higher current density. Therefore, even the baseline electrolyte shows a more stable interface at a lower current density. However, we still observe an improvement of the interface by the addition of the fumed silica.

5.3.2 Li(Ni)/Electrolyte/Li Cycling

In the above Li/electrolyte/Li cycling, the total amount of available lithium is several hundred to thousand times of the amount of lithium actually cycled (560 C/cm^2 vs. 120 mC/cm^2 or 1 C/cm^2). It is not possible to determine lithium cycling efficiency and cycleability from such studies. Accordingly, a Li(Ni)/electrolyte/Li cell with a controlled amount of excess lithium was employed (9 times excess of lithium cycled). Figure 5.7 shows Li(Ni)/electrolyte/Li cycling results at 0.2 mA/cm^2 and illustrates that deposited Li becomes "dead Li" after the first 3 cycles in the absence of fumed silica but addition of 10 wt% of R805 improves Li cycleability dramatically. Thus, n = 3 is used in the cycling efficiency calculation for the baseline electrolyte instead of 20 in the case of 10% R805 composite electrolyte. The cycling efficiency of the baseline electrolyte for 3 cycles is 25% due to the fast loss of cycleable Li. However, the cycling efficiency of 10% R805 composite is about 70% for 20 cycles under the same experimental conditions. This significant improvement of cycling efficiency of composite electrolyte can be also attributed to the stabilizing effect of fumed silica to the electrolyte-lithium interface.

5.3.3 Full-Cell Cycling

The effect of fumed silica surface chemistry on full-cell cycling behavior was studied using a standard $LiCoO_2$ cathode composition (91% $LiCoO_2$, 6% graphite SFG 15, and 3% PVDF) at a C/40 rate (Figure 5.8). Three types of fumed silica were used: native hydroxyl group A200, octyl-modified R805, and EO-modified FS-EG3. Cell capacity quickly fades after the first few cycles in the absence of fumed silica but

addition of 10 wt% particulates diminishes the capacity fade, with the effect dependent upon the silica surface chemistry. The native fumed silica, A200, shows the best improvement while EO-modified fumed silica FS-EG3 shows the least effect. This trend agrees with the Li/electrolyte/Li cycling results.

A different cathode material does not alter the beneficial effect of fumed silica on full-cell cycling behavior. Figure 5.9 shows charge and discharge behavior of rechargeable lithium cells using lithium manganese oxide cathodes at a C rate of C/40 with 10% R805 composite and its baseline electrolyte. From Figure 5.9, we see that the addition of fumed silica again improves discharge capacity. In addition, a cell with 10% R805 shows less capacity fading. These improvements may be due to the enhancement of the interfacial stability between composite electrolyte and lithium metal.

Although the presence of fumed silica increases discharge capacity and reduces capacity fading in 4V lithium metal cells, the capacity fading is still severe even in the best case, i.e., 27% after 10 cycles for 10% A200 composite system with a $LiCoO_2$ cathode. Since our baseline and composite electrolytes are electrochemically stable up to 5.5 V [5], severe capacity fading is possibly due to the pitting corrosion of aluminum cathode current collector induced by TFSI anion at potentials greater than 3.5 V vs. Li [37-39]. In order to increase the capacity stability of electrolytes containing LiTFSI salt, a 3-V cathode material V_6O_{13} was employed in full-cell cycling studies. Figure 5.10 shows cell cycling behavior of the cell with the baseline electrolyte, 10% R805 and 10% A200 composite electrolytes at C/75 (0.08 mA/cm^2). As shown in Figure 5.10, the capacity for the first discharge cycle of Li/V_6O_{13} cells is as high as 297 mAh/g (5.7

Li/V_6O_{13}) for the baseline electrolyte, 306 mAh/g (5.8 Li/V_6O_{13}) for 10% R805 composite electrolyte, and 321 mAh/g (6.1 Li/V_6O_{13}) for 10% A200 composite electrolyte. The capacity of the cell using 10% A200 composite electrolyte is the highest throughout cycling, followed by 10% R805 composite and the baseline electrolyte. Capacity differences between cells increase from the initial values after 8 cycles. From Figures 5.8 and 5.9, we see that discharge capacity of 4V lithium cells decays dramatically after 3 or 4 cycles and decreases to essentially zero after 6 cycles in absence of fumed silica. Unlike 4-V lithium cells, the discharge capacity of a Li/V_6O_{13} cell with a baseline electrolyte does not drop significantly after 3 or 4 cycles. It remains fairly high even after 8 cycles: 252 mAh/g (4.8 Li/V_6O_{13}). The switch from 4-V to 3-V cathode material apparently reduces capacity fade of the baseline electrolyte system. As seen in 4-V cells, fumed silica also shows beneficial effects of increasing discharge capacity and diminishing the capacity fading seen in 3-V cells. Again, A200 shows a stronger improvement than R805.

5.4 Summary

Li/electrolyte/Li, Li(Ni)/electrolyte/Li, and full-cell cycling data show that fumed silica stabilizes the lithium/electrolyte interface, as shown by a lower polarization and interfacial resistance of a Li/composite-electrolyte/Li cell compared to a Li/baseline-electrolyte/Li cell. Also, Li(Ni)/electrolyte/Li cycling shows that a higher cycling efficiency is achieved with composite electrolytes; a full cell with composite electrolytes

shows a higher discharge capacity and less capacity fading than that with a baseline electrolyte.

Although the fumed silica-surface chemistry does not affect the stabilizing effect on the lithium-solvent interface, it does affect the extent of stabilization. The best-improved interfacial stability from Li/electrolyte/Li and full-cell cycling results is seen between lithium and A200 with hydroxyl surface groups. The improvement effect increases with the increasing content of fumed silica.

5.5 Acknowledgements

We gratefully acknowledge funding from the Department of Energy, Office of Basic Energy Sciences and Office of Transportation Technologies. We also thank 3M for providing LiTFSI salt, Degussa for supplying fumed silica, OM Group, Inc. for giving us $LiCoO_2$, and the Baker group at Michigan State University for synthesizing EO-modified fumed silica.

5.6 References

[1] G. B. Appetecchi, S. Scaccia, and S. Passerini, *J. Electrochem. Soc.*, **147**, 4448 (2000).

[2] G. B. Appetecchi, F. Croce, L. Persi, F. Ronci, and B. Scrosati, *Electrochim. Acta*, **45**, 1481 (2000).

[3] F. Capuano, F. Croce, and B. Scrosati, *J. Electrochem. Soc.*, **138**, 1918 (1991).

[4] B. Kumar and L. G. Scanlon, *J. Power Sources*, **52**, 261 (1994).

[5] J. Fan and P. S. Fedkiw, *J. Electrochem. Soc.*, **144**, 399 (1997).

[6] J. Fan, S. R. Raghavan, X. Y. Yu, S. A. Khan, P. S. Fedkiw, J. Hou, and G. L. Baker, *Solid State Ion.*, **111**, 117 (1998).

[7] M. C. Borghini, M. Mastragostino, S. Passerini, and B. Scrosati, *J. Electrochem. Soc.*, **142**, 2118 (1995).

[8] J. E. Weston and B. C. H. Steele, *Solid State Ion.*, **7**, 75 (1982).

[9] S. Skaarup, K. West, and B. Zachauchristiansen, *Solid State Ion.*, **28**, 975 (1988).

[10] J. Plocharski and W. Wieczorek, *Solid State Ion.*, **28**, 979 (1988).

[11] J. Plocharski, W. Wieczorek, J. Przyluski, and K. Such, *Appl. Phy. A-Mater. Sci. & Proc.*, **49**, 55 (1989).

[12] B. K. Choi, Y. W. Kim, and K. H. Shin, *J. Power Sources*, **68**, 357 (1997).

[13] Y. Dai, Y. Wang, S. G. Greenbaum, S. A. Bajue, D. Golodnitsky, G. Ardel, E. Strauss, and E. Peled, *Electrochim. Acta*, **43**, 1557 (1998).

[14] F. Croce, R. Curini, A. Martinelli, L. Persi, F. Ronci, B. Scrosati, and R. Caminiti, *J. Phy. Chem. B*, **103**, 10632 (1999).

[15] W. Wieczorek, K. Such, H. Wycislik, and J. Plocharski, *Solid State Ion.*, **36**, 255 (1989).

[16] B. Scrosati, F. Croce, and L. Persi, *J. Electrochem. Soc.*, **147**, 1718 (2000).

[17] B. Kumar, S. J. Rodrigues, and L. G. Scanlon, *J. Electrochem. Soc.*, **148**, A1191 (2001).

[18] S. A. Khan, G. L. Baker, and S. Colson, *Chem. Mater.*, **6**, 2359 (1994).

[19] H. J. Walls, J. Zhou, J. A. Yerian, P. S. Fedkiw, S. A. Khan, M. K. Stowe, and G. L. Baker, *J. Power Sources*, **89**, 156 (2000).

[20] S. R. Raghavan, M. W. Riley, P. S. Fedkiw, and S. A. Khan, *Chem. Mater.*, **10**, 244 (1998).

[21] G. Michael and H. Ferch, *Basic Characteristics of Aerosil*, Degussa Technical Bulletin Pigment No. 11, (1998).

[22] H. Barthel, L. Rosch, and J. Weis, in: J. Weis (Ed.), *Organosilicon Chemistry II. from molecules to materials*, VCH, Weinheim, p. 761 (1996).

[23] J. Hou, *Composite Polymer Electrolytes Using Functionalized Fumed Silica and Low Molecular Weight PEO: Synthesis and Characterization*, Ph.D. Thesis, Ann Arbor (1997).

[24] R. K. Iler, *The Chemistry of Silica: Solubility, Polymerization, Colloid and Surface Properties, and Biochemsitry*, John Wiley & Sons, New York (1979).

[25] H. J. Walls, P. S. Fedkiw, S. A. Khan, and T. Zawodzinski, A., Jr., *J. Electrochem. Soc.* (*submitted*, 2002).

[26] J. Fan and P. S. Fedkiw, *J. Power Sources*, **72**, 165 (1998).

[27] D. Aurbach, Y. Gofer, and J. Langzam, *J. Electrochem. Soc.*, **136**, 3198 (1989).

[28] D. Fauteux, *Solid State Ion.*, **17**, 133 (1985).

[29] F. Croce, L. Persi, F. Ronci, and B. Scrosati, *Solid State Ion.*, **135**, 47 (2000).

[30] G. B. Appetecchi, F. Croce, G. Dautzenberg, M. Mastragostino, F. Ronci, B. Scrosati, F. Soavi, A. Zanelli, F. Alessandrini, and P. P. Prosini, *J. Electrochem. Soc.*, **145**, 4126 (1998).

[31] S. R. Raghavan, J. Hou, G. L. Baker, and S. A. Khan, *Langmuir*, **16**, 1066 (2000).

[32] Y. U. Jeong and A. Manthiram, *Electrochem. Solid-State Letters*, **2**, 421 (1999).

[33] S. R. Raghavan, H. J. Walls, and S. A. Khan, *Langmuir*, **16**, 7920 (2000).

[34] J. Przyluski, M. Siekierski, and W. Wieczorek, *Electrochim. Acta*, **40**, 2101 (1995).

[35] W. Wieczorek, Z. Florjanczyk, and J. R. Stevens, *Electrochim. Acta*, **40**, 2251 (1995).

[36] M. Arakawa, S. Tobishima, Y. Nemoto, M. Ichimura, and J. Yamaki, *J. Power Sources*, **43**, 27 (1993).

[37] W. K. Behl and E. J. Plichta, *J. Power Sources*, **72**, 132 (1998).

[38] L. J. Krause, W. Lamanna, J. Summerfield, M. Engle, G. Korba, R. Loch, and R. Atanasoski, *J. Power Sources*, **68**, 320 (1997).

[39] X. Wang, E. Yasukawa, and S. Mori, *Electrochim. Acta*, **45**, 2677 (2000).

Table 5. 1. Characteristics of fumed silicas used in this study

Fumed silica	**Dominant surface group(s)**	**Fraction of surface substituted (mol%)[23,31]**	**Fraction of unreacted Si-OH (mol%)**
A200	Si-OH [silanol]	0	100
R974	Si-$(CH_3)_2$ [di-methyl)	50	50
R805	Si-C_8H_{17} [octyl]	48	52
FS-EG3	Si-$(CH_2)_3(O\text{-}CH_2\text{-}CH_2)_3\text{-}OCH_3$	35	65

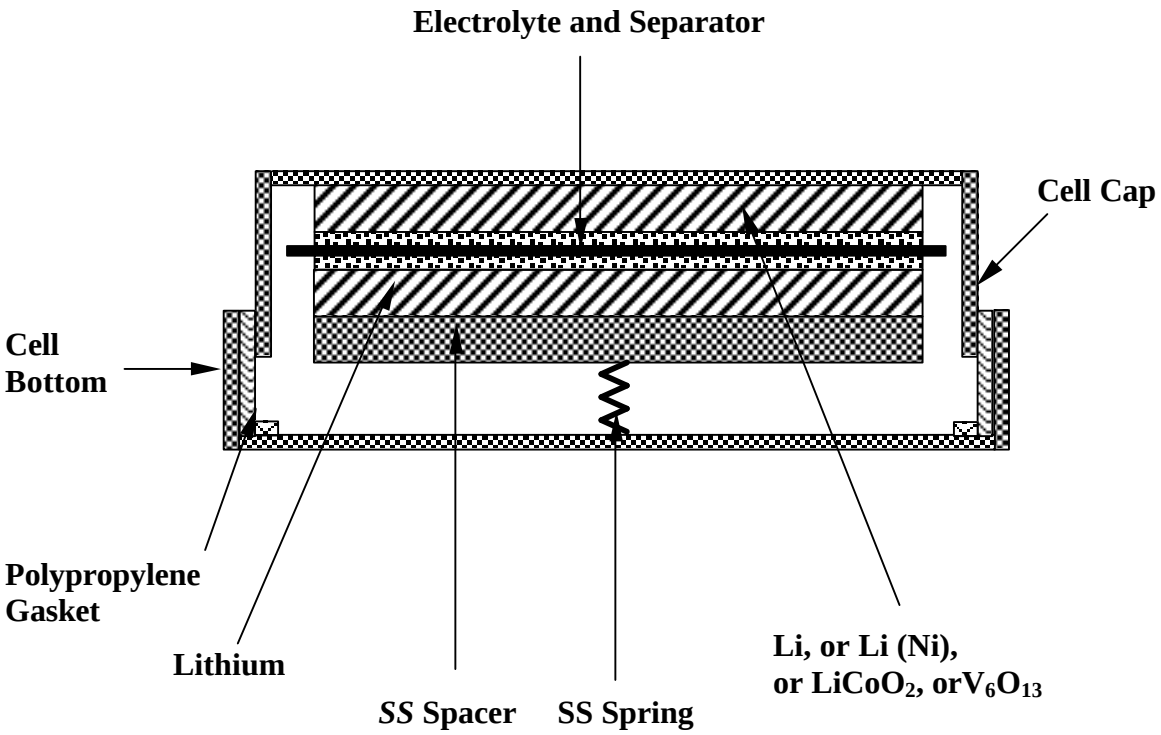

Figure 5. 1. Coin cell for cycling studies (Not to scale).

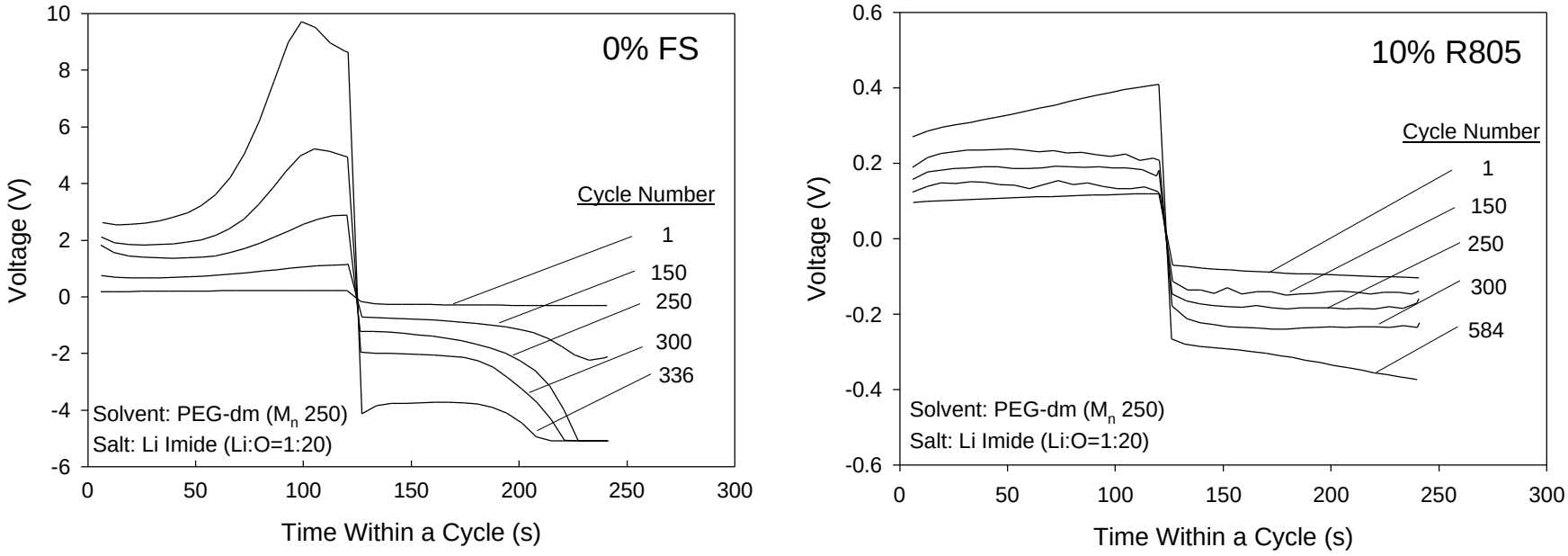

Figure 5. 2. Voltage waveform of Li/electrolyte/Li cells without (left) and with (right) fumed silica cycled at 1 mA/cm^2. (FS: Fumed silica; R805: Octyl-modified fumed silica)

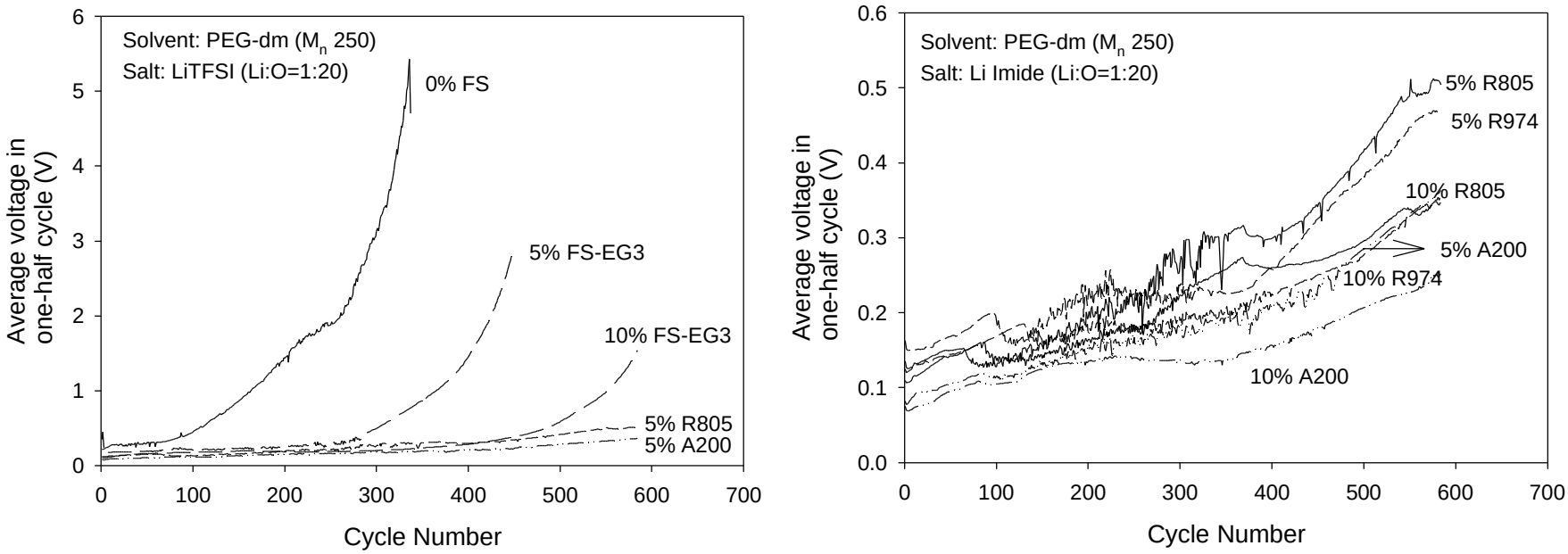

Figure 5. 3. Effect of fumed silica surface chemistry on voltage response of Li/electrolyte/Li cells at 1 mA/cm^2. (FS: Fumed silica; A200: Native –OH surface groups; R805: Octyl-modified fumed silica; R974: Methyl-modified fumed silica; FS-EG3: Ethylene oxide-modified fumed silica).

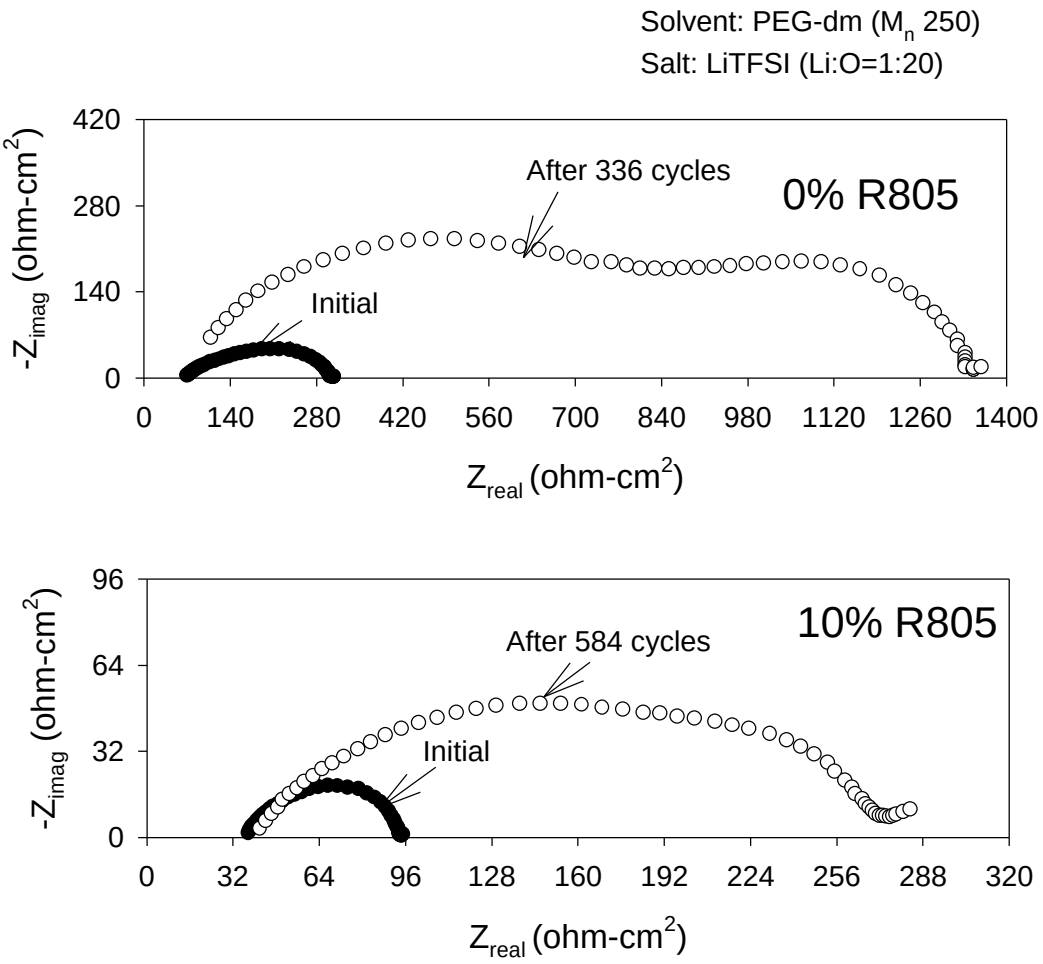

Figure 5. 4. Nyquist plot of baseline (top) and composite electrolyte (bottom) systems before and after cycling Li/electrolyte/Li cells at 1 mA/cm^2.

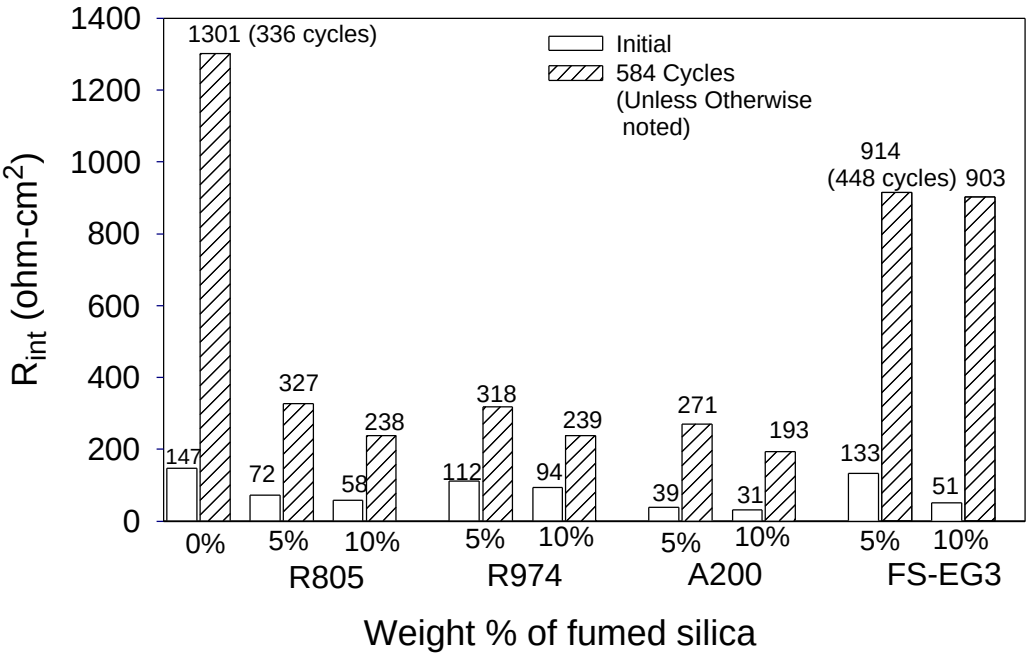

Figure 5. 5. Effect of fumed silica and its surface chemistry on interfacial resistance for cycled cells shown in Figure 5.3.

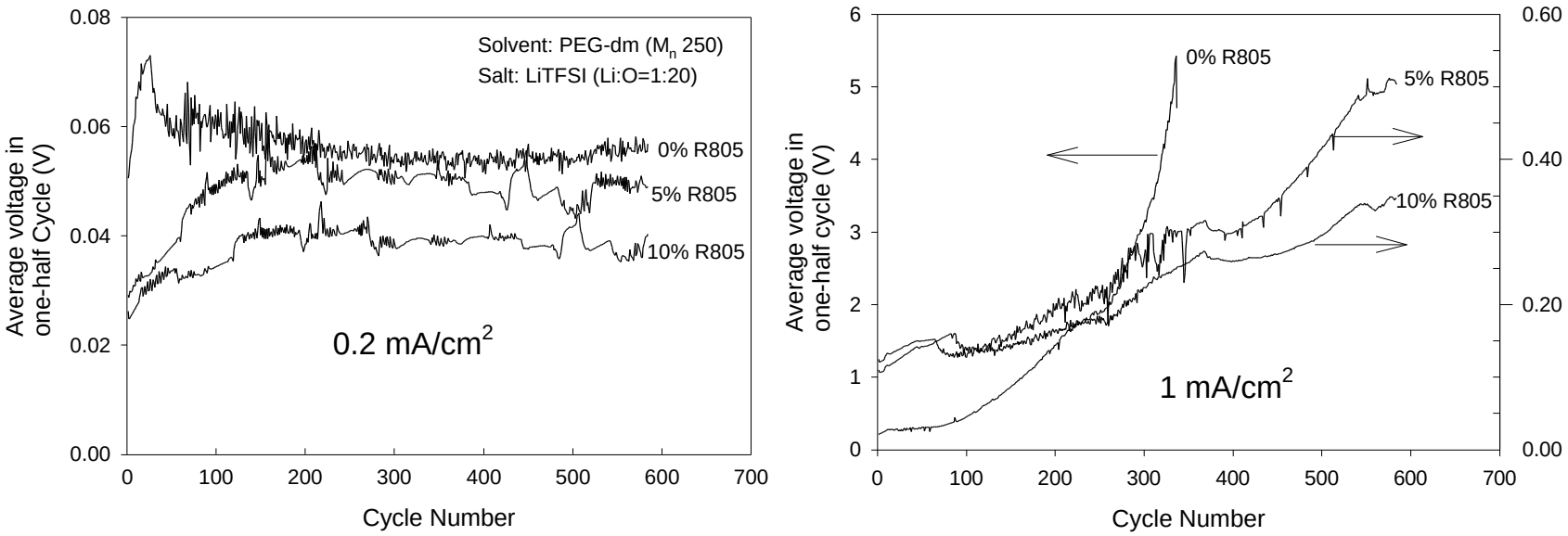

Figure 5. 6. Effect of current density on cycling behavior of Li/electrolyte/Li cells for baseline and composite systems.

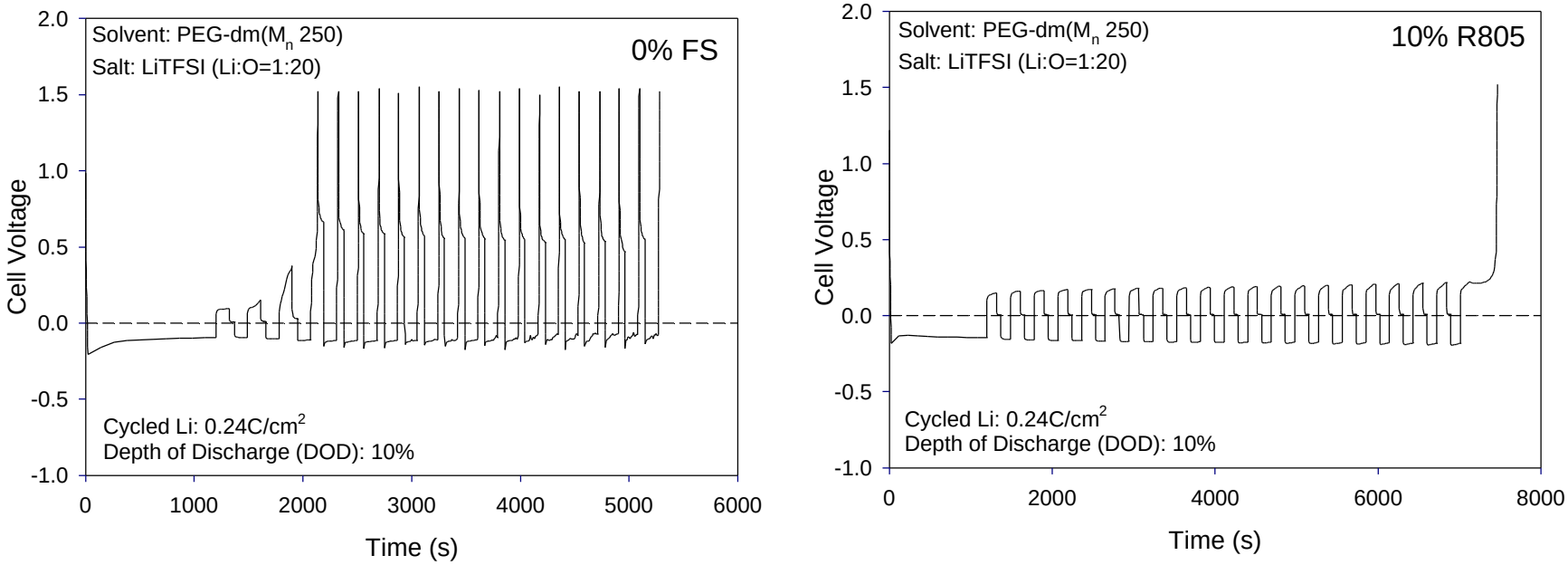

Figure 5. 7. Effect of fumed silica on cycling behavior of Li(Ni)/electrolyte/Li cells without (left) and with (right) fumed silica.

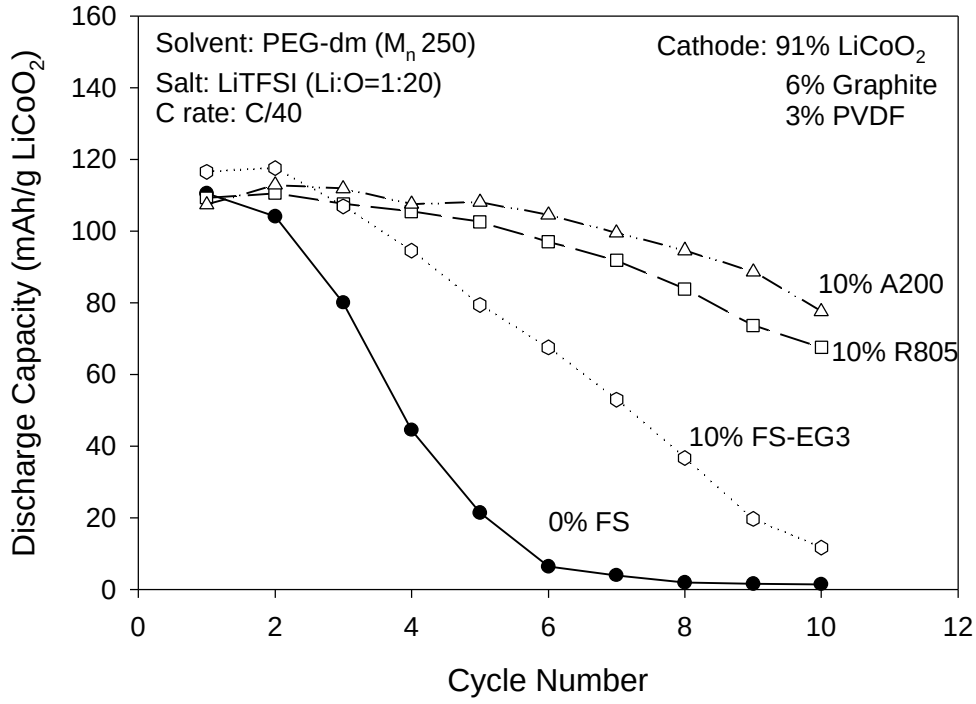

Figure 5. 8. Effect of fumed silica surface chemistry on full-cell cycling of Li/electrolyte/$LiCoO_2$ cells at C/40 (i=0.08 mA/cm^2).

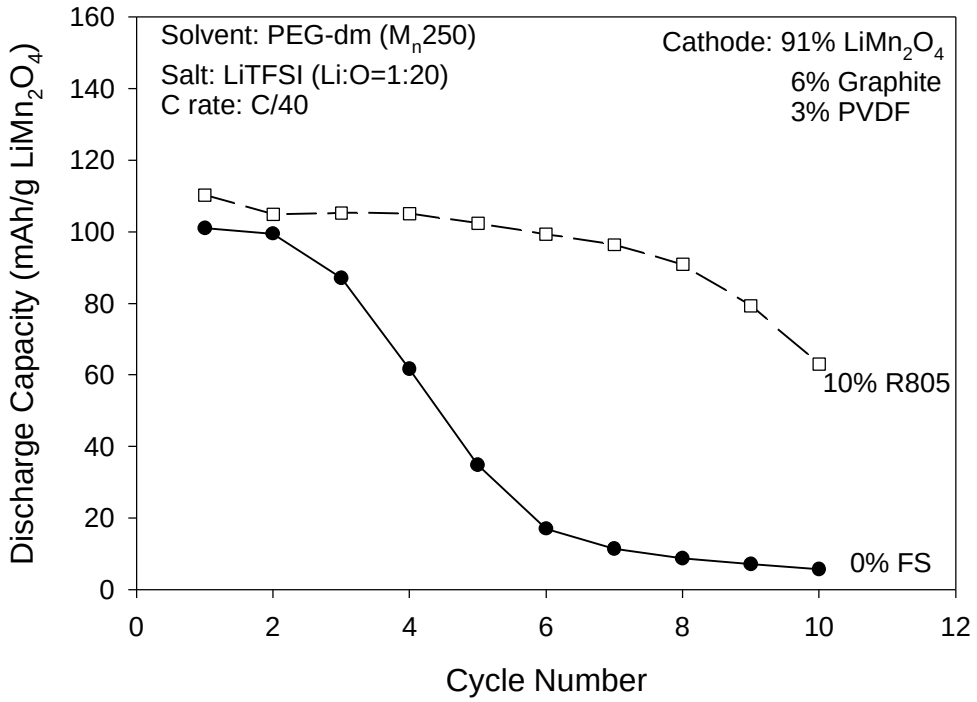

Figure 5. 9. Effect of fumed silica surface chemistry on full-cell cycling of Li/electrolyte/$LiMn_2O_4$ cells at C/40 (i=0.08 mA/cm^2).

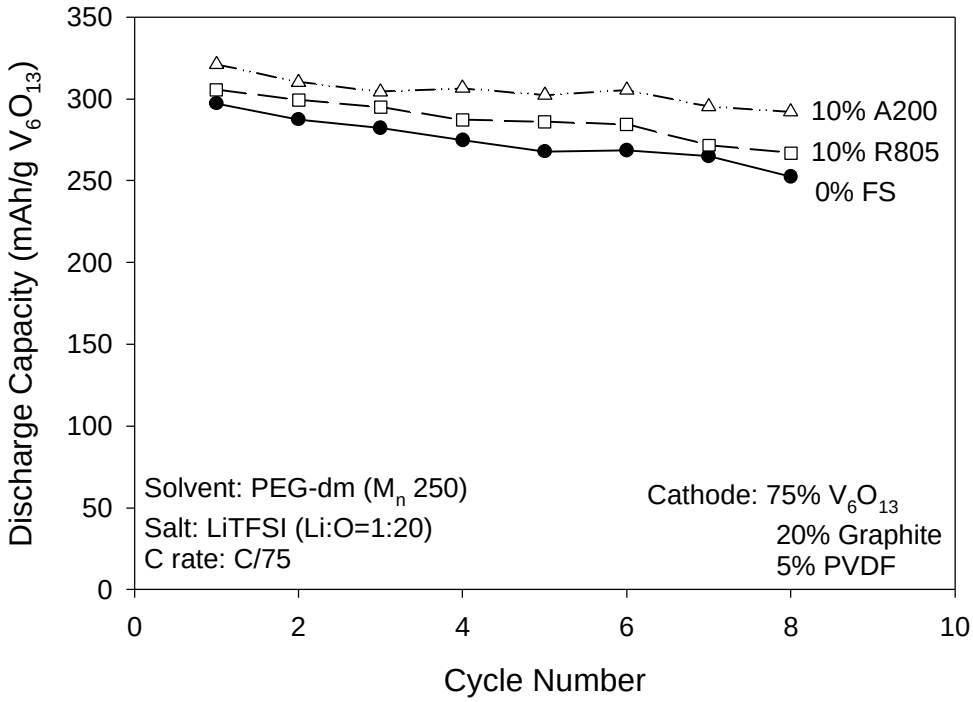

Figure 5. 10. Effect of fumed silica surface chemistry on full-cell cycling of Li/electrolyte/V_6O_{13} cells at C/75 (i=0.08 mA/cm^2).

Chapter 6: Cycling of Lithium/Metal Oxide Cells Using PEO Oligomer Composite Electrolytes Containing Fumed Silicas

Jian Zhou and Peter S. Fedkiw

Department of Chemical Engineering

North Carolina State University

Raleigh, NC 27695-7905

In preparation for submission to

Electrochimica Acta

December 18, 2002

Abstract

The effect on cycle capacity is reported of cathode material (metal oxide, carbon, and current collector) in lithium/metal oxide cells cycled with fumed silica-based composite electrolytes. Three types of electrolytes are compared: filler-free electrolyte consisting of methyl-terminated poly(ethylene oxide) (PEO) oligomer (M_w=250) + lithium bis(trifluromethylsufonyl)imide (LiTFSI) (Li:O=1:20), and two composite systems of the above baseline liquid electrolyte containing 10 wt% A200 (hydrophilic fumed silica) or R805 (hydrophobic fumed silica with octyl surface group). The composite electrolytes are solid-like gels. Three cathode active materials ($LiCoO_2$, V_6O_{13}, and Li_xMnO_2), four conducting carbons (graphite Timrex® SFG 15, SFG 44, carbon black Vulcan XC72R and Ketjenblack EC-600JD), and three current collector materials (Al, Ni, and carbon fiber) were studied. Cells with composite electrolytes show higher capacity and less cell polarization than those with filler-free electrolyte. Among the three active materials studied, V_6O_{13} cathodes deliver the highest capacity and Li_xMnO_2 cathodes render the best capacity retention. Discharge capacity of Li/$LiCoO_2$ cells is affected greatly by cathode carbon type, and the capacity decreases in the order of Ketjenblack > SFG 15 > SFG 44 > Vulcan. Current collector material also plays a significant role in cell cycling performance. Lithium/vanadium oxide (V_6O_{13}) cells deliver increased capacity using Ni foil and carbon fiber current collectors in comparison to an Al foil current collector.

Keywords: Composite electrolyte, Fumed silica, PEG oligomer, Rechargeable lithium cell, cell cycling

6.1. Introduction

Due to the low density of metallic lithium and its highly negative redox potential, rechargeable lithium batteries are potential power sources for high-energy and high-power applications such as portable electronic devices (e.g., laptop, cellular phone, etc.), electric vehicles, and implantable biomedical devices (e.g., left ventricular assist device and artificial heart) [1-3]. However, the high reactivity of lithium greatly limits the choice of usable electrolytes and impedes the commercialization of secondary lithium batteries. In recent years, various researchers have reported composite electrolytes which incorporate various ceramic fillers (e.g., Al_2O_3, SiO_2, TiO_2) are promising materials for rechargeable metallic lithium batteries [4-9]. Compared with their filler-free counterparts, composite electrolytes show improved lithium interfacial stability, better cycleability, comparable or superior ambient-temperature ionic conductivity, and good mechanical strength [4-9]. Fumed silica-based composite electrolytes developed in our lab showed improved mechanical strength, interfacial stability with lithium, and cell cycleability with insignificant conductivity loss in comparison to the baseline liquid [5,6,10-12].

This communication reports the effect of cathode compositions on cell cycling performance with fumed silica-based composite electrolytes. Cathodes for rechargeable lithium batteries normally consist of active metal oxides (e.g., $LiCoO_2$ [13-17], Li_xMnO_2 [18,19], or V_6O_{13} [14,20-27]), electronic conductors (e.g., graphite [11,12,28-30] or carbon blacks [28,29,31-36]), and polymer binders [e.g., polyvinylidenefluoride (PVDF) [11,12,28-31,34] or polytetrafluoroethylene (PTFE) [33,35,37]. Normally cathode pastes

are coated on a current collector that connects to the power supply or load. The relative content of the components (active material, polymer binder, and electronic conductor) and their physicochemical properties are responsible for the electrochemical response of cathodes. The corrosion resistivity of current collector and the adherence between cathode materials and current collector also affect the cathode performance. In this communication, three types of metal oxides, $LiCoO_2$, V_6O_{13}, and Li_xMnO_2, are studied to explore the effect of cathode active material on cell performance with fumed silica-based composite electrolytes. Four individual carbon additives (graphite Timrex® SFG 15, SFG 44, carbon black Vulcan XC72R, and Ketjenblack EC-600JD) and one binary mixture of graphite Timrex® KS6 and carbon black Ketjenblack EC-600JD are employed to investigate the effect of electronic conductor on cell cycling performance. The cycling performance of lithium/vanadium oxide (V_6O_{13}) cells using Al, Ni, and carbon fiber current collectors is also compared.

6.2. Experimental

6.2.1 Fumed Silica

Fumed silica is an amorphous, nonporous form of silicon dioxide (SiO_2) prepared by flame hydrolysis of silicon tetrachloride [38]. The predominant particle structures of fumed silica are branch-like aggregates (ca. 0.1-μm long), which consist of partially fused primary particles (ca. 12-nm diameter) that cannot be disrupted by shear [39]. Two types of fumed silicas are used in this study: A200 (native surface hydroxyl groups) and

R805 (octyl-modified surface). The octyl-modified R805 is obtained by reacting A200 with octyltrimethoxysilane (OTMS) and both are commercial products of Degussa.

6.2.2 Electrically Conducting Carbon Additives

Carbon additives used in this study include three types of graphite from Timcal, Ltd. (Timrex® SFG 15, SFG 44, and KS 6), and two types of carbon blacks (Vulcan XC72R from Cabot Corp. and Ketjenblack (KJB) EC-600JD from Akzo Nobel Inc.). The KS graphite consists of round particles, whereas the SFG type is in the form of flat flakes [40]. The number in the graphite designation indicates the particle size; that is, in SFG 15, SFG 44, and KS6, ~ 90% of the particles are smaller than 15, 44, and 6 μm, respectively. For round particles, as in the KS-type graphite, more prismatic surfaces are expected than for flat flakes (SFG type). Carbon properties and cathode compositions are listed in Table 6.1.

6.2.3 Preparation of Composite Electrolytes

The composite electrolytes consist of three materials: lithium bis(trifluromethylsulfonyl)imide [$LiN(CF_3SO_2)_2$] (LiTFSI, 3M), fumed silica (Degussa), and poly(ethylene glycol) dimethyl ether (PEG-dm, M_w=250, Aldrich). The lithium salt, LiTFSI, was dried at 110°C under vacuum for 24 hours before use. Poly(ethylene glycol) dimethyl ether (PEG-dm) was dried over 4Å molecular sieves for at least one week. Water content of both materials was controlled under 20 ppm, as determined by Karl-

Fisher titration. Fumed silicas were dried at 120°C under vacuum for 3-4 days to achieve a water content of 150-200 ppm before being transferred to an argon-filled glove box.

Composite electrolytes were prepared in a glove box. First, a baseline electrolyte was made by dissolving LiTFSI in PEG-dm oligomer in a Li:O ratio of 1:20 (1M LiTFSI solution) to maintain the highest conductivity [5]. A certain weight of fumed silica was then added to the baseline electrolyte to get the desired concentration and dispersed into the electrolyte using a high-shear mixer (Tissue Tearor™, Model 398, BioSpec Products, Inc.) [41]. Water content of the baseline electrolyte and the composites was under 20 and 50 ppm, respectively. The baseline electrolyte is a liquid while composite electrolytes are solid-like gels with rheological and transport properties reported elsewhere [42].

6.2.4 Preparation of Cathodes

All components of metal-oxide cathodes, $LiCoO_2$ (OM Group, Inc., OMG), V_6O_{13} (Kerr-McGee), or Li_xMnO_2 (synthesized by Doeff's group at Lawrence Berkeley National Laboratory [18]), poly(vinylidene fluoride) (PVDF, Kynar® Flex 2800-00, Elf Atochem North America), carbon additives, and 1-methyl-2-pyrrolidinone (NMP, Aldrich), were used as received. The effect of carbon type is studied in $LiCoO_2$ cathode materials. In $LiCoO_2$ electrodes, 6 wt% graphite (Timrex® SFG 15 or SFG 44) or 3 wt% carbon black (KJB EC-600JD or Vulcan XC72R) was used as the electronic conductor. In all $LiCoO_2$ cathodes except those containing KJB, 3% PVDF was used as the binder; in the latter case, 5% PVDF was used due to the high-surface area of KJB particles. Aluminum foil (0.024-mm thick, Fisher Scientific) was used as the current collector for

$LiCoO_2$ cathodes. The effect of current collector materials is studied using V_6O_{13} cathodes, which consist of 75% V_6O_{13}, 20% SFG15 graphite, and 5% PVDF. The current collectors are: Al foil, Ni foil (0.125-mm thick, Aldrich), and 0.127-mm thick sheet of carbon fiber (Techimat® 6100-035, Lydall Technical Papers). Lithium manganese dioxide cathodes are composed of 84% Li_xMnO_2, 8% binary carbon mixture (graphite KS6: KJB = 1:1), and 8% PVDF. Aluminum foil (24-μm thick) was used as the current collector. Usually, a fixed amount of metal oxide and carbon additive(s) are thoroughly ground and mixed using mortar and pestle. Then, the mixture of metal oxide and carbon(s) was dispersed into a solution of PVDF using NMP as solvent. The resulting slurry was coated onto the current collector by a doctor blade, and the final thickness of wet cathode films was approximately 0.20 mm for cathodes using Al current collector and 0.30 mm for those with thicker Ni foil or carbon fiber current collector, 125 and 127 μm, respectivley. The film was dried at 80°C overnight and was cut into 12.7-mm diameter disks that were hot-compacted by a hydraulic press at 150°C and 770 MPa. After compaction, cathode disks were dried at 150°C under vacuum for 24 h.

6.2.5 Preparation of Coin Cells

Coin cells in which an electrolyte/separator is sandwiched between a thin sheet of lithium metal and cathode of 1.27-cm diameter active material were used in the cycling measurements (cell configuration reported elsewhere [11]). In these cells, a Celgard® 2400 separator (25-μm thick) is either wetted by the baseline electrolyte or sandwiched between two layers of composite electrolyte.

6.2.6 Methods and Measurements

An Arbin battery cycler (Model BT2042) controlled by Arbin ABTS software is employed to carry out constant-current cell cycling. Lithium/lithium cobalt dioxide cells were cycled between 2.5 to 4.2 V at a constant current density of 0.11 mA/cm^2 (C/40) for graphite-containing cathodes, 0.08 mA/cm^2 (C/40) for Vulcan XC72R-containing cathodes, and 0.08 mA/cm^2 (C/17), 0.39 mA/cm^2 (C/3.4), and 0.80 mA/cm^2 (C/1.7) for KJB-containing cathodes. Lithium/vanadium oxide (V_6O_{13}) cells were cycled between 2.5 to 3.6 V at 0.08 mA/cm^2 (C/55) between 1.8 to 3.0 V, while Li/Li_xMnO_2 cells were cycled at 0.05 mA/cm^2 (C/10).

6.3. Results

6.3.1 Li/$LiCoO_2$ Cycling

Figure 6.1 shows typical cycling curves of Li/$LiCoO_2$ cells using graphite SFG 15 as the conducting agent with the baseline liquid electrolyte (Figure 6.1a) and composites with 10 wt% R805 added to the baseline electrolyte (Figure 6.1b). The upon-assembly, open-circuit voltage of Li/$LiCoO_2$ cells is around 1.8 V. All cycling curves of Li/$LiCoO_2$ cells using different carbon additives are qualitatively similar to those illustrated in Figure 6.1. During a charge half-cycle, the cell voltage rapidly increases from 2.5 V to a plateau around 4.0 V (corresponding to ~$Li_{0.8}CoO_2$ [15]) followed by a voltage increase to 4.2 V (corresponding to ~$Li_{0.5}CoO_2$) near the end of charge. Similarly, during Li

intercalation, the voltage decreases from 4.2 V to a plateau around 3.9 V (corresponding to ~$Li_{0.8}CoO_2$) and drops to 2.5 V rapidly at the end of intercalation.

6.3.1.1 Effect of Electronically Conducting Carbon Types

Figure 6.2 shows discharge capacities of Li/$LiCoO_2$ cells with the baseline liquid electrolyte [PEG-dm (250) + LiTFSI (Li:O=1:20)] (left) and composite electrolyte containing 10 wt% R805 (right) using different types of carbon: graphite Timrex® SFG 15, graphite Timrex® SFG 44, Cabot Vulcan XC72R, and Ketjenblack (KJB) EC-600JD. The cathode compositions are shown in Table 6.1. Cells are cycled from 2.5 to 4.2 V at 0.11 mA/cm^2 (C/40) for graphite-based cathodes and 0.08 mA/cm^2 (C/40 for Vulcan XC72R, C/17 for KJB EC-600JD) for carbon black-based cathodes. At the same C-rate and cathode composition, composite electrolytes show higher capacity than filler-free electrolytes. The discharge capacity increases with carbon type in the order of Vulcan XC72R < SFG 44 < SFG 15< KJB EC-600JD for both baseline and composite electrolytes. The first-cycle discharge capacities at the best condition are around 130 mAh/g $LiCoO_2$ for composite electrolyte containing 10 wt% R805 and filler-free electrolytes. As expected, cell capacity with smaller metal-oxide particles is greater than that with larger particles within the same group of carbon types. For example, cells containing graphite SFG 15 have higher discharge capacities than cells with SFG 44, and cells containing KJB EC-600JD carbon black have higher capacities than those with Vulcan XC72R. Using smaller particle carbons not only increases discharge capacity but also decreases capacity fade, except for the composite electrolytes containing 10 wt%

R805 using SFG 15 and SFG 44. The capacity fade over the first five cycles for cells with 10% R805 composite electrolyte is about the same using both types of graphite. The beneficial effect of using smaller particle carbons is more significant with filler-free electrolytes than with composite electrolytes. Surprisingly, cells with Vulcan XC72R carbon black show lower capacity and more severe capacity fade than those with graphite, even though the carbon black particle size is smaller than that of graphite.

6.3.1.2 Effect of C-Rate

Since cathodes containing KJB EC-600JD show the best performance in Li/$LiCoO_2$ cells using fumed silica-based composite electrolytes, we studied its rate capability. Figure 6.3 shows cycling behavior of cells with filler-free electrolyte and composite electrolytes containing 10 wt% R805 and 10 wt% A200 at three current densities: 0.08 mA/cm^2 (C/17), 0.39 mA/cm^2 (C/3.4), and 0.80 mA/cm^2 (C/1.7). All cathodes are comprised of 92% $LiCoO_2$, 3% KJB, and 5% PVDF. Cell capacity decreases with increasing current density due to the increasing cell polarization, but capacity loss is more significant for filler-free electrolyte than composite electrolytes. Overall, cells containing 10% A200 composite electrolyte shows the best capacity for all current densities, followed by 10% R805 composite, and filler-free electrolytes. At C/17 the discharge capacity is around 130 mAh/g $LiCoO_2$ for the first cycle and remains above 100 mAh/g $LiCoO_2$ after seven cycles for all electrolytes. At C/3.4 the first-cycle discharge capacity of composite electrolytes is around 106 mAh/g $LiCoO_2$ and the capacity reaches 97 mAh/g $LiCoO_2$ after seven cycles. Although cells with filler-free

electrolyte supplies about 100 mAh/g $LiCoO_2$ capacity for the first cycle, it retains less than 40 mAh/g $LiCoO_2$ capacity after three cycles. At C/1.7 the first-cycle discharge capacity of 10% A200 composite is above 100 mAh/g $LiCoO_2$ and the capacity after seven cycles is about 87 mAh/g $LiCoO_2$. The discharge capacity of 10% R805 composite decreases from 89 to 63 mAh/g $LiCoO_2$ after seven cycles. Although the cell with baseline liquid electrolyte has comparable initial discharge capacity as that with 10% R805 composite, its capacity drops dramatically to less than 40 mAh/g $LiCoO_2$ after three cycles.

6.3.2 Li/V_6O_{13} Cycling

Vanadium oxide (V_6O_{13}) cathodes with three types of current collectors (Al, Ni, and carbon fiber) are studied. Although KJB was the best carbon in terms of cathode capacity and capacity retention for $Li/LiCoO_2$ cells, graphite Timrex® SFG 15 was used in V_6O_{13} cathodes in order to get a uniform dispersion of cathode materials and prevent the cathode mix from cracking after drying. Figure 6.4 shows typical cycling curves of Li/V_6O_{13} cells cycled at 0.08 mA/cm^2 using carbon fiber as the current collector for the baseline electrolyte (Figure 6.4a), 10% R805 composite electrolyte (Figure 6.4b), and 10% A200 composite electrolyte (Figure 6.4c). Cell-cycling curves using Al and Ni current collectors are qualitatively similar. Unlike $LiCoO_2$, V_6O_{13} is delithiated at cell assembly; thus, all Li/V_6O_{13} cells are first discharged. Both charge and discharge curves display three distinct voltage plateaus (Figure 6.4). The discharge plateaus are approximately 2.7 V ($Li_{1.5}V_6O_{13}$), 2.5 V ($Li_3V_6O_{13}$), and 2.1 V ($Li_6V_6O_{13}$) [25] and are

slightly higher during charge at 2.8, 2.6, 2.2 V, respectively. The upon-assembly, open-circuit voltage of the Li/V_6O_{13} cell is around 2.8 V, which is lower than the charge cut-off voltage 3.0V.

6.3.2.1 Effect of Current Collector Type

Figure 6.5 illustrates discharge capacity of Li/V_6O_{13} cells cycled at 0.08 mA/cm^2 (C/55) with a cathode composition of 75% V_6O_{13} + 20% SFG 15 + 5% PVDF using three types of current collector: Al, Ni, and carbon fiber. The electrolytes tested are baseline liquid electrolyte, and composite electrolytes containing 10 wt% R805 and 10 wt% A200. In cells with Al current collector, composite electrolytes containing 10 wt% R805 or A200 deliver higher capacity than baseline liquid electrolyte. Both composite electrolytes provide comparable discharge capacity. In the case of Ni current collector, all three electrolytes essentially supply the same capacity. Discharge capacity of cells with carbon fiber current collector increases in the order of filler-free < 10 wt% R805 < 10 wt% A200, and the increases is approximately 4.5% and 8% upon addition of R805 and A200 into baseline liquid electrolyte, respectively. Overall, cells with Al current collector supply the lowest capacity for all three electrolytes while those with Ni and carbon fiber current collectors provide greater but comparable discharge.

6.3.3 Li/Li_xMnO_2 Cycling

Although Li/V_6O_{13} cells show less capacity fade than Li/$LiCoO_2$ cells, the capacity fade rate is still not acceptable for practical applications. Capacity fade in these

cells is often associated with structural change of the active cathode material during Li^+ insertion/removal. A cathode material that does not undergo significant structural change would be advantageous. Recently, Doeff and coworkers [18] synthesized stable non-spinel Li_xMnO_2 with the $Na_{0.44}MnO_2$ structure and observed good cycleability with high-M_w PEO-based electrolytes. We have examined the performance of this material with low-M_w PEG-dm-based electrolytes. Figure 6.6 demonstrates typical cycling curves of Li/Li_xMnO_2 cells with filler-free electrolyte (Figure 6.6a), 10% R805 composite electrolyte (Figure 6.6b), and 10% A200 composite electrolyte (Figure 6.6c) cycled at 0.05 mA/cm^2 (C/10) with a cathode composition of 84% Li_xMnO_2 + 4% graphite Timrex® KS6 + 4% KJB EC-600JD + 8% PVDF. The average particle size of Li_xMnO_2 is 2.6 μm [43]. As mentioned earlier, micrometer-size graphite can be uniformly dispersed in the cathode mix due to its comparable particle size as that of metal oxide while nanoscale carbon black possesses superior electrical conductivity. Binary mixtures consisting of graphite and carbon black often provide better cathode performance than individual graphite or carbon black [28,29]. Thus, carbon additives consisting of KS6: KJB in 1:1 mass ratio were employed in Li_xMnO_2 cathodes. Higher content (8% rather than 3% for $LiCoO_2$ or 5% for V_6O_{13} cathodes) of PVDF is necessary to prevent cracking of the cathode paste with Li_xMnO_2. The upon-assembly, open-circuit voltage of Li/Li_xMnO_2 cells varied from 3.1 to 3.2 V, corresponding to a partially discharged (lithiated) state ($Li_{0.4}MnO_2$ [18,19]). All cells are first discharged to 2.5 V ($Li_{0.67}MnO_2$ [19]) then re-charged to 3.6 V ($Li_{0.32}MnO_2$ [19]). Figure 6.6 reports the first five charge-

discharge cycles after the initial discharge. All discharge curves exhibit two small voltage plateaus at around 3.3 V and 3.0 V, as reported by Doeff et al. [18]

Figure 6.7 illustrates the discharge capacity of Li/Li_xMnO_2 cells versus cycle number with filler-free, 10% R805, and 10% A200 composite electrolytes for 25 cycles. Cell capacity is greatly affected by electrolyte type and decreases in the order 10% A200 composite electrolyte (100 mAh/g) > 10% R805 composite electrolyte (88 mAh/g) > filler-free electrolyte (83 mAh/g). No noticeable capacity fade was observed for all electrolytes. The coulombic efficiency is above 95% for all cells.

6.3.4 Effect of Cathode Active Material

Figure 6.8 summarizes the effect of cathode metal-oxide material on discharge capacity with filler-free electrolyte and composite electrolytes containing 10 wt% R805 and 10 wt% A200. All cells are cycled at C-rates lower than C/10 to study intrinsic properties of cathode active materials. For comparison, we normalize discharge capacities for the different metal oxides based on their practical capacity. Practical capacities are chosen as: 137 mAh/g for $LiCoO_2$ [14], 313 mAh/g for V_6O_{13} [24], and 100 mAh/g for Li_xMnO_2 [18]. High capacity and good capacity retention over cycles are desirable properties for rechargeable cells. Thus, we plot the initial discharge capacities for the first cycle and capacities at the 5^{th} cycle for $LiCoO_2$, V_6O_{13}, and Li_xMnO_2 and at the 25^{th} cycle for Li_xMnO_2 ($Li/LiCoO_2$ and Li/V_6O_{13} cell cycling was terminated before 25^{th} cycle due to severe capacity fade) in Figure 6.8. For each cathode active material, the best results in this study are compared. For example, the results of $LiCoO_2$ cathodes

containing KJB and V_6O_{13} cathodes with carbon fiber current collector are shown in Figure 6.8. Composite electrolytes deliver higher capacities than the baseline electrolyte throughout cycling under all operating conditions with all active materials. In general, 10% A200 composite electrolyte shows the highest capacities among the three types of electrolytes. For the first cycle, Li/V_6O_{13} cells, with or without filler, deliver the highest percentage of practical capacity than cells based on other two cathode materials. The Li/V_6O_{13} and Li/Li_xMnO_2 cells containing 10% A200 composite electrolytes, however, both deliver 100% of practical capacity. The lowest percentage of practical capacity at first cycle is observed with Li/Li_xMnO_2 cells for filler-free. After cycling, Li/$LiCoO_2$ cells deliver the lowest percentage of practical capacity, Li/Li_xMnO_2 cells with A200 show the highest. The capacity fade of Li/$LiCoO_2$ and Li/V_6O_{13} is severe even after the first five cycles: 11% for Li/$LiCoO_2$ and 6% for Li/V_6O_{13} cells. In contrast, no noticeable fade occurs for Li/Li_xMnO_2 cells even after 25 cycles. Overall, Li/V_6O_{13} delivers the highest capacity and Li/Li_xMnO_2 holds the best capacity retention for low-M_w PEG-dm based electrolytes.

6.4. Discussion

6.4.1 Composite Electrolytes

Cells with fumed silica-based composite electrolytes show higher capacity than filler-free electrolyte regardless of cathode active material type (Figure 6.8). The independence of cathode type supports the interpretation that the improvement in cycling performance is mainly due to enhanced interfacial stability between lithium and

electrolyte upon incorporation of fumed silica into the baseline electrolyte [11]. The enhancement in interfacial stability in the presence of fumed silica can be attributed to a reduction in lithium corrosion and dendrite formation. Fumed silica scavenges water impurities in the electrolyte to prevent lithium from corrosion. In addition, addition of fumed silica increases electrolyte elasticity which inhibits dendrite formation and propagation, as Newman deduces from his electrochemical modeling [44]. Hydrophilic fumed silica, A200, shows better improvement than hydrophobic R805 since it contains more surface hydroxyl groups that can form hydrogen bond with trace water [11] and it has a higher elasticity [5]. The beneficial effect of filler inclusion is more significant at higher current density (Figure 6.3) since cell polarization becomes more severe, especially for cells with high-interfacial resistance (filler-free electrolyte). Unlike high-M_w PEO based composite electrolytes, PEO oligomer-based composite electrolytes can deliver at least 90% (100% in some cases) of practical capacity without incorporation of large amount of (e.g., 35% [45] or higher) polymer electrolytes in the cathode mix for Li^+ transport. In contrast, less than 10% of PVDF binder (normally 5%) is incorporated in the cathodes formulated for this study (Table 6.1). The incorporation of a large quantity of polymer electrolyte in the cathode mix lowers the overall cell capacity and introduces complexity into the cathode fabrication. We purposely impregnated cathodes (cathode mix or cathode disks) with the baseline liquid electrolyte [PEG-dm (250) + LiTFSI (Li:O=1:20)] before cell assembly and observed no improvement in cathode capacity or capacity retention. It seems that fumed silica-based composite electrolytes do not require incorporation of electrolyte into the cathode mix prior to cell assembly to enhance Li^+

transport. Thus, we can apply the existing cathode-fabrication technique without significant modifications for fumed silica-based composite electrolytes. This processing advantage in addition to high room-temperature conductivity (> 10^{-3} S/cm) [5,6], high mechanical strength [5,6], and enhanced interfacial stability with lithium metal [11] makes fumed silica-based composite electrolytes promising materials for rechargeable metallic lithium batteries. However, cell performance of fumed silica-based composite electrolytes is closely related to cathode material. The optimization of cathode mix and current collector remains necessary to meet practical application requirements.

6.4.2 Effect of Carbon Additive Type

Cells with smaller carbon particles of the same type (graphite or carbon black) show higher capacities than those with larger particles (Figure 6.2) since smaller particles provide better electrical contact and lower percolation threshold [46] to achieve good electrical conductivity. A comparison between graphite and carbon blacks using particle size, however, is not appropriate since the structure of the two carbons differs. In general, carbon black is a better electrical conductor than graphite but graphite assists a more uniform dispersion of cathode-mix slurries. Both high-electrical conductivity and uniform dispersion lead to better cathode performance during cycling. A possible reason that cathodes containing Vulcan XC72R show the worst performance (Figure 6.2) is the non-uniform dispersion of material within the mix (visual observation) plus poor adhesion within the cathode matrix and to the current collector. (We observed that these cathodes could easily crack and fall off the current collector while being punched into

disks.) These problems originate from the small particles of Vulcan XC72R carbon black. Being aware of this issue, we increased the PVDF content to 5% to enhance the adhesion of KJB EC-600JD (which has smaller particle size than Vulcan XC72R) to the current collector and cathode mix, thus preventing cracking within cathode paste. Narkis et al. [47] report that KJB EC-600JD has the highest electrical conductivity of the various carbon blacks from different manufacturers they studied. Jang and Oh [33] also report the best cell performance with KJB EC-type carbon blacks among five carbon blacks tested, including Vulcan XC-72R. Our data also shows that $LiCoO_2$ cathodes with KJB EC-600JD as the conducting agent have the best cycling performance (Figure 6.2), which may be due to the superior electric conductivity of KJB EC-600JD. However, it is extremely difficult to use KJB alone as the conducting agent in V_6O_{13} or Li_xMnO_2 cathode material; structured graphite with larger particles must be incorporated into these mixes in order to get a continuous cathode paste that does not crack. Thus, graphite Timrex® SFG 15 was used in V_6O_{13} cathodes. Hong et al. [28] and Cheon et al. [29] showed that binary mixtures of graphite and carbon black ensures better cycling performance than individual graphite or carbon black. Accordingly, binary mixtures consisting of small-particle graphite KS6 (6 μm) and carbon black KJB EC-600JD (0.03-0.1 μm) were used in Li_xMnO_2 cathodes. There are two reasons for choosing KS6 instead of SFG15 or SFG 44 graphite: (1) smaller particle size lowers percolation threshold [46] and provides better cell performance, and (2) 6 μm is closer to the Li_xMnO_2 particle size (2.6 μm) than 15 (SFG 15) or 44 μm (SFG 44) and less particle size difference leads to a more homogeneous dispersion [28].

6.4.3 Effect of Current Collector Material

Pitting corrosion of Al current collectors is a common problem in rechargeable lithium batteries [48-52]. In addition, LiTFSI aggravates pitting corrosion of Al, especially at voltages above 3.5 V [48]. The corrosion decreases cell capacity and capacity retention [48-52]. In order to find corrosion-resistant current collector for LiTFSI salt, Ni and carbon current collector were also tested for comparison. In this preliminary study of current collector material, the thickness of Ni foil (0.125 mm) and carbon fiber (0.127 mm) was not optimized and is about five times that of Al foil (0.024 mm). The large thickness is not practical but serves the material comparison purpose in this study. In general, the use of Ni and carbon fiber current collectors enhances cell capacity and capacity retention for both filler-free and composite electrolytes (Figure 6.5). The improvement in cell cycling performance using Ni rather than Al is attributed to a better resistance to LiTFSI-induced corrosion, as suggested by Simoneau et al. [53]. These authors observed a factor of five decay in interfacial resistance of lithium/polyether-LiTFSI/vanadium oxide cells with a Ni current collector in comparison to Al. The authors noticed a slight corrosion of Ni at 60°C and negligible corrosion at 40°C. Evans and coworkers [54], however, noted significant pitting corrosion in lithium/PEO-LiTFSI/V_6O_{13} cells with Al current collector. Carbon fiber is selected as an alternative current collector material due to its high-electrical conductivity, high-corrosion resistance, and good adhesion property. When the cathode mix is spread onto the carbon fiber, the slurry is absorbed by the microporous carbon fiber matrix and stays

within and on the surface of the carbon fiber sheet, thus forming good contact. The microporous carbon fiber current collector not only provides a continuous matrix to accommodate the cathode mix but also can absorb and retain electrolyte solution to allow an intimate contact between Li^+ ions and active material, thereby, leading to improved utilization of active material. Our results show that a carbon fiber current collector improves the cell cycling performance (Figure 6.5). Although Ni and carbon fiber prove to be better current collector materials for LiTFSI-containing electrolytes, Al foil was used in the Li_xMnO_2 cathodes since the thickness of Ni and carbon fiber is not optimized for practical application. However, we believe that Ni and carbon fiber with optimized thickness might replace Al in practical rechargeable lithium batteries for LiTFSI-based electroytes.

6.4.4 Effect of Cathode Active Material

Since $LiCoO_2$ is the most widely used cathode material in commercial lithium-ion batteries, it is a good starting point for a rechargeable lithium battery as well. Although fumed silica-based composite electrolytes can initially deliver above 95% of practical capacity of $LiCoO_2$, the capacity fades rapidly during cycling (Figure 6.3). Capacity fade in Li/$LiCoO_2$ cells is due to electrolyte oxidation, corrosion of Al current collector, and volume change of Li_xCoO_2 cathode during Li^+ insertion and removal. Electrolytes undergo oxidation in a $LiCoO_2$ cathode due to high-charge voltage of $LiCoO_2$. The conducting carbon within the cathode mix can also catalyze electrolyte oxidation that

leads to its accelerated decomposition. Use of 3-V V_6O_{13} cathode material is based on following considerations:

(1) A lower-charge voltage than 4 V can mitigate the corrosion of Al current collector. It is widely accepted [48,50,51] that Al corrosion becomes severe only above an onset voltage. The onset voltage for Al pitting was reported as 3.2 V in 1 M LiTFSI/ethylene carbonate (EC) + dimethoxymethane (DME) by Zhang and coworkers [50]. Wang and coworkers [48], however, observed Al corrosion at 3.5 V with the same electrolyte. Kanamura et al. [51] found the onset corrosion potential between 4.0 to 4.2 V in 1 M LiTFSI/propylene carbonate (PC). Chen et al. [52] claimed that Al pitting corrosion initiates after a certain induction time at cell voltages between 3.6 to 3.8 V in the polymer electrolyte, poly(ethylene oxide) (PEO)-LiTFSI.

(2) V_6O_{13} can reversibly incorporate up to 6 Li per V_6O_{13} formula, which provides high-specific capacity and power. The combination of V_6O_{13} cathode and corrosion-resistant carbon fiber current collector apparently leads to less capacity fade and higher utilization of cathode active material (i.e., higher percentage of theoretical reversible capacity is delivered) than using $LiCoO_2$ and Al current collector (Figure 6.8).

However, capacity fade associated with large-volume change (~15% between V_6O_{13} and $Li_6V_6O_{13}$ [20,21]) during Li^+ intercalation and deintercalation cycles is inevitable. A cathode material with good capacity retention (e.g., Li_xMnO_2 with the $Na_{0.44}MnO_2$-structure) should be used in rechargeable lithium batteries, especially for large-size power sources for long-term operations such as the batteries for electric vehicles. The discharge capacity of Li/Li_xMnO_2 cells is ~ 80 mAh/g for filler-free

electrolyte, ~90 mAh/g for 10% R805 composite electrolyte, and ~100 mAh/g for 10% A200 composite electrolyte at C/10 (Figure 6.7). These capacities are within the range reported in the literature: 85-90 mAh/g with 1 M $LiAsF_6$-PC electrolyte at room temperature [19], 100-120 mAh/g with 1M $LiPF_6$-EC:DMC (1:2) at room temperature [18], and 100 mAh/g with high-M_w $P(EO)_8$LiTFSI at 85°C [18]. The difference in capacity reported by different groups is probably caused by: (1) different electrolyte material, which determines different interfacial stability between electrolyte and cathode, and (2) different cathode composition, preparation methods, and current collector materials, which greatly affect cell cycling performance. The Armstrong et al. [19] cathode mix of 80% $Li_{0.44}MnO_2$ + 13% carbon black + 7% PTFE was dry-mixed and pressed on an Al grid. Doeff et al. [18] used the mixture of Li_xMnO_2, carbon black, and ethylene/propylene diene terpolymer binder (EPDM) as a paste composition for carbonate electrolyte with stainless steel or graphite foil as the current collector. For the polymer electrolyte, they also incorporated a certain amount of polymer electrolyte in the cathode mix. However, no detailed composition was reported. We used the composition of 84% Li_xMnO_2 + 4% graphite Timrex® KS 6 + 4% KJB EC-600JD + 8% PVDF binder as the cathode mix with Al foil as the current collector. Our cathode preparation involves dissolution of cathode mix in NMP solvent and evaporation of the solvent afterwards. Comparing our results with those of Armstrong et al. [19], we would expect a capacity increase due to a better utilization of cathode active material with the usage of binary carbon mixtures (our group) versus individual carbon black (Armstrong's group). However, trace NMP contamination may remain in the cathode that lowers specific

capacity than using the dry-mixing method employed by Armstrong and coworkers. In addition, PEG-dm oligomer-based electrolytes are expected to deliver lower capacity than carbonate electrolyte because of larger ohmic loss. The comparison between our results and Doeff et al.'s [18] is somewhat difficult since they did not report the exact cathode composition. The use of stainless steel or graphite foil (Doeff's group) is expected to increase the capacity than using Al foil (our group) because of less corrosion. The polymer electrolyte, $P(EO)_8LiTFSI$, is completely amorphous at 85°C. We might expect it to deliver comparable capacity at 85°C as composite electrolytes based on low-M_w PEO oligomers at ambient temperature since both electrolytes are completely amorphous and both have ethylene oxide (EO) repeating units. In this sense, our results are in good agreement with the results reported by Armstrong et al. or Doeff et al. Like their cells, Li/Li_xMnO_2 cells with PEG-dm (250) based electrolytes, with and without fumed silica, show remarkable capacity retention without any noticeable capacity fade (Figure 6.7). With such good capacity retention, we would expect no capacity fade over a larger number of cycles, perhaps 100 cycles as in literature [18,19].

6.5. Summary

The effects of cathode active material, carbon additives, and current collectors have been demonstrated in lithium/metal oxide cells cycled with fumed silica-based composite electrolytes. Three types of electrolytes are compared in this study: filler-free electrolyte consisting of methyl-terminated poly(ethylene glycol) (PEG) oligomer (M_w=250) + lithium bis(trifluromethylsufonyl)imide (LiTFSI) (Li:O=1:20), and

composite electrolytes of the baseline liquid electrolyte containing 10 wt% A200 (hydrophilic fumed silica) or 10 wt% R805 (hydrophobic fumed silica with octyl surface group). Three cathode active materials ($LiCoO_2$, V_6O_{13}, and Li_xMnO_2), four conducting carbons (graphite SFG 15, SFG 44, carbon black Vulcan XC72R, and Ketjenblack EC-600JD), and three current collector materials (Al, Ni, and carbon fiber) were studied. Composite electrolytes show higher capacity than filler-free electrolyte under all operating conditions in the order of 10% A200 > 10% R805 > filler-free regardless of cathode materials. The increase in capacity and capacity retention upon addition of fumed silica can be ascribed to the improved interfacial stability of electrolytes with lithium and the decrease in cell polarization because of the impurity-scavenging and elasticity-enhancing effect of fumed silicas. Hydrophilic A200 has a better impurity-scavenging effect than hydrophobic R805 because of a higher number of surface hydroxyl groups.

Cell discharge capacity is greatly affected by cathode active material, carbon type, and current collector material. Among the three types of cathode active material tested, Li_xMnO_2 shows no noticeable capacity fade while $LiCoO_2$ renders the fastest capacity fade. Lithium/vanadium oxide (V_6O_{13}) cells deliver the highest percentage of practical capacity but still suffer severe capacity fade. For applications that require high power and capacity but can tolerate a certain degree of capacity fade, V_6O_{13} will be the best cathode candidate among three. If the applications require large-size power storage for long-term operations, Li_xMnO_2 is the best cathode material. Carbon type in the cathode mix also plays a significant role in cell cycling performance: Li/$LiCoO_2$ cells with

various carbon additives deliver discharge capacities in the order of KJB EC-600JD > SFG 15 > SFG 44 > Vulcan XC72R. Larger surface area (smaller particle size) renders higher capacity within the same carbon type: SFG 15 (8.5 m^2/g) > SFG 44 (4.3 m^2/g) for graphite and KJB (1250 m^2/g) > Vulcan (254 m^2/g) for carbon blacks. Normally, carbon blacks have higher electrical conductivities than graphite due to their amorphous structure and larger surface areas. However, the huge increase of surface area from graphite to carbon black also introduces non-uniform dispersion problems in the cathode mix associated with small particles. This may account for the lowest capacity of Vulcan carbon black. The increase of PVDF binder content in KJB-containing cathode along with the superior electrical conductivity of KJB carbon, however, provides the highest capacity. Pitting corrosion of widely used Al current collector exists in all system, especially with the LiTFSI salt at voltages above 3.5 V. The corrosion greatly reduces capacity and capacity retention. Nickel and carbon fiber shows better corrosion-resistance than Al current collector, and thus enhances cell cycling performance. In order to obtain best performance of rechargeable metallic lithium battery performance, the optimization of all cell materials including electrolyte, cathode active material, electronic conductors, and current collector material is required.

6.6. Acknowledgements

The authors gratefully acknowledge funding from the Department of Energy, Office of Basic Energy Sciences and Office of Transportation Technologies. We also thank 3M for providing LiTFSI salt and Degussa for supplying fumed silicas. The

authors would also like to express our gratitude towards cathode material suppliers: OM group, Inc. for $LiCoO_2$; Kerr-McGee for V_6O_{13}; Dr. Doeff at Lawrence Berkeley National Laboratory for Li_xMnO_2; Timcal Ltd. and Akzo Nobel, Inc. for carbon additives; and, Lydall Technical Papers for carbon fiber.

6.7 References

[1] G.-A. Nazri, *MRS Bull.*, **27**, 628 (2002).

[2] D. R. Sadoway and A. M. Mayes, *MRS Bull.*, **27**, 590 (2002).

[3] E. S. Takeuchi and R. A. Leising, *MRS Bull.*, **27**, 624 (2002).

[4] B. Kumar and L. G. Scanlon, *J. Power Sources*, **52**, 261 (1994).

[5] J. Fan, S. R. Raghavan, X. Y. Yu, S. A. Khan, P. S. Fedkiw, J. Hou, and G. L. Baker, *Solid State Ion.*, **111**, 117 (1998).

[6] J. Fan and P. S. Fedkiw, *J. Electrochem. Soc.*, **144**, 399 (1997).

[7] G. B. Appetecchi, S. Scaccia, and S. Passerini, *J. Electrochem. Soc.*, **147**, 4448 (2000).

[8] G. B. Appetecchi, F. Croce, L. Persi, F. Ronci, and B. Scrosati, *Electrochim. Acta*, **45**, 1481 (2000).

[9] F. Capuano, F. Croce, and B. Scrosati, *J. Electrochem. Soc.*, **138**, 1918 (1991).

[10] H. J. Walls, J. Zhou, J. A. Yerian, P. S. Fedkiw, S. A. Khan, M. K. Stowe, and G. L. Baker, *J. Power Sources*, **89**, 156 (2000).

[11] J. Zhou, P. S. Fedkiw, and S. A. Khan, *J. Electrochem. Soc.*, **149**, A1121 (2002).

[12] J. Fan and P. S. Fedkiw, *J. Power Sources*, **72**, 165 (1998).

[13] J. B. Goodenough, K. Mizushima, and T. Takeda, *Japn. J. Appl. Phy.*, **19**, 305 (1980).

[14] M. Winter, J. O. Besenhard, M. E. Spahr, and P. Novak, *Adv. Mater.*, **10**, 725 (1998).

[15] J. N. Reimers and J. R. Dahn, *J. Electrochem. Soc.*, **140**, 2752 (1993).

[16] H. Wang, Y. Jang, B. Huang, D. R. Sadoway, and Y.-M. Chiang, *J. Electrochem. Soc.*, **146**, 473 (1999).

[17] J. Cho, Y. J. Kim, and B. Park, *J. Electrochem. Soc.*, **148**, A1110 (2001).

[18] M. M. Doeff, A. Anapolsky, L. Edman, T. J. Richardson, and L. C. D. Jonghe, *J. Electrochem. Soc.*, **148**, A230 (2001).

[19] A. R. Armstrong, H. Huang, R. A. Jennings, and P. G. Bruce, *J. Mater. Chem.* **8**, 255 (1998).

[20] K. West, B. Zachau-Christiansen, T. Jacobsen, and S. Atlung, *Journal of Power Sources*, **14**, 325 (1985).

[21] K. West, B. Zachau-Christiansen, and T. Jacobsen, *Electrochim. Acta*, **28**, 1829 (1983).

[22] D. W. Murphy, P. A. Christian, F. J. Disalvo, and J. N. Carides, *J. Electrochem. Soc.*, **126**, 497 (1979).

[23] D. W. Murphy, P. A. Christian, F. J. Disalvo, J. N. Carides, and J. V. Waszczak, *J. Electrochem. Soc.*, **128**, 2053 (1981).

[24] K. M. Abraham, J. L. Goldman, and M. D. Dempsey, *J. Electrochem. Soc.*, **128**, 2493 (1981).

[25] C. Lampe-Onnerud and J. O. Thomas, *J. Electrochem. Soc.*, **142**, 3648 (1995).

[26] N. C. Chaklanabish and H. S. Maiti, *Solid State Ion.*, **21**, 207 (1986).

[27] W. J. Macklin, R. J. Neat, and S. S. Sandhu, *Electrochim. Acta*, **37**, 1715 (1992).

[28] J. K. Hong, J. H. Lee, and S. M. Oh, *J. Power Sources*, **111**, 90 (2002).

[29] S. E. Cheon, C. W. Kwon, D. B. Kim, S. J. Hong, H. T. Kim, and S. W. Kim, *Electrochim. Acta*, **46**, 599 (2000).

[30] S. Ahn, Y. Kim, K. J. Kim, T. H. Kim, H. Lee, and M. H. Kim, *J. Power Sources*, **81-82**, 896 (1999).

[31] S. Mandal, J. M. Amarilla, J. Ibanez, and J. M. Rojo, *J. Electrochem. Soc.*, **148**, A24 (2001).

[32] P. P. Prosini and S. Passerini, *Europ. Polym. J.*, **37**, 65 (2001).

[33] D. H. Jang and S. M. Oh, *Electrochim. Acta*, **43**, 1023 (1998).

[34] Z. Liu, J. Y. Lee, and H. J. Lindner, *J. Power Sources*, **97-98**, 361 (2001).

[35] C. A. Frysz, X. Shui, and D. D. L. Chung, *J. Power Sources*, **58**, 41 (1996).

[36] L. Fransson, T. Eriksson, K. Edstrom, T. Gustafsson, and J. O. Thomas, *J. Power Sources*, **101**, 1 (2001).

[37] Z. Liu, A. Yu, and J. Y. Lee, *J. Power Sources*, **74**, 228 (1998).

[38] G. Michael and H. Ferch, *Basic Characteristics of Aerosil*, Degussa Technical Bulletin Pigment No. 11, (1998).

[39] H. Barthel, L. Rosch, and J. Weis, in: J. Weis (Ed.), *Organosilicon Chemistry II. from molecules to materials*, VCH, Weinheim, p. 761, 1996.

[40] M. Winter, P. Novak, and A. Monnier, *J. Electrochem. Soc.*, **145**, 428 (1998).

[41] H. J. Walls, J. Zhou, J. A. Yerian, P. S. Fedkiw, S. A. Khan, M. K. Stowe, and G. L. Baker, *J. Power Sources*, **89**, 156 (2000).

[42] H. J. Walls, P. S. Fedkiw, S. A. Khan, and J. T. A. Zawodzinski, *J. Electrochem. Soc.*, (submitted, 2002).

[43] M. M. Doeff (private communication, 2001).

[44] J. Newman, *Improved electrochemical models*. 2002: BATT review meeting.

[45] G. B. Appetecchi, F. Alessandrini, M. Carewska, T. Caruso, P. P. Prosini, S. Scaccia, and S. Passerini, *J. Power Sources*, **97-98**, 790 (2001).

[46] X. Jing, W. Zhao, and L. Lan, *J. Mater. Sci. Let.*, **19**, 377 (2000).

[47] M. Narkis, G. Lidor, A. Vaxman, and L. Zuri, *J. Electrostat.*, **47**, 201 (1999).

[48] X. Wang, E. Yasukawa, and S. Mori, *Electrochim. Acta*, **45**, 2677 (2000).

[49] J. W. Braithwaite, A. Gonzales, G. Nagasubramanian, S. J. Lucero, D. E. Peebles, J. A. Ohlhausen, and W. R. Cieslak, *J. Electrochem. Soc.*, **146**, 448 (1999).

[50] S. S. Zhang and T. R. Jow, *J. Power Sources*, **109**, 458 (2002).

[51] K. Kanamura, T. Umegaki, S. Shiraishi, M. Ohashi, and Z.-i. Takehara, *Journal of the Electrochemical Society*, **149**, A185 (2002).

[52] Y. Chen, T. M. Devine, J. W. Evans, O. R. Monteiro, and I. G. Brown, *J. Electrochem. Soc.*, **146**, 1310 (1999).

[53] M. Simoneau, A. Belanger, Y. Choquette, B. Kapfer, K. Zaghib, and M. Gauthier, *Electrochem. Soc. Proceed.*, **98-15**, 417 (1998).

[54] Y. Chen, T. M. Devine, and J. M. Evans, *Electrochem. Soc. Proceed.*, **96-17**, 187 (1996).

Table 6. 1. Cathode Compositions and Carbon Properties

Carbon Name	Carbon Type	Manufacturer	Particle Size (μm)	BET Surface Area (m^2/g)	Cathode Composition
Timrex® SFG 15	Graphite	Timcal, Ltd.	15	8.5	**4V**: 91% $LiCoO_2$ 6% SFG 15 3% PVDF **3V**: 75% V_6O_{13} 20% SFG 15 5% PVDF
Timrex® SFG 44	Graphite	Timcal, Ltd.	44	4.3	**4V**: 91% $LiCoO_2$ 6% SFG 44 3% PVDF
Ketjenblack EC-600JD	Carbon Black	Akzo Nobel, Inc.	0.03-0.1	1250	**4V**: 92% $LiCoO_2$ 3% KJB 5% PVDF
Vulcan XC72R	Carbon Black	Cabot Corp.	0.03	254	**4V**: 94% $LiCoO_2$ 3% Vulcan 3% PVDF
Timrex® KS6	Graphite	Timcal, Ltd.	6	19.4	**3V**: 84% Li_xMnO_2 4% KS6 + 4% KJB 8% PVDF

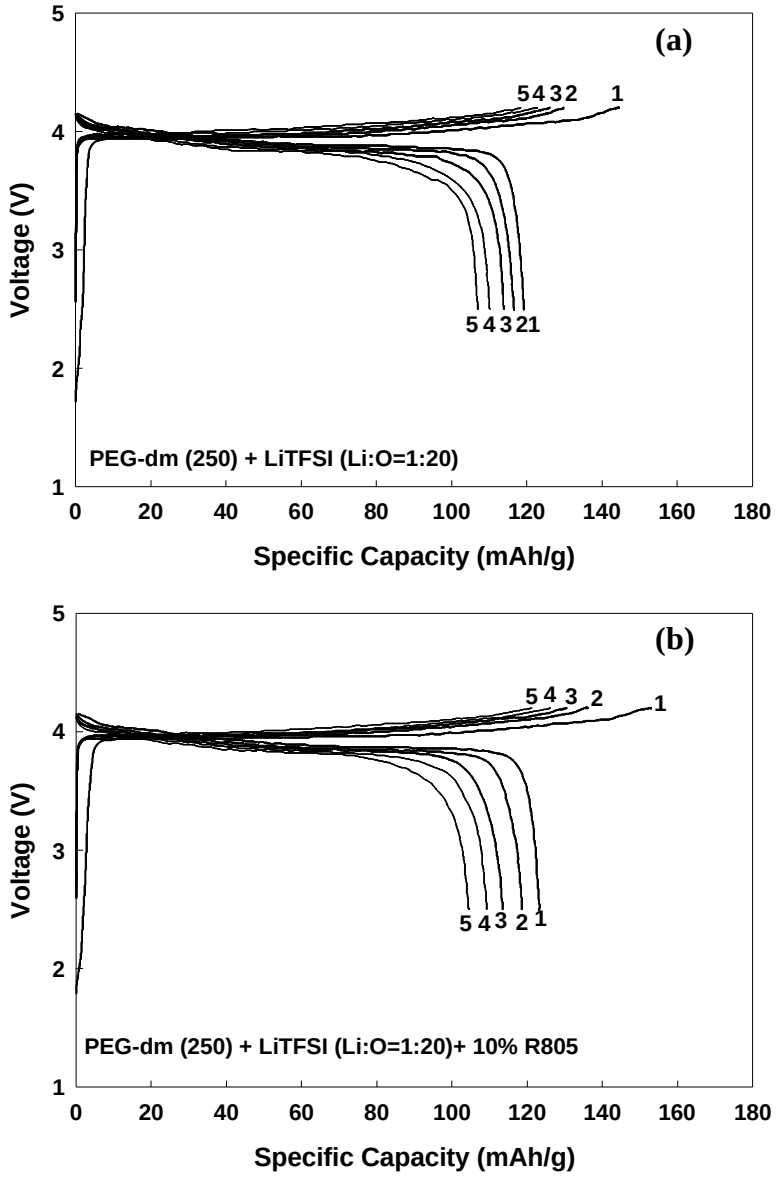

Figure 6. 1. Typical charge/discharge voltage profiles of Li/$LiCoO_2$ cells at C/40 (0.11 mA/cm^2): (a) baseline liquid electrolyte [PEG-dm (250) + LiTFSI (Li:O=1:20)], and (b) baseline electrolyte + 10 wt% R805. The composition of $LiCoO_2$ cathode is 91 wt% $LiCoO_2$ + 6 wt% graphite SFG 15 + 3 wt% PVDF with an Al current collector.

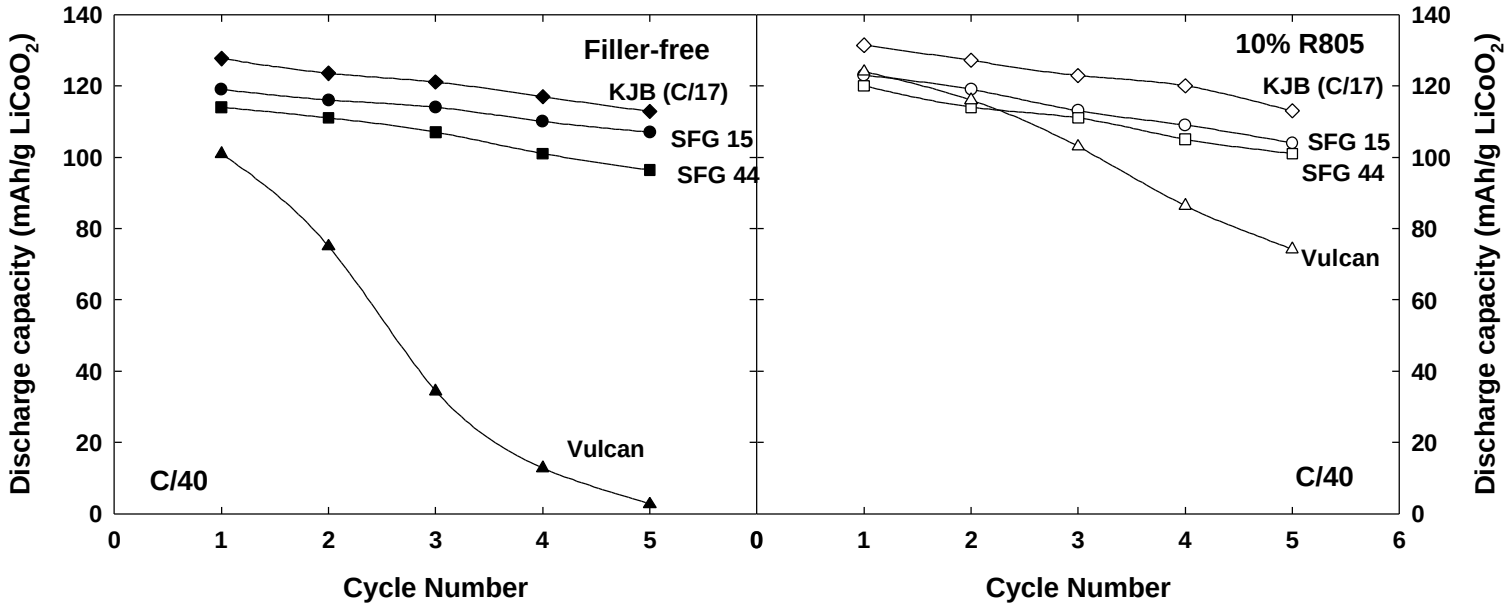

Figure 6. 2. Discharge capacity of Li/$LiCoO_2$ cells with baseline liquid electrolyte [PEG-dm (250) + LiTFSI (Li:O=1:20)] (left), and baseline liquid electrolyte + 10 wt% R805 (right) using different carbon types: graphite Timrex® SFG 15, graphite Timrex® SFG 44, carbon black Cabot Vulcan XC72R, and carbon black Ketjenblack (KJB) EC-600JD.

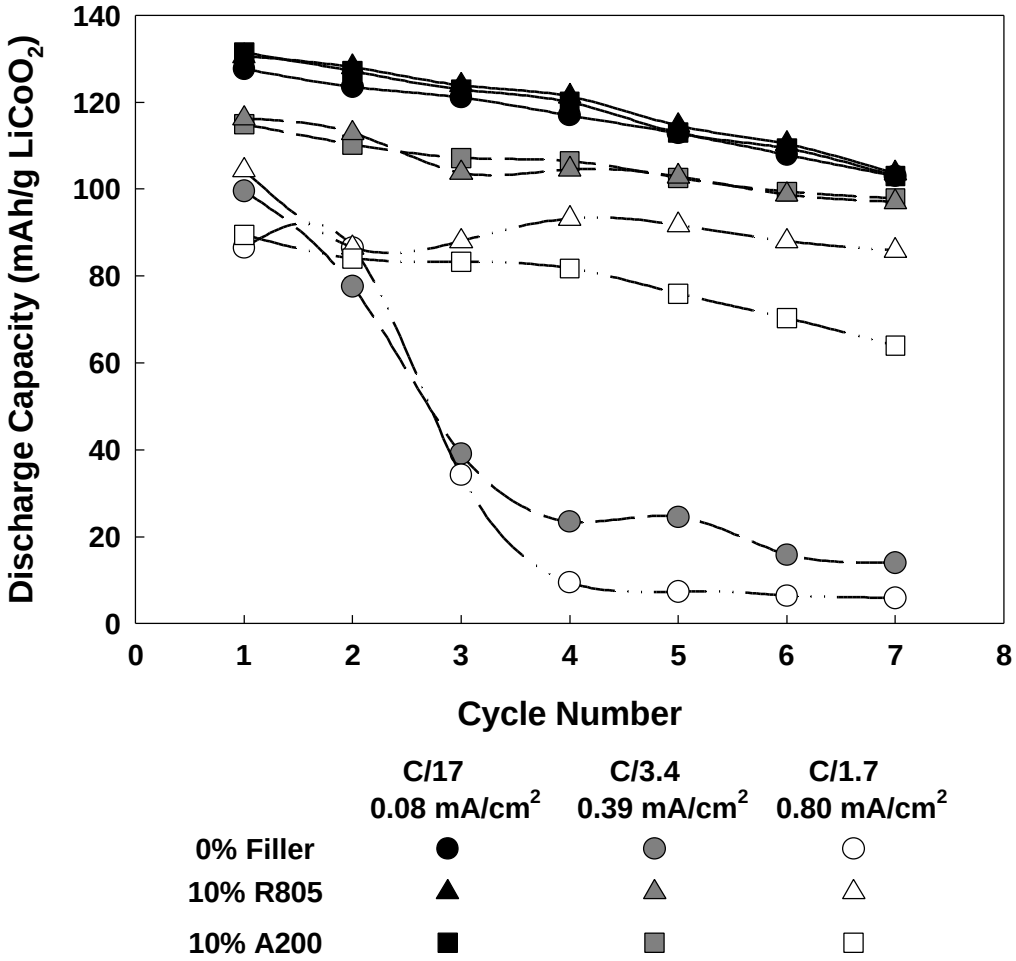

Figure 6. 3. Discharge capacity of Li/$LiCoO_2$ cells with a cathode composition of 92% $LiCoO_2$ + 3% Ketjenblack EC-600 JD + 5% PVDF. The electrolytes are: baseline liquid PEG-dm (250) + LiTFSI (Li:O=1:20); baseline + 10 wt% R805; and baseline + 10 wt% A200. The cathode current collector is Al.

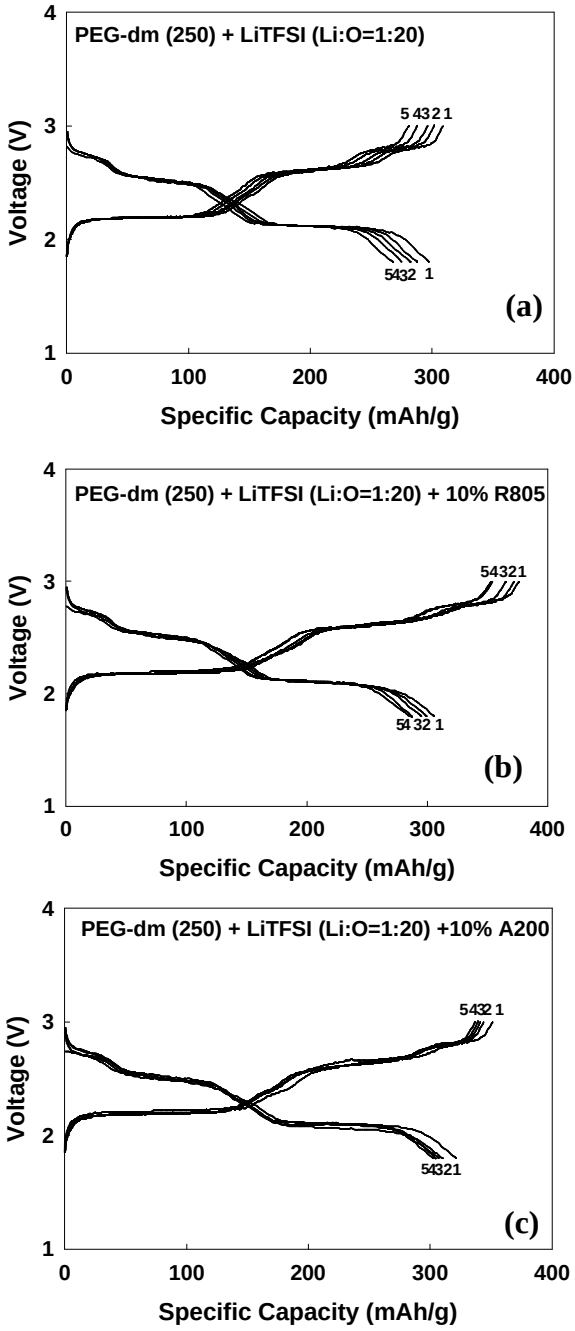

Figure 6. 4. Typical charge/discharge voltage profiles of Li/V_6O_{13} cells at C/55 (0.08 mA/cm^2) with: (a) baseline liquid electrolyte PEG-dm (250) + LiTFSI (Li:O=1:20); (b) baseline electrolyte + 10 wt% R805; and, (c) baseline electrolyte + 10 wt% A200 electrolytes. The V_6O_{13} cathode composition is 75 wt% V_6O_{13} + 20 wt% graphite SFG 15 + 5 wt% PVDF with a carbon fiber current collector.

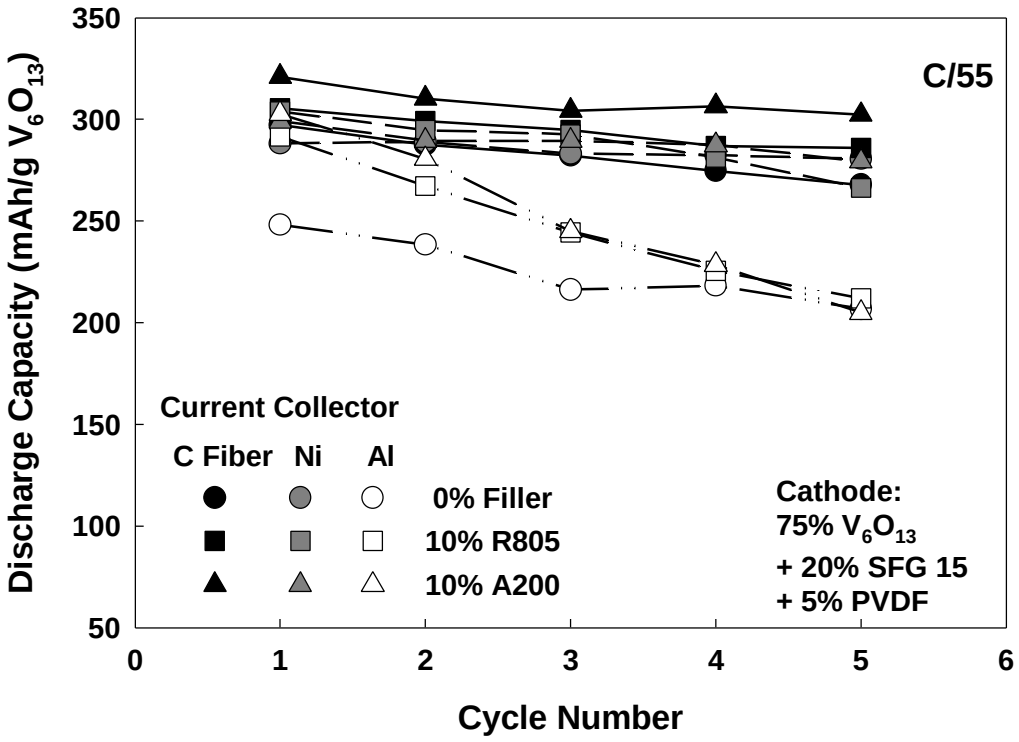

Figure 6. 5. Effect of cathode current collector material on discharge capacity of Li/V_6O_{13} cells. The current collector materials are carbon fiber, Ni, and Al. The electrolytes are baseline liquid electrolyte PEG-dm (250) + LiTFSI (Li:O=1:20), baseline electrolyte + 10 wt% R805, and baseline electrolyte + 10 wt% A200.

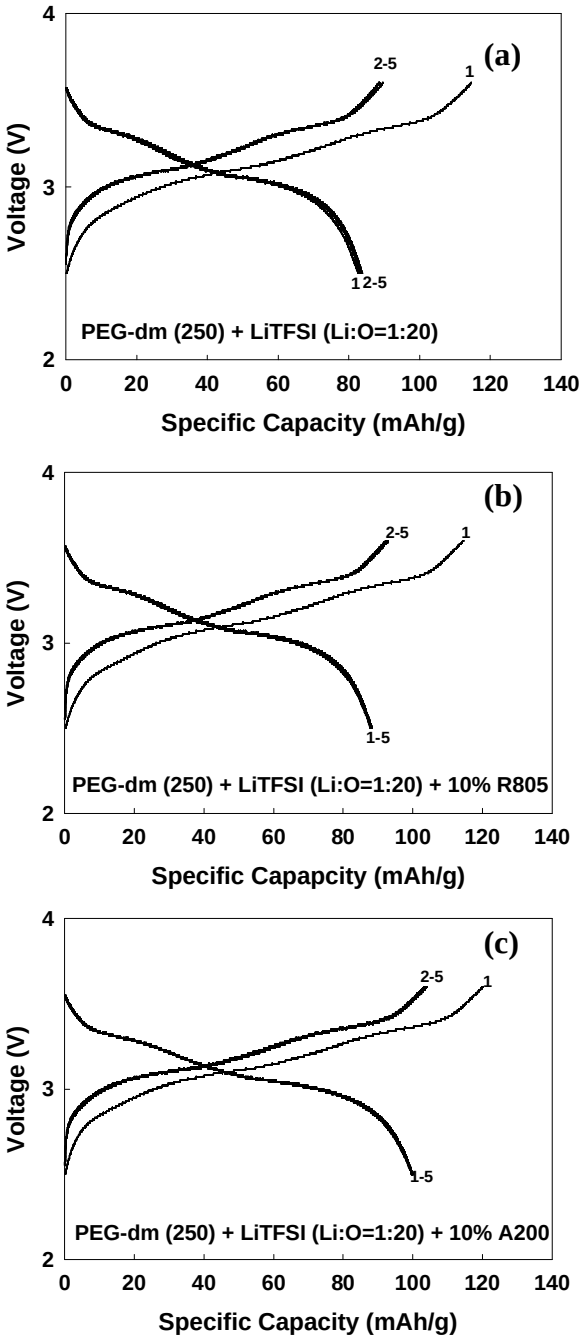

Figure 6. 6. Typical charge/discharge voltage profiles of Li/Li_xMnO_2 cells at C/10 (0.05 mA/cm^2) with different electrolytes: (a) baseline liquid electrolyte PEG-dm (250) + LiTFSI (Li:O=1:20); (b) baseline electrolyte + 10 wt% R805; and, (c) baseline electrolyte + 10 wt% A200. The Li_xMnO_2 cathode composition is 84 wt% Li_xMnO_2 + 4 wt% graphite KS6 + 4 wt% Ketjenblack EC-600JD + 8 wt% PVDF with an Al current collector.

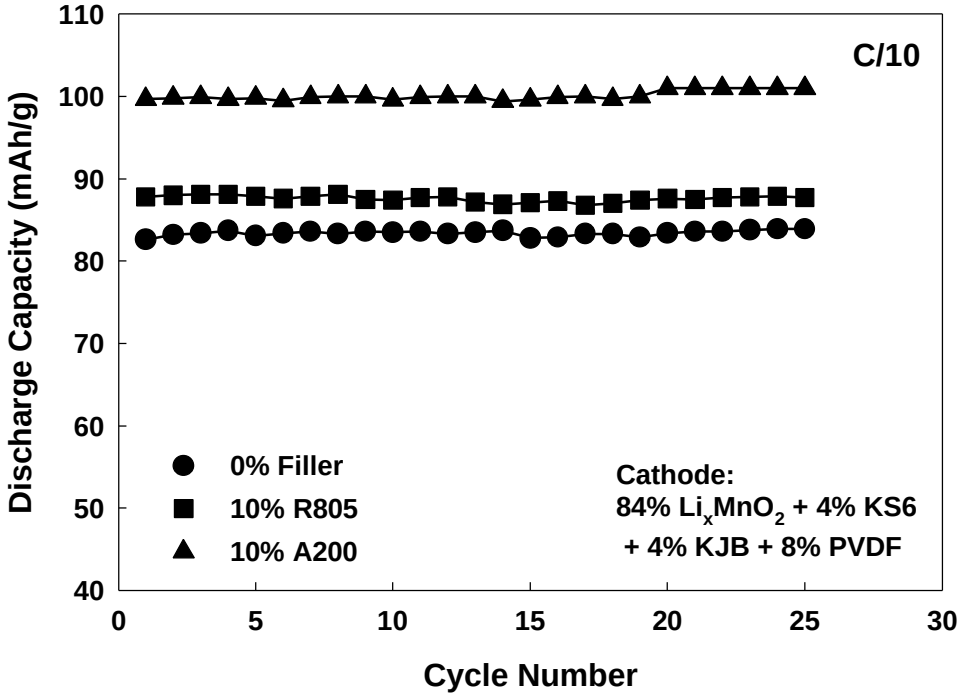

Figure 6. 7. Discharge capacity of Li/Li_xMnO_2 cells using Al current collector at C/10 with different electrolytes: baseline liquid electrolyte PEG-dm (250) + LiTFSI (Li:O=1:20); baseline electrolyte + 10% R805; and, baseline electrolyte + 10% A200 with an Al current collector.

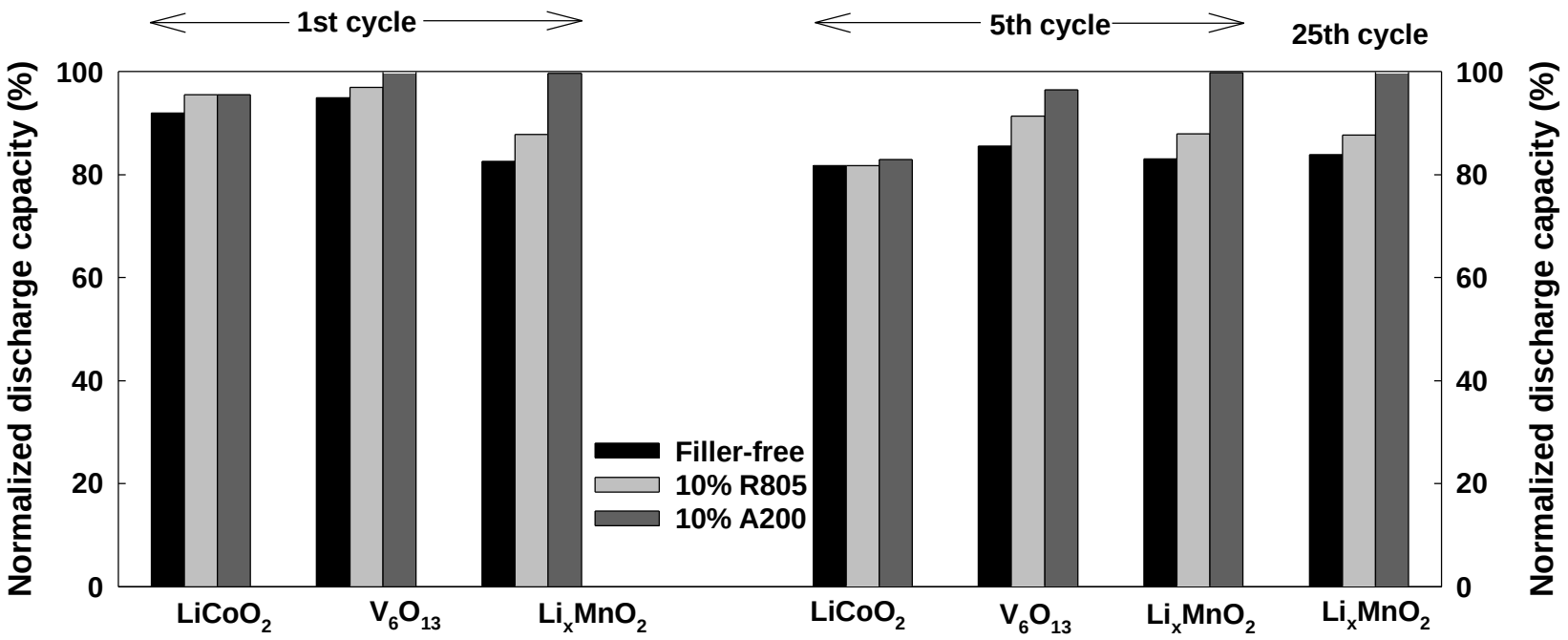

Figure 6. 8. Normalized discharge capacities based on practical capacity of lithium cells with various cathode materials for 1st, 5th, and 25th cycles: $LiCoO_2$ cathode composition, 92% $LiCoO_2$ + 3% Ketjenblack EC-600 JD + 5% PVDF with a practical capacity of 137 mAh/g; V_6O_{13} cathode composition, 75% V_6O_{13} + 20% graphite SFG 15 + 5% PVDF with a practical capacity of 313 mAh/g; and, Li_xMnO_2 cathode composition, 84% Li_xMnO_2 + 4% graphite KS6 + 4% Ketjenblack EC-600 JD + 8% PVDF with a practical capacity for PEO systems of 100 mAh/g [18].

Chapter 7: Rheological Behavior of Fumed Oxide-Based Composite Electrolytes

Jian Zhou, Peter S. Fedkiw, and Saad A. Khan

Department of Chemical Engineering

North Carolina State University

Raleigh, NC 27695-7905

December 10, 2002

Abstract

Effects of filler type and oligomer molecular weight on rheological properties of fumed oxide-based composite electrolytes are studied using lithium bis(trifluromethylsulfonyl)imide [$LiN(CF_3SO_2)_2$] (LiTFSI) solutions in methyl-ended poly(ethylene oxide) (PEO) oligomers as the baseline material. Fumed oxides under study include fumed silica, alumina, titiania, and binary fumed silica and alumina mixtures, all with surface hydroxyl groups. Oligomer molecular weight (M_w) varies from 250 to 2000. Addition of fumed oxides increases electrolyte viscosity for all oligomer M_ws at all concentrations examined and the extent of enhancement varies with filler type. In general, fumed silica shows the largest thickening effect while fumed titania shows the least; composite electrolytes containing fumed silica are gels and those containing titania are suspensions at concentrations range from 5 to 20 wt%. However, there is a liquid (suspension) to solid (gel) transition of composite electrolytes containing fumed alumina and binary fumed silica and alumina mixtures between 5 to 10 wt% in PEG-dm (250) + LiTFSI (Li:O=1:20) at 25°C. Elastic modulus, yield stress, and normalized viscosity of gel-type composite electrolytes containing fumed silica and binary fumed silica and alumina mixtures decrease with increasing oligomer M_w at 60°C (above the melting point of electrolyte). The reduction in structure strength might be ascribed to the enhanced interactions between surface hydroxyl groups on fumed oxides and polyether oxygens. Thus, the number of accessible –OH groups is reduced for interactions among fumed oxide particles, which dictates the strength of solid-like structure.

7.1. Introduction

Rechargeable lithium batteries with high-specific energies are promising power sources required for modern portable electronic products and electrical cars since lithium is the lightest metal (equivalent weight = 6.94 g/mol, and specific gravity = 0.53 g/cm^3) and has the most negative redox potential (Li/Li^+ couple is –3.04 V vs. standard hydrogen electrode, SHE) [1]. In addition, the small size of lithium cation allows a range of intercalation cathode materials, which gives some design freedom of storage systems to suit different applications [2]. However, the reactivity of lithium metal greatly limits the choice of usable electrolytes and impedes the commercialization of secondary lithium metal batteries. Since liquid electrolytes significantly decrease lithium battery lifetime and safety, solid and solid-like electrolytes appear more suitable for high-capacity lithium batteries [2]. Among all solid and solid-like electrolytes, composite electrolytes with promising electrochemical properties (e.g., conductivity, interfacial stability, and ionic transport properties) and mechanical properties (e.g., viscous and elastic moduli, yield stress) are viable in secondary lithium battery applications [3-8]. High room-temperature conductivity (e.g., > 10^{-3} S/cm) and good mechanical strength (e.g., elastic modulus $G' > 10^5$ Pa for benchmark material) are required for electrolyte materials in ambient or sub-ambient applications. Fumed oxide-based composite electrolytes combine high room-temperature conductivity of lithium salt-solutions in low-molecular weight (M_w) poly(ethylene oxide) (PEO) with good mechanical strength provided by thickening agents, fumed oxides. Conductivity of this type of composite electrolytes is reported elsewhere [9].

In this present work, the rheological properties are reported of composite electrolytes based on methyl-terminated oligo(ethylene oxide) with a M_w range from 250 to 2000 and a variety of fumed oxide fillers (e.g., SiO_2, Al_2O_3, TiO_2, and SiO_2/Al_2O_3). Oligomers are liquids at 250 and 500 M_w and wax-like solids at 1000 and 2000 M_w at room temperature. The effects of filler type and oligomer M_w are studied by steady state and dynamic rheology measurements.

Five types of fumed oxides commercially available from Degussa Corp. are employed in this study: (I) fumed silica: Aerosil® 200; (II) fumed alumina: Aluminum Oxide C; (III) fumed titania: hydrophilic P25; (IV) fumed silica and alumina mixture COK 84 with 84% A200 and 16% Al_2O_3 C; and (V) mixed fumed oxide MOX 170 consisting of 99% SiO_2 doped with 1% Al_2O_3. All fumed oxides are hereafter designated with Degussa's nomenclature. Fumed oxides including fumed silica, alumina, and titania are synthesized by high-temperature hydrolysis of the corresponding gaseous metal chlorides ($SiCl_4$, $AlCl_3$, and $TiCl_4$) in an O_2/H_2 flame [10,11]. Due to the pyrogenic synthesis method, all fumed oxides possess unique properties: high-chemical purity (e.g., fumed silica >99.8%, fumed alumina >99.6%, and fumed titania > 99.5% for Degussa products) [10,11], nanoscale spherical primary particles (5-50 nm) [12], large specific surface area (up to 600 m^2/g) [12], and nonporous structure [10,11]. The predominant particle structures are branch-like aggregates (100-500 nm, apparent density is about 30% of SiO_2, Al_2O_3, or TiO_2), which cannot be disrupted by shear and consist of partially fused primary particles (~10 nm) [12-15]. Agglomerates (> 1 μm) with a significant fractality (mass fractal dimension of ≈2.1) can be formed as a result of dipole-dipole

forces, hydrogen-bonding (H-bonding), and other non-specific forces between aggregates but can be disturbed by simple mixing [12,14,15]. Another important property of native fumed oxides is that they are hydrophilic due to surface hydroxyl groups, which determine many of physicochemical properties of these materials [12]. Although fumed silicas are amorphous, fumed alumina and titania are crystalline. Aluminum Oxide C crystallographically belongs to the δ-group based on X-ray diffraction (XRD) data. Degussa's P25 TiO_2 is a mixture of 70 wt% anatase and 30 wt% rutile. The crystalline mixture results from high temperature and short residence time in the hot zone during synthesis [16]. There are equimolar amounts of acidic and basic hydroxyl groups on the surface of TiO_2; one half of these hydroxyl groups reacts acidically, and accumulates ammonia or is esterified with diazomethane, while the other half has a basic character and can be interchanged with certain anions [17,18]. The coexistence of equimolar amounts of acidic and basic hydroxyl groups is also evident from the zeta potential, which at an almost neutral pH about 6.5 [10]. In addition to individual fumed oxides, binary and ternary fumed oxides with various compositions synthesized by high-temperature hydrolysis of the corresponding metal chloride mixtures are also widely used as pigments, fillers, additives, adsorbents, catalysts, and catalyst supports [11,12,19]. The Brønsted (B) acid sites of $-\overset{|}{\underset{|}{M_{(1)}}}-O(H)-\overset{|}{\underset{|}{M_{(2)}}}$ ($M_{(1)}$, $M_{(2)}$=Al, Si, Ti, etc.) in mixed fumed oxides play an important role in particle-medium and particle-particle interactions, which significantly differ from those in individual fumed oxide systems. The physicochemical properties of mixed fumed oxides can also be manipulated by varying

the compositions of metal chloride mixtures during the synthesis [12,20]. There are two types of dual fumed oxide systems: (1) a simple mixture of two types of fumed oxides and (2) mixed fumed oxides generated by flame hydrolysis of the corresponding metal chloride mixture. Aerosil® COK 84 belongs to the first category and MOX 170 belongs to the second.

7.2. Experimental

7.2.1 Preparation of Composite Electrolytes

The composite electrolytes consist of three materials: lithium bis(trifluromethylsulfonyl)imide [$LiN(CF_3SO_2)_2$] (LiTFSI, 3M), fumed oxide (Degussa), and poly(ethylene glycol) dimethyl ether (PEG-dm, M_w=250 to 2000 Aldrich). For low-M_w (250 and 500) oligomers, the inhibitor [butylated hydroxytoluene (BHT), 100 ppm] was first removed using an inhibitor-removing column (Aldrich). The PEG-dm was then dried over 4Å molecular sieves for at least two weeks prior to use. Medium-M_w (1000 and 2000) oligomers were melted and dried over 4Å molecular sieves in a sealed container at 80°C for at least a month before being transferred to the argon-filled glove box. The lithium salt, LiTFSI, was dried at 110°C under vacuum for 24 hours before use. Water content of lithium salt and oligomer was controlled under 20 ppm, as determined by Karl-Fisher titration. Fumed oxides were dried at 120°C under vacuum for 3-4 days to achieve a water content of 150-200 ppm before being transferred to an argon-filled glove box.

Composite electrolytes were prepared in an argon-filled glove box. First, a baseline electrolyte was made by dissolving LiTFSI in a PEG-dm oligomer liquid (room-temperature) or melt (~ 80°C for M_w =1000 and 2000) with a fixed ratio of Li:O (1:20) to maintain high conductivity [4]. The appropriate weight of fumed oxide was then added to the baseline electrolyte and dispersed by use of a high-shear mixer (Tissue Tearor^{TM}, Model 398, BioSpec Products, Inc.) [21]. After preparation, the electrolytes based on PEG-dm (M_w=1000 and 2000), with and without fillers, are solids at room temperature. The baseline electrolytes based on low-M_w PEG-dm (M_w=250 and 500) are liquids, while the corresponding composite electrolytes are solid-like gels except for TiO_2 composites, which are suspensions. Water content of the baseline electrolyte and composite electrolytes was under 20 and 50 ppm, respectively.

7.2.2 Methods and Measurements

Rheological measurements were conducted using a Rheometrics Dynamic Stress Rheometer (DSR II) (Rheometric Scientific). Cone and plate or serrated parallel plate geometries of 25 mm diameter were used for the measurements. Cone and plate thickness was set at 0.05 mm, while that for the serrated plates was 1 mm. Test geometry temperature was maintained with a Polyscience recirculating bath (50:50 mix of water and ethylene glycol) that is an integral part of the DSR II setup. All measurements were performed at 60°C (above the melting point of electrolytes) with cone and plate and room temperature (approximately 25°C) with serrated parallel plate geometry. Electrolyte samples were allowed to sit overnight in the glove box and stored in a desiccator prior to

rheological measurement to minimize water absorbance. Samples were loaded on the lower rhoemeter plate. The top rheometer plate or cone was lowered to a separation of 0.02 mm more than the final gap, excess sample was removed from the edges of the geometries using a spatula, and the top plate or cone was lowered to a the final separation of 1.00 mm or 0.05 mm. Samples remained in the rheomter for a period of five minutes before measurements.

Dynamic stress sweeps were used to determine the linear viscoelastic regime (LVE) of each sample (with a frequency of 1 rad/s) and were stopped prior to exceeding the sample yield stress. Dynamic frequency sweeps with constant stress were employed to examine the elastic (G′) and viscous (G″) moduli in the LVE regime. The relative magnitude and shapes of G′ and G″ curves indicate the type and extent of microstructure of samples [22]. Dynamic stress sweeps were run again to determine the dynamic yield stress (τ_y) for each sample. Another load of sample is used to run steady-state stress sweeps to determine apparent viscosities of samples.

7.3. Results and Discussion

7.3.1 Effect of Filler Type

At room temperature (approximately 25°C), composite electrolytes containing 5 wt% of fillers with surface hydroxyl groups are suspensions (liquids) in PEG-dm (250) + LiTFSI (Li:O=1:20) except fumed silica-based electrolyte, which is a gel with solid-like structures. Solid-like structures form upon addition of 10 wt% of fumed oxides with surface hydroxyl groups except fumed titania, in which case the surface interactions

among fillers are too weak even at 20 wt% and fumed titania-based electrolytes are suspensions at all concentrations examined.

7.3.1.1 Apparent Viscosity

Figure 7.1 presents the normalized viscosity [η_0=19 cP [23] for filler-free electrolyte, PEG-dm (250) + LiTFSI (Li:O=1:20)] of composite electrolytes containing 5 wt% fillers, all with surface hydroxyl groups, as a function of shear rate. All electrolytes show shear-thinning behavior, which is a preferable property for material processing. Addition of fumed oxides increases electrolyte viscosity (i.e., $h/h_0 > 1$) and the extent of thickening effect varies with filler type in the order of TiO_2 < Al_2O_3 < MOX 170 < COK 84 < A200.

7.3.1.2 Dynamic Moduli

Figure 7.2 shows elastic (G′) and viscous (G″) moduli of composite electrolytes containing 5 to 20 wt% COK 84, the mixture of 84% SiO_2 and 16% Al_2O_3 in PEG-dm (250) + LiTFSI (Li:O=1:20). From Figure 7.2, we see that G″ is higher than G′ for 5% composite electrolyte indicating a liquid-like (suspension) structure of the electrolyte. However, for 10% composite electrolyte G′ is higher than G″ and both G′ and G″ are independent of frequency indicating a solid-like (gel) structure of the electrolyte. For the clarity purpose, G″ of composite electrolytes containing 15 and 20 wt% is not shown but both electrolytes behave like gels as 10% composite electrolyte. Elastic (G′) modulus

increases with increasing filler content implying an increase in strength of solid-like structure. Figure 7.3 summarizes the effect of filler content on mechanical strength of composite electrolytes containing fumed oxide fillers with surface hydroxyl groups. Composite electrolytes containing fumed alumina and 1% Al_2O_3 doped SiO_2 (MOX 170) fillers show similar behavior as those containing COK 84: the electrolyte is a suspension (liquid-like) at 5% but forms gel (solid-like) at concentrations above 10%. Fumed silica-based composite electrolytes are gels and fumed titania-based electrolytes are suspensions at all concentrations (5 to 20 wt%) examined.

7.3.2 Effect of PEO Oligomer MolecularWeight (M_w)

7.3.2.1 Apparent Viscosity

Because of the limitation of the rheometer, solid composite electrolytes based PEG-dm (2000) + LiTFSI (Li:O=1:20) are too rigid to be tested at 25°C. Hence, all composite electrolytes were measured at the melt state (60°C) for comparison. The steady-state stress sweep data shows that filler-free electrolytes behave like Newtonian fluid (constant viscosity independent of shear rate) while composite electrolytes have shear-thinning behavior (viscosity decreases with increasing shear rate). Apparent viscosity of composite electrolytes at the shear rate of 1 s^{-1} is normalized to that of baseline liquid electrolyte (η_0 = 3.8, 14.5, 35.0, 100.0 cP for filler-free electrolyte based on PEO oligomers with M_w = 250, 500, 1000, and 2000, respectively) and plotted as a function of oligomer M_w in Figure 7.4. Fillers examined are A200 (SiO_2), Al_2O_3, TiO_2, COK 84 (84% SiO_2 + 16% Al_2O_3), and MOX 170 (1% Al_2O_3 doped SiO_2), all at 10 wt%

and with surface hydroxyl groups. In general, the thickening effect of fillers decreases with increasing PEO oligomer M_w except TiO_2, in which case η/η_0 practically stays constant. Increase in oligomer M_w (i.e., chain length) leads to a reduction in polymer chain flexibility, thus resulting in an increae in viscosity of filler-free electrolyte. Assuming that when oligomers are amorphous, their M_w does not affect surface interactions among fumed oxides, whose relative contribution to electrolyte viscosity decreases with increasing viscosity of the baseline material. Composite electrolytes containing 10 wt% fumed silica (A200) and binary fumed silica and alumina mixtures (COK 84 and MOX 170) are gels at 60°C at all M_w. No solid-like structure was formed upon addition of TiO_2 into melted baseline electrolyte at all M_w. The weaker interactions among fumed TiO_2 particles than other fumed oxide fillers are due to its relatively larger primary particle size (22 nm vs. 12 nm) and fewer available surface groups at the same content. The difference in viscosity of solution and suspension is probably independent of oligomer M_w but proportional to filler concentration, thus leading to the constant normalized viscosity of composite electrolytes containing 10 wt% TiO_2. Different from other fillers, fumed alumina affects electrolyte viscosity differently in liquid (M_w=250 and 500) and melted (M_w = 1000 and 2000) oligomers: more than three orders of magnitude increase in viscosity for the former but only two to three times increase for the latter. It is an ongoing effort to understand the cause of such a significant difference in thickening behavior of fumed alumina. Although significant increase (up to more than five orders of magnitude) in viscosity can be achieved upon incorporation of 10 wt%

fumed oxide fillers, the decrease in conductivity due to the insulating nature of fillers is only up to 20% [9].

7.3.2.2 Dynamic Rheological Properties

Figure 7.5 presents effect of oligomer M_w on elastic (G′) modulus of gel-type composite electrolytes containing fumed silica (A200) and binary fumed silica and alumina mixtures (COK 84 and MOX 170). Increase in oligomer M_w shows decreasing or little enhancing effect in gel strength at temperatures above the melting point of polymer electrolytes. Figure 7.6a shows a typical dynamic stress sweep curve of gel-type composite electrolyte for the determination the yield stress (τ_y) by visual observation. Elastic (G′) modulus stays constant at low stress with little disturbance of the structure, and then it drops dramatically when the structure breaks down at high stress. The critical stress where the transition occurs is determined as τ_y. A more accurate way to determine τ_y is to plot the elastic stress (strain × G′) versus strain and obtain the maximum elastic stress as τ_y, shown in Figure 7.6b. Figure 7.7 illustrates the effect of oligomer M_w on yield stress of gel-type electrolytes shown in Figure 7.5. In general, yield stress decreases with increasing M_w, i.e., the force exerted to break down solid-like structure decreases with M_w indicating surface interaction among fillers weakens with increasing chain length when oligomers are amorphous. The possible reason is that Lewis acid-base interactions between surface hydroxyl groups on fumed oxides and polyether oxygens get stronger (supported by FTIR data [9]) when the polymer chain become longer due to increase in number of available oxygen sites on the chain. The surface chemistry of

fillers is transiently "modified" from hydrophilic (hydroxyl) to hydrophobic (ethylene oxide). The hydroxyl groups on filler surface are shielded by long ethylene oxide chain leading to a reduced number of accessible hydroxyl groups for the formation of three-dimensional network by fumed oxides [24]. Fumed oxide particles can act as transient crosslinking centers for polyether chains via Lewis acid-base interactions between surface hydroxyl groups and polyether oxygens. Thus, "effective" oligomer chain-length increases resulting in an increase in viscosity (or structure strength). The reduction in surface interactions among fillers weakens solid-like structure and increase in "effective" oligomer chain-length enhances the structure with increasing oligomer M_w. Elastic modulus and yield stress might increase or decrease depending on the net effect of two competing factors.

7.4. Summary

Effects of filler type and oligomer molecular weight on rheological properties of fumed oxide-based composite electrolytes are studied using LiTFSI solutions in methyl-ended poly(ethylene oxide) (PEO) oligomers as the baseline material. Fumed oxides under study include fumed silica (A200), alumina, titiania, and binary fumed silica and alumina mixtures (COK 84: 84% SiO_2 + 16% Al_2O_3 and MOX 170: 1% Al_2O_3 doped SiO_2), all with surface hydroxyl groups. Oligomer molecular weight varies from 250 to 2000. All composite electrolytes show shear-thinning behavior indicating electrolyte materials are processable. Addition of fumed oxides increases electrolyte viscosity for all oligomer M_ws at all filler concentrations examined and the extent of enhancement varies

with filler type. No solid-like structure is formed upon addition of fumed titania into baseline electrolytes due to its relatively large primary particle size of 22 nm. In addition, normalized viscosity of fumed titania-based composite electrolytes is independent of oligomer M_w. Composite electrolytes containing fumed silica A200 are gels because of strong interactions among silica particles. There is a liquid (suspension) to solid (gel) transition of composite electrolytes containing fumed alumina and binary fumed silica and alumina mixtures between 5 to 10 wt% in PEG-dm (250) + LiTFSI (Li:O=1:20) at 25°C. In general, normalized viscosity, elastic modulus, and yield stress of gel-type composite electrolytes containing fumed silica and binary fumed silica and alumina mixtures decrease with increasing oligomer M_w at 60°C (above the melting point of electrolyte). The reduction in structure strength might be ascribed to enhanced interactions between surface hydroxyl groups on fumed oxides and polyether oxygens that might reduce the number of accessible –OH groups for interactions among fumed oxide particles, which dictates the strength of solid-like structure. Composite electrolytes containing 10 wt% fumed alumina are gels with three-dimensional network in low-M_w oliogmers (M_w = 250 and 500, liquids at room temperature) but are suspension in medium-M_w oliogmers (M_w = 1000 and 2000, solids at room temperature) at 60°C.

7.5. Acknowledgements

The authors gratefully acknowledge funding from the Department of Energy, Office of Basic Energy Sciences and Office of Transportation Technologies. We also thank 3M for providing LiTFSI salt and Degussa for supplying fumed oxides.

7.6 References

[1] J.-M. Tarascon and M. Armand, *Nature*, **414**, 359 (2001).

[2] R. Arnaud, D. Benrabah, and J.-Y. Sanchez, *J. Phys. Chem.*, **100**, 10882 (1996).

[3] B. Kumar and L. G. Scanlon, *J. Power Sources*, **52**, 261 (1994).

[4] J. Fan, S. R. Raghavan, X. Y. Yu, S. A. Khan, P. S. Fedkiw, J. Hou, and G. L. Baker, *Solid State Ion.*, **111**, 117 (1998).

[5] J. Fan and P. S. Fedkiw, *J. Electrochem. Soc.*, **144**, 399 (1997).

[6] G. B. Appetecchi, S. Scaccia, and S. Passerini, *J. Electrochem. Soc.*, **147**, 4448 (2000).

[7] G. B. Appetecchi, F. Croce, L. Persi, F. Ronci, and B. Scrosati, *Electrochim. Acta*, **45**, 1481 (2000).

[8] F. Capuano, F. Croce, and B. Scrosati, *J. Electrochem. Soc.*, **138**, 1918 (1991).

[9] J. Zhou and P. S. Fedkiw, *Solid State Ion.* (*to be submitted*, 2002).

[10] M. Ettlinger, *Highly Dispersed Metallic Oxides Produced by the AEROSIL® Process*, Degussa Technical Bulletin Pigments No. 56, Akron, OH (2002).

[11] G. Michael and H. Ferch, *Basic Characteristics of AEROSlL®*, Degussa Technical Bulletin Pigment No. 11, Akron, OH (1998).

[12] V. M. Gun'ko, V. I. Zarko, V. V. Turov, R. Leboda, E. Chibowski, E. M. Pakhlov, E. V. Goncharuk, M. Marciniak, E. F. Voronin, and A. A. Chuiko, *J. Colloid Interf. Sci.*, **220**, 302 (1999).

[13] V. Khavryutchenko, A. Khavryutchenko, and H. Barthel, *Macromol. Symp.*, **169**, 1 (2001).

[14] V. Khavryutchenko, H. Barthel, and E. Nikitina, *Macromol. Symp.*, **169**, 7 (2001).

[15] H. Barthel, L. Rosch, and J. Weis, in: N. Auner, J. Weis (Ed.), *Organosilicon Chemistry II. from molecules to materials*, VCH, Weinheim, p. 761 (1996).

[16] M. Bankmann, R. Brand, B. H. Engler, and J. Ohmer, *Catal. Today*, **14**, 225 (1992).

[17] H. P. Boehm, *Discuss. Faraday Soc.*, **52**, 264 (1971).

[18] H. P. Boehm, *Angewandte chemie international edition*, **5**, 533 (1966).

[19] V. M. Gun'ko, V. I. Zarko, R. Leboda, M. Marciniak, W. Janusz, and S. Chibowski, *J. Colloid Interf. Sci.*, **230**, 396 (2000).

[20] V. M. Gun'ko, V. I. Zarko, R. Leboda, and E. Chibowski, *Adv. Colloid & Interf. Sci.*, **91**, 1 (2001).

[21] H. J. Walls, J. Zhou, J. A. Yerian, P. S. Fedkiw, S. A. Khan, M. K. Stowe, and G. L. Baker, *J. Power Sources*, **89**, 156 (2000).

[22] C. W. Macosko, *Rheology: Principles, Measurements, and Applications*, VCH publishers, Inc., New York (1994).

[23] H. J. Walls, P. S. Fedkiw, S. A. Khan, and T. A. Z. Jr., *J. Electrochem. Soc.*, (*submitted*, 2002).

[24] J. Zhou, P. S. Fedkiw, and S. A. Khan, *J. Electrochem. Soc.*, **149**, A1121 (2002).

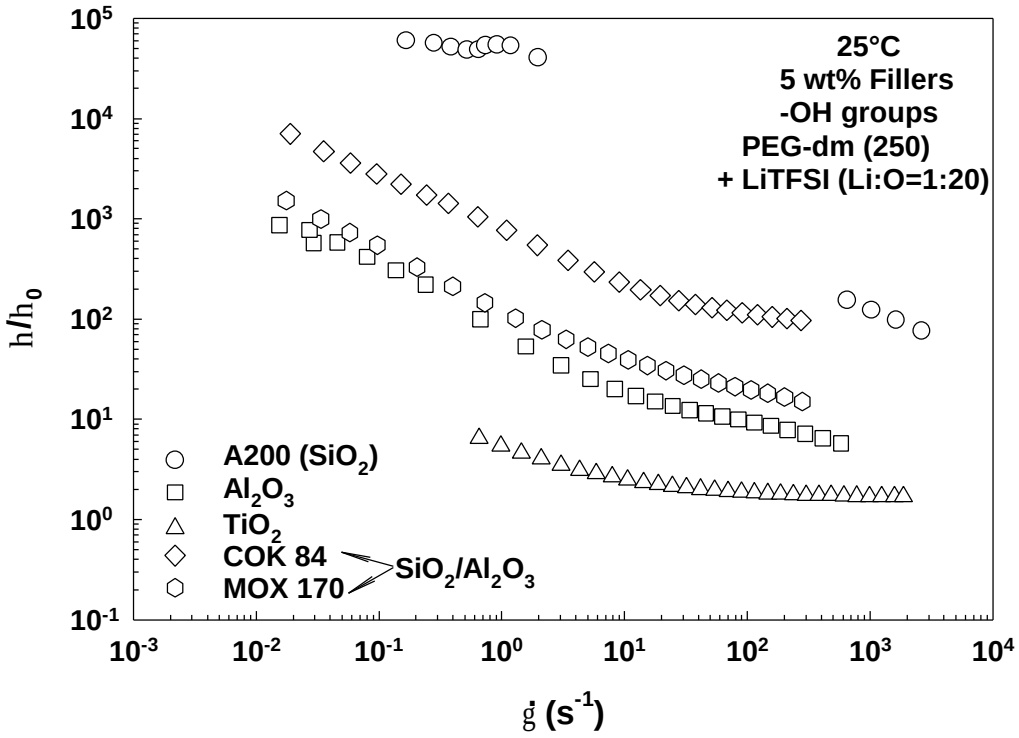

Figure 7. 1. Normalized apparent viscosity of composite electrolytes containing 5 wt% of fumed oxides, all with surface hydroxyl groups, at 25°C. The viscosity of the baseline liquid electrolyte [PEG-dm (250) + LiTFSI (Li:O=1:20) is 19 cP [23].

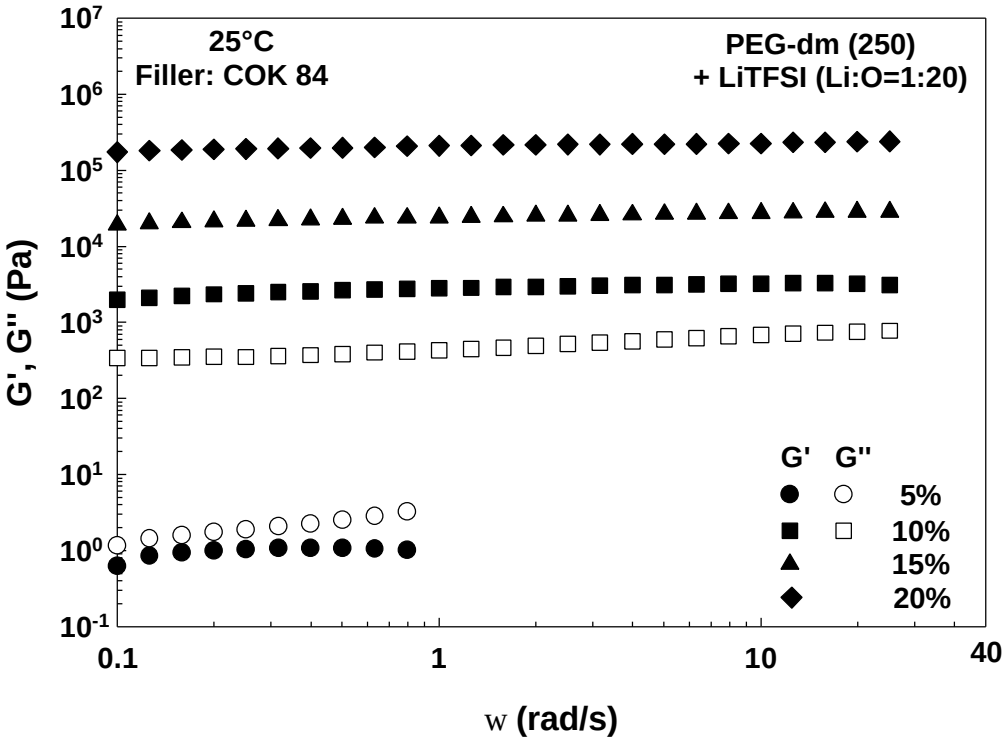

Figure 7. 2. Elastic (G′) and viscous (G″) moduli of composite electrolytes containing 5 to 20 wt% COK 84 (84% SiO_2 + 16% Al_2O_3).

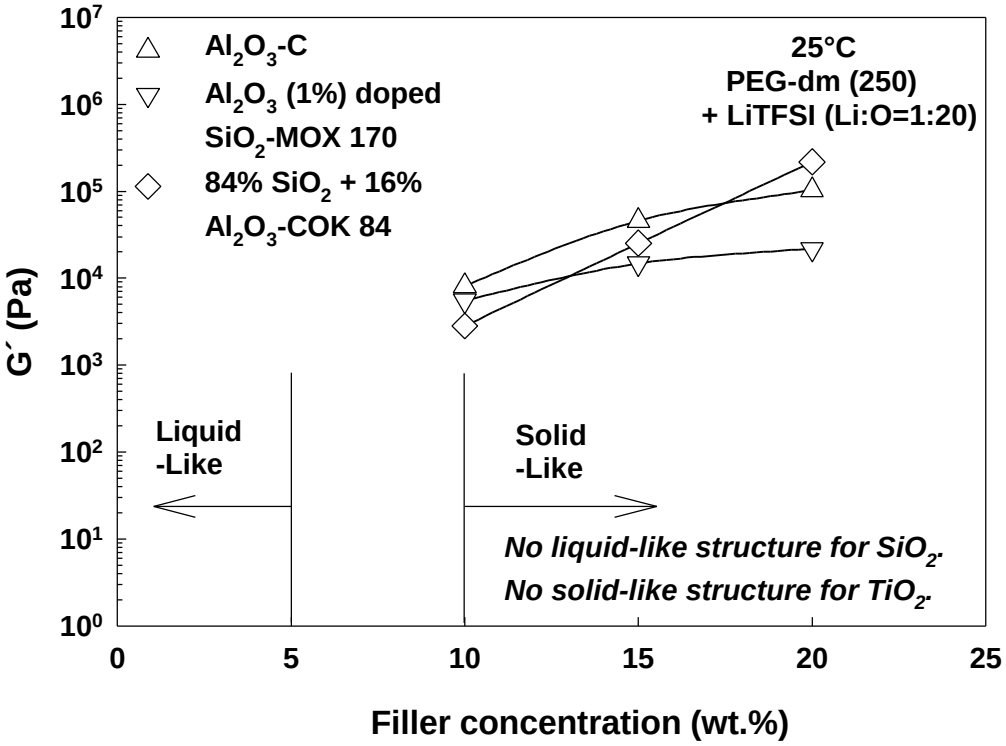

Figure 7. 3. Effect of filler content on mechanical properties of composite electrolytes with various fillers: A200 (SiO_2), Al_2O_3, P25 (TiO_2), COK 84 (84% SiO_2 + 16% Al_2O_3), and MOX 170 (1% Al_2O_3 doped SiO_2), all with surface hydroxyl groups.

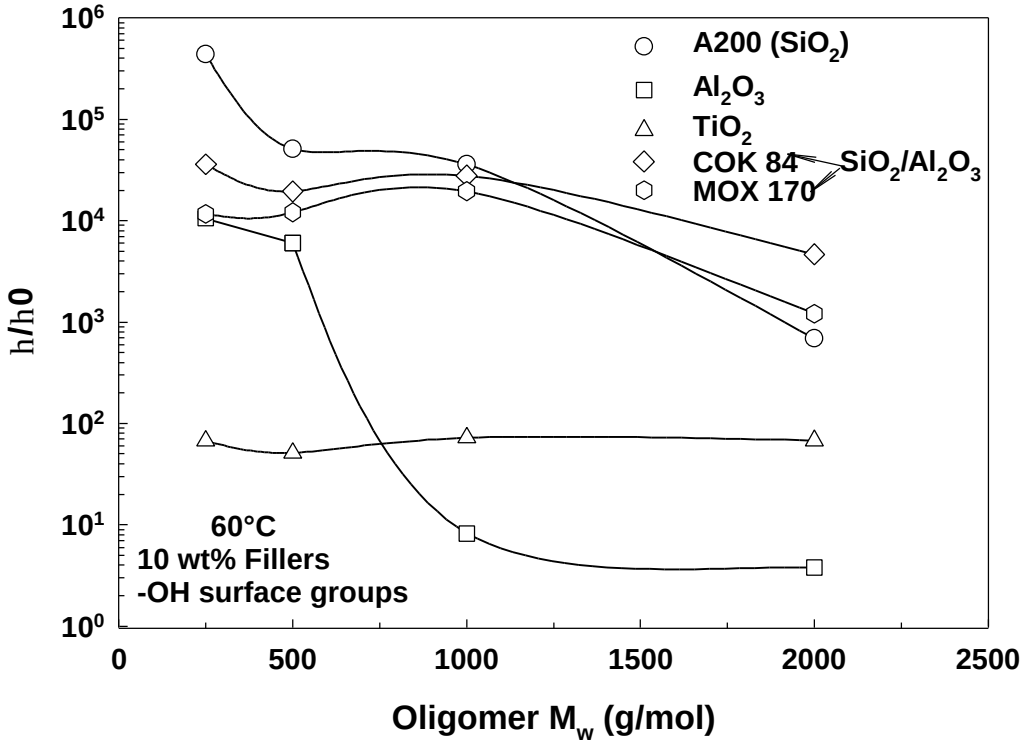

Figure 7. 4. Effect of oligomer molecular weight (from 250 to 2000 g/mol) on normalized apparent viscosity (at the shear rate of 1 s^{-1}) of melted composite electrolytes (at 60°C) containing 10 wt% fumed oxide fillers: A200 (SiO_2), Al_2O_3, TiO_2, COK 84 (84% SiO_2 + 16% Al_2O_3), and MOX 170 (1% Al_2O_3 doped SiO_2), all with surface hydroxyl groups.

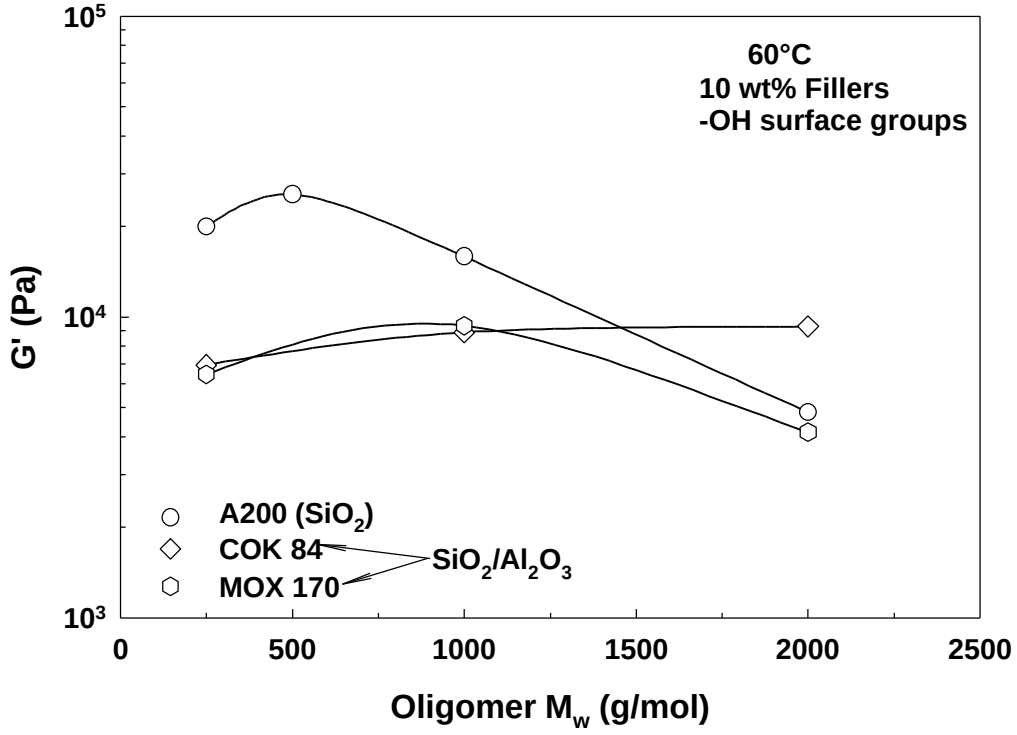

Figure 7. 5. Effect of oligomer molecular weight (from 250 to 2000 g/mol) on elastic (G′) modulus of melted composite electrolytes (at 60°C) containing 10 wt% fumed oxide fillers: A200 (SiO_2), COK 84 (84% SiO_2 + 16% Al_2O_3), and MOX 170 (1% Al_2O_3 doped SiO_2), all with surface hydroxyl groups.

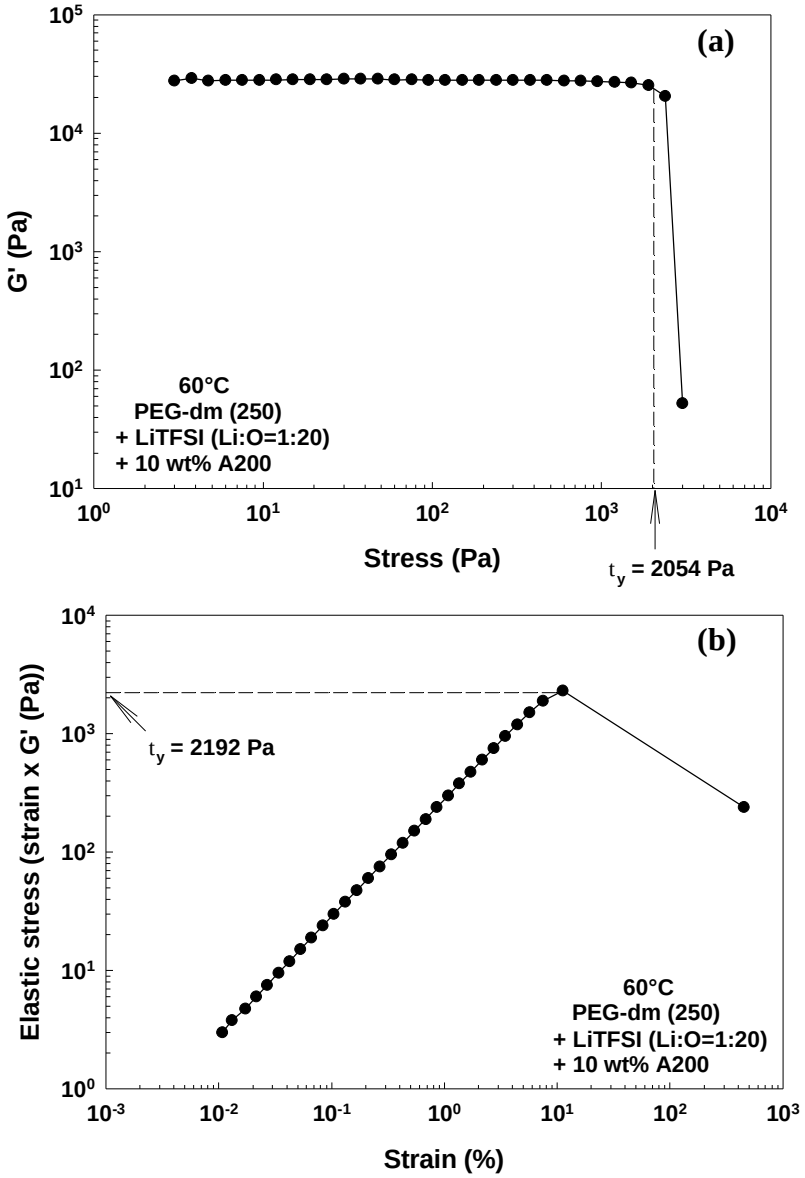

Figure 7. 6. Example of dynamic yield stress (τ_y) determination by (a) visual inspection of stress vs. G′ and (b) elastic stress method in which dynamic yield stress is the maximum elastic stress.

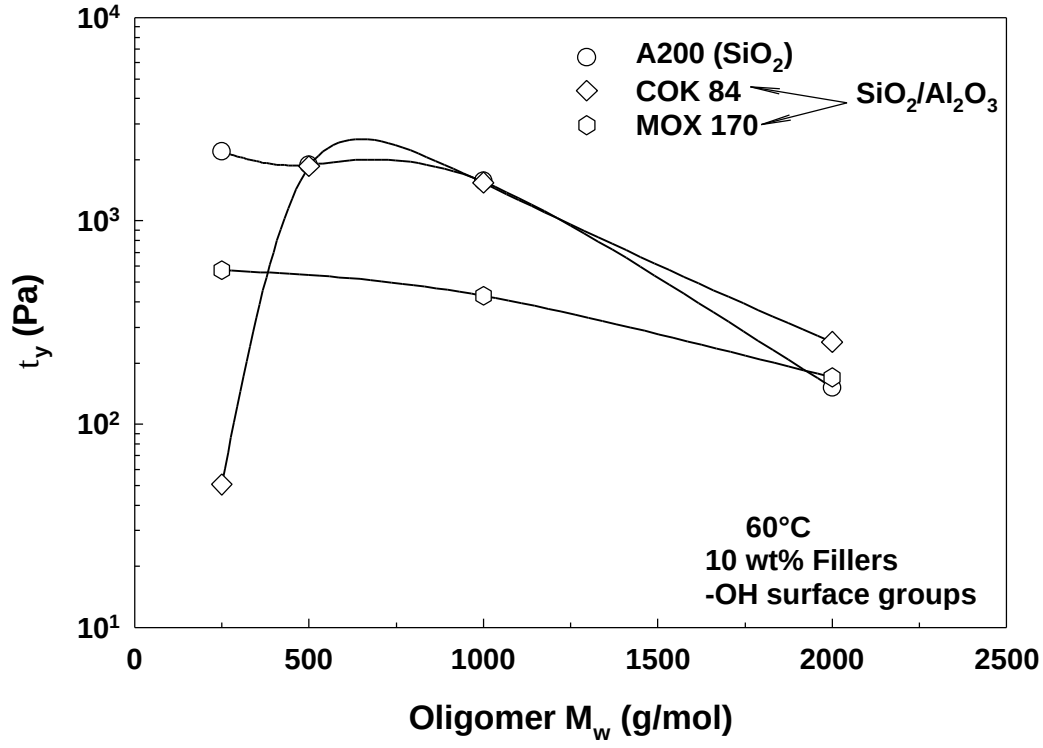

Figure 7. 7. Effect of oligomer molecular weight (from 250 to 2000 g/mol) on elastic (G′) modulus of melted composite electrolytes (at 60°C) containing 10 wt% fumed oxide fillers: A200 (SiO_2), COK 84 (84% SiO_2 + 16% Al_2O_3), and MOX 170 (1% Al_2O_3 doped SiO_2), all with surface hydroxyl groups.

Chapter 8: Conclusions and Recommendations

8.1 Conclusions

This work has demonstrated that nanocomposite polymer electrolytes based on methyl-capped poly(ethylene oxide) (PEO) oligomers using fumed oxides as thickening agents are attractive candidates for use in rechargeable lithium batteries due to their high-ionic conductivity (> 10^{-3} S/cm at 25°C for M_w =250 oligomer), good mechanical strength (elastic modulus >10^5 Pa and yield stress > 10^3 Pa for fumed silica-based composites), shearing-thinning behavior for easy processbility, and enhanced electrochemical stability with lithium. My research focused on characterizing these electrolytes in four areas: lithium-ion transport properties, rheological properties, interfacial stability between electrolyte and lithium, and suitable cathode composition for good cell performance.

8.1.1 Lithium-Ion Transport

The effects of individual fumed oxide fillers and binary mixtures of oxide fillers on ionic conductivity of composite electrolytes based on PEG-dm + LiTFSI (Li:O=1:20) are studied using EIS, DSC, and FTIR-ATR techniques. Lithium ionic conductivity increases at temperatures below the melting point (T_m) and decreases at temperatures above upon incorporation of fumed oxides into the baseline electrolytes. The addition of fillers induces an enhancement in Li^+-polymer coordination thus an increase in T_g and decrease in polymer chain flexibility. No change in number of charge carriers (free Li^+)

is observed by the IR data. The increase in conductivity at temperatures below T_m upon addition of fillers is not due to the increase in polymer chain flexibility nor the number of charge carriers. There are two pathways for Li^+ to transport in composite electrolytes: (1) Li^+ ions hop from one polymer segment to another, which is dependent on the flexibility of polymer segments, and (2) Li^+ ions are transferred along the filler surface. The ion transport by the movement of polymer segments is comparable with that occurring on the filler surface when electrolytes are amorphous (above T_m); whereas Li^+ transport on the filler surface is much faster and preferable when electrolytes are semicrystalline (below T_m). Lewis acid-base interactions between salt ions and filler surface groups generate additional sites for ion migration, thus improving ion mobility and increasing conductivity below T_m. In contrast, the insulating nature of fillers and the stiffening of polymer electrolytes upon addition of fillers cause a decrease in conductivity at temperatures above T_m. No significant effect of filler type, surface chemistry, and surface area on conductivity is expected due to the similar degree of interactions between polymer chains and filler surface groups.

8.1.2 Rheological Properties

All composite electrolytes show shear-thinning behavior indicating electrolyte materials can be easily processed. Addition of fumed oxides increases electrolyte viscosity for all oligomer M_ws and filler concentrations examined, and the extent of enhancement varies with filler type. No solid-like structure is formed upon addition of fumed titania into baseline electrolytes due to its relatively large primary particle size of

22 nm. In addition, normalized viscosity of fumed titania-based composite electrolytes is independent of oligomer M_w. Composite electrolytes containing fumed silica A200 are gels because of strong interactions among silica particles. There is a liquid (suspension) to solid (gel) transition of composite electrolytes containing fumed alumina and binary mixtures of fumed silica and alumina between 5 to 10 wt% in PEG-dm (250) + LiTFSI (Li:O=1:20) at 25°C. In general, normalized viscosity, elastic modulus, and yield stress of gel-type composite electrolytes containing fumed silica and binary fumed silica and alumina mixtures decrease with increasing oligomer M_w at 60°C (above the melting point of electrolyte). The reduction in structure strength may be ascribed to enhanced interactions between surface hydroxyl groups on fumed oxides and polyether oxygens that reduce the number of accessible –OH groups for interactions among fumed oxide particles, which dictates the strength of solid-like structure. Composite electrolytes containing 10 wt% fumed alumina are gels with three-dimensional network in low-M_w oliogmers (M_w = 250 and 500, liquids at room temperature) but are suspensions in medium-M_w oliogmers (M_w = 1000 and 2000, solids at room temperature) at 60°C.

8.1.3 Interfacial Stability Between Electrolyte and Lithium

Li/electrolyte/Li, Li(Ni)/electrolyte/Li, and full-cell cycling data show that fumed silica stabilizes the lithium/electrolyte interface, as shown by a lower polarization and interfacial resistance of a Li/composite-electrolyte/Li cell compared to a Li/baseline-electrolyte/Li cell. Also, Li(Ni)/electrolyte/Li cycling data show that a higher cycling efficiency is achieved with composite electrolytes; a full cell with composite electrolytes

shows a higher discharge capacity and less capacity fade than that with a baseline electrolyte. Although the fumed silica-surface chemistry does not affect the stabilizing effect on the lithium-solvent interface, it does affect the extent of stabilization. The best-improved interfacial stability from Li/electrolyte/Li and full-cell cycling results is seen between lithium and A200 with hydroxyl surface groups. The improvement effect increases with the content of fumed silica due to an increase in electrolyte elasticity. Newman [1] predicted from his modeling work that electrolytes with higher values of shear modulus (elasticity) are more likely to inhibit dendrites, thus resulting in a better interfacial stability between electrolyte and lithium.

8.1.4 Effect of Cathode Composition on Cell Performance

Composite electrolytes show higher capacity than filler-free electrolyte under all operating conditions in the order of 10% A200 > 10% R805 > filler-free regardless of cathode materials. The increase in capacity and capacity retention upon addition of fumed silica can be ascribed to the improved interfacial stability with lithium and the decrease in cell polarization because of the impurity-scavenging and elasticity-enhancing effect of fumed silicas. Hydrophilic A200 has a better impurity-scavenging effect and higher elasticity than hydrophobic R805 because of a higher number of surface hydroxyl groups and stronger hydrogen bonding.

Cell discharge capacity is greatly affected by cathode active material, carbon type, and current collector material. Among three types of cathode active material ($LiCoO_2$, V_6O_{13}, and Li_xMnO_2) tested, Li/Li_xMnO_2 cells show no noticeable capacity fade while

$Li/LiCoO_2$ cells render the fastest capacity fade. Lithium/vanadium oxide (V_6O_{13}) cells deliver the highest percentage of practical capacity but still suffer severe capacity fade. For the applications that require high power and capacity but can tolerate a certain degree of capacity fade, V_6O_{13} will be the best cathode candidate among three. If the applications require large-size power storage for long-term operations, Li_xMnO_2 is the best cathode material. Carbon additive type also plays a significant role in cell cycling performance: $Li/LiCoO_2$ cells with various carbon additives deliver discharge capacities in the order of KJB EC-600JD > SFG 15 > SFG 44 > Vulcan XC72R. Larger-surface area (smaller-particle size) renders higher capacity within the same carbon type: SFG 15 (8.5 m^2/g) > SFG 44 (4.3 m^2/g) for graphite and KJB (1250 m^2/g) > Vulcan (254 m^2/g) for carbon blacks. Normally, carbon blacks have higher electrical conductivities than graphite due to their amorphous structure and larger-surface areas. However, the huge increase of surface area from graphite to carbon black also introduces non-uniform dispersion problem associated with small particles. The non-uniform dispersion may account for the lowest capacity seen using Vulcan carbon black. The increase of PVDF binder amount in KJB-containing cathode along with the superior electrical conductivity of KJB carbon, however, provides the highest capacity. Pitting corrosion of widely used Al current collectors exists in all systems, especially with LiTFSI salt at voltages above 3.5 V. The corrosion greatly reduces capacity and capacity retention. A nickel foil and carbon fiber shows better corrosion-resistance than an Al foil current collector, and thus enhances cell cycling performance. In order to obtain best performance of rechargeable a metallic lithium battery, the optimization of all cell materials including electrolyte,

cathode active material, electronic conductors, and current collector material is required, which is a study beyond the scope of my research.

8.2 Recommendations

8.2.1 Systematic Study of Lithium-Ion Transport in Fumed Oxide-Based Composite Electrolytes

This work investigated the lithium-ion transport properties based on PEO oligomers and LiTFSI salt at a fixed Li:O ratio (1:20, ~1 mol/kg). Effect of lithium salt type and content can also be studied. Lithium salts of interest are $LiClO_4$, lithium triflate ($LiCF_3SO_3$), lithium methide ($Li[C(SO_2CF_3)_3]$), and lithium bis(perfluoroethylsulfonyl)imide (LiBETI, $Li[N(C_2F_5SO_2)_2]$). Salt concentration can be extended to a range roughly from 10^{-6} mol/kg to 10 mol/kg depending on the solubility of salt in PEO oligomers. We can also extend PEO solvent from oligomers to high-M_w (M_w = 6 $\times 10^5$, 4×10^5, and 5×10^6) polymers to correlate data in both low-M_w and high-M_w systems. All fumed oxides studied in this work have Lewis acid surface groups (-OH groups). We can purposely change the acidity of surface groups by high-temperature calcinations of fumed oxides (e.g., 900°C for fumed silica [2]) to reduce surface hydroxyl groups. Capiglia et al. [2] observe a higher conductivity upon addition of fumed silica calcined at 900°C than addition of fumed silica dried at 100°C in amorphous PEO_8-$LiClO_4$ and PEO_8-$LiN(CF_3SO_2)_2$ systems. This increase in conductivity might be ascribed to the change of surface acidity of fumed silica.

This work has demonstrated that addition of fumed oxides increases conductivity at temperatures below T_m (semicrystalline electrolytes) but decreases conductivity at temperatures above (amorphous electrolytes). In this work, ion-pairing is studied using FTIR at room temperature for composite electrolytes with all M_w studied (electrolytes are amorphous at M_w = 250 and 500 and semicrystalline at M_w = 1000 and 2000). The FTIR measurements should also be taken at temperatures above and below T_m to see whether there is any difference in ion aggregation when electrolytes are amorphous and semicrystalline.

Scrosati et al. [3-5] and Kumar and Scanlon [6] observe an increase in conductivity of composite electrolytes after annealing at temperatures above the melting point and the enhancement in conductivity increases with increasing annealing temperature. Such enhancement is ascribed to the preservation of amorphousness of composite electrolyte by ceramic fillers. In this work, all conductivity data are obtained from low- to high-temperatures in a heating scan. We can also measure conductivity data for several heating and cooling scans, i.e., measure conductivity from low- to high-temperatures first, followed by annealing electrolytes at 100°C for a certain period of time, then measure conductivity from high- to low-temperatures to see whether there is an increase in conductivity, especially at ambient temperature to see whether fumed oxides can slow the crystallization of EO-based materials.

8.2.2 Rheology Measurements

Solid-like composite electrolytes based on medium-M_w (i.e., 2000) PEO oligomer cannot be rheologically characterized at room temperature using Rheometrics Dynamic Stress Rheometer (DSR II). These electrolytes can be tested on a solid analyzer, RSA II (Rheometric Scientific). Thus, rheological properties of composite electrolytes at both amorphous and semicrystalline state can be characterized. This work illustrates that gel strength (elastic modulus and yield stress) decreases with increasing oligomer M_w at temperatures above T_m (amorphous state). However, gel strength increases at temperatures above T_m, as evidenced by visual observation. Apparently, there are two different mechanisms that control electrolyte microstructure. By correlating elastic modulus and critical strain (where yield stress appears) with filler volume fraction [7], we can obtain the fractal dimension (i.e., microstructure) of composite electrolytes at amorphous (data from DSR II) and semicrystalline (data from RSA II) states. For that purpose, more samples have to be prepared with a larger range of volume fraction than that used in this work.

8.2.3 Interface Between Composite Electrolyte and Lithium

This work mainly used electrochemical techniques to study the interface between composite electrolyte and lithium at room temperature. The change of interfacial resistance of lithium/electrolyte/lithium cells should also be tested by electrochemical impedance spectroscopy during storage and cell cycling at different temperatures to see

how temperature affects interfacial stability, especially for the comparison of composite electrolytes at amorphous and semicrystalline states.

The morphology of deposited lithium on lithium anode surface is an important indicator of interfacial stability between lithium and composite electrolytes. Since it is hard to remove gel-type fumed oxide-based electrolytes on lithium surface after cell disassembly, it is impossible to characterize surface morphology of lithium post cycling using scanning electron microscopy (SEM). An alternative way is to use optical microscopy equipped with a digital camera to record lithium morphology change. A piece of lithium metal with gel-type composite electrolyte on the surface can be sandwiched between two glass slides, Figure 8.1. Two rubber O-rings with micrometer-size thickness can be placed between the glass slides to fix the thickness of electrolyte on the surface and prevent lithium metal from contacting with atmosphere. The lithium morphology change with time can be monitored since a thin layer of gel electrolytes is transparent. To minimize possible atmosphere contamination, the microscope can be encased in an argon-filled glove bag and the samples can be stored in the glove box between measurements. Cells after cycling can be disassembled in the glove box and the lithium anode with electrolytes on the surface can also be prepared the same way for morphology measurements. In order to monitor *in-situ* the change of lithium morphology during measurement, a cell similar to that reported in the literature [8,9] has to be designed for both electrochemical and microscopic measurements. If a good way can be developed to get rid of gel electrolytes on lithium surface without disturbing the surface

film, SEM and atomic force microscopy can be employed to study morphology and topology of lithium.

Several techniques (FTIR [10-12], X-ray photoelectron spectroscopy (XPS) [13,14]) are reported in the literature for chemical analysis of surface species produced on lithium in rechargeable lithium cells. Lithium must be in contact with electrolytes either at open-circuit or during cell cycling to allow electrochemical and chemical reactions occur at the surface before FTIR or XPS measurements. Since FTIR and XPS are surface characterization techniques, electrolytes must be removed from the lithium surface without destroying the surface film. Removing fumed oxide-based composite electrolytes from the lithium surface and keeping the surface layer intact is extremely difficult. An alternative way is to measure the change in electrolytes after contacting with lithium using FTIR, either transmission or reflectance mode. One type of experiment is to monitor the chemical change at open-circuit. Basically, we can immerse a small piece of lithium metal with a fresh surface into excess electrolytes and take FTIR spectra of the electrolyte to see the change with time. The surface film of lithium can also scraped and mixed uniformly with electrolyte as the FTIR sample. Cells after cycling can also be disassembled in the glove box and the mixture of the electrolyte and the surface film scraped from lithium metal can be used for FTIR measurements.

8.3 References

[1] J. Newman, *Improved electrochemical models*, BATT review meeting (2002).

[2] C. Capiglia, P. Mustarelli, E. Quartarone, C. Tomasi, and A. Magistris, *Solid State Ion.*, **118**, 73 (1999).

[3] F. Croce, G. B. Appetecchi, L. Persi, and B. Scrosati, *Nature*, **394**, 456 (1998).

[4] B. Scrosati, F. Croce, and L. Persi, *J. Electrochem. Soc.*, **147**, 1718 (2000).

[5] S. H. Chung, Y. Wang, L. Persi, F. Croce, S. G. Greenbaum, B. Scrosati, and E. Plichta, *J. Power Sources*, **97-98**, 644 (2001).

[6] B. Kumar and L. G. Scanlon, *Solid State Ion.*, **124**, 239 (1999).

[7] W.-H. Shih, W. Y. Shih, S.-I. Kim, J. Liu, and I. A. Aksay, *Phys. review A*, **42**, 4772 (1990).

[8] C. Brissot, M. Rosso, J.-N. Chazalviel, P. Baudry, and S. Lascaud, *Electrochim. Acta*, **43**, 1569 (1998).

[9] T. Tatsuma, M. Taguchi, and N. Oyama, *Electrochim. Acta*, **46**, 1201 (2001).

[10] D. Aurbach and O. Chusid, *J. Power Sources*, **68**, 463 (1997).

[11] E. Goren, O. C. (Youngman), and D. Aurbach, *J. Electrochem. Soc.*, **138**, L6 (1991).

[12] K.-i. Morigaki, *J. Power Sources*, **104**, 13 (2002).

[13] J. Kuratomi, T. Iguchi, T. Bando, Y. Aihara, T. Ono, and K. Kuwana, *J. Power Sources*, **97-98**, 801 (2001).

[14] D. Aurbach, *J. Power Sources*, **89**, 206 (2000).

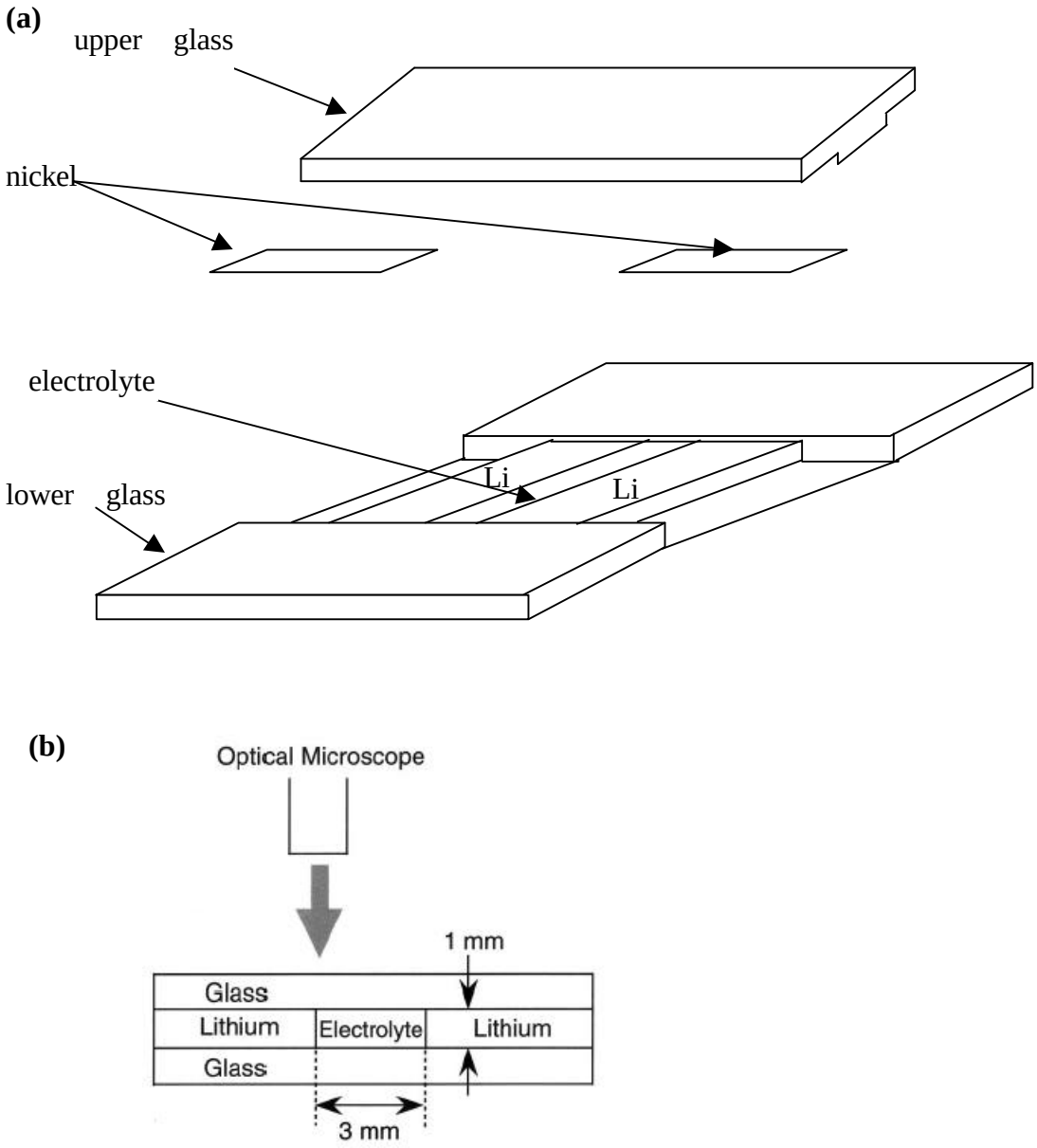

Figure 8. 1. Schematic representation of (a) an electrochemical cell (not to scale) [8], and (b) experimental setup [9] for lithium morphology measurements.